



**UNIVERSITÀ
DEGLI STUDI
DI PADOVA**

**UNIVERSITÀ DEGLI STUDI DI PADOVA
DIPARTIMENTO DI INGEGNERIA INDUSTRIALE**

**CORSO DI DOTTORATO DI RICERCA IN
INGEGNERIA INDUSTRIALE**

CURRICULUM: Ingegneria dei Materiali

CICLO XXVIII

**Direct ink writing of SiOC ceramics from preceramic
polymers**

Direttore del Corso: Prof.Dr.Ing. Giulio Rosati

Coordinatore di curriculum: Prof.Dr.Ing. Paolo Sgarbossa

Supervisore: Prof.Dr.Ing. Paolo Colombo

Dottorando: *Kai Huang*

ANNO 2021

Abstract

Ceramic fabrication from preceramic polymer by Direct ink writing, one of the Additive manufacturing techniques, has attracted a lot of attentions due to the combination of fast and facile processing without de-binding and its ability to fabricate sophisticated structures for meeting increasing requirements of advanced applications. This research focuses on the direct ink writing of SiOC ceramic components from different preceramic polymers with assistive techniques, aiming at addressing the limitations of direct ink writing on fabrication of complex ceramic structures (such as with large overhanging features). In this work, firstly origami was utilized for the secondary shaping on the printed 2D pattern for the structures with large spanning features in terms of high printability and flexibility of a commercially available silicone elastomer. Then, a robotic arm was employed for the printing of cylindrical lattices which is not possible for normal direct ink writing. Besides the controlling of macro ceramic structures achieved by direct ink writing, hierarchical porous structures with controllable pore size from several centimeters to hundreds of nanometers were fabricated with the assistance of sacrificial templates. In addition, to eliminate the influence of gravity on the suspended features, direct ink writing was performed by extruding an ink of preceramic polymer into a soft medium comprised of vegetable oil and fumed silica. Excellent printability was achieved by optimizing the content of fumed silica, printing speed and pressure. With this method, suspended coils and beams with large length-to-diameter ratio were fabricated without shape distortion both after printing and pyrolysis. We also explored the possibility of extending the method to other materials, including metal and ceramic powder, suggesting the high potential in the field of additive manufacturing of multi-materials components system. Finally, we investigated the mechanical properties and permeability of scaffolds with different structures fabricated by direct ink writing, showing the possibility of performance enhancement by structure designing without reducing the porosity. The structure-

relationship from this work could also be extended to other ceramic systems or other materials.

Keywords: Additive manufacturing, SiOC ceramic, direct ink writing, preceramic polymer, porosity

Acknowledgements

I would like to express the deepest appreciations to my supervisor Prof. Paolo Colombo who gave me continuous supporting, creative ideas and quick responses during those rich and full three-year-life at the University of Padova. It's my honor to work with him in the Advanced Ceramic and Glass (ACG) group and enjoy the freedom of putting my ideas into practice for which he would always offer me sincere helps whenever I need. This thesis would not be fulfilled without his help and encouragements. Thanks again to my knowledgeable, patient and gentle supervisor.

I wish to give thanks to Prof. Enrico Bernardo for his wonderful courses like Fundamental Materials Selection and Eco-Informed Materials Choice which brought me a deep sense of materials science and engineering.

A sincere thank goes to Dr. Hamada Elsayed and Dr. Giorgia Franchin who assisted me a lot during my Ph.D. They helped me adopt to the new experimental situation by teaching me how to use 3D printer and furnaces, bringing me to geoscience department for rheological test and chemical department for SEM, discussing about researches and inspiring new ideas, for which I couldn't say more thanks to them.

I would like to give thanks to all members of ACG group with whom I shared the great time both inside and outside laboratory. I express special thanks to all the friends that I met in Italy. It's a great pleasure to spend the beautiful time with you all and gain the friendship that I treasure so much.

Thanks for the chance and financial supporting provided by China Scholarship Council (CSC201804910741).

Finally, I sincerely give my gratitude to my family for their selfless loves. My parents have always been open to my choice of life and given solid backing on the decision of studying abroad. The caring and encouragements from my sisters always raised my spirits as well as the joys my cute nephews brought to me. I couldn't make it this far without their support, for which I owe them a lot.

Table of Content

Abstract.....	3
Acknowledgements.....	5
Table of Content.....	7
1. Overview on polymer-derived ceramics	11
1.1 Introduction	11
1.1 Structure and Synthesis of preceramic polymers	12
1.2 Processing of preceramic polymers.....	15
1.3 Structures and Properties of PDCs	18
1.4 Applications of PDCs	24
1.5 Additive manufacturing of PDCs	29
1.5.1 Direct ink writing.....	30
1.5.2 Vat photopolymerization.....	33
1.5.3 Fused Deposition Modeling.....	37
1.6 Aim of research	39
1.7 Summary.....	39
1.8 References	40
2. Production and properties of SiOC ceramic structures from a silicone elastomer	54
2.1 Complex SiOC ceramic structures by direct ink writing and origami	54
2.1.1 Introduction	54
2.1.2 Experimental Section.....	56

2.1.3	Results and Discussion	59
2.1.4	Conclusions	73
2.1.5	References	74
2.2	SiOC scaffolds with tunable structure-performance relationship.....	78
2.2.1	Introduction	78
2.2.2	Experimental.....	79
2.2.3	Results and discussion.....	81
2.2.4	Conclusions	95
2.2.5	References	96
2.3	Cylindrical SiOC lattices by Direct Ink Writing with a robotic arm	102
2.3.1	Introduction	102
2.3.2	Materials and Methods	104
2.3.3	Results and Discussion	108
2.3.4	Conclusions	115
2.3.5	References	116
3.	Hierarchically porous polymer-derived SiOC scaffolds from a silicone resin and fillers	118
3.1	Introduction	118
3.2	Experimental.....	120
3.2.1	Ink preparation for DIW	120
3.2.2	Fabrication of porous scaffolds by DIW	121

3.2.3	Characterization.....	121
3.3	Result and discussion.....	123
3.3.1	Rheological properties of the inks	123
3.3.2	Pyrolysis and microstructure of printed scaffolds	125
3.3.3	Mechanical properties of printed scaffolds.....	138
3.4	Conclusions	144
3.5	References	146
4.	Embedded Direct Ink Writing of Freeform Ceramic Components	151
4.1	Introduction	151
4.2	Experimental.....	153
4.2.1	Materials	153
4.2.2	Preparation of the supporting medium	154
4.2.3	Preparation of the inks	154
4.2.4	Heating treatments	155
4.2.5	Characterization.....	155
4.3	Result and discussion.....	155
4.3.1	Rheological properties.....	155
4.3.2	Ink printability and control of the filament diameter in different supporting media.....	162
4.3.3	Embedded DIW	166
4.4	Conclusions	173

4.5	References	174
5.	Concluding remarks and future perspectives	176
	Curriculum Vitae.....	178
	List of publications related to this thesis.....	179
	List of conference presentations related to this thesis	180

1. Overview on polymer-derived ceramics

1.1 Introduction

Preceramic polymers are precursors for the fabrication of mainly silicon-based ceramics which have been denoted as polymer-derived ceramics (PDCs). It generally comprises inorganic/organometallic systems that provide a tailored chemical composition and a closely defined nanostructural organization by proper thermal treatment under a controlled atmosphere[1]. Even though the first production of non-oxide ceramic from molecule precursors was reported by Ainger and Herbert[2], as well as Chantrell and Popper[3] in the early 1960s, the active research on preceramic polymer happened in early 1970s prompted by the demand of modern high technologies, especially high-temperature ceramic for replacing metal and metallic alloys in defense/aerospace industry[4]. In 1974, Verbeek and Winter[5,6] reported for the first time the transformation of polysilazanes from polymer to ceramic to obtain $\text{Si}_3\text{N}_4/\text{SiC}$ ceramic fibers for high-temperature applications. Then, the fabrication of SiC ceramic fibers was reported by Yajima[7] through pyrolysis of polycarbosilanes. Ever since then, the field of preceramic polymers witnessed a rapid development into a large family consisting of polysilane, polycarbosilane, polysiloxane, polysilazane, polyborosilazane, polyborazine, etc. Meanwhile, the composition of PDCs extended from most classic binary systems (Si_3N_4 , SiC) to ternary (SiOC, SiCN) and quaternary (SiBCN, SiAlCN), even pentanary systems (SiHfBCN, SiHfCNO)[8-20], which are difficult to fabricate by traditional ceramic fabrication methods. Consequently, during last 30 years, there has been a rapid increasing in the publications concerning PDCs, with total number up to 2989 (**Fig. 1.1**). In Particular, the number of publications clearly denoted as “PDCs” in the past 10 years (2010–2020) is around 2000, which is more than that of all the publications before 2010.

Total Publications
2,989 Analyze

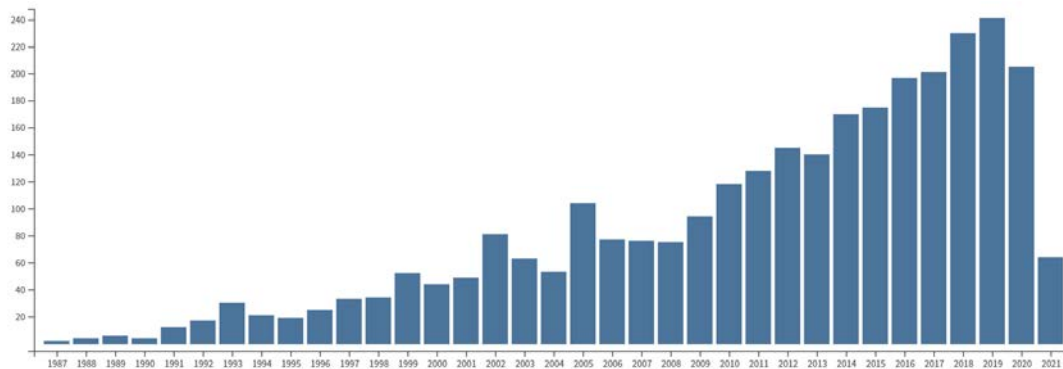


Fig. 1.1 Number of publications resulting from a search with the keyword “polymer derived ceramics” in “All databases” on “web of science”, from 1987 up to the end of April 2021.

Differing from the conventional ceramic processing technology involving powder processing and sintering at high temperature, PDCs from preceramic polymer can be fabricated at relative lower temperature (e.g., 1100 – 1300 °C) and the precursors are quite suitable for ceramic fiber[21,22], coating/films[23-25], and ceramic matrix composites[26-28], which is not easy for powder processing technology. Owing to the ability of designing molecule structures at the nanoscale level, the desired structural and functional properties could be achieved easily, such as high hardness and strength, wear resistance, excellent thermal stability and chemical stability, which have found the important interest in several fields including high temperature thermal barrier coating[29,30], energy storage[31-34], electromagnetic absorbing and shielding[35-37], biomedical and tissue engineering[38-43] and so on.

1.1 Structure and Synthesis of preceramic polymers

To fabricate PDCs, the synthesis of the preceramic polymer is a key step since the phase composition and microstructure of final produced ceramic would be greatly affected by the chemical composition and molecular structure of the preceramic polymer. Therefore, the structural and functional properties of PDCs vary as a function

of the different design of the preceramic polymers. In addition, in order to meet the requirement of thermal pyrolysis processing and practical applications, preceramic polymer should possess a suitable chain structure to avoid the volatilization and assure high ceramic yield, appropriate solubility for shaping, latent reactivity (presence of functional groups) for the curing and cross-linking step.

Here, the preceramic polymers are mainly divided into polysilane, polycarbosilane, polysilazane, polysiloxane, polysilylcarbodiimide, representative synthetic routes of which have been summaries in **Fig. 1.2**.

(1) Polysilane is a kind of polymer with a simple one-dimensional silicon backbone ($-R_1R_2-Si-$). Its properties and functions are mainly affected by the side chain groups attached to silicon and the molecular weight. Owing to promising optoelectronic and photochemical properties derived from the delocalization of σ electrons along silicon backbone (σ conjugation), Polysilane has found its applications in many fields involving photoresists, photoconductors, and semiconductors[44-46]. Besides the most common synthetic method in which chlorosilanes react with sodium or lithium dispersion (Wurtz-like coupling reaction) followed by reducing in boiling solvents[47], the catalytic dehydrogenation of silanes[48,49] and anionic polymerization of masked disilenes[50,51] have also been employed to form polysilane.

(2) Polycarbosilane has a general backbone structure of $-R_1R_2-Si-R-$, in which R represents organic groups like methylene, vinylidene, phenylene, etc. Several methods have been reported concerning synthesis of polycarbosilane, including the most commonly used Kumada rearrangement of polysilanes[52], ring-opening polymerization[53], dehydrocoupling reaction of trimethylsilane and Grignard coupling reaction[54]. As the precursor of SiC, Polycarbosilane is a good candidate (such as PCS- $[MeHSiCH_2]_n-$ and PMCS (PCS with metal $M = Ti, Zr, Al$)) for the fabrication SiC fibers because its high ceramic yield. The quality of produced SiC is related to carbon content, which would increase with the increasing of molecular weight[55].

(3) Polysilazane is the preceramic polymer with a backbone structure containing silicon-carbon bonds, mainly used as the precursor of Si_3N_4 and SiCN ceramics[56-58]. Since the first fabrication of polysilazane was reported in 1885[59], there has been several synthesis method developed, among which ammonolysis reactions of chlorosilanes with ammonia or by aminolysis with different primary amines are two popular strategies. However, separating polymeric product from solid byproducts is difficult for both methods[60]. In addition, for the practical purpose of enhancing structural and functional properties, modification of silazane oligomers has been widely explored, such as using KH basic catalyst, transition-metal complexes and urea or isocyanate-containing compounds[61-63].

(4) Polysiloxane, also denoted as silicone, is composed of basic silicon-oxygen bonds, and has been widely used in industries due to its excellent physical and chemical properties[64,65]. These properties result from the segmental chain mobility related to intrinsic chain flexibility and weak interaction between and within molecules[66]. The general formation of polysiloxane involves reaction between chlorosilanes with water, mainly including ring-opening polymerization of cyclic silaethers and the polycondensation of linear silanes terminated with active functional groups[67-69]. In order to achieve a high degree of cross-linking and then a high ceramic yield, modification of polysiloxane has been also extensively reported in recent years. Generally, this is achieved by grafting chain groups suitable for thermal or UV light curing[70]. Furthermore, sol-gel method involving co-hydrolysis and polycondensation was used for controlling and tuning composition of produced polysiloxane, for example, the content ratio of silicon to carbon and doping of metal within pyrolysis production of SiOC[71-73].

(5) Polysilylcarbodiimide is the second class of precursors of SiCN , with general formula of $-\text{[R}_1\text{R}_2\text{Si-X]}_n-$, where X is N=C=N and R groups represent hydrogen, phenyl, methyl, ethyl, and others[74]. The synthesis of polysilylcarbodiimide was firstly reported by Pump and Rochow as well as Klebe and Murray with dichlorosilanes and

disilylcyanamide or chlorosilanes and bis(trimethylsilyl) carbodiimide as starting materials[75,76]. Then, Riedel for the first time explored the transformation of Polysilylcarbodiimide to SiCN ceramics, which greatly inspired the interest of researchers in this field[77-79]. The microstructures and thermal properties of its PDCs could vary depending on the structure of Polysilylcarbodiimide resulting from different starting materials, such as dichloro silanes generating cyclic or linear polymers and trichloro silanes generating highly branched ones[74,80-82]. It is worth noting that first ternary crystalline in Si-C-N system (SiC_2N_4 and Si_2CN_4) was fabricated from polymers synthesized by reaction of tetrachloro silane with bis(trimethylsilylcarbodiimide)[20].

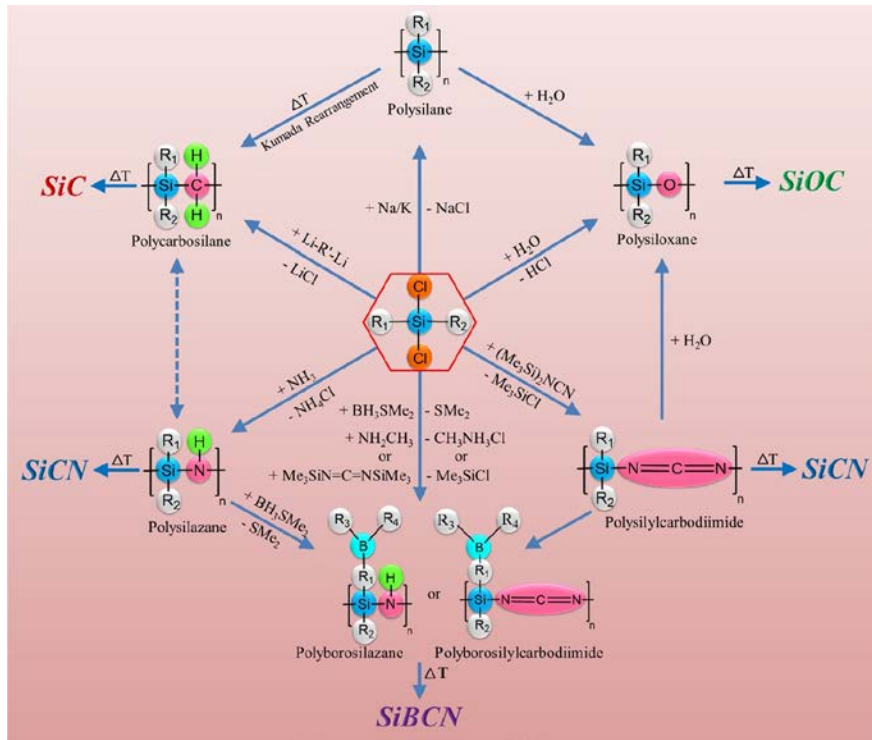


Fig. 1.2 Synthetic routes for the most representative classes of Si-based polymers and corresponding ceramics from organo-chlorosilanes[83].

1.2 Processing of preceramic polymers

In general, the processing of preceramic polymers to produce ceramics includes

shaping, cross-linking, pyrolysis and ceramization, as indicated in **Fig. 1.3**.

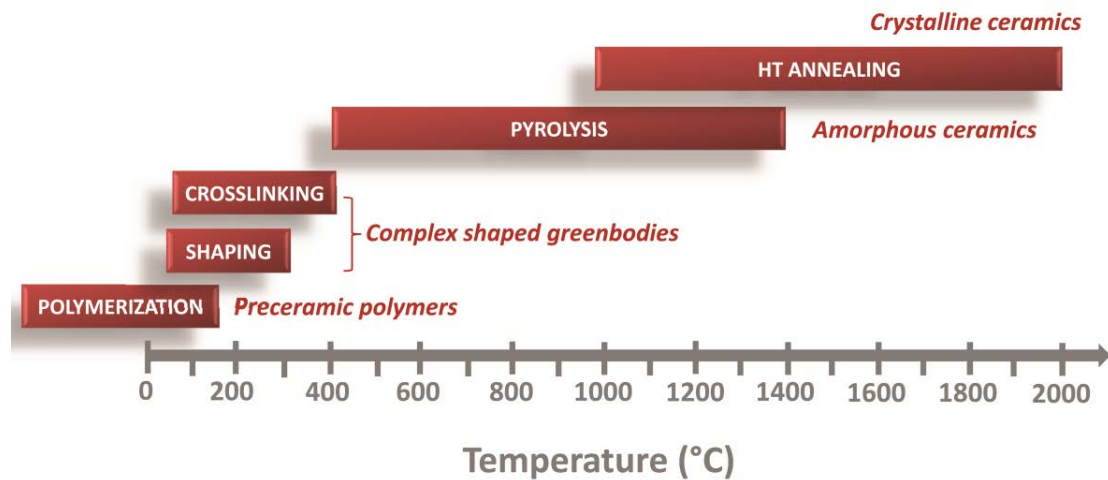


Fig. 1.3 Polymer-to-ceramic transformation of preceramic polymers[84].

Compared with the ceramic powder technologies, the shaping of preceramic polymer is highly facile and flexible without requiring long processing involving powder preparation and drying since preceramic polymers usually are soluble in several organic solvent or meltable under low temperature ($< 150\text{ }^{\circ}\text{C}$). This allows for a variety of shaping methods available for preceramic polymers, including injection molding[85], impregnation/infiltration[86-88], blow molding[89,90], extrusion molding[91,92], coating[23,24,93], electrospinning[22,94,95], 3D printing[96-98], etc.

The second step is cross-linking of preceramic polymers with assistance of catalysts, triggered by heating or radiation at low temperature. Cross-linking plays an important role in processing, not only for the capability of retaining its shape during subsequent pyrolysis but also for avoiding the evaporation of oligomers and increasing the ceramic yield[99-101]. It's worth noting that the extent of cross-linking would affect the rheological properties of preceramic polymers, especially in extrusion-based processing like direct ink writing. Furthermore, several curing methods have been explored depending on the functional group grafted to backbone of preceramic polymers, such as oxidative curing[102], γ radiation[103,104], e-beam[105], UV

light[106,107], etc. it should be pointed out that cross-linking may be not necessary when fillers are added into the preceramic polymer due to their ability to offer sufficient support to the polymer matrix. In some typical cases, for instance where SiC or Si₃N₄ was used as filler, additional advantages would be afforded, such as reducing the shrinkage and minimizing the presence of defects (pores or cracks)[108-110].

As shown in **Fig. 1.4**, depending on the X in the preceramic polymer -R₁R₂-Si-X-, several PDCs could be obtained from the thermal decomposition of silicon-based polymers with various ratio of Si to X, including SiC, Si_xC_yO₂, Si_xC_yN_z. In addition, the ratio of Si/C could be tuned by the composition of organic group of R₁ and R₂. Generally, the pyrolysis involves the decomposition and elimination of organic parts such as Si-H, Si-OH, Si-NH_x, as well as methyl, phenyl, vinyl groups. Subsequently, the ceramization step at higher temperature could lead to amorphous or crystalline ceramics with volume shrinkage up to 50 vol%, sometimes which might introduce pores and cracks into produced PDCs, especially for bulk components. To complete the polymer-to-ceramic conversion, various methods were reported including thermal and non-thermal processing, specifically plasma spraying and laser pyrolysis for ceramic coating and nanoceramics[111-113], microwave pyrolysis for nanocomposites and ceramic joining[114-116], ion irradiation for ceramic film[117,118]. Parameters concerning pyrolysis and ceramization would determine the microstructures and composition of the produced ceramics, involving heating rate and temperature, atmosphere, pressure, dwelling time, etc., which have been widely evaluated by previous literature[119-122]. It deserves to be mentioned that the ceramization of preceramic polymer might be not necessary to complete in some cases, where micro- and meso-porous structures, net-shape processing and lower thermal resistance are desired[123,124].

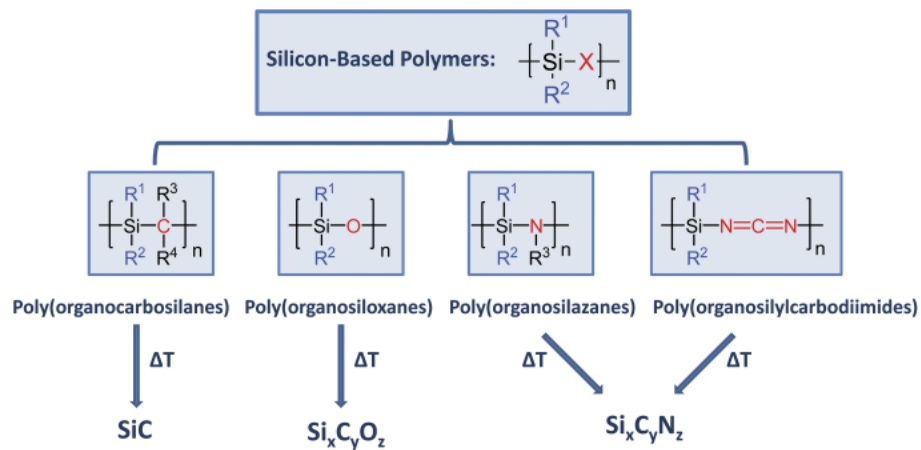


Fig. 1.4 Thermal decomposition of silicon-based polymers (oversimplified representation of the molecular structure of the precursors)[125].

1.3 Structures and Properties of PDCs

(1) Binary silicon-based ceramics

SiC and Si₃N₄, as the most common binary PDCs, are derived from polycarbosilane and carbon-free polysilazane. In general, the detection of free carbon in polycarbosilane-derived SiC is inevitable, especially at intermediate temperature. In order to understand the evolution of polymer-derived SiC, Want et al. fabricated SiC powder using polycarbosilane under different pyrolysis temperature from 1300-1900°C. As shown in **Fig. 1.5**, SiC nanocrystal, turbostratic and amorphous carbon were detected in all the samples. With the increasing of temperature, SiC nanocrystal size and turbostratic content increased, meanwhile, the residual carbon tended to transform from amorphous into turbostratic structure because of a phenomenon of regional enrichment, Consequently, leading to large impact on the performance of microwave absorbing materials[126]. Yao et al. fabricated continuous free standing SiC films from polycarbosilane using two different curing method, oxidation and irradiation. SiC film from irradiation demonstrated larger size of nanocrystal β-SiC and higher volume ratio of free carbon phase than oxidation, resulting in higher electrical conductivity. In addition, the high modulus and surface hardness suggests a promising application in microelectromechanical systems[127].

Si_3N_4 has attracted lots of attention due to its excellent mechanical and thermal properties, widely used for high-temperature applications like turbine engine[128,129]. Perhydro-polysilazanes, containing only Si, N, O, were employed to prepare Si_3N_4 composed of fine crystallites[130]. Yang et al. fabricated ultralong single-crystalline α - Si_3N_4 nanowires from polyureasilazane with FeCl_2 as catalyst without detected structural defects or amorphous layers[131]. However, compared with SiC, there are relatively less reports concerning single-phase Si_3N_4 from preceramic polymer due to the existence of free carbon, which leads to the formation of Si-C-N instead. To conclude, the polymer derived SiC and Si_3N_4 ceramic have been applied in several applications for their high strength, chemical stability, thermal-shock resistance, high hardness, etc.

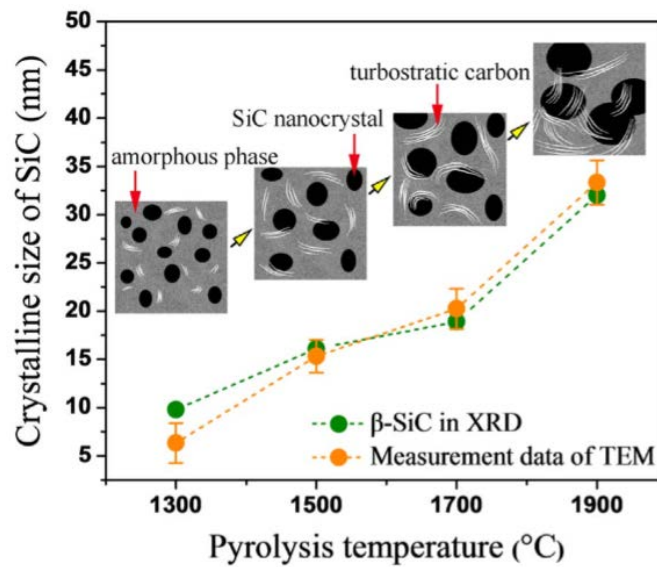


Fig. 1.5 The size of SiC nanocrystals pyrolyzed at different temperatures and schematic illustration of microstructural evolution of the PCS-derived SiC[126].

(2) Ternary silicon-based ceramics

SiOC is a typical ternary PDCs which has high flexibility in tuning microstructures and phase composition depending on the pyrolysis temperature. At low pyrolysis temperature (< 1100 °C), according to the analysis using TEM, NMR, XRD, SAXS,

etc.[132], it is assumed that the microstructure (as indicated in **Fig. 1.6a**) of SiOC consists of cluster of silica tetrahedra (Si-C and Si-O but no C-O) that form a nanodomain core, surrounded by a monolayer of mixed bonds of $\text{SiO}_{4-n}\text{C}_n$, and a graphene cage-like network that encases the domains. Another model[133] (**Fig. 1.6b**) was proposed in which O-rich SiO_xC_y structural units forms a fractal backbone while carbon-rich SiO_xC_y structural units are located as interface between the backbone and free carbon. Consequently, besides the carbon (sp^3 -hybridized) incorporated inside the SiOC network, the second carbon was defined as free carbon (sp^2 -hybridized) segregated from SiOC phase[134]. At higher temperature, SiOC evolves into more thermodynamical stable β -SiC, amorphous SiO_2 nanodomain and free carbon[135,136]. Compared with silica or silicate ceramic, the presence of amorphous carbon within SiOC provides a network with a significantly higher connectivity. Some studies[137-139] have reported that the nanodomain is the key factor of high performance of SiOC, such as high Young's modulus and hardness, and thermal-mechanical durability. Furthermore, the content of free carbon also greatly affects the mechanical properties of polymer derived SiOC. Sorarù et al. revealed that the Young's modulus and the hardness decrease with increasing of free carbon content[140]. Hyojun Lim et al. used phenyl group-containing additives to tune the free carbon content of SiOC as potential anode for lithium-ion secondary batteries, in which a remarkable electrochemical performance was achieved[141]. In addition, other functional properties have been explored for practical applications like thermal transport[142-144], piezoresistive behavior[145-147], optical properties[148-150].

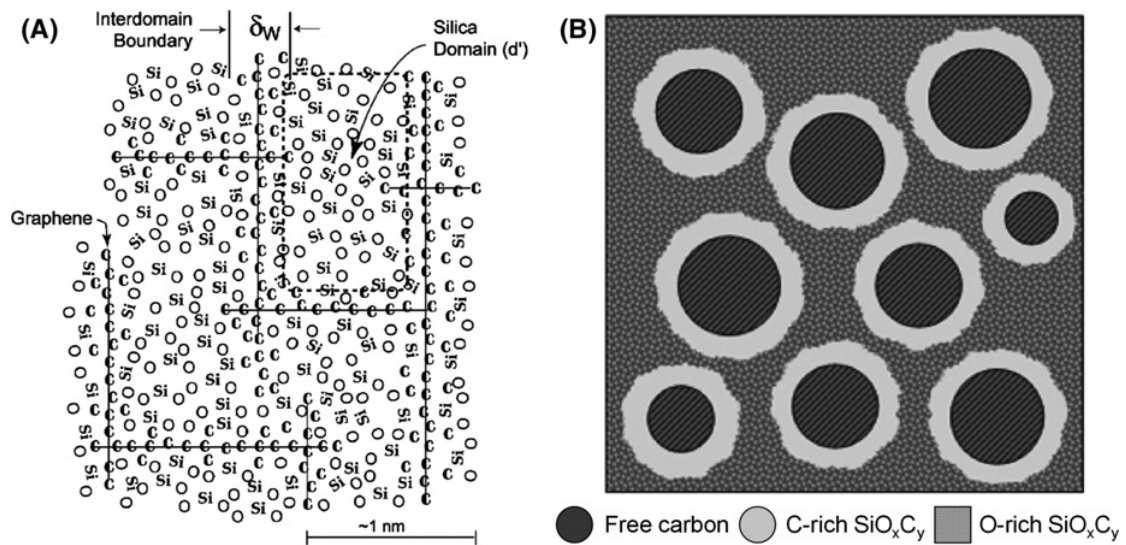


Fig. 1.6 Two models of nanodomain structures in polymer-derived SiOC[132,133].

SiCN is another ternary PDC which remains amorphous up to 1400 – 1500 °C in inert atmosphere such as N₂[56,151]. The microstructure of polymer derived SiCN varies from different precursors. As shown in **Fig. 1.7**[80,125], polysilazanes-derived SiCN has single amorphous SiC_xN_y phase in which Si is bonded to C and N without phase separation. While, in the case of polysilylcarbodiimides, three amorphous phases were found in derived SiCN without mixed bonds, namely Si₃N₄, SiC and C cluster, forming a particular structure that retards the crystallization and phase partitioning processes of the thermodynamically stable phases Si₃N₄ and SiC. Furthermore, the crystallization behavior of polymer-derived SiCN is related to the chemical composition, molecular structure, and chemical homogeneity of the amorphous Si-C-N network. Research have found that high content of free carbon in SiCN works as a diffusion barrier, leading to higher resistance to crystallization[152,153]. Similarly to SiOC, the mechanical properties are strictly related to the carbon content, and a correlation was found between the amount of free carbon vs carbide carbon and the associated elastic modulus and hardness[154,155]. Liu et al. investigated the dielectric and microwave absorption properties of polymer-derived SiCN ceramic, where increasing the annealing temperature helps to improve the permittivity and then microwave absorbance[156,157]. Electrochemical properties of SiCN were studied for

its application in Li ion battery, revealing that the free carbon phase acts as an active site for the insertion of Li ions while the amorphous SiCN network provides a path for Li-ion transfer[158,159].

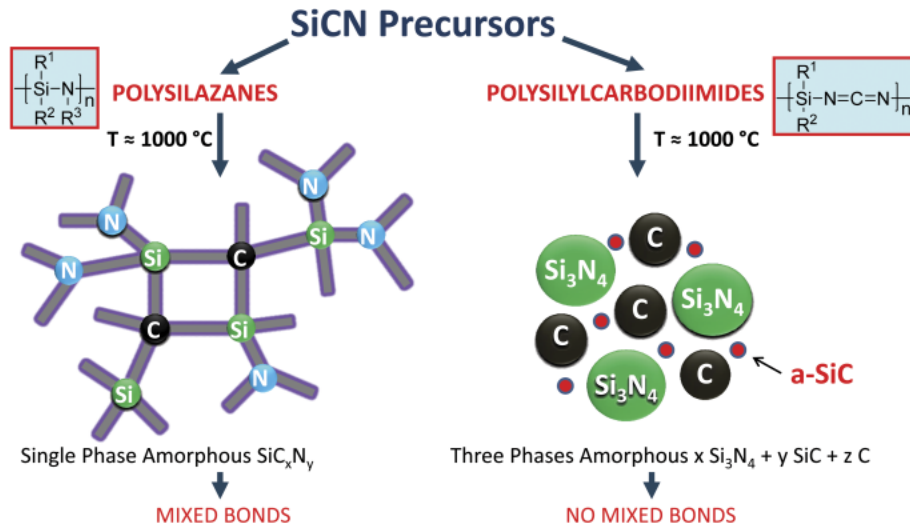


Fig. 1.7 Microstructure of amorphous SiCN ceramics derived from polysilazanes and from polysilylcarbodiimides[80,125].

(3) Quaternary silicon-based ceramics

The most common quaternary PDCs are achieved based on the ternary PDCs by the introduction of boron. For example, SiBCN is very thermally stable with high crystallization temperature over 1800 °C because of the low atomic mobility in this system[160]. It was proposed that boron would react with nitrogen in SiBCN to produce turbostratic BN, which is located at the interface of nanocrystalline Si₃N₄ and SiC phase and prevents the further crystallization of these phases[161]. Wang et al.[162] reported that the main structural units of amorphous SiBCN fiber sintered at 1400°C are Si–N, B–N, sp²-hybridized C–C, and Si–C bonds (as indicated in **Fig. 1.8**). Research has reported that lowering content of boron would result in decreasing of electrical resistivity and optical gap, allowing to tailor the properties of SiBCN toward high thermal stability and electrical conductivity[163]. In addition, the electromagnetic wave absorption of SiBCN was explored with respect to the temperature and dopant

type[164-166]. Considering the excellent thermal mechanical properties, SiBCN found extensive interest in high-temperature application. Besides the doping of boron, many studies have been performed on the doping of a variety of alloys and metal oxides into SiCN. For example, hafnium alkoxide-modified polysilazane was employed to fabricate SiHfCN(O) with Hf phase that was distributed throughout the SiCN(O) matrix[167]. It is worth noting that there was a phase separation without mixed bonds (such as SiN₄ sites and segregated free carbon phase), which was different from the structural composition of polysilazane-derived SiCN in which only single-phase SiC_xN_y existed. It was assumed this happened as the consequence of the molecular structure of modified polysilazane, which greatly affected the rearrangement processes in the polymer-to-ceramic transformation.

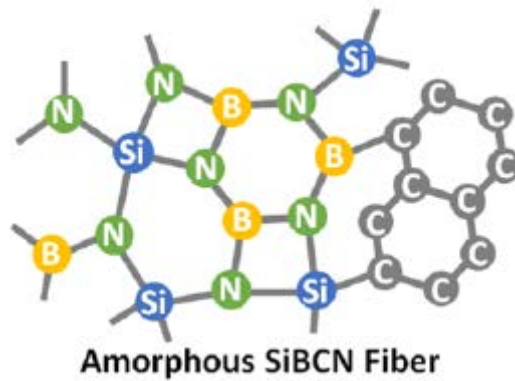


Fig. 1.8 Schematic of amorphous SiBCN fiber sintered at 1400°C[162].

Similar investigations were also carried on SiOC ceramics by incorporating metal oxides. The thermal stability of SiAlOC was highly enhanced by the introducing of aluminum due to its ability to hinder the carbothermal reduction[168]. The chemical shift of Si depended on both the number of bridging oxygens (m) per SiO₄ unit and the number of aluminum ions (n) connected by oxygen with the SiO₄ unit. Si-O-Al linkage was formed in the system with the increasing of temperature. Liviu et al.[169] introduced nano-sized aluminum into polymethylsilsesquioxane to decrease the crystallization temperature to 800°C, owing to the high reactivity between nano

aluminum and amorphous silica. Giant piezoresistivity of polymer-derived amorphous SiAlOC was reported, showing promising application in high-temperature sensors[170]. In addition, other elements, such as Ti, Hf, B etc., were introduced into SiOC for achieving high performances toward applications in photocatalytic, oxidative resistance, medical instruments, luminescence[171-173].

1.4 Applications of PDCs

(1) Fiber and ceramic matrix composites

Ceramic fiber from preceramic polymers has been widely investigated due to its ability of fabricating complex shape and controllable properties by manipulating the composition and properties of preceramic polymers, especially as reinforcement of ceramic matrix composites (CMCs) for high-tech applications, such as engine tail nozzle, supporter of satellite, brake disks for airplane[174]. Two typical methods were applied to fabricate ceramic fibers: melt-spinning and electrospinning[175-178]. As shown in **Fig. 1.9**, the melted polymer goes through the holes and solidifies before being collected to a take-up wheel. For electrospinning, when the voltage surpasses a threshold value to overcome the surface tension, a jet is emitted and moves towards the collector electrode. Both of them will allow the orientation of fibers by stretching extruded fiber using a rotating take-up wheel to create a stronger ceramic fiber with more ordered crystalline. Nippon Carbon in Japan developed the first commercially available SiC Nicalon[®] fiber from preceramic polymer, after which SiBCN, SiTiCO, SiOC, BN fibers have been developed as well[67,179-182].

Generally, the preparation of fiber-reinforced CMCs involves infiltration of the inorganic polymer or silicon into porous woven fiber parts using one of those four technologies, which are polymer impregnation and pyrolysis (PIP), reactive melt infiltration (RMI), chemical vapor infiltration (CVI), slurry infiltration and hot pressing (SIHP)[183]. Each of those processing possesses advantages and disadvantages: suitability to sophisticated components but time-consuming for PIP; fast densification

processing but high tendency of causing damages to fiber for RMI; high purity and well-controlled composition and structures but lower production rate for CVI; difficulty in sintering ceramic powder (e.g. SiC) for SIHP[184]. Therefore, hybrid processing containing two or three processing above is sometimes employed to fabricate CMCs by fully taking advantages of their strongpoints in different phases of processing[185].

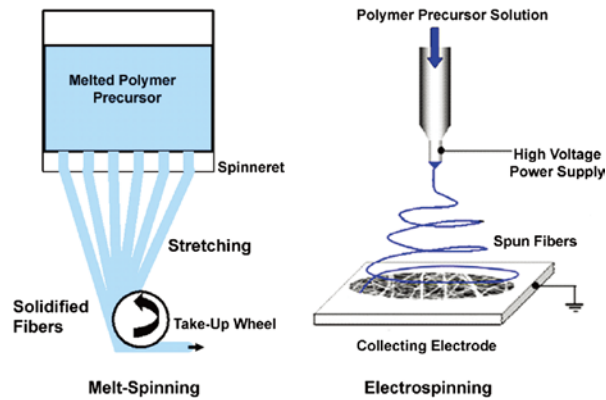


Fig. 1.9 illustration of melt-spinning and electrospinning[186].

(2) Coatings and membranes

Ceramic coating is a promising approach to improve the chemical and physical properties of a substrate by a modification of its surface. Compared with well-established methods including chemical vapor deposition (CVD), atmospheric plasma spraying (APS) and electron-beam physical vapor deposition (EBPVD)[187-189], inexpensive processing of preceramic polymer is an alternative candidate to achieve large-scale deposition of a ceramic coatings on different complex surfaces. Owing to the relatively low processing temperature of preceramic polymer, the damage to substrate materials could be reduce to a minimum. In addition, excellent control of properties of resulted ceramic coating, such as volumetric shrinkage control, enhancement of electrical and thermal properties, could result from the modification of preceramic polymer as well as fillers (as show in **Fig. 1.10**)[29]. What's more, other advantages indicate the applicability of preceramic polymer in ceramic coating, including high ceramic yield, deposition in liquid phase (suspensions and solutions)

and high flexibility concerning the parameter of cross-linking and ceramization[190].

Recently, microporous precursor-derived ceramic membranes have gained attentions due to their application in gas separation such as hydrogen purification, especially at high temperature and in hostile environment. Gurlo et al.[191] prepared hierarchical microporous SiBCN/ γ -Al₂O₃/ α -Al₂O₃ membranes (in **Fig. 1.11**) with higher H₂/CO permselectivities, suggesting the potential in hydrogen separation due to their superior stability under high temperature and pressure. Hauser et al. employed dip-coating to fabricate SiBCN membrane on porous alumina as molecule sieve for high-temperature separation of gas molecule, showing high thermal stability up to 1800 °C[192].

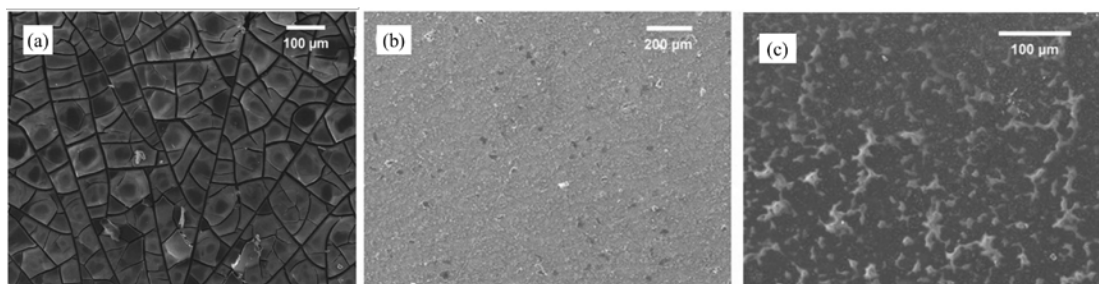


Fig. 1.10 (a) pyrolyzed SiOC coating with cracks, (b) and (c) pyrolyzed SiOC coating with ZrO₂ and Ag fillers, respectively[29].

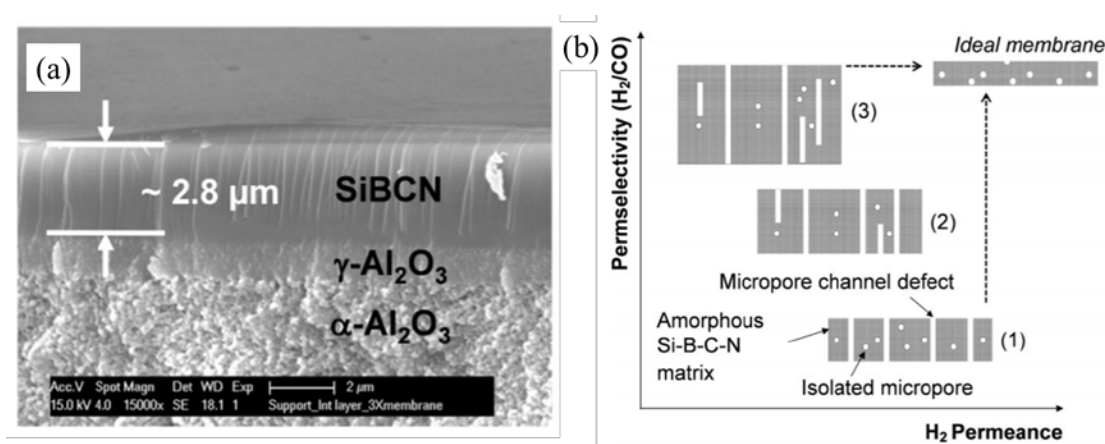


Fig. 1.11 (a) SEM images of the cross-section and relationship between microstructure and porosity in multilayer amorphous SiBCN/ γ -Al₂O₃/ α -Al₂O₃

membranes[191].

(3) Porous components

Ceramic containing tailored porosity usually exhibits different properties compared with their dense counterparts, such as electrical resistivity, thermal conductivity, strength and modulus, etc. (**Fig. 1.12**)[193], resulting in their use in applications including electrode, insulators, heat exchange, biomedicine and catalyst supporters[194]. In term of the different applications, it's not only the chemical composition of ceramic that matters but also the characteristics of pores, such as pore size, morphology, distribution and specific surface area. Generally, interconnected macropores confer high convective heat, improved mixing as well as high mass transfer rate, while the microporous framework provides the desired functionalities. For example, when employed into biomedicine, macro porosity will enable the penetration of cells and micro porosity enhance the attachment of cell due to its high specific surface area[195,196]. Therefore, PDCs components with hierarchical pore distribution could meet the increasing requirements of multi-functions. In addition, the alignment of pores (especially porous ceramic by freeze casting) is capable of greatly improving performances (e.g. thermal and electrical properties, permeability) in one direction[197,198]. So far, several approaches, such as sacrificial templating, etching, emulsion, and additive manufacturing techniques were applied to fabricate porous ceramics from different preceramic polymers[199].

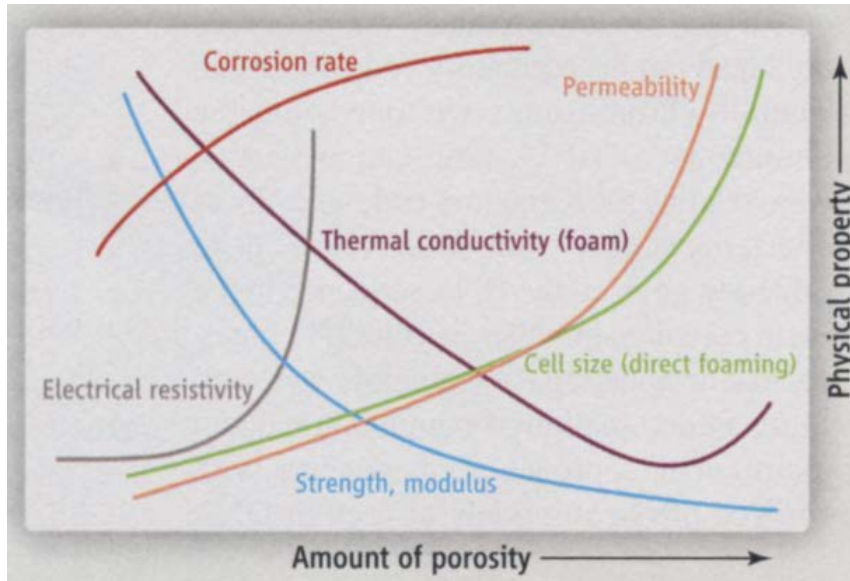


Fig. 1.12 The relationship between physical properties and the amount of porosity[193].

(4) Microelectromechanical systems (MEMS) and semiconductors

Considering the semiconducting features of PDCs of which electrical conductivity is tunable with the variation of annealing temperature[200], PDCs has been widely employed as high-temperature sensor with higher gauge factors (one magnitude higher than other commercial materials, such as Ge, Si, SiC or diamond), for monitoring the environment in jet engine turbines and energy generation turbines[201]. Compared with other materials based on powder route for MEMS, precursors for PDCs could be designed according to the desired functionalities and shaped into sophisticated architectures a liquid route. In addition, with this PDCs processing MEMS with high resolution (sub 100 nm) could be achieved which is several magnitude smaller than that by conventional powder methods[202,203]. Liew et al.[204] firstly investigated the fabrication of SiCN ceramic MEMS (as shown in **Fig. 1.13**) with high resolution from preceramic polymer as well as enhanced mechanical properties in comparison to the powder route. Grossenbacher et al. proposed a molding method with Teflon-like C_4F_8 and carbon coatings for fabricating micrometer-scale PDCs MEMS with high aspect ratio, resulting in precise filling and easy de-molding[205]. Nowadays, PDCs MEMS

are fabricated in way not being possible before by the combination of advanced microfabrication techniques for highly precise controlling of the shape, including lithography, two-photon polymerization 3D printing and thermal scanning probe lithography[206-208].

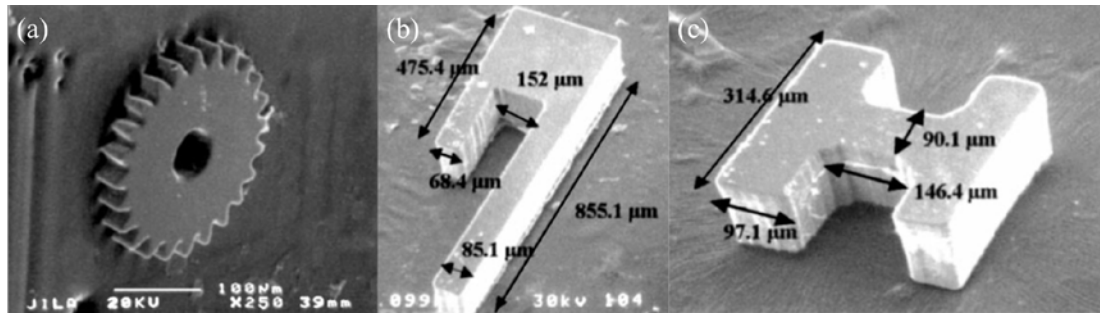


Fig. 1.13 (a) Gear (200mm diameter and 45mm thick); (b) cantilever beam (137mm thick); (c) tensile test sample (142mmthick) [204].

1.5 Additive manufacturing of PDCs

Additive manufacturing (AM) techniques is the standard terms for processing of joining materials into objects from 3D model, as opposed to the traditional subtractive manufacturing technologies[209]. The long history of AM of polymer dates back to the several decades ago due to the properties of polymer materials that it could be easily transferred into liquid from solid by dissolving or melting, and the other way round by solvent evaporation or cooling down or cross-linking, suitable for using as feedstocks for various AM techniques[210]. Considering the difficulties of processing, particularly shaping ceramic into complex architectures in comparison with metal and polymer, combining AM techniques with preceramic polymers could be a promising strategy for the fabrication of complex ceramic components due to their polymeric characteristics and ability of conversion into a ceramic. Differing from powder-based AM in which time-consuming de-binder is required and residual porosity is typically unavoidable, AM of preceramic polymer needs no such processing and enables the fabrication of ceramic components with high density and therefore superior mechanical performances.

Nowadays, several AM techniques have been employed in fabricating ceramic from preceramic polymers.

1.5.1 Direct ink writing

Direct ink writing (DIW), also known as robocasting, is a quite common AM technique based on the robotic deposition of ink extruded from a nozzle, with ease of fabrication and few requirements on the materials except the rheological properties. To enable DIW, the viscosity should decrease with the increasing of shear rate, which is termed as shear thinning behavior that allows ink to be extruded from nozzle under high shear stress and recover to achieve the shape retention after extrusion. In addition, a high storage modulus is required to prevent the sagging or deformation when printing structures with overhangs and spanning features. To achieve this, high content solid fillers in preceramic polymer could help to fabricate ceramic components with large span features, especially cooperating with low-boiling point solvent that contributes to rapid solidification. Zocca et al.[211] reported the fabrication of bio-ceramic scaffolds using polymethylsilsesquioxane with ZnO and CaCO₃ as fillers, which helped to improve the rheological properties of ink and also became part of final ceramic component. Franchin et al.[109] investigated DIW of ceramic matrix composites from poly(methyl-silsesquioxane) (Silres MK, Wacker Chemie AG, Nünchritz, Germany) reinforced by carbon fiber and SiC powder (see **Fig. 1.14**). Therefore, the filler not only help to enable the DIW but also enhanced the performances of printed ceramic components like mechanical properties, biocompatibility, etc. However, this approach may result in the limitation to the resolution which is defined by nozzle diameter, due to the possible clogging rendered by inhomogeneous dispersion or excessive drying. In addition, the ink with suitable rheological properties could also be formed by the assistance of additives like fumed silica, carboxymethyl cellulose and Pluronic F127[212-214], generally forming a reversible network which is sensitive to shear stress.

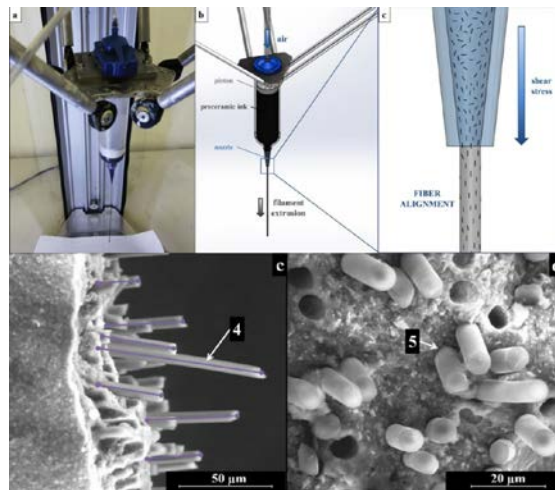


Fig. 1.14 Diagram of DIW of preceramic polymer reinforced by carbon fibers and SEM images of filament cross-section[109].

It's worth noting that, aiming to meet requirements for fabrication of geometrically complex structures, other techniques have been employed to assist DIW for the fabrication of ceramic components from preceramic polymer, like origami/kirigami, UV light, supporting bath, etc. Liu et al.[215] made use of the flexibility of elastomeric poly(dimethylsiloxane) (the preceramic polymer used in their work) to achieve the secondary shaping to the printed green body with origami as well as programmable architectures spanning three orders of magnitude from 200 μm to 10 cm (see **Fig. 1.15a**). In addition, to minimize the influence of viscosity of ink, UV light was used for instant curing during the printing, which enables freeform 3D printing in the air without supporting. Maeng et al.[216] use the ceramic and photocurable polymer to achieve dual-scale porous and self-supporting structures with the assistance of UV light (see **Fig. 1.15b**), which is not possible without any supporting using conventional DIW technique. Wei et al.[217] reported the fabrication of SiOC from modified photocurable preceramic polymer via UV-assisted DIW, indicating this approach could be applied to other ceramic precursor by modifying at the molecular scale. Recently, embedded DIW was reported as alternative for fabricating complex and self-supporting ceramic

architectures free from influence of gravity. It has been widely used in bio-printing but it is still novel for the fabrication of ceramics. By printing inside a supporting bath, usually self-healing gel with shear-thinning behavior and being chemically inert with respect to the ink, overhanging or suspended structures could be realized without sagging, followed by solidification either through thermal or UV light curing. Differing from conventional AM technique (like Fused Deposition Manufacturing or Stereolithography) in which printed supporting parts need to be removed carefully, printed structures by embedded DIW could be easily exacted from the supporting bath without causing damages. Mahmoudi et al.[218] fabricated helical springs in transparent mineral oil and demonstrated potential application of the process to print structures for harsh environments (see **Fig. 1.15c**). Karyappa et al.[219] presented the fabrication of 2D microstructures within media (e.g., methanol, ethanol, isopropanol) by embedded ink writing of polysiloxane inks, enabling the printing of unyielded and non-photocurable resin. Those techniques above greatly extended the application of direct ink writing, finding new approaches for fabrication of PDCs.

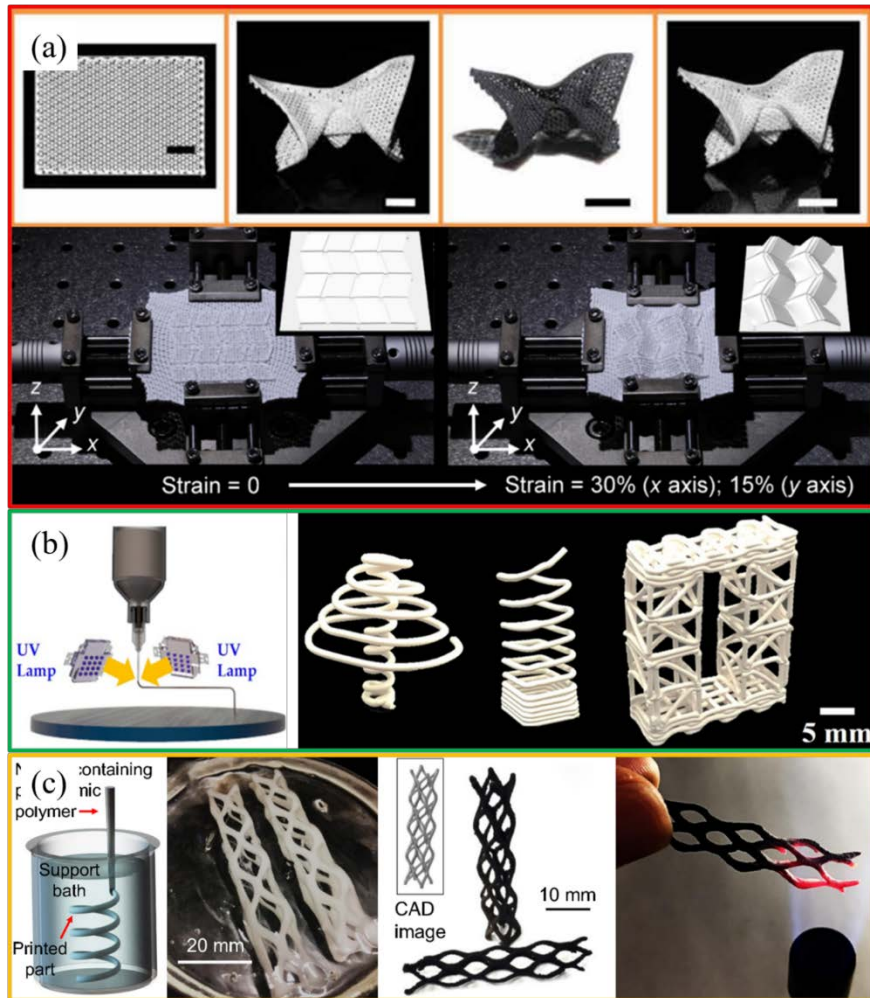


Fig. 1.15 (a) Origami of printed elastomer green body and the pyrolyzed and fabrication processing of programmable architecture, (b) UV light assisted direct ink writing of biphasic calcium phosphate and photopolymer, (c) Embedded direct ink writing of silicone in mineral oil[215,216,218].

1.5.2 Vat photopolymerization

Vat photopolymerization is an AM technique that liquid photopolymer in a vat is selectively cured by light-activated (usually UV light, sometimes visible light) polymerization layer by layer[220], which has been successfully used for the tooling and manufacturing of a number of consumer products due to its ability to create large parts with sub-millimeter details. So far, several vat photopolymerization techniques have been developed, including Stereo Lithography Apparatus (SLA), Digital light

processing (DLP), Two-photon polymerization (TPP). As shown in **Fig. 1.16**[221], the main differences between them are light source and imaging system. In SLA, a beam of laser scans over the surface of resin in vat solidifying the resin a point at once, varying from DLP in which digital micromirror devices (DMD) comprising large arrays of micromirrors can produce an image of patterned light and cure the entire surface at once, being much faster than SLA. However, SLA possesses higher resolution down to 25 μm in Z direction, while DLP struggles to go below 50 μm . Somewhat similar to SLA, TPP enables resin cured at the point where two lasers (with larger wavelength than that used for SLA) intersect instead of using one laser. A resolution of 0.1 μm could be realized for TPP by controlling the laser pulse energy and frequency, which is useful for micro-optoelectronic devices (photonic crystal at sub sub-micrometer scales). Although with greatly high resolution, the parts fabricated by TPP are usually smaller than 1 mm^3 , which is not practical for applications at macro level.

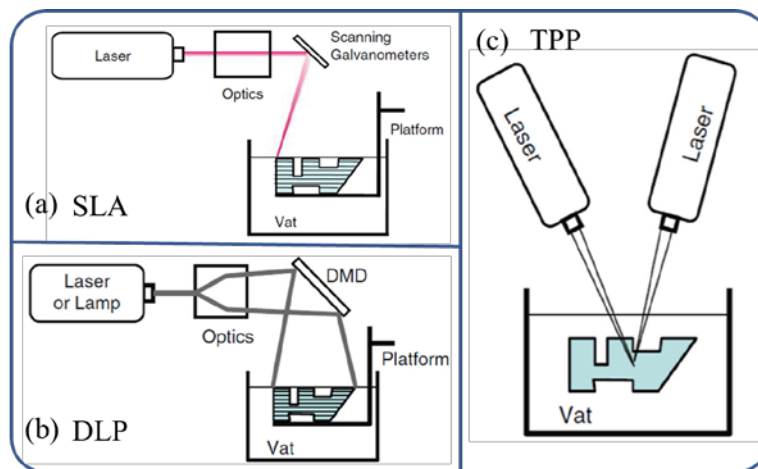


Fig. 1.16 Schematics of several Vat photopolymerization: (a) SLA, (b) DLP, (c) TPP[221].

Initially ceramic components were fabricated by vat photopolymerization from mixer of ceramic powder and photopolymer, which requires high solid content to assure dense ceramic and avoid defects (like delamination, cracks, pores)[222]. However, high

sold loading may result in high viscosity hindering the flow of surrounding slurry to the printing region. Furthermore, ceramic particles that absorb or scatter light (e.g., SiC) is difficult to use. Therefore, the preceramic polymer becomes a promising alternative for ceramic fabrication using vat photopolymerization because either it's liquid or can be dissolved into organic solvents to obtain relatively low viscosity without reducing ceramic yield, meanwhile there is no need to worry about scattering of light by particles. In general, either mixer of non-photocurable preceramic polymer and photopolymer or preceramic polymer containing photocured groups were used for vat photopolymerization. The former seems simple and could be applied to several preceramic polymers, but there are some issues to address, such as controlling phase separation and avoiding the softening and flowing of the uncured preceramic polymer. Schmidt et al.[223] investigated the possibility by physically blending a commercial photocurable polymer with several different preceramic polymer for DLP, demonstrating high tunability on ceramic yield, shrinkage, chemical position and resolution (see **Fig. 1.17a**). The latter requires that the preceramic polymer possesses photocurable groups and simultaneously high ceramic yield, which is difficult to be satisfied by commercially available preceramic polymers. Therefore, it was explored to chemically modify a commercially available, high ceramic yield preceramic polymer by grafting of photocurable moieties. Zanchetta et al.[224] obtained siloxane resin modified by 3-(trimethoxysilyl) propyl methacrylate using sol-gel, indicating for the first time that non-photo preceramic polymer could also be applied for vat photopolymerization by chemical modification and it is transferable to other PDCs system (see **Fig. 1.17b**). Though vat photopolymerization is quite suitable for fabricating complex ceramic components, there are still some challenges to cope with, such as the intrinsic stair stepping effect and the projection area for DLP restricting the size of ceramic parts, requiring only highly transparent resins and slow printing rate for TPP, etc.[225].

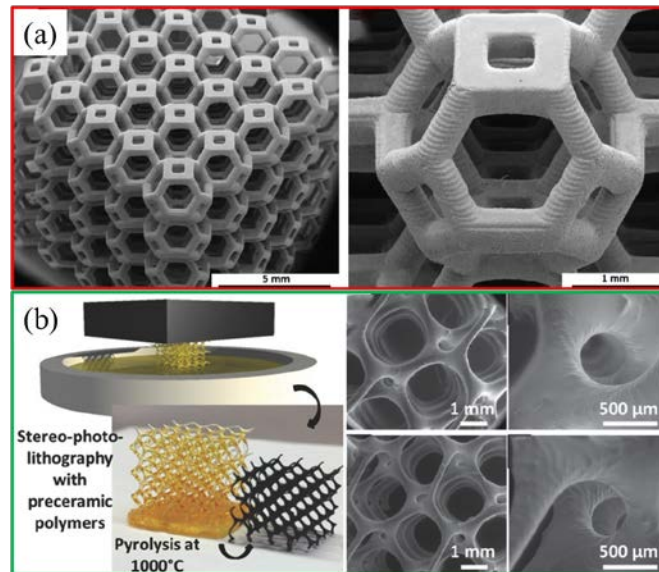


Fig. 1.17 (a) Kelvin cell printed with mixer of preceramic and photocurable polymer, (d) cellular structures printed with chemically modified preceramic polymer containing a photocurable group[223,224].

Besides those AM techniques mentioned above, recently it was reported that another novel AM technique based on Vat photopolymerization called Volumetric Additive Manufacturing (VAM) was developed and attracted lots of attentions due to its high building rate and continuous CAD model eliminating the constrains on speed, geometry and surface quality (avoiding “stair stepping” effect). Inspired by the image reconstruction procedures of computed tomography (CT), Kelly et al.[226] designed a system in which a digital video projector deliver computed intensity-modulated projections to the liquid resin, of which the non-linear response incurred by oxygen inhibition process helps to set a critical dose threshold. They demonstrated a fast-printing speed and the possibility of building components that encase other pre-existing solid objects. In addition, a linear VAM called xolography was developed by introducing local polymerization inside a confined monomer volume upon linear excitation by intersecting of two lights with different wavelengths[227]. High surface quality and enclosed system (like ball in cage without attachment) were realized by linearly moving of a cuvette that contains resin and continuous projection of sliced

images with high resolution (50 μm , with potential to go below 10 μm by further optimizing the optical system) and speed (55 $\text{mm}^3 \text{s}^{-1}$). This novel vat photopolymerization technique is greatly promising for the rapid fabrication of ceramic parts from micro to macro scale.

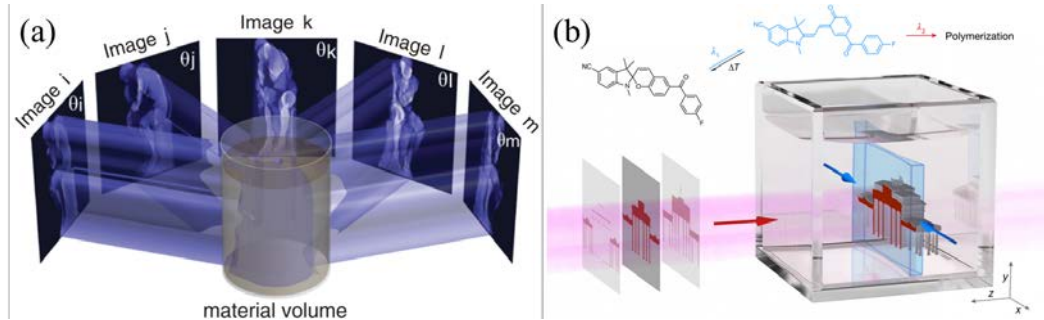


Fig. 1.18 (a) Patterned illumination from many directions delivers a computed 3D exposure dose to a photoresponsive material, (b) Rendered illustration of the printing zone and associated photoinduced reaction pathway[226,227].

1.5.3 Fused Deposition Modeling

Fused Deposition Modeling (FDM), also known as Fused Filament Fabrication (FFF), is a widely popular AM technique for polymer materials, based on which consumer-grade 3D printers were developed for professionals and amateurs. In FDM processing, a thermoplastic polymer filament (e.g., Acrylonitrile Butadiene Styrene Acrylonitrile Butadiene Styrene (ABS) and PolyLactic Acid (PLA)) is fed into heated printing head through filament pulling system and melts, followed by extrusion from nozzle and solidification upon cooling while nozzle moving according to designed pathway (**Fig. 1.19a**). Unlike the other AM techniques mentioned above, few research works about FDM of preceramic polymer have been reported, though. It is probably due to the fact that most preceramic polymers with high ceramic yield have a glass transition temperature well over room temperature ($> 50 \text{ }^\circ\text{C}$), making the filament from preceramic polymers rigid and difficult to feed into printing head[210]. Early FDM was involved into fabrication of PDCs in the way that thermoplastic materials were printed

by FDM as templates, which were impregnated with preceramic polymer and pyrolyzed[228-231]. For example, Baux et al. reported that elastomer green body was fabricated by FDM using composite polyvinyl alcohol/elastomer wire and impregnated with allylhydridopolycarbosilane. Then porous SiC ceramic was obtained by pyrolysis and reinforcement by CVD with $\text{CH}_3\text{SiCl}_3/\text{H}_2$ (see **Fig. 1.19b**). However, time-consuming impregnation and usually inevitable defects after pyrolysis due to the removal of polymer templates giving restriction to this method.

Recently, to overcome the problem of rigid filament, Gorjan et al.[232] mixed polymethylsiloxane ceramic precursor with plastifying agent and Alumina to fabricate flexible filament with good quality of surface and shaping, successfully used for mullite structure by FDM (see **Fig. 1.19c**). In addition, Zhao et al.[233] fabricated SiOC ceramic from a mix of polycarbosilane and a small amount of polypropylene (≤ 5 wt.%) by FDM, demonstrating high ceramic yield over 80 wt% and making debinding unnecessary (see **Fig. 1.19d**). Much more efforts are required to expand the number of additives that makes preceramic polymer stable FDM feedstocks or develop commercially available preceramic polymer with high ceramic yield which can be directly used in FDM.

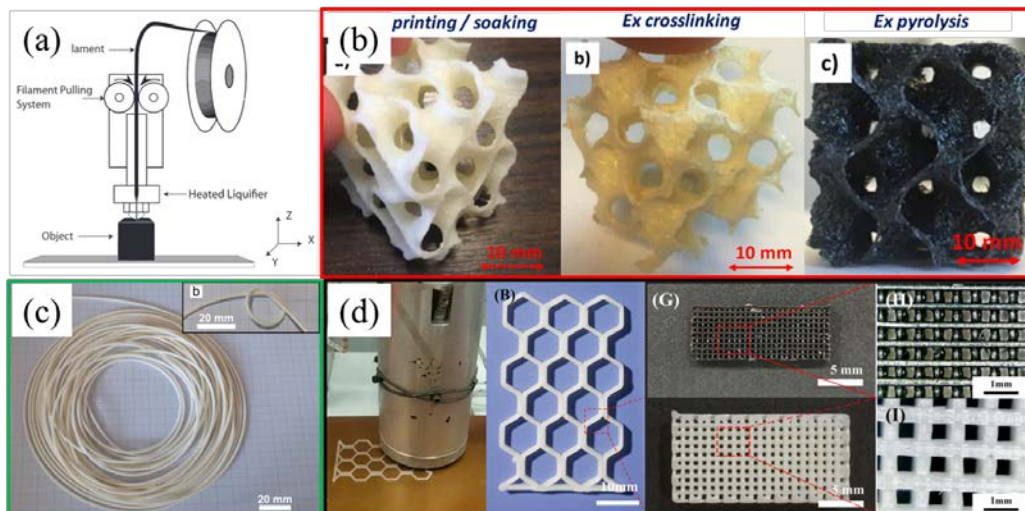


Fig. 1.19 (a) schematic of FDM, (b) Porous geopolymer components through negative replica, (c) filaments fabricated from preceramic polymer and alumina, (d) FDM of

feedstocks comprising preceramic polymer and thermoplastic polymer[231-233].

1.6 Aim of research

The aim of this thesis was to focus on the direct ink writing of PDCs, due to the facts that DIW is a facile processing and has less requirements, with no need for expensive tooling, dies, or litho-graphic masks. We explored the limitation of DIW with respect to printability of complex structure and resolution. SiOC was selected because it's a pretty representative PDCs system with excellent properties and lots of applications, usually generated from polysiloxanes which are insensitive to air and moisture, inexpensive and widely commercially available. In addition, we tried to investigate the structure-dependence relationship for 3D printed SiOC components, aiming at greatly enhance their performance and extend the applications. The results could be also extended to ceramic components obtained from other preceramic precursors, or other materials.

1.7 Summary

Research about the fabrication of ceramic components, in particular complex ceramic structures, have been widely shifted to AM techniques, which shows features of high flexibility, rapidity, and limited cost. With the development of preceramic polymers, great potential can be expected from its combination with AM techniques, especially based on vat photopolymerization. The absence of a sintering step enables lower processing temperatures without the need for pressure, as compared with classical ceramic powder methods, and the absence of sintering additives results in improved thermomechanical properties.

1.8 References

- [1] P. Colombo, G. Mera, R. Riedel, G.D. Soraru, Polymer-derived ceramics: 40 years of research and innovation in advanced ceramics, *J Am Ceram Soc* 93(7) (2010) 1805-1837.
- [2] F. Ainger, J. Herbert, The preparation of phosphorus-nitrogen compounds as non-porous solids, *Angew Chem Int Edit*, WILEY-V CH VERLAG GMBH MUHLENSTRASSE 33-34, D-13187 BERLIN, GERMANY, 1959, pp. 653-653.
- [3] P. Chantrell, P. Popper, *Special Ceramics 1964*, ed. Popper, P., Academic Press, New York (1965) 87.
- [4] D. Seyferth, *Preceramic polymers: Past, present and future*, MASSACHUSETTS INST OF TECH CAMBRIDGE DEPT OF CHEMISTRY, 1992.
- [5] W. Verbeek, G. Winter, *Formkoerper aus siliciumcarbide und verfahren zu ihrer herstellung*, DE Patent 2236078 (1974) A1.
- [6] G.D. Winter, W.D. Verbeek, M.D. Mansmann, *Formkoerper aus homogenen mischungen von siliciumcarbide und siliciumnitride und verfahren zu ihrer herstellung*, Google Patents, 1974.
- [7] S. Yajima, J. Hayashi, M. Omori, Continuous silicon carbide fiber of high tensile strength, *Chemistry Letters* 4(9) (1975) 931-934.
- [8] K. Terauds, R. Raj, Limits to the Stability of the Amorphous Nature of Polymer-Derived HfSiCNO Compounds, *J Am Ceram Soc* 96(7) (2013) 2117-2123.
- [9] K. Terauds, R. Raj, P. Kroll, Ab initio and FTIR studies of HfSiCNO processed from the polymer route, *J Am Ceram Soc* 97(3) (2014) 742-749.
- [10] J. Yuan, X. Luan, R. Riedel, E. Ionescu, Preparation and hydrothermal corrosion behavior of Cf/SiCN and Cf/SiHfBCN ceramic matrix composites, *Journal of the European Ceramic Society* 35(12) (2015) 3329-3337.
- [11] J. Yuan, S. Hapis, H. Breitzke, Y. Xu, C. Fasel, H.-J. Kleebe, G. Buntkowsky, R. Riedel, E. Ionescu, Single-source-precursor synthesis of hafnium-containing ultrahigh-temperature ceramic nanocomposites (UHTC-NCs), *Inorganic chemistry* 53(19) (2014) 10443-10455.
- [12] Y. Wang, W. Fei, L. An, Oxidation/corrosion of polymer-derived SiAlCN ceramics in water vapor, *J Am Ceram Soc* 89(3) (2006) 1079-1082.
- [13] Y. Wang, Y. Fan, L. Zhang, W. Zhang, L. An, Polymer-derived SiAlCN ceramics resist oxidation at 1400 C, *Scripta materialia* 55(4) (2006) 295-297.
- [14] S. Bernard, M. Weinmann, D. Cornu, P. Miele, F. Aldinger, Preparation of high-temperature stable SiBCN fibers from tailored single source polyborosilazanes, *Journal of the European Ceramic Society* 25(2-3) (2005) 251-256.
- [15] C. Vakifahmetoglu, P. Colombo, A Direct Method for the Fabrication of Macro-Porous SiOC Ceramics from Preceramic Polymers, *Adv Eng Mater* 10(3) (2008) 256-259.
- [16] R. Riedel, A. Kienzle, W. Dressler, L. Ruwisch, J. Bill, F. Aldinger, A silicoboron carbonitride ceramic stable to 2,000 C, *Nature* 382(6594) (1996) 796-798.
- [17] R. Pena-Alonso, G. Mariotto, C. Gervais, F. Babonneau, G.D. Soraru, New insights on the high-temperature nanostructure evolution of SiOC and B-doped SiBOC polymer-derived glasses, *Chemistry of Materials* 19(23) (2007) 5694-5702.
- [18] G.D. Soraru, L. Pederiva, J. Latournerie, R. Raj, Pyrolysis kinetics for the conversion of a polymer

- into an amorphous silicon oxycarbide ceramic, *J Am Ceram Soc* 85(9) (2002) 2181-2187.
- [19] G. Mera, A. Navrotsky, S. Sen, H.-J. Kleebe, R. Riedel, Polymer-derived SiCN and SiOC ceramics—structure and energetics at the nanoscale, *Journal of Materials Chemistry A* 1(12) (2013) 3826-3836.
- [20] R. Riedel, A. Greiner, G. Miehe, W. Dressler, H. Fuess, J. Bill, F. Aldinger, The First Crystalline Solids in the Ternary Si-C-N System, *Angewandte Chemie International Edition in English* 36(6) (1997) 603-606.
- [21] S. Sarkar, J. Zou, J. Liu, C. Xu, L. An, L. Zhai, Polymer-derived ceramic composite fibers with aligned pristine multiwalled carbon nanotubes, *ACS applied materials & interfaces* 2(4) (2010) 1150-1156.
- [22] S. Sarkar, A. Chunder, W. Fei, L. An, L. Zhai, Superhydrophobic mats of polymer-derived ceramic fibers, *J Am Ceram Soc* 91(8) (2008) 2751-2755.
- [23] J.D. Torrey, R.K. Bordia, Processing of polymer-derived ceramic composite coatings on steel, *J Am Ceram Soc* 91(1) (2008) 41-45.
- [24] J.D. Torrey, R.K. Bordia, Mechanical properties of polymer-derived ceramic composite coatings on steel, *Journal of the European Ceramic Society* 28(1) (2008) 253-257.
- [25] K. Wang, J. Unger, J.D. Torrey, B.D. Flinn, R.K. Bordia, Corrosion resistant polymer derived ceramic composite environmental barrier coatings, *Journal of the European Ceramic Society* 34(15) (2014) 3597-3606.
- [26] R. Jones, A. Szweda, D. Petrak, Polymer derived ceramic matrix composites, *Composites Part A: Applied Science and Manufacturing* 30(4) (1999) 569-575.
- [27] D. King, Z. Apostolov, T. Key, C. Carney, M. Cinibulk, Novel processing approach to polymer-derived ceramic matrix composites, *International Journal of Applied Ceramic Technology* 15(2) (2018) 399-408.
- [28] L. An, W. Xu, S. Rajagopalan, C. Wang, H. Wang, Y. Fan, L. Zhang, D. Jiang, J. Kapat, L. Chow, Carbon-nanotube-reinforced polymer-derived ceramic composites, *Adv Mater* 16(22) (2004) 2036-2040.
- [29] S.A. Alvi, F. Akhtar, High temperature tribology of polymer derived ceramic composite coatings, *Scientific reports* 8(1) (2018) 1-10.
- [30] G. Barroso, Thermal barrier coating by polymer-derived ceramic technique for application in exhaust systems, Cuvillier Verlag 2018.
- [31] Z. Zhang, J.E. Calderon, S. Fahad, L. Ju, D.-X. Antony, Y. Yang, A. Kushima, L. Zhai, Polymer-Derived Ceramic Nanoparticle/Edge-Functionalized Graphene Oxide Composites for Lithium-Ion Storage, *ACS Applied Materials & Interfaces* 13(8) (2021) 9794-9803.
- [32] V. Ahilan, M. Wilhelm, K. Rezwani, Porous polymer derived ceramic (PDC)-montmorillonite-H₃PMo₁₂O₄₀/SiO₂ composite membranes for microbial fuel cell (MFC) application, *Ceramics International* 44(16) (2018) 19191-19199.
- [33] L. David, K. Shareef, M. Abass, G. Singh, Three-dimensional polymer-derived ceramic/graphene paper as a Li-ion battery and supercapacitor electrode, *RSC advances* 6(59) (2016) 53894-53902.
- [34] S. Mukherjee, Z. Ren, G. Singh, Molecular polymer-derived ceramics for applications in electrochemical energy storage devices, *Journal of Physics D: Applied Physics* 51(46) (2018) 463001.
- [35] Y. Jia, M.A.R. Chowdhury, C. Xu, Electromagnetic property of polymer derived SiC-C solid

- solution formed at ultra-high temperature, *Carbon* 162 (2020) 74-85.
- [36] W. Zhao, G. Shao, M. Jiang, B. Zhao, H. Wang, D. Chen, H. Xu, X. Li, R. Zhang, L. An, Ultralight polymer-derived ceramic aerogels with wide bandwidth and effective electromagnetic absorption properties, *Journal of the European Ceramic Society* 37(13) (2017) 3973-3980.
- [37] L. Chen, J. Zhao, L. Wang, F. Peng, H. Liu, J. Zhang, J. Gu, Z. Guo, In-situ pyrolyzed polymethylsilsesquioxane multi-walled carbon nanotubes derived ceramic nanocomposites for electromagnetic wave absorption, *Ceramics International* 45(9) (2019) 11756-11764.
- [38] D.M. Yunos, O. Bretcanu, A.R. Boccaccini, Polymer-bioceramic composites for tissue engineering scaffolds, *Journal of Materials Science* 43(13) (2008) 4433-4442.
- [39] L. Fiocco, S. Li, M. Stevens, E. Bernardo, J. Jones, Biocompatibility and bioactivity of porous polymer-derived Ca-Mg silicate ceramics, *Acta biomaterialia* 50 (2017) 56-67.
- [40] Q.Z. Chen, I.D. Thompson, A.R. Boccaccini, 45S5 Bioglass®-derived glass-ceramic scaffolds for bone tissue engineering, *Biomaterials* 27(11) (2006) 2414-2425.
- [41] M. Dziadek, E. Stodolak-Zych, K. Cholewa-Kowalska, Biodegradable ceramic-polymer composites for biomedical applications: A review, *Materials Science and Engineering: C* 71 (2017) 1175-1191.
- [42] F. Dalcanale, *Polymer Derived Ceramics Process in Biomedical Applications: Pacemaker Electrode*, ETH Zurich, 2017.
- [43] A. Francis, Progress in polymer-derived functional silicon-based ceramic composites for biomedical and engineering applications, *Materials Research Express* 5(6) (2018) 062003.
- [44] R.D. Miller, J. Michl, Polysilane high polymers, *Chemical Reviews* 89(6) (1989) 1359-1410.
- [45] G. Mera, M. Gallei, S. Bernard, E. Ionescu, Ceramic Nanocomposites from Tailor-Made Preceramic Polymers, *Nanomaterials (Basel)* 5(2) (2015) 468-540.
- [46] J.M. Zeigler, F. Fearon, Silicon-based polymer science, *International Topical Workshop Advances in Silicon-Based Polymer Science (1987: Makaha, Hawaii)*, American Chemical Society, 1990.
- [47] R.G. Jones, S.J. Holder, Synthesis of polysilanes by the wurtz reductive-coupling reaction, *Silicon-Containing Polymers*, Springer 2000, pp. 353-373.
- [48] C.T. Aitken, J.F. Harrod, E. Samuel, Identification of some intermediates in the titanocene-catalyzed dehydrogenative coupling of primary organosilanes, *J Am Chem Soc* 108(14) (1986) 4059-4066.
- [49] C. Aitken, J.F. Harrod, E. Samuel, Polymerization of primary silanes to linear polysilanes catalyzed by titanocene derivatives, *Journal of organometallic chemistry* 279(1-2) (1985) C11-C13.
- [50] T. Sanji, K. Nakayama, H. Azuma, H. Sakurai, Synthesis of poly (ethylene oxide)-b-polysilane by anionic polymerization of masked disilenes using a macroinitiator method, *Silicon Chemistry* 2(1) (2003) 93-97.
- [51] T. Sanji, K. Kawabata, H. Sakurai, Alkoxide initiation of anionic polymerization of masked disilenes to polysilanes, *Journal of Organometallic Chemistry* 611(1-2) (2000) 32-35.
- [52] K. Shiina, M. Kumada, Thermal rearrangement of hexamethyldisilane to trimethyl (dimethylsilylmethyl) silane, *The Journal of Organic Chemistry* 23(1) (1958) 139-139.
- [53] H.J. Wu, L.V. Interrante, Preparation of poly (dichlorosilaethylene) and poly (silaethylene) via ring-opening polymerization, *Macromolecules* 25(6) (1992) 1840-1841.
- [54] L. He, Z. Zhang, X. Yang, L. Jiao, Y. Li, C. Xu, Liquid polycarbosilanes: synthesis and evaluation as precursors for SiC ceramic, *Polymer International* 64(8) (2015) 979-985.

- [55] S.K. Shukla, R. Tiwari, A. Ranjan, A. Saxena, G. Mathur, Some thermal studies of polysilanes and polycarbosilanes, *Thermochimica acta* 424(1-2) (2004) 209-217.
- [56] E. Kroke, Y.-L. Li, C. Konetschny, E. Lecomte, C. Fasel, R. Riedel, Silazane derived ceramics and related materials, *Materials Science and Engineering: R: Reports* 26(4-6) (2000) 97-199.
- [57] D. Seyferth, G.H. Wiseman, C. Prud'homme, A liquid silazane precursor to silicon nitride, *J Am Ceram Soc* 66(1) (1983) C-13-C-14.
- [58] D.M. Narsavage, L.V. Interrante, P.S. Marchetti, G.E. Maciel, Condensation polymerization of tetrakis (ethylamino) silane and its thermal decomposition to silicon nitride (Si₃N₄/silicon carbide (SiC)) ceramics, *Chemistry of Materials* 3(4) (1991) 721-730.
- [59] P. Schutzenberger, C. Colson, Silicon, *Rendus Hebd. Seances Acad. Sci* 92 (1885) 1508-1511.
- [60] M. Hörz, A. Zern, F. Berger, J. Haug, K. Müller, F. Aldinger, M. Weinmann, Novel polysilazanes as precursors for silicon nitride/silicon carbide composites without “free” carbon, *Journal of the European Ceramic Society* 25(2-3) (2005) 99-110.
- [61] D. Seyferth, R.M. Stewart, Synthesis and polymerization of cyclotetrasilazanes, *Applied organometallic chemistry* 11(10-11) (1997) 813-832.
- [62] R.M. Laine, Transition metal catalysed synthesis of oligo-and polysilazanes, *Platinum Metals Review* 32(2) (1988) 64-71.
- [63] J. Schwark, Isocyanate-modified polysilazane ceramic precursors, ABSTRACTS OF PAPERS OF THE AMERICAN CHEMICAL SOCIETY, AMER CHEMICAL SOC 1155 16TH ST, NW, WASHINGTON, DC 20036, 1991, pp. 339-POLY.
- [64] P. Boehm, M. Mondeshki, H. Frey, Polysiloxane-Backbone Block Copolymers in a One-Pot Synthesis: A Silicone Platform for Facile Functionalization, *Macromolecular rapid communications* 33(21) (2012) 1861-1867.
- [65] J. Chojnowski, M. Cypryk, J. Kurjata, Organic polysilanes interrupted by heteroatoms, *Progress in polymer science* 28(5) (2003) 691-728.
- [66] R.G. Jones, W. Ando, J. Chojnowski, Silicon-containing polymers: the science and technology of their synthesis and applications, Springer Science & Business Media 2013.
- [67] R. Riedel, G. Mera, R. Hauser, A. Klönczynski, Silicon-based polymer-derived ceramics: synthesis properties and applications-a review dedicated to Prof. Dr. Fritz Aldinger on the occasion of his 65th birthday, *Journal of the Ceramic Society of Japan (日本セラミックス協会学術論文誌)* 114(1330) (2006) 425-444.
- [68] J. Chojnowski, J. Kurjata, S. Rubinsztajn, Poly (oxymultisilane) s by ring-opening polymerization. Fully methylated silicon analogues of oxirane and THF polymers, *Die Makromolekulare Chemie, Rapid Communications* 9(7) (1988) 469-475.
- [69] J.M. Zeigler, Interrupted polysilanes useful as photoresists, Google Patents, 1988.
- [70] W. Zhou, H. Yang, X. Guo, J. Lu, Thermal degradation behaviors of some branched and linear polysiloxanes, *Polymer degradation and stability* 91(7) (2006) 1471-1475.
- [71] G.D. Sorarù, G. D'andrea, R. Camprostrini, F. Babonneau, G. Mariotto, Structural characterization and high-temperature behavior of silicon oxycarbide glasses prepared from sol-gel precursors containing Si-H bonds, *J Am Ceram Soc* 78(2) (1995) 379-387.
- [72] H.H. Huang, B. Orler, G.L. Wilkes, Structure-property behavior of new hybrid materials incorporating oligomeric species into sol-gel glasses. 3. Effect of acid content, tetraethoxysilane content, and molecular weight of poly (dimethylsiloxane), *Macromolecules* 20(6) (1987) 1322-

- [73] S. Diré, F. Babonneau, C. Sanchez, J. Livage, Sol–gel synthesis of siloxane–oxide hybrid coatings [Si (CH₃)₂O·MO_x: M= Si, Ti, Zr, Al] with luminescent properties, *Journal of Materials Chemistry* 2(2) (1992) 239-244.
- [74] S. Widgeon, G. Mera, Y. Gao, E. Stoyanov, S. Sen, A. Navrotsky, R. Riedel, Nanostructure and energetics of carbon-rich SiCN ceramics derived from polysilylcarbodiimides: Role of the nanodomain interfaces, *Chemistry of Materials* 24(6) (2012) 1181-1191.
- [75] J. Pump, E. Rochow, Silylcarbodiimide. IV. Sila-polycarbodiimide, *Zeitschrift für anorganische und allgemeine Chemie* 330(1-2) (1964) 101-106.
- [76] J.F. Klebe, J.G. Murray, Organosiliconcarbodiimide polymers and process for their preparation, Google Patents, 1967.
- [77] R. Riedel, E. Kroke, A. Greiner, A.O. Gabriel, L. Ruwisch, J. Nicolich, P. Kroll, Inorganic solid-state chemistry with main group element carbodiimides, *Chemistry of materials* 10(10) (1998) 2964-2979.
- [78] A.O. Gabriel, R. Riedel, S. Storck, W.F. Maier, Synthesis and thermally induced ceramization of a non-oxidic poly (methylsilsesquicarbodi-imide) gel, *Applied organometallic chemistry* 11(10-11) (1997) 833-841.
- [79] A. Kienzle, J. Bill, F. Aldinger, R. Riedel, Nanosized Si–C–N-powder by pyrolysis of highly crosslinked silylcarbodiimide, *Nanostructured Materials* 6(1-4) (1995) 349-352.
- [80] Y. Iwamoto, W. Völger, E. Kroke, R. Riedel, T. Saitou, K. Matsunaga, Crystallization behavior of amorphous silicon carbonitride ceramics derived from organometallic precursors, *J Am Ceram Soc* 84(10) (2001) 2170-2178.
- [81] A.O. Gabriel, R. Riedel, W. Dressler, S. Reichert, C. Gervais, J. Maquet, F. Babonneau, Thermal Decomposition of Poly (methylsilsesquicarbodiimide) to Amorphous Si–C–N Ceramics, *Chemistry of materials* 11(2) (1999) 412-420.
- [82] S. Nahar-Borchert, E. Kroke, R. Riedel, B. Boury, R.J. Corriu, Synthesis and characterization of alkylene-bridged silsesquicarbodiimide hybrid xerogels, *Journal of organometallic chemistry* 686(1-2) (2003) 127-133.
- [83] Q. Wen, Z. Yu, R. Riedel, The fate and role of in situ formed carbon in polymer-derived ceramics, *Progress in Materials Science* 109 (2020) 100623.
- [84] N.P. Bansal, A.R. Boccaccini, *Ceramics and composites processing methods*, John Wiley & Sons 2012.
- [85] S. Walter, D. Suttor, T. Erny, B. Hahn, P. Greil, Injection moulding of polysiloxane/filler mixtures for oxycarbide ceramic composites, *Journal of the European Ceramic Society* 16(4) (1996) 387-393.
- [86] M. Erdal, S.I. Güçeri, S.C. Danforth, Impregnation molding of particle-filled preceramic polymers: process modeling, *J Am Ceram Soc* 82(8) (1999) 2017-2028.
- [87] M. Stalin, K. Rajaguru, L. Rangaraj, Processing of Cf/SiC composites by hot pressing using polymer binders followed by polymer impregnation and pyrolysis, *Journal of the European Ceramic Society* 40(2) (2020) 290-297.
- [88] S.H. Lee, M. Weinmann, F. Aldinger, Processing and properties of C/Si–B–C–N fiber–reinforced ceramic matrix composites prepared by precursor impregnation and pyrolysis, *Acta materialia* 56(7) (2008) 1529-1538.

- [89] J. Zeschky, T. Höfner, C. Arnold, R. Weißmann, D. Bahloul-Hourlier, M. Scheffler, P. Greil, Polysilsesquioxane derived ceramic foams with gradient porosity, *Acta Materialia* 53(4) (2005) 927-937.
- [90] Y.-W. Kim, C.B. Park, Processing of microcellular preceramics using carbon dioxide, *Composites science and technology* 63(16) (2003) 2371-2377.
- [91] B.C. Mutsuddy, Use of organometallic polymer for making ceramic parts by plastic forming techniques, *Ceramics International* 13(1) (1987) 41-53.
- [92] Y.W. Kim, J.H. Eom, C. Wang, C.B. Park, Processing of porous silicon carbide ceramics from carbon-filled polysiloxane by extrusion and carbothermal reduction, *J Am Ceram Soc* 91(4) (2008) 1361-1364.
- [93] J. Bill, D. Heimann, Polymer-derived ceramic coatings on C/C-SiC composites, *Journal of the European Ceramic Society* 16(10) (1996) 1115-1120.
- [94] A. Guo, M. Roso, M. Modesti, J. Liu, P. Colombo, Hierarchically structured polymer-derived ceramic fibers by electrospinning and catalyst-assisted pyrolysis, *Journal of the European Ceramic Society* 34(2) (2014) 549-554.
- [95] V. Salles, S. Bernard, A. Brioude, D. Cornu, P. Miele, A new class of boron nitride fibers with tunable properties by combining an electrospinning process and the polymer-derived ceramics route, *Nanoscale* 2(2) (2010) 215-217.
- [96] H. Windsheimer, N. Travitzky, A. Hofenauer, P. Greil, Laminated Object Manufacturing of Preceramic-Paper-Derived Si³N₄/SiC Composites, *Adv Mater* 19(24) (2007) 4515-4519.
- [97] H. Chen, X. Wang, F. Xue, Y. Huang, K. Zhou, D. Zhang, 3D printing of SiC ceramic: Direct ink writing with a solution of preceramic polymers, *Journal of the European Ceramic Society* 38(16) (2018) 5294-5300.
- [98] S. Fu, W. Liu, S. Liu, S. Zhao, Y. Zhu, 3D printed porous β -Ca₂SiO₄ scaffolds derived from preceramic resin and their physicochemical and biological properties, *Science and technology of advanced materials* 19(1) (2018) 495-506.
- [99] R. Harshe, C. Balan, R. Riedel, Amorphous Si (Al) OC ceramic from polysiloxanes: bulk ceramic processing, crystallization behavior and applications, *Journal of the European Ceramic Society* 24(12) (2004) 3471-3482.
- [100] N. Janakiraman, F. Aldinger, Fabrication and characterization of fully dense Si-C-N ceramics from a poly (ureamethylvinyl) silazane precursor, *Journal of the European Ceramic Society* 29(1) (2009) 163-173.
- [101] C. Balan, R. Riedel, Rheological investigations of a polymeric precursor for ceramic materials: experiments and theoretical modeling, *Journal of Optoelectronics and Advanced Materials* 8(2) (2006) 561.
- [102] T. Taki, S. Maeda, K. Okamura, M. Sato, T. Matsuzawa, Oxidation curing mechanism of polycarbosilane fibres by solid-state ²⁹Si high-resolution NMR, *Journal of materials science letters* 6(7) (1987) 826-828.
- [103] M. Narisawa, A. Idesaki, S. Kitano, K. Okamura, M. Sugimoto, T. Seguchi, M. Itoh, Use of blended precursors of poly (vinylsilane) in polycarbosilane for silicon carbide fiber synthesis with radiation curing, *J Am Ceram Soc* 82(4) (1999) 1045-1051.
- [104] A. Idesaki, M. Sugimoto, S. Tanaka, M. Narisawa, K. Okamura, M. Itoh, Synthesis of a minute SiC product from polyvinylsilane with radiation curing Part I Radiation curing of polyvinylsilane,

- Journal of materials science 39(18) (2004) 5689-5694.
- [105] A. Idesaki, M. Narisawa, K. Okamura, M. Sugimoto, Y. Morita, T. Seguchi, M. Itoh, Application of electron beam curing for silicon carbide fiber synthesis from blend polymer of polycarbosilane and polyvinylsilane, *Radiation Physics and Chemistry* 60(4-5) (2001) 483-487.
- [106] M. Schulz, M. Börner, J. Götttert, T. Hanemann, J. Haußelt, G. Motz, Cross linking behavior of preceramic polymers effected by UV-and synchrotron radiation, *Adv Eng Mater* 6(8) (2004) 676-680.
- [107] J. SONG, L. CHEN, Y. WANG, R. WANG, PYROLYSIS AND DEGRADATION KINETICS OF UV CURED MULTI THIOL-VINYL SILIZANE PRECERAMIC, *Acta Polymerica Sinica* (2009) 11.
- [108] K. Schwartz, D.J. Rowcliffe, Modeling density contributions in preceramic polymer/ceramic powder systems, *J Am Ceram Soc* 69(5) (1986) C-106-C-108.
- [109] G. Franchin, H.S. Maden, L. Wahl, A. Baliello, M. Pasetto, P. Colombo, Optimization and Characterization of Preceramic Inks for Direct Ink Writing of Ceramic Matrix Composite Structures, *Materials (Basel)* 11(4) (2018).
- [110] P. Greil, Active-filler-controlled pyrolysis of preceramic polymers, *J Am Ceram Soc* 78(4) (1995) 835-848.
- [111] U. Krüger, R. Ullrich, Producing a ceramic layer by spraying polymer ceramic precursor particles onto a surface comprises using a cold gas spray nozzle, German: Siemens AG (2006).
- [112] K. Tangermann-Gerk, G. Barroso, B. Weisenseel, P. Greil, T. Fey, M. Schmidt, G. Motz, Laser pyrolysis of an organosilazane-based glass/ZrO₂ composite coating system, *Materials & Design* 109 (2016) 644-651.
- [113] A. Horcher, K. Tangermann-Gerk, G. Barroso, M. Schmidt, G. Motz, Laser and furnace pyrolyzed organosilazane-based glass/ZrO₂ composite coating system—A comparison, *Journal of the European Ceramic Society* 40(7) (2020) 2642-2651.
- [114] G.A. Danko, R. Silbergliitt, P. Colombo, E. Pippel, J. Woltersdorf, Comparison of microwave hybrid and conventional heating of preceramic polymers to form silicon carbide and silicon oxycarbide ceramics, *J Am Ceram Soc* 83(7) (2000) 1617-1625.
- [115] N. Patil, A.C. Camacho, N.K. Mishra, P. Singhla, C.B. Sweeney, M.A. Saed, M. Radovic, M.J. Green, Radio frequency and microwave heating of preceramic polymer nanocomposites with applications in mold-free processing, *Adv Eng Mater* 21(8) (2019) 1900276.
- [116] P. Colombo, A. Donato, B. Riccardi, J. Woltersdorf, E. Pippel, R. Silbergliitt, G. Danko, C. Lewinsohn, R. Jones, Joining SiC-based ceramics and composites with preceramic polymers, *Ceramic Transactions(USA)* 144 (2002) 323-334.
- [117] J.C. Pivin, P. Colombo, M. Tonidandel, Ion irradiation of preceramic polymer thin films, *J Am Ceram Soc* 79(7) (1996) 1967-1970.
- [118] J. Pivin, P. Colombo, Ceramic coatings by ion irradiation of polycarbosilanes and polysiloxanes: Part II Hardness and thermochemical stability, *Journal of materials science* 32(23) (1997) 6175-6182.
- [119] P. Colombo, *Polymer derived ceramics: from nano-structure to applications*, DEStech Publications, Inc2010.
- [120] S.H. Yu, R.E. Riman, S.C. Danforth, R.Y. Leung, Pyrolysis of titanium-metal-filled poly (siloxane) preceramic polymers: effect of atmosphere on pyrolysis product chemistry, *J Am Ceram Soc* 78(7)

- (1995) 1818-1824.
- [121] P. Colombo, T. Paulson, C.G. Pantano, Atmosphere effects in the processing of silicon carbide and silicon oxycarbide thin films and coatings, *Journal of Sol-Gel Science and Technology* 2(1) (1994) 601-604.
- [122] Q.-S. Ma, Z.-H. Chen, W.-W. Zheng, H.-F. Hu, Effects of pyrolysis processes on microstructure and mechanical properties of Cf/SiOC composites fabricated by preceramic polymer pyrolysis, *Ceramics international* 31(2) (2005) 305-314.
- [123] M. Wilhelm, C. Soltmann, D. Koch, G. Grathwohl, Ceramers—functional materials for adsorption techniques, *Journal of the European Ceramic Society* 25(2-3) (2005) 271-276.
- [124] T.-H. Yoon, S.-H. Park, K.-I. Min, X. Zhang, S.J. Haswell, D.-P. Kim, Novel inorganic polymer derived microreactors for organic microchemistry applications, *Lab on a Chip* 8(9) (2008) 1454-1459.
- [125] P. Colombo, G. Mera, R. Riedel, G.D. Soraru, Polymer-Derived Ceramics: 40 Years of Research and Innovation in Advanced Ceramics, *J Am Ceram Soc* 93(7) (2010) 1805-1837.
- [126] Y. Wang, P. Xiao, W. Zhou, H. Luo, Z. Li, W. Chen, Y. Li, Microstructures, dielectric response and microwave absorption properties of polycarbosilane derived SiC powders, *Ceramics International* 44(4) (2018) 3606-3613.
- [127] R. Yao, Z. Feng, Y. Yu, S. Li, L. Chen, Y. Zhang, Synthesis and characterization of continuous freestanding silicon carbide films with polycarbosilane (PCS), *Journal of the European Ceramic Society* 29(10) (2009) 2079-2085.
- [128] O. Lyckfeldt, E. Liden, M. Persson, R. Carlsson, P. Apell, Progress in the fabrication of Si₃N₄ turbine rotors by pressure slip casting, *Journal of the European Ceramic Society* 14(5) (1994) 383-395.
- [129] G. Pezzotti, Si₃N₄/SiC-Platelet Composite without Sintering Aids: A Candidate for Gas Turbine Engines, *J Am Ceram Soc* 76(5) (1993) 1313-1320.
- [130] S.T. Schwab, R.A. Page, Nanostructure of polymer-derived silicon nitride, *Materials Science and Engineering: A* 204(1-2) (1995) 201-204.
- [131] W. Yang, Z. Xie, J. Li, H. Miao, L. Zhang, L. An, Ultra-long single-crystalline α -Si₃N₄ nanowires: derived from a polymeric precursor, *J Am Ceram Soc* 88(6) (2005) 1647-1650.
- [132] A. Saha, R. Raj, D.L. Williamson, A model for the nanodomains in polymer-derived SiCO, *J Am Ceram Soc* 89(7) (2006) 2188-2195.
- [133] S. Widgeon, S. Sen, G. Mera, E. Ionescu, R. Riedel, A. Navrotsky, ²⁹Si and ¹³C solid-state NMR spectroscopic study of nanometer-scale structure and mass fractal characteristics of amorphous polymer derived silicon oxycarbide ceramics, *Chemistry of Materials* 22(23) (2010) 6221-6228.
- [134] C. Stabler, E. Ionescu, M. Graczyk-Zajac, I. Gonzalo-Juan, R. Riedel, Silicon oxycarbide glasses and glass-ceramics: "All-Rounder" materials for advanced structural and functional applications, *J Am Ceram Soc* 101(11) (2018) 4817-4856.
- [135] G.D. Sorarù, R. Pena-Alonso, M. Leoni, C-rich micro/mesoporous Si (B) OC: in situ diffraction analysis of the HF etching process, *Microporous and mesoporous materials* 172 (2013) 125-130.
- [136] M.A. Mazo, A. Tamayo, A.C. Caballero, J. Rubio, Electrical and thermal response of silicon oxycarbide materials obtained by spark plasma sintering, *Journal of the European Ceramic Society* 37(5) (2017) 2011-2020.
- [137] S. Yajima, J. Hayashi, M. Omori, K. Okamura, Development of a silicon carbide fibre with high

- tensile strength, *Nature* 261(5562) (1976) 683-685.
- [138] G.M. Renlund, S. Prochazka, R.H. Doremus, Silicon oxycarbide glasses: Part II. Structure and properties, *Journal of Materials Research* 6(12) (1991) 2723-2734.
- [139] G.D. Sorarù, E. Dallapiccola, G. D'Andrea, Mechanical Characterization of Sol–Gel-Derived Silicon Oxycarbide Glasses, *J Am Ceram Soc* 79(8) (1996) 2074-2080.
- [140] G.D. Sorarù, L. Kundanati, B. Santhosh, N. Pugno, Influence of free carbon on the Young's modulus and hardness of polymer-derived silicon oxycarbide glasses, *J Am Ceram Soc* 102(3) (2019) 907-913.
- [141] H. Lim, H. Kim, S.-O. Kim, K.J. Kim, W. Choi, Novel approach for controlling free-carbon domain in silicone oil-derived silicon oxycarbide (SiOC) as an anode material in secondary batteries, *Chemical Engineering Journal* 404 (2021) 126581.
- [142] C. Stabler, A. Reitz, P. Stein, B. Albert, R. Riedel, E. Ionescu, Thermal properties of SiOC glasses and glass ceramics at elevated temperatures, *Materials* 11(2) (2018) 279.
- [143] A. Gurlo, E. Ionescu, R. Riedel, D.R. Clarke, The Thermal Conductivity of Polymer-Derived Amorphous Si–O–C Compounds and Nano-Composites, *J Am Ceram Soc* 99(1) (2016) 281-285.
- [144] B. Santhosh, C. Vakifahmetoglu, E. Ionescu, A. Reitz, B. Albert, G.D. Soraru, Processing and thermal characterization of polymer derived SiCN (O) and SiOC reticulated foams, *Ceramics International* 46(5) (2020) 5594-5601.
- [145] R. Riedel, L. Toma, E. Janssen, J. Nuffer, T. Melz, H. Hanselka, Piezoresistive effect in SiOC ceramics for integrated pressure sensors, *J Am Ceram Soc* 93(4) (2010) 920-924.
- [146] F. Roth, C. Schmerbauch, E. Ionescu, N. Nicoloso, O. Guillon, R. Riedel, High-temperature piezoresistive C/SiOC sensors, *Journal of Sensors and Sensor Systems* 4(1) (2015) 133-136.
- [147] F. Rosenburg, The state of carbon and the piezoresistive effect in silicon oxycarbide ceramics, (2018).
- [148] T. Oh, Optical properties of SiOC film by PL spectrometer and reflectance, *Materials Research Bulletin* 47(10) (2012) 3020-3022.
- [149] A. Karakuscu, R. Guider, L. Pavesi, G.D. Soraru, White luminescence from sol–gel-derived SiOC thin films, *J Am Ceram Soc* 92(12) (2009) 2969-2974.
- [150] I. Menapace, G. Mera, R. Riedel, E. Erdem, R.-A. Eichel, A. Pauletti, G.A. Appleby, Luminescence of heat-treated silicon-based polymers: promising materials for LED applications, *Journal of materials science* 43(17) (2008) 5790-5796.
- [151] R.M. Laine, F. Babonneau, K.Y. Blowhowiak, R.A. Kennish, J.A. Rahn, G.J. Exarhos, K. Waldner, The Evolutionary Process during Pyrolytic Transformation of Poly (N-methylsilazane) from a Pre-ceramic Polymer into an Amorphous Silicon Nitride/Carbon Composite, *J Am Ceram Soc* 78(1) (1995) 137-145.
- [152] G. Mera, R. Riedel, F. Poli, K. Müller, Carbon-rich SiCN ceramics derived from phenyl-containing poly (silylcarbodiimides), *Journal of the European Ceramic Society* 29(13) (2009) 2873-2883.
- [153] A. Klausmann, K. Morita, K.E. Johanns, C. Fasel, K. Durst, G. Mera, R. Riedel, E. Ionescu, Synthesis and high-temperature evolution of polysilylcarbodiimide-derived SiCN ceramic coatings, *Journal of the European Ceramic Society* 35(14) (2015) 3771-3780.
- [154] S.R. Shah, R. Raj, Nanoscale Densification Creep in Polymer-Derived Silicon Carbonitrides at 1350° C, *J Am Ceram Soc* 84(10) (2001) 2208-2212.
- [155] S.R. Shah, R. Raj, Mechanical properties of a fully dense polymer derived ceramic made by a

- novel pressure casting process, *Acta Materialia* 50(16) (2002) 4093-4103.
- [156] Q. Li, X. Yin, W. Duan, B. Hao, L. Kong, X. Liu, Dielectric and microwave absorption properties of polymer derived SiCN ceramics annealed in N₂ atmosphere, *Journal of the European Ceramic Society* 34(3) (2014) 589-598.
- [157] X. Guo, Y. Feng, X. Lin, Y. Liu, H. Gong, Y. Zhang, The dielectric and microwave absorption properties of polymer-derived SiCN ceramics, *Journal of the European Ceramic Society* 38(4) (2018) 1327-1333.
- [158] D. Su, Y.L. Li, Y. Feng, J. Jin, Electrochemical properties of polymer-derived SiCN materials as the anode in lithium ion batteries, *J Am Ceram Soc* 92(12) (2009) 2962-2968.
- [159] Y. Feng, Electrochemical properties of heat-treated polymer-derived SiCN anode for lithium ion batteries, *Electrochimica acta* 55(20) (2010) 5860-5866.
- [160] H.J. Seifert, J. Peng, J. Golczewski, F. Aldinger, Phase equilibria of precursor-derived Si-(B-) C-N ceramics, *Applied organometallic chemistry* 15(10) (2001) 794-808.
- [161] E. Barrios, L. Zhai, A review of the evolution of the nanostructure of SiCN and SiOC polymer derived ceramics and the impact on mechanical properties, *Molecular Systems Design & Engineering* 5(10) (2020) 1606-1641.
- [162] X. Ji, S. Wang, C. Shao, H. Wang, High-Temperature Corrosion Behavior of SiBCN Fibers for Aerospace Applications, *ACS Appl Mater Interfaces* 10(23) (2018) 19712-19720.
- [163] V. Petrman, J. Houska, S. Kos, P. Calta, J. Vlcek, Effect of nitrogen content on electronic structure and properties of SiBCN materials, *Acta Materialia* 59(6) (2011) 2341-2349.
- [164] F. Ye, L. Zhang, X. Yin, Y. Zhang, L. Kong, Q. Li, Y. Liu, L. Cheng, Dielectric and EMW absorbing properties of PDCs-SiBCN annealed at different temperatures, *Journal of the European Ceramic Society* 33(8) (2013) 1469-1477.
- [165] C. Luo, T. Jiao, Y. Tang, J. Kong, Excellent electromagnetic wave absorption of iron-containing SiBCN ceramics at 1158 K high-temperature, *Adv Eng Mater* 20(6) (2018) 1701168.
- [166] C. Luo, T. Jiao, J. Gu, Y. Tang, J. Kong, Graphene shield by SiBCN ceramic: a promising high-temperature electromagnetic wave-absorbing material with oxidation resistance, *ACS applied materials & interfaces* 10(45) (2018) 39307-39318.
- [167] E. Ionescu, B. Papendorf, H.-J. Kleebe, H. Breitzke, K. Nonnenmacher, G. Buntkowsky, R. Riedel, Phase separation of a hafnium alkoxide-modified polysilazane upon polymer-to-ceramic transformation—A case study, *Journal of the European Ceramic Society* 32(9) (2012) 1873-1881.
- [168] T. Xu, Q. Ma, Z. Chen, The effect of aluminum additive on structure evolution of silicon oxycarbide derived from polysiloxane, *Materials letters* 65(3) (2011) 433-435.
- [169] L. Toma, C. Fasel, S. Lauterbach, H.-J. Kleebe, R. Riedel, Influence of nano-aluminum filler on the microstructure of SiOC ceramics, *Journal of the European Ceramic Society* 31(9) (2011) 1779-1789.
- [170] Y. Cao, X. Yang, R. Zhao, Y. Chen, N. Li, L. An, Giant piezoresistivity in polymer-derived amorphous SiAlCO ceramics, *Journal of materials science* 51(12) (2016) 5646-5650.
- [171] E. Wasan Awin, A. Lale, K.C.N.H. Kumar, U. Bilge Demirci, S. Bernard, R. Kumar, Novel precursor-derived meso-/macroporous TiO₂/SiOC nanocomposites with highly stable anatase nanophase providing visible light photocatalytic activity and superior adsorption of organic dyes, *Materials* 11(3) (2018) 362.
- [172] R. Anand, S.P. Sahoo, B.B. Nayak, S.K. Behera, Phase evolution, nanostructure, and oxidation

- resistance of polymer derived SiTiOC ceramic hybrid, *Ceramics International* 45(5) (2019) 6570-6576.
- [173] Z. Lin, Y. Guo, X. Wang, C. Song, J. Song, Y. Zhang, R. Huang, Strong blue light emission from Eu-doped SiOC prepared by magnetron sputtering, *International Symposium on Photonics and Optoelectronics 2015*, International Society for Optics and Photonics, 2015, p. 96560R.
- [174] W. Krenkel, *Ceramic matrix composites: fiber reinforced ceramics and their applications*, John Wiley & Sons 2008.
- [175] S. Bernard, M. Weinmann, P. Gerstel, P. Miele, F. Aldinger, Boron-modified polysilazane as a novel single-source precursor for SiBCN ceramic fibers: synthesis, melt-spinning, curing and ceramic conversion, *Journal of materials chemistry* 15(2) (2005) 289-299.
- [176] Y. Jia, H. Keqing, Z. Xi, P. Yuqing, W. Zhenghui, D. Zhihua, Y. Muhuo, Melt spinning process and characterization of precursors for SiBN (C) ceramic fiber [J], *China Synthetic Fiber Industry* 3 (2011).
- [177] V. Maneeratana, W.M. Sigmund, Continuous hollow alumina gel fibers by direct electrospinning of an alkoxide-based precursor, *Chemical Engineering Journal* 137(1) (2008) 137-143.
- [178] H. Wu, W. Pan, D. Lin, H. Li, Electrospinning of ceramic nanofibers: Fabrication, assembly and applications, *Journal of Advanced Ceramics* 1(1) (2012) 2-23.
- [179] P. Baldus, M. Jansen, D. Sporn, Ceramic fibers for matrix composites in high-temperature engine applications, *Science* 285(5428) (1999) 699-703.
- [180] S.B. Mujib, R. Cuccato, S. Mukherjee, G. Franchin, P. Colombo, G. Singh, Electrospun SiOC ceramic fiber mats as freestanding electrodes for electrochemical energy storage applications, *Ceramics International* 46(3) (2020) 3565-3573.
- [181] S. Bernard, D. Cornu, S. Duperrier, B. Toury, P. Miele, Borazine based preceramic polymers for advanced BN materials, *Inorganic and Organometallic Macromolecules*, Springer 2008, pp. 351-371.
- [182] M. Shibuya, T. Yamamura, Characteristics of a continuous Si-Ti-CO fibre with low oxygen content using an organometallic polymer precursor, *Journal of materials science* 31(12) (1996) 3231-3235.
- [183] R.R. Naslain, SiC-matrix composites: nonbrittle ceramics for thermo-structural application, *International Journal of Applied Ceramic Technology* 2(2) (2005) 75-84.
- [184] R. Naslain, Design, preparation and properties of non-oxide CMCs for application in engines and nuclear reactors: an overview, *Composites Science and Technology* 64(2) (2004) 155-170.
- [185] K. Suzuki, S. Kume, K. Nakano, T. Chou, Fabrication and characterization of 3D C/SiC composites via slurry and PCVI joint process, *Key Engineering Materials* 164 (1999).
- [186] S. Sarkar, L. Zhai, Polymer-Derived Non-Oxide Ceramic Fibers—Past, Present and Future, *Materials Express* 1(1) (2011) 18-29.
- [187] T. Goto, Thermal barrier coatings deposited by laser CVD, *Surface and Coatings Technology* 198(1-3) (2005) 367-371.
- [188] T. Arai, H. Fujita, M. Watanabe, Evaluation of adhesion strength of thin hard coatings, *Thin Solid Films* 154(1-2) (1987) 387-401.
- [189] J.T. McGinn, Y. Blum, S.M. Johnson, M.I. Gusman, G.A. McDermott, Interactions Between Crystalline Si₃N₄ and Preceramic Polymers at High Temperature, *MRS Online Proceedings Library Archive* 346 (1994).
- [190] G. Barroso, T. Kraus, U. Degenhardt, M. Scheffler, G. Motz, Functional coatings based on

- preceramic polymers, *Adv Eng Mater* 18(5) (2016) 746-753.
- [191] R.M. Prasad, Y. Iwamoto, R. Riedel, A. Gurlo, Multilayer Amorphous-Si-B-C-N/ γ -Al₂O₃/ α -Al₂O₃ Membranes for Hydrogen Purification, *Adv Eng Mater* 12(6) (2010) 522-528.
- [192] R. Hauser, S. Nahar-Borchard, R. Riedel, Y.H. Ikuhara, Y. Iwamoto, Polymer-Derived SiBCN Ceramic and their Potential Application for High Temperature Membranes Dedicated to Prof. Dr.-Ing. Dr. hc Hartmut Fuess on the occasion of his 65th birthday, *Journal of the Ceramic Society of Japan (日本セラミックス協会学術論文誌)* 114(1330) (2006) 524-528.
- [193] L. Gibson, M. Ashby, *Cellular Solids: Structure and Properties*. Cambridge Univ Press, Cambridge, UK (1999).
- [194] P. Colombo, In praise of pores, *Science* (2008) 381-383.
- [195] M. Xu, H. Li, D. Zhai, J. Chang, S. Chen, C. Wu, Hierarchically porous nagelschmidite bioceramic–silk scaffolds for bone tissue engineering, *J Mater Chem B* 3(18) (2015) 3799-3809.
- [196] D. Khang, J. Choi, Y.-M. Im, Y.-J. Kim, J.-H. Jang, S.S. Kang, T.-H. Nam, J. Song, J.-W. Park, Role of subnano-, nano-and submicron-surface features on osteoblast differentiation of bone marrow mesenchymal stem cells, *Biomaterials* 33(26) (2012) 5997-6007.
- [197] S.H. Lee, S.H. Jun, H.E. Kim, Y.H. Koh, Piezoelectric properties of PZT-based ceramic with highly aligned pores, *J Am Ceram Soc* 91(6) (2008) 1912-1915.
- [198] T. Isobe, Y. Kameshima, A. Nakajima, K. Okada, Y. Hotta, Gas permeability and mechanical properties of porous alumina ceramics with unidirectionally aligned pores, *Journal of the European Ceramic Society* 27(1) (2007) 53-59.
- [199] C. Vakifahmetoglu, D. Zeydanli, P. Colombo, Porous polymer derived ceramics, *Materials Science and Engineering: R: Reports* 106 (2016) 1-30.
- [200] H.Y. Ryu, Q. Wang, R. Raj, Ultrahigh-temperature semiconductors made from polymer-derived ceramics, *J Am Ceram Soc* 93(6) (2010) 1668-1676.
- [201] V. Liebau-Kunzmann, C. Fasel, R. Kolb, R. Riedel, Lithium containing silazanes as precursors for SiCN: Li ceramics—a potential material for electrochemical applications, *Journal of the European Ceramic Society* 26(16) (2006) 3897-3901.
- [202] B. Duong, P. Gangopadhyay, J. Brent, S. Seraphin, R.O. Loutfy, N. Peyghambarian, J. Thomas, Printed sub-100 nm polymer-derived ceramic structures, *ACS applied materials & interfaces* 5(9) (2013) 3894-3899.
- [203] F. Fang, K. Liu, T. Kurfess, G. Lim, Tool-based micro machining and applications in MEMS, MEMS/NEMS, Springer 2006, pp. 678-740.
- [204] L.-A. Liew, W. Zhang, V.M. Bright, L. An, M.L. Dunn, R. Raj, Fabrication of SiCN ceramic MEMS using injectable polymer-precursor technique, *Sensors and Actuators A: Physical* 89(1-2) (2001) 64-70.
- [205] J. Grossenbacher, M.R. Gullo, V. Bakumov, G. Blugan, J. Kuebler, J. Brugger, On the micrometre precise mould filling of liquid polymer derived ceramic precursor for 300- μ m-thick high aspect ratio ceramic MEMS, *Ceramics International* 41(1) (2015) 623-629.
- [206] G. Konstantinou, E. Kakkava, L. Hagelüken, P.V.W. Sasikumar, J. Wang, M.G. Makowska, G. Blugan, N. Nianias, F. Marone, H. Van Swygenhoven, Additive micro-manufacturing of crack-free PDCs by two-photon polymerization of a single, low-shrinkage preceramic resin, *Additive Manufacturing* 35 (2020) 101343.
- [207] S.T. Howell, A. Grushina, F. Holzner, J. Brugger, Thermal scanning probe lithography—A review,

- Microsystems & Nanoengineering 6(1) (2020) 1-24.
- [208] J. Wang, H. Wang, L. Lai, Y. Li, Preparation of Microneedle Array Mold Based on MEMS Lithography Technology, *Micromachines* 12(1) (2021) 23.
- [209] A. Standard, Standard terminology for additive manufacturing technologies, ASTM International F2792-12a (2012).
- [210] P. Colombo, J. Schmidt, G. Franchin, A. Zocca, J. Günster, Additive manufacturing techniques for fabricating complex ceramic components from preceramic polymers, *Am. Ceram. Soc. Bull* 96(3) (2017) 16-23.
- [211] A. Zocca, G. Franchin, H. Elsayed, E. Gioffredi, E. Bernardo, P. Colombo, Direct ink writing of a preceramic polymer and fillers to produce hardystonite ($\text{Ca}_2\text{ZnSi}_2\text{O}_7$) bioceramic scaffolds, *J Am Ceram Soc* 99(6) (2016) 1960-1967.
- [212] H. Jin, Z. Yang, J. Zhong, D. Cai, H. Li, D. Jia, Y. Zhou, Mechanical and dielectric properties of 3D printed highly porous ceramics fabricated via stable and durable gel ink, *Journal of the European Ceramic Society* 39(15) (2019) 4680-4687.
- [213] D. Mohan, Z.K. Teong, M.S. Sajab, N.H.N. Kamarudin, H. Kaco, Intact Fibrillated 3D-Printed Cellulose Macrofibrils/ CaCO_3 for Controlled Drug Delivery, *Polymers* 13(12) (2021) 1912.
- [214] S.L. Dong, L. Han, C.X. Du, X.Y. Wang, L.H. Li, Y. Wei, 3D printing of aniline tetramer-grafted-polyethylenimine and pluronic F127 composites for electroactive scaffolds, *Macromolecular rapid communications* 38(4) (2017) 1600551.
- [215] G. Liu, Y. Zhao, G. Wu, J. Lu, Origami and 4D printing of elastomer-derived ceramic structures, *Sci Adv* 4(8) (2018).
- [216] W.-Y. Maeng, J.-W. Jeon, J.-B. Lee, H. Lee, Y.-H. Koh, H.-E. Kim, Photocurable ceramic/monomer feedstocks containing terpene crystals as sublimable porogen for UV curing-assisted 3D plotting, *Journal of the European Ceramic Society* (2020).
- [217] L. Wei, J. Li, S. Zhang, B. Li, Y. Liu, F. Wang, S. Dong, Fabrication of SiOC ceramic with cellular structure via UV-Assisted direct ink writing, *Ceramics International* (2019).
- [218] M. Mahmoudi, C. Wang, S. Moreno, S.R. Burlison, D. Alatalo, F. Hassanipour, S.E. Smith, M. Naraghi, M. Minary-Jolandan, Three-Dimensional Printing of Ceramics through "Carving" a Gel and "Filling in" the Precursor Polymer, *ACS Appl Mater Interfaces* (2020).
- [219] R. Karyappa, T. Ching, M. Hashimoto, Embedded Ink Writing (EIW) of Polysiloxane Inks, *ACS Appl Mater Interfaces* 12(20) (2020) 23565-23575.
- [220] I. Astm, ASTM52900-15 standard terminology for additive manufacturing—general principles—terminology, ASTM International, West Conshohocken, PA 3(4) (2015) 5.
- [221] N.A. Chartrain, C.B. Williams, A.R. Whittington, A review on fabricating tissue scaffolds using vat photopolymerization, *Acta Biomater* 74 (2018) 90-111.
- [222] M.L. Griffith, J.W. Halloran, Freeform fabrication of ceramics via stereolithography, *J Am Ceram Soc* 79(10) (1996) 2601-2608.
- [223] J. Schmidt, P. Colombo, Digital light processing of ceramic components from polysiloxanes, *Journal of the European Ceramic Society* 38(1) (2018) 57-66.
- [224] E. Zanchetta, M. Cattaldo, G. Franchin, M. Schwentenwein, J. Homa, G. Brusatin, P. Colombo, Stereolithography of SiOC Ceramic Microcomponents, *Adv Mater* 28(2) (2016) 370-376.
- [225] S.A. Rasaki, D. Xiong, S. Xiong, F. Su, M. Idrees, Z. Chen, Photopolymerization-based additive manufacturing of ceramics: A systematic review, *Journal of Advanced Ceramics* 10(3) (2021) 442-

471.

- [226] B.E. Kelly, I. Bhattacharya, H. Heidari, M. Shusteff, C.M. Spadaccini, H.K. Taylor, Volumetric additive manufacturing via tomographic reconstruction, *Science* 363(6431) (2019) 1075-1079.
- [227] M. Regehly, Y. Garmshausen, M. Reuter, N.F. König, E. Israel, D.P. Kelly, C.-Y. Chou, K. Koch, B. Asfari, S. Hecht, Xolography for linear volumetric 3D printing, *Nature* 588(7839) (2020) 620-624.
- [228] A. Kulkarni, G.D. Sorarù, J.M. Pearce, Polymer-derived SiOC replica of material extrusion-based 3-D printed plastics, *Additive Manufacturing* 32 (2020) 100988.
- [229] G. Franchin, P. Colombo, Porous geopolymer components through inverse replica of 3D printed sacrificial templates, *Journal of Ceramic Science and Technology* 6(2) (2015) 105-111.
- [230] H. Xiong, L. Zhao, H. Chen, H. Luo, X. Yuan, K. Zhou, D. Zhang, Building SiC-based composites from polycarbosilane-derived 3D-SiC scaffolds via polymer impregnation and pyrolysis (PIP), *Journal of the European Ceramic Society* 41(2) (2021) 1121-1131.
- [231] A. Baux, S. Jacques, A. Allemand, G.L. Vignoles, P. David, T. Piquero, M.P. Stempin, G. Chollon, Complex geometry macroporous SiC ceramics obtained by 3D-printing, polymer impregnation and pyrolysis (PIP) and chemical vapor deposition (CVD), *Journal of the European Ceramic Society* 41(6) (2021) 3274-3284.
- [232] L. Gorjan, R. Tonello, T. Sebastian, P. Colombo, F. Clemens, Fused deposition modeling of mullite structures from a preceramic polymer and γ -alumina, *Journal of the European Ceramic Society* 39(7) (2019) 2463-2471.
- [233] L. Zhao, X. Wang, H. Xiong, K. Zhou, D. Zhang, Optimized preceramic polymer for 3D structured ceramics via fused deposition modeling, *Journal of the European Ceramic Society* 41(10) (2021) 5066-5074.

2. Production and properties of SiOC ceramic structures from a silicone elastomer

2.1 Complex SiOC ceramic structures by direct ink writing and origami

2.1.1 Introduction

Origami, the ancient art of paper folding developed in Japan several centuries ago, has demonstrated the possibility of creating complex three-dimensional structures starting from two-dimensional patterns that are cut or folded into desired geometries through bending along predefined lines [1,2].

With the use of elastomeric or foldable materials, several researchers have exploited this approach to fabricate topological meta-materials [3-5], reconfigurable structures [6-8] or adaptive architectures [9,10], which have broad applications such as solar arrays [11,12] and components for tissue engineering [13], energy storage [14], soft robotics [15-17] and so on. The application of the origami technique is not just limited to macro-size parts, but can be exploited also in the micro-scale: from mesoscale biomedical devices [18,19] to nano-scale protein and DNA-based objects [20-25]. Recently, the rapid development of additive manufacturing technologies has enabled the precise 3D fabrication of components with resolution from the hundreds of nanometers to tens of centimeters without restriction on the spatial arrangement of the constituting material. Several works report that much more complicated and functional 3D structures could be achieved by combining origami technique and 3D printing, with benefits both in term of manufacturing speed and low-cost fabrication. For example, Hester et al. [26] obtained flexible microwave electronics by origami-assisted inkjet printing. Zhao et al. [27] suggested a mechanochemical regulation strategy to create 3D origami structures by a transfer printing method based on stiffness mismatch. Lewis et al. [28] combined direct ink writing with wet-folding origami technique to create simple polyhedrons and intricate 3D origami forms. Therefore, making use of the advantages

of 3D printing and origami opens new possibilities for advanced fabrication of very complex regular shapes.

Additive manufacturing of preceramic polymers to fabricate 3D polymer derived ceramics (PDCs) has recently attracted a lot of interest, with researchers employing a wide range of technologies for the production of ceramic components [29-34]. However, the inherent brittleness and high hardness of ceramics after pyrolysis, resulting from their ionic or covalent bond, limit their further reconfiguration toward more intricate shapes [35]. A potential alternative is performing the reconfiguration towards the selected architecture using a flexible polymeric green body before pyrolysis. To this end, Liu et al. printed flexible preceramic parts enhanced by nano-particles, and obtained high-resolution complex and mechanically robust ceramics with the use of origami technique [36]. However, their use of an iron wire as aid to the manufacturing process (to keep the folded part in shape during pyrolysis) may cause local stress concentrations due to mismatch in the coefficient of expansion and contamination during subsequent firing. Zhan et al. [37] reported 3D printing of flexible green parts with yttria-stabilized zirconia powder by self-assembly-assisted shaping and mold-assisted shaping. This approach, however, is limited by the complicated procedure involving the addition of a significant number of polymeric additives and UV-crosslinking.

In this work, we provide very simple approaches for the fabrication the complex SiOC ceramics derived from a commercially available, two-part silicone elastomer by Direct Ink Writing (DIW) printing assisted by the origami technique, with no need to add nanoparticles for reinforcement or use a metal wire for shaping. As shown in **Fig. 1**, the ink was prepared by homogenously mixing the silicone with its curing agent at a 10:1 weight ratio, as indicated by the manufacturer. The prepared ink was then transferred into syringes for printing using Direct Ink Writing. After printing, we followed two approaches to fabricate components possessing complex architectures:

(I) **Filament-assisted origami:** reconfiguration of printed sheets was carried out

with the assistance of silicone filaments to keep the folded part in shape during pyrolysis. Such filaments were extruded from a 400 μm nozzle using the same silicone material employed for the fabrication of the sheets. Before folding, the sheets were thermally cross-linked at 75°C for 30 min. Using this filament, having the same shrinkage as the sheet upon pyrolysis, prevented local stress concentrations during the ceramization of the origami structures and could, for some geometries, be removed after pyrolysis without damaging the folded patterns.

(II) **Self-adhesive origami**: instead of thermally cross-linking the sheets, they were simply dried at room temperature (RT) for two days. After that, the sheets displayed a degree of self-adhesion achievable by manually applying a light pressure, which enabled the folded structures to maintain their shape without using a filament. The folded samples were then heated at 75°C for 30 min to complete the cross-linking. Obviously, not having to use a wire to bind the sides of the sheets nor having to eliminate it after pyrolysis greatly simplifies the fabrication of complex architectures.

Furthermore, additional experiments were carried out by assembling separate sheets (without folding them), either by using a filament to bind them or by exploiting the self-adhesion between sheets. This approach cannot be considered to be based on the origami technique, but it further expands the post-printing fabrication possibilities.

2.1.2 Experimental Section

2.1.2.1 3D printing of 2D sheets

A two-part silicone adhesive (DOWSIL™ SE 1700, Dow, USA; data sheet is reported in **Tab. 2.1**) was used as the polymer precursor for SiOC ceramics. As shown in **Fig. 2.1**, the ink was prepared by mixing the silicone base (part A) with its proprietary curing agent (part B) at a 10:1 weight ratio, as suggested by the manufacturer, in a planetary mixer (ARE 250, Thinky, Japan) for 15 mins (2000 rpm/min). The ink was then transferred into syringes equipped with conical plastic nozzle (Nordson, USA), followed by degassing in the mixer before printing. DIW was performed at the room

temperature by using a delta printer (2040 Turbo, Wasproject, Italy). The ink was extruded from the nozzle to form the 2D patterns layer by layer with well-defined inter-layer spacing (80 % of the nozzle diameter), with a pressure of 0.3-0.6 MPa and X-Y motion speeds of 5-10 mm/s. For generating the 2D patterns with different inter-filament spacing, ranging from 0.2 to 2 mm, the selected nozzle diameter was 400 μm . The samples were all printed within 1h of mixing the two-part silicone precursor. The designing of 2D patterns and folded 3D models in this paper was performed using the open-source 3D modeling software Blender 2.79 (Blender Foundation, Amsterdam, the Netherlands).

Tab. 2.1 Details for DOWSIL™ SE 1700, according to the manufacturer’s data sheet

Property	Unit	Data
Viscosity (after mixing)	cP	54200
Working Time @25°C (pot life)	hours	8
Heat Cure Time @150°	minutes	30
Specific Gravity (Cured)	g/cm ³	1.13
Tensile Strength	MPa	6.8
Elongation	%	355
Durometer Shore A		48
Unprimed Adhesion – Lap Shear to Aluminum	MPa	2.7

2.1.2.2 Filament-assisted origami folding of printed structures

To demonstrate folding using the origami technique, firstly the 2D printed sheets were put into muffle furnace at 75°C for 30 min to achieve cross-linking. Then, a low stress was manually applied to single sheets, causing simple deformations such as bending, stretching, twisting, followed by binding with thin elastomeric filaments, obtained by extruding through a 400 μm nozzle the same silicone ink and cured at 75°C

for 30 min, to retain the given shape. 3D structures based on regular polyhedrons, including tetrahedron, hexahedron, octahedron, dodecahedron, as well as spirals or other shapes were manufactured by this approach. Alternatively, separate flat 2D parts were assembled and bound together with a filament.

2.1.2.3 Self-adhesive origami of printed structures

Firstly, the 2D printed sheets were dried at room temperature (RT) for 2 days (the same effect could be achieved by placing into a muffle at 75 °C for only 5 min). The edges of bent sheets were lightly pressed together to achieve adhesion, and the folded 3D structures were then cross-linked at 75°C for 30 min in a muffle furnace. No filaments were used in this approach to assist retaining of the obtained shape.

2.1.2.4 Ceramization

The samples were pyrolyzed in a tube furnace under inert atmosphere (99.99 % N₂), with a heating rate of 1°C/min from room temperature to 300 °C, with a hold time of 3h, followed by heating to 1000 °C at the same rate, with a hold time of 2h. Cooling was carried out in the furnace, without controlling the rate.

2.1.2.5 Characterization

The rheological properties of the inks were investigated using a rheometer (Discovery HR-1 hybrid rheometer, TA Instruments, UK). All the analyses were conducted using a cone/plate set-up with a gap of 0.5 mm. Thermo-gravimetric (TG) analysis (STA409, Netzsch, Germany) was carried out to investigate the polymer to ceramic conversion of this silicone precursor. Fourier-transform infrared spectrometry (FTIR, Is10, Nicolet, Thermo Scientific, USA) was used to characterize the printed samples before and after sintering. The crystalline phase assemblage was investigated by X-ray diffraction (XRD, AXS D8 Advance, Bruker, Germany) on powders obtained by grinding pyrolyzed samples. The morphology and microstructure of the samples

were observed by scanning electron microscopy (SEM, Quanta 200 ESEM, FEI, The Netherlands), equipped with energy dispersive X-ray Spectroscopy.

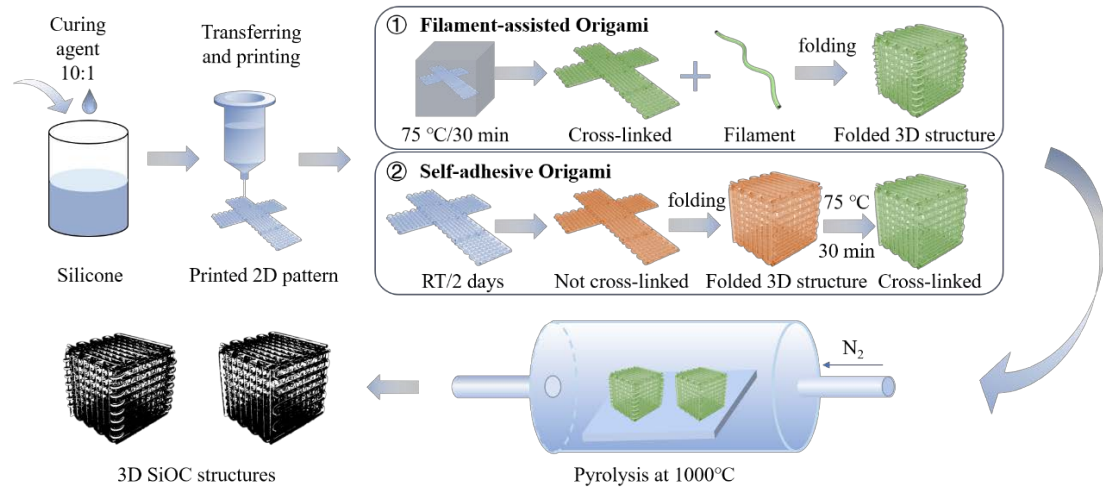


Fig. 2.1 Schematic of the fabrication of SiOC samples with complex architecture from 3D printing and origami technique.

2.1.3 Results and Discussion

2.1.3.1 Rheological Properties

For extrusion-based additive manufacturing (DIW) of 3D components, the rheological properties of the ink play a crucial role in the processing and characteristics of the printed samples. On the one hand, a shear-thinning, low viscosity under high shear rate is required for easy extrusion through narrow nozzles when pressure is applied on the reservoir containing the material. On the other hand, the ink should quickly recover a high viscosity to enable the precise retention of the desired architecture after extrusion, without sagging of unsupported or spanning features. Finally, the ink should possess a suitably high yield stress, in order to generate components comprised of several layers that do not collapse under the weight of the printed structure itself.

Fig. 2.2a reports the viscosity of the elastomeric silicone ink as the function of

shear rate, and the influence of storage time. Taking the sample with storage time of 0h, for example, the viscosity of the ink decreased from 3.6×10^5 Pa·s to 10^2 Pa·s in the range of shear rate 10^{-3} - 10 s⁻¹, which indicates that the prepared ink is a typical non-Newtonian fluid with shear-thinning behavior under increasing shear rate [38]. The shear-thinning behavior could still be detected after storage for 24h, but the material was barely printable with the pressures that could be applied in our equipment, and more suitable processing conditions were retained up to 8h of storage, demonstrating that the ink possessed a favorably long storage time. To determine the viscosity recovery after extrusion, a different shear rate test was performed (**Fig. 2.2b**). The ink was first stressed at the shear rate of 0.04 s⁻¹ for 60 sec, during which it displayed a viscosity of 10^4 ~ 10^5 Pa·s, and subsequently the shear rate was decreased to nearly 0 s⁻¹; in these conditions, the ink almost immediately recovered a high viscosity value (10^6 ~ 10^7 Pa·s), showing that it possessed a rapid recovery enabling the fabrication of self-supported features without significant deformation in the green state (before curing and pyrolysis). **Fig. 2.2c** shows the storage modulus (G') and loss modulus (G'') as a function of shear strain, and also their variation with storage time. Similarly to the viscosity behavior, few changes were observed even after 24h of storage, further confirming the high stability of the ink. Taking the sample with storage time of 0h for example, both storage and loss modulus showed suitably high plateau values at the beginning of the test, 2×10^5 and 4×10^4 Pa, respectively, suggesting that complex 3D lattice architectures could be obtained. The storage modulus was independent on the applied stress and nearly one order of magnitude higher than the loss modulus, indicating a solid-like behavior of the ink below the yield stress; therefore, the material resided within the linear viscoelastic region [39]. When the shear strain increased over 0.68 % (shear yield stress $\tau_y = 840$ Pa), both moduli decreased rapidly, and the loss modulus became higher than the storage modulus. This indicates the predominance of viscous deformation in the viscoelastic ink properties, and the material behaved as a liquid, proving the possibility of achieving a smooth and continuous flow under limited

pressure. Frequency sweep tests (**Fig. 2.2d**) showed that both moduli were stable when the frequency increased.

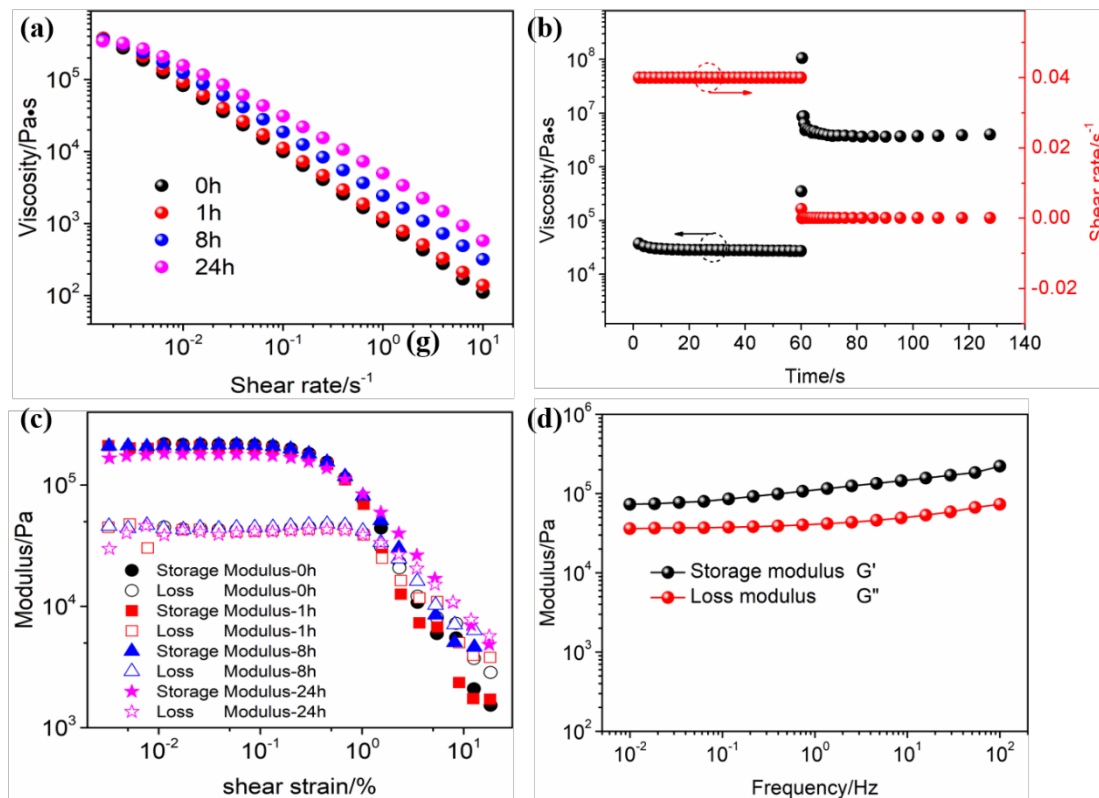


Fig. 2.2 Rheological properties of the silicone ink: (a) apparent viscosity as a function of shear rate with storage time = 0, 1, 8, 24h; (b) apparent viscosity and shear rate changes with time and shear stress value; (c) storage (G') and loss modulus (G'') as a function of shear strain with storage time = 0, 1, 8, 24h; (d) small amplitude oscillatory shear modulus measurements as a function of frequency.

2.1.3.2 Material's Characterization

Since this specific silicone elastomer was, so far, never employed as a precursor for SiOC ceramics, its evolution with firing temperature was investigated using TG and FTIR. Thermogravimetric analysis (see **Fig. 2.3a**) shows a weight decrease starting only from about 200°C, indicating that a high degree of cross-linking was achieved in

the material after curing at 75°C for 30 min. The polymer-to-ceramic transformation occurred in the usual 400-to-800°C range, after which no further significant weight loss was observed, demonstrating the reaching of a fully ceramic phase. The total weight loss at 1000°C was ~27.5 wt%, thereby giving a high ceramic yield of 72.5 wt%, which is within the range of values typically observed for other precursors (see **Tab. 2.2**).

Tab. 2.2 Ceramic yield of various precursors (pyrolysis in inert atmosphere)

Pre-ceramic precursor	Yield (wt%)	Reference
RC711 (silicone acrylate)	7.4	
H44 (silicone resin)	76.5	[40]
Silres 601 (silicone resin)	66.8	
MK (silicone resin)	83.0	[41]
Polymethylhydrosiloxane	59.5	[42]
Perhydropolysilazane	63.0	[43]
Polycarbosilane	61.5	[44]
Polyvinylsilazane	70	[45]
(Mercaptopropyl)methylsiloxane/vinylmethoxysiloxane	59	[46]
Liquid-phase polysilazane	32	[47]

The crystalline phase assemblage of pyrolyzed SiOC is shown in **Fig. 2.3b**; the broad peak indicates the formation of an amorphous material, without the formation of any SiC, SiO₂, Si, or C crystallites. The FTIR patterns (**Fig. 2.4a**) show the characteristic absorption bands of the silicone (part A), cross-linker (part B), printed materials after drying at room temperature for 2 days and after cross-linking at 75°C for 30 min, with peaks located at around 475 cm⁻¹ (Si-O-Si rocking vibration), 802, 1261 and 2963 cm⁻¹ (-CH₃ rocking, -CH₃ deformation and asymmetric -CH₃ stretching in Si-CH₃), 1023 and 1096 cm⁻¹ (Si-O-Si stretching vibration), 2160 cm⁻¹ (Si-CH=CH₂

stretching vibration) and 1412 cm^{-1} (Si-H stretching vibration) [48-51]. In particular, the Si-H band (part B, **Fig. 2.4b**) decreases in intensity with the progression of cross-linking. For the SiOC material, the peaks are located at around 460 cm^{-1} (Si-O-Si rocking vibration), 800 cm^{-1} (Si-C stretching vibration), 1630 cm^{-1} and 1700 cm^{-1} (C=C and C=O stretching vibration) [52-55]. In addition, the broad peak visible in the 900 to 1300 cm^{-1} range was composed of overlapping vibrational modes from various bond structures. According to literature, it was possible to deconvolute it into five peaks located at ~ 1175 , 1101 , 1023 , 1216 and 957 cm^{-1} (**Fig. 2.4c**), attributable to Si-O-C cage link and open link structures, Si-O-Si and Si-C stretching vibration, respectively [56-58].

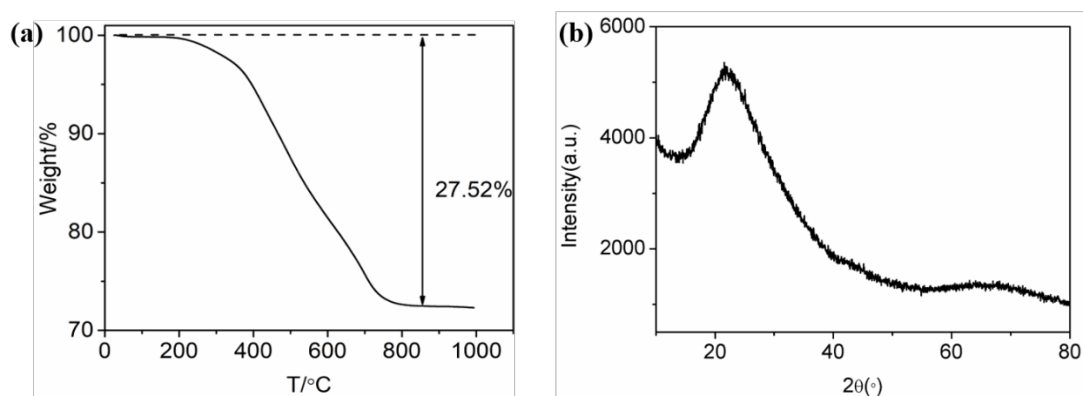


Fig. 2.3 (a) thermal gravimetric analysis (TG) of the silicone elastomer (after 30 min at 75°C); (b) XRD pattern of a sample pyrolyzed at 1000°C .

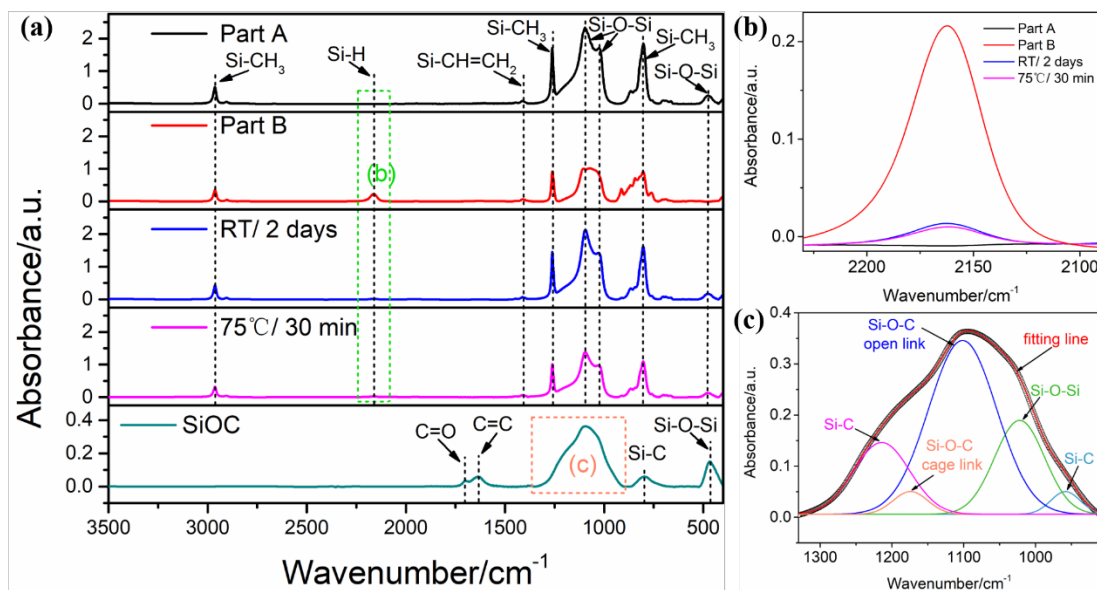


Fig. 2.4 (a) FTIR spectra of as printed silicone and pyrolyzed SiOC, (b) magnified regions for pure silicone constituents, after drying at room temperature (RT) and after cross-linking at 75°C (2090-2230 cm^{-1}), (c) magnified region for SiOC (900-1300 cm^{-1}), with peak deconvolution.

2.1.3.3 Printing of 2D Patterns and Filament-assisted Origami Folding

For the complex architectures obtained using the origami technique, 2D patterns comprising only 3 layers separated by less than the thickness of one strut (320 μm), to ensure good adhesion between layers during printing, were manufactured by DIW. Obviously, 2D sheets made of a single layer could be used as well, but we chose to employ multilayer 2D structures to add another degree of freedom and complexity to the overall final design. In fact, even thicker sheets could be folded, generating structures with a smaller internal void encased in a multilayer thick shell. In separate experiments (not reported here for the sake of brevity) we folded multilayer sheets with a thickness in the 2-10 mm range. In addition, foldability does not only depend on the thickness of a sheet, but also on its width; theoretically, a sheet could be folded as long as its width is much larger than its thickness.

Due to the high flexibility and stretchability of the silicone elastomer (355 % elongation, according to the manufacturer's specifications in **Tab. 2.1**), the printed patterns could go through reversible shaping under deformation, such as stretching, twisting and folding at very large angles, without generating any damage in the struts (see **Fig. 2.5a-d**). Two different geometries for the sheets were used as the base for shaping complex architectures: 1) a 100x10 mm rectangle with a 0.4 mm spacing between filaments in the x-y plane, used for rolling and twisting into a cylinder and a spiral; 2) a 35×35 mm² with different spacing between filaments in the x-y plane (1 and 2.1 mm), used for folding along diagonal lines. After printing, the 2D patterns were folded, and were enabled to retain their shape by binding them, at selected locations, using an extruded 400 μm filament made from the same silicone material. It should be noted that during printing the wet filaments comprising the 2D sheets join well together, because each layer is printed at a height slightly lower than the spacing in z-direction between adjacent layers, thereby forcing the contact between the two layers. Thermal cross-linking (either applied before or after folding of the sheets) further stabilizes the material. When a filament is then used to bind the sheets together, this does not stick permanently to the polymeric silicone structure because the latter one is already well crosslinked and fully dry, and no pressure is added to force the contact. Therefore, the removal of this filament after pyrolysis does not cause any damage to the folded sheets. The folded structures retain their shape also when heated at lower temperatures than 1000°C, for instance when heating at 300°C, evidently because the silicone loses its elastomeric properties due to the starting of the polymer-to-ceramic conversion. However, the structures heat treated at such temperature are quite fragile, and therefore the removal of the filament used for binding at this stage can cause some unwanted damage.

Fig. 2.5e-g show the morphology of printed, single sheets, before and after folding, as-printed (after cross-linking) or after pyrolysis. **Fig. 2.5e** shows the well-defined printed wood-pile structures, with continuous filaments and no sagging in the spanning

regions (with length of 1 and 2.1 mm), indicating the high ability for shape retention after printing of the silicone elastomer. After pyrolysis (**Fig. 2.5f**), no cracks or pores can be observed on the surface and cross-section of the filaments. From the SEM images of a curved sample, reported in **Fig. 2.5g**, we can infer that no damage was generated in the whole structure because of the folding. The good bonding between adjacent layers provided an excellent structural integrity even when undergoing a shrinkage upon pyrolysis (diameter of pyrolyzed filament was $\sim 300\ \mu\text{m}$).

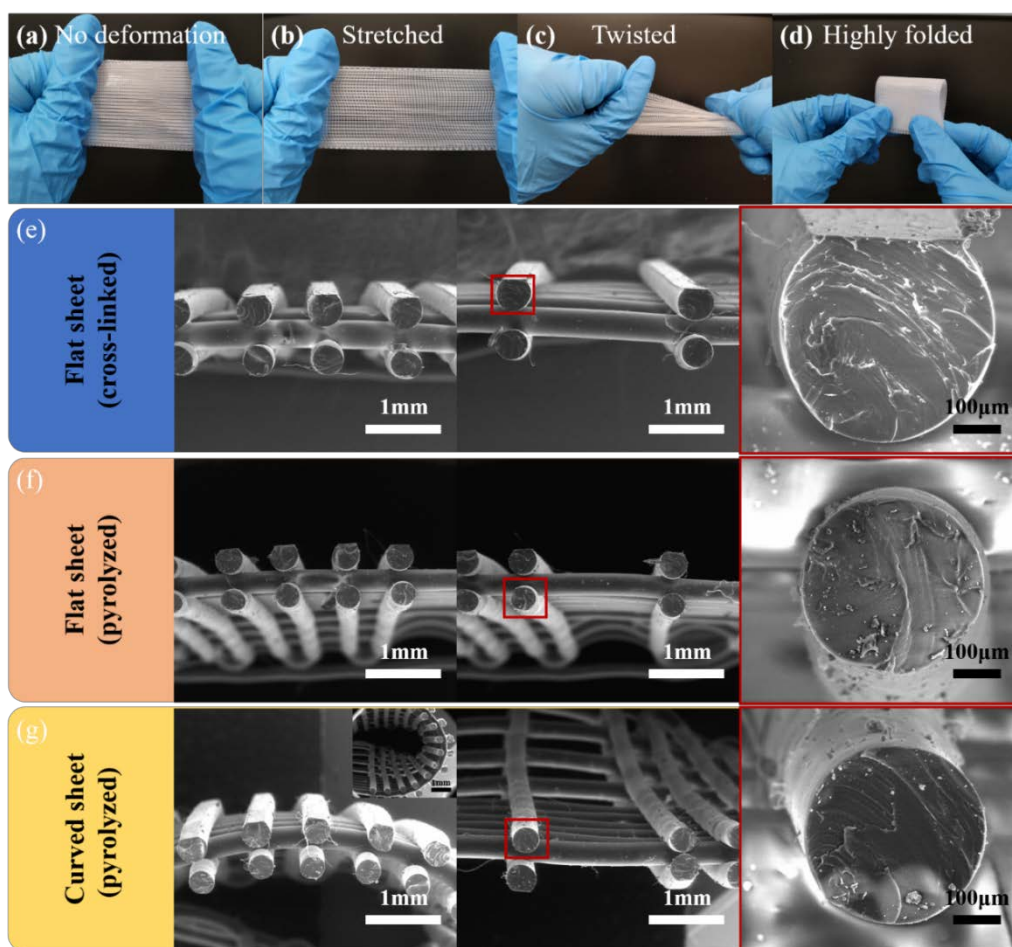


Fig. 2.5 Printed single 2D sheet: (a) no deformation; (b) stretched; (c) twisted; (d) highly folded. Microstructure of a single 2D sheet, as printed (after cross-linking at 75°C) or after pyrolysis: (e) flat sheet (cross-linked); (f) flat sheet (pyrolyzed); (g) curved sheet (pyrolyzed).

Representative images of the whole process are shown in **Fig. 2.6**, including the designed patterns, printed patterns, and folded 3D structures before and after pyrolysis. All samples obtained using the two different 2D patterns led to SiOC ceramic parts that fully retained their given shape. The linear shrinkage after pyrolysis, measured using a digital caliper, was isotropic and $\sim 25\%$, which is rather typical for high ceramic yield preceramic polymers. Again, no cracks were visible both in the material before and after pyrolysis, indicating that folding did not cause detrimental residual stresses and that this approach for the easy fabrication of components with highly complex architectures is viable.

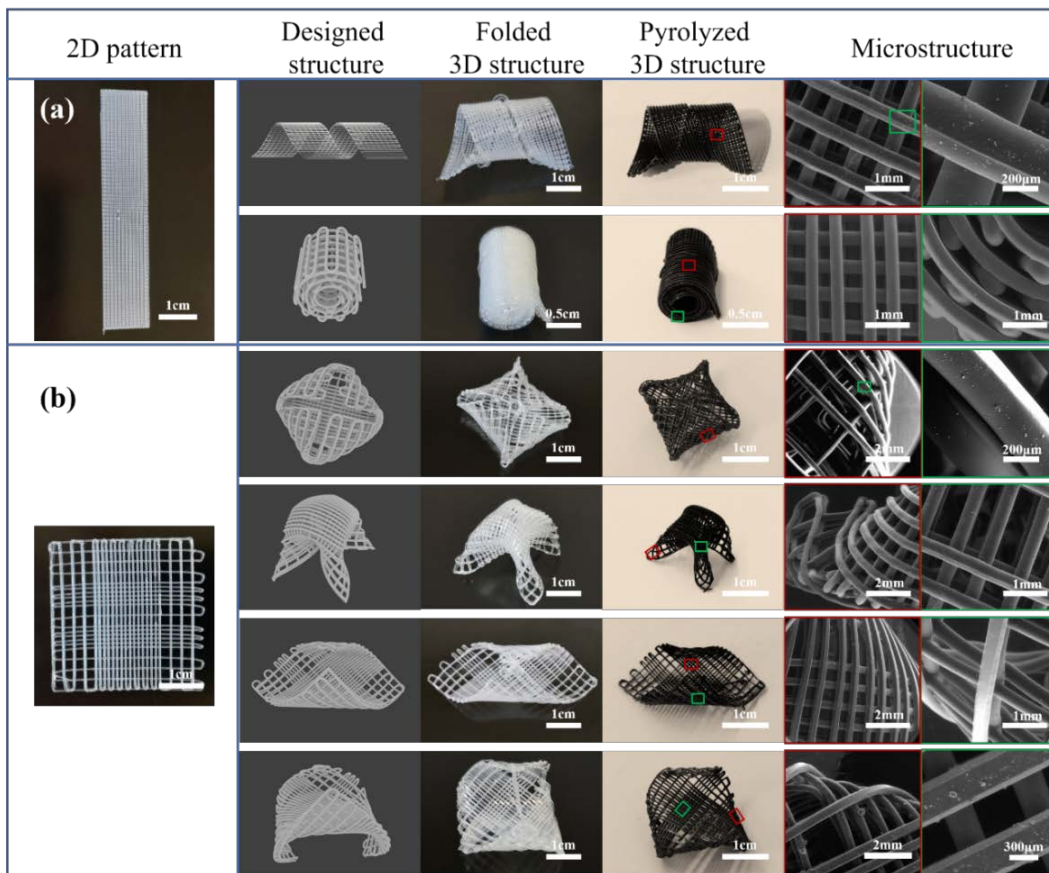


Fig. 2.6 Complex 3D architectures generated by means of the origami technique starting from 2D printed sheets with different patterns, using a silicone filament to maintain the desired shape after folding.

The parts that were fabricated starting from the 2D pattern designed with different spacings, using a very high folding angle (**Fig. 2.6b**), further confirmed the ability of the material to retain its integrity under deformation and its shape after pyrolysis, as high curvatures (folding angle close to 180°) were applied with no sign of damage anywhere in the resulting ceramic structure. Furthermore, with this silicone material it was possible to print large unsupported overhangs (spans of 2.1 mm, up to five times more than the filament's diameter) confirming its highly suitable rheological behavior for DIW processing.

In addition to the above procedure using binding with a silicone filament of bent structures based on a multi-part sheet, it should be noted that, when assembling printed structures starting from 2D sheets, several further possibilities could be explored (see **Fig. 2.7**). For instance, a tetrahedron structure could be obtained by folding a single sheet, followed by binding with a filament (**Fig. 2.7a**). In this case, however, some deformation of the structure (rounding of the surfaces and edges) can be observed, due to the deformation of the green layer before pyrolysis. Furthermore, the same structure can be fabricated either using a single sheet containing different structures that are linked at the edges (**Fig. 2.7b**) or by assembling separate parts (**Fig. 2.7c**). Using a single 2D sheet, containing different structures linked at the edges, requires a lower amount of stitching with an additional filament, when assembling the final structure. Note that, strictly speaking, the simple assembling of separate flat parts cannot be considered to be an origami technique. Finally, the 2D sheets themselves could have additional hollow patterns, besides the one provided by the presence of the struts, further increasing the degree of freedom and complexity that can be achieved in the developed structures (**Fig. 2.7d**).



Fig. 2.7 Illustration of different processing possibilities to fabricate a tetrahedron structure: (a) folding and binding of a single sheet; (b) folding and binding of a single sheet containing different structures, linked at the edges; (c) assembling and binding of separate parts; (d) folding and binding of a single sheet containing different structures with additional porosity, linked at the edges. A silicone filament was used to bind the different parts, in all examples.

Other regular polyhedra, flower-like, knot and bow tie structures derived from designed 2D patterns, comprised again of 3 layers, were also obtained by binding the whole structure together with a silicone filament (**Fig. 2.8**). Similarly to the tetrahedron, the other regular shapes were also well retained after pyrolysis, without deformation or defects. However, when generating these structures, the edges had to be bound with long lengths of filament in order to obtain a stable assemblage, and therefore it was not possible to remove it after pyrolysis. The edges of these folded structures did not join during pyrolysis. Furthermore, when assembling the type of structures shown in **Fig.**

2.7 and Fig. 2.8, an additional degree of complexity can be added by embedding one structure inside another one, before forming the latter by origami and before pyrolysis. An example is shown in Fig. 2.8g,h, where a small cube was embedded inside a larger cube. It should be noted that, after pyrolysis, the two cubes remained separate, with no adhesion among the two structures, due to the good degree of crosslinking obtained during curing. These geometrically complex architectures, which are quite difficult to obtain without supporting materials or conventional ceramic fabrication approaches, could be fabricated easily, quickly and effectively using 3D printing coupled with the origami technique.

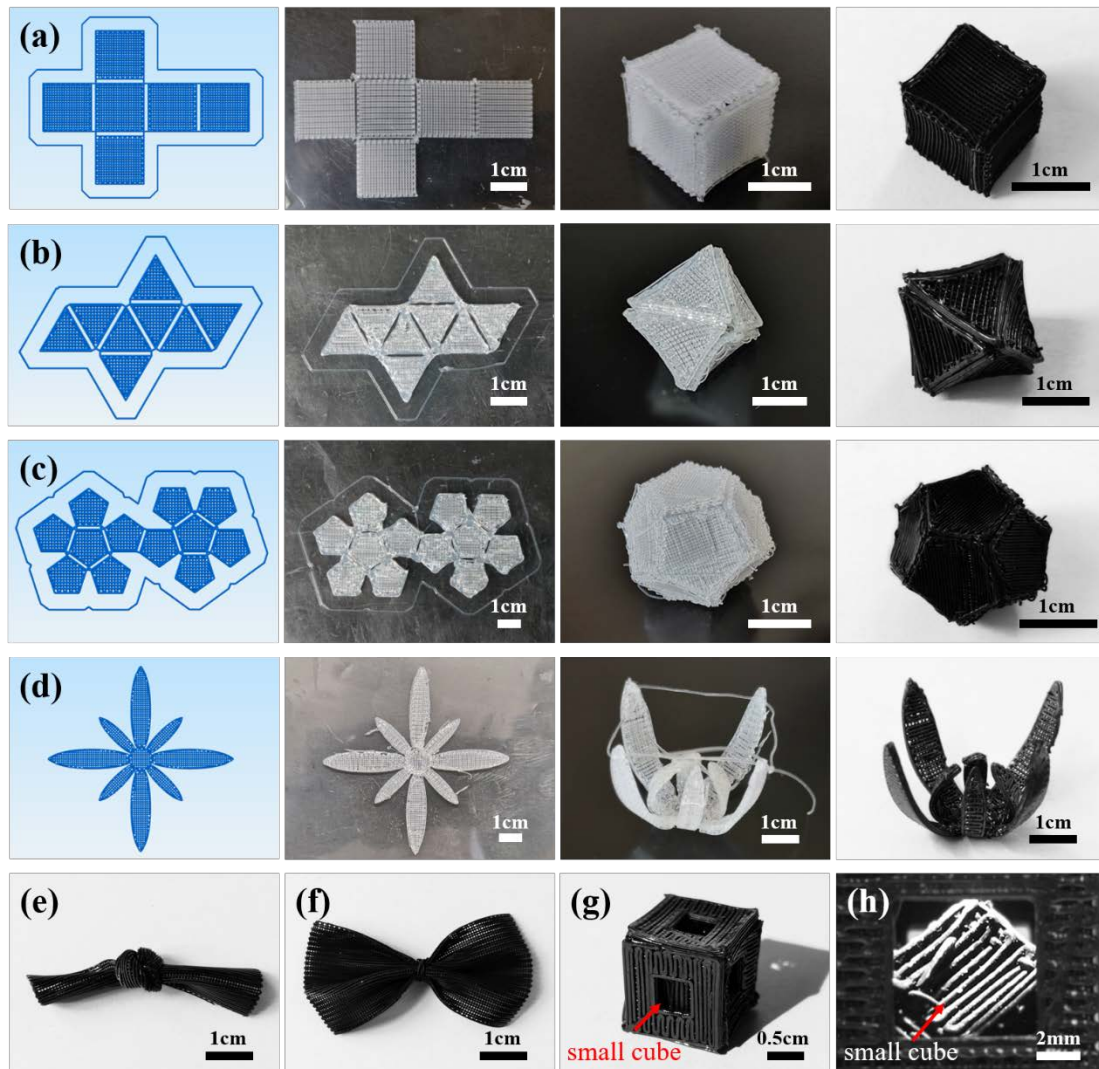


Fig. 2.8 Illustration of the whole process, from the designing of 2D patterns to folded 3D polyhedra and structures, before and after pyrolysis: (a) hexahedron; (b)

octahedron; (c) dodecahedron; (d) flower-like; (e) knot; (f) bow tie; (g) and (h) smaller cube inside a hollow cube. A silicone filament was used to bind the different parts, in all examples.

2.1.3.4 Self-adhesive Origami Folding

Besides origami assisted by filaments, we followed another strategy for obtaining ceramic components with complex architectures. Taking into account the fact that sheets that were not subjected to thermal cross-linking could adhere to each other by the simple manual application of a light pressure, we fabricated some parts using this approach. The subsequent cross-linking at 75°C for 30 min was sufficient to establish a strong bond between the juxtaposed parts, due to the presence of R-CH=CH₂ and H-Si-R available moieties in the material (see FTIR patterns in **Fig. 2.4c-e**). Indeed, when a circular band obtained by joining the two ends of a single sheet was cut, the two resulting segments could be similarly stretched, without debonding (**Fig. 2.9a**). Therefore, different structures were fabricated using this approach, demonstrating again good shape retention before and after pyrolysis (**Fig. 2.9b-e**). No defects could be observed in the highly twisted part of the “Möbius” band (**Fig. 2.10**). SEM images of the areas where the adhesion between the parts was realized, reported in **Fig. 2.9f,g**, show that the region is without defects and a continuous bond was achieved, providing integrity to the whole structure. In this way, the possibility of fabricating ceramics with complex architectures is further enhanced, using a simple and efficient secondary-shaping approach following the 3D printing of 2D sheets.

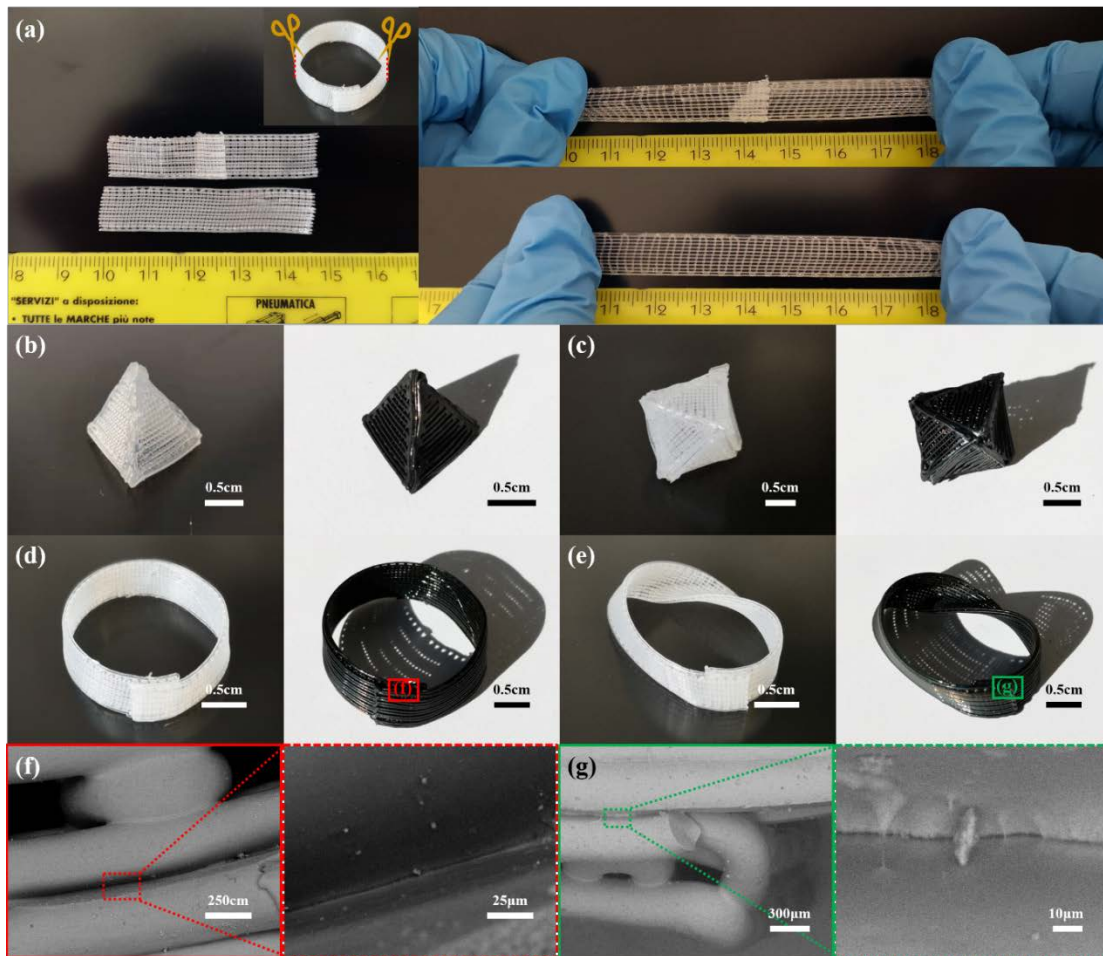


Fig. 2.9 (a) two parts cut from a band undergoing similar stretching (with no debonding); (b) tetrahedron; (c) octahedron; (d) circular band; (e) “Möbius” band, before and after pyrolysis. (g-h) SEM images of joined parts (after pyrolysis), demonstrating the good bonding.

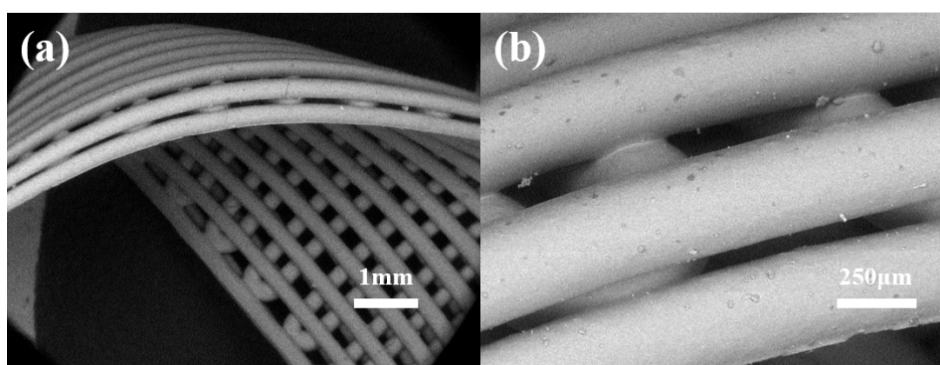


Fig. 2.10 SEM images of the highly twisted part on “Möbius” band. High retention of shape and no cracks could be observed.

2.1.4 Conclusions

In summary, we demonstrated a facile and effective approach for fabricating complex SiOC ceramic 3D architectures by additive manufacturing assisted by the origami technique or by the assembling of separate parts. The use of a highly stretchable silicone elastomer enabled folding at very high angles, without damaging the resulting structures either before or after pyrolysis. The parts could retain their shape after folding and during the pyrolysis process, either because they were kept in place using a filament made of the same silicone material, that could be removed (from samples of selected geometries) after pyrolysis, or exploiting the adhesion between sheets before cross-linking. The synergistic strategy of 3D printing and origami reported here further widens the possibility of fabricating ceramic components with complex structures, using a simplified approach that could be automated and integrated into continuous processes.

Furthermore, the introduction of suitable additives to the elastomeric preceramic polymer, in the form of particulate or chemical precursors, could enable the manufacture of components with additional functionalities (photo-catalytic, electromagnetic, biological, etc.).

2.1.5 References

- [1] Z. Song, T. Ma, R. Tang, Q. Cheng, X. Wang, D. Krishnaraju, R. Panat, C.K. Chan, H. Yu, H. Jiang, Origami lithium-ion batteries, *Nat Commun* 5 (2014) 3140.
- [2] S. Li, H. Fang, S. Sadeghi, P. Bhovad, K.W. Wang, Architected Origami Materials: How Folding Creates Sophisticated Mechanical Properties, *Adv Mater* 31(5) (2019) e1805282.
- [3] B. Liu, J.L. Silverberg, A.A. Evans, C.D. Santangelo, R.J. Lang, T.C. Hull, I. Cohen, Topological kinematics of origami metamaterials, *Nat Phys* 14(8) (2018) 811-+.
- [4] S. Janbaz, N. Noordzij, D.S. Widyaratih, C.W. Hagen, L.E. Fratila-Apachitei, A.A. Zadpoor, Origami lattices with free-form surface ornaments, *Sci Adv* 3(11) (2017).
- [5] S.C. Shan, S.H. Kang, P. Wang, C.Y. Qu, S. Shian, E.R. Chen, K. Bertoldi, Harnessing Multiple Folding Mechanisms in Soft Periodic Structures for Tunable Control of Elastic Waves, *Adv Funct Mater* 24(31) (2014) 4935-4942.
- [6] J.A. Faber, A.F. Arrieta, A.R. Studart, Bioinspired spring origami, *Science* 359(6382) (2018) 1386-+.
- [7] E.T. Filipov, T. Tachi, G.H. Paulino, Origami tubes assembled into stiff, yet reconfigurable structures and metamaterials, *P Natl Acad Sci USA* 112(40) (2015) 12321-12326.
- [8] Z.J. Wang, L.Q. Jing, K. Yao, Y.H. Yang, B. Zheng, C.M. Soukoulis, H.S. Chen, Y.M. Liu, Origami-Based Reconfigurable Metamaterials for Tunable Chirality, *Adv Mater* 29(27) (2017).
- [9] S. Daynes, R.S. Trask, P.M. Weaver, Bio-inspired structural bistability employing elastomeric origami for morphing applications, *Smart Mater Struct* 23(12) (2014).
- [10] G.V. Rodrigues, L.M. Fonseca, M.A. Savi, A. Paiva, Nonlinear dynamics of an adaptive origami-stent system, *Int J Mech Sci* 133 (2017) 303-318.
- [11] Q. Qiao, J.P. Yuan, Y. Shi, X. Ning, F. Wang, Structure, Design, and Modeling of an Origami-Inspired Pneumatic Solar Tracking System for the NPU-Phonesat, *J Mech Robot* 9(1) (2017).
- [12] S.A. Zirbel, R.J. Lang, M.W. Thomson, D.A. Sigel, P.E. Walkemeyer, B.P. Trease, S.P. Magleby, L.L. Howell, Accommodating Thickness in Origami-Based Deployable Arrays, *J Mech Design* 135(11) (2013).
- [13] K. Kuribayashi, K. Tsuchiya, Z. You, D. Tomus, M. Umemoto, T. Ito, M. Sasaki, Self-deployable origami stent grafts as a biomedical application of Ni-rich TiNi shape memory alloy foil, *Mat Sci Eng a-Struct* 419(1-2) (2006) 131-137.
- [14] R. Tang, H. Huang, H.E. Tu, H.S. Liang, M.B. Liang, Z.M. Song, Y. Xu, H.Q. Jiang, H.Y. Yu, Origami-enabled deformable silicon solar cells, *Appl Phys Lett* 104(8) (2014).
- [15] R.V. Martinez, C.R. Fish, X. Chen, G.M. Whitesides, Elastomeric Origami: Programmable Paper-Elastomer Composites as Pneumatic Actuators, *Adv Funct Mater* 22(7) (2012) 1376-1384.
- [16] D. Rus, M.T. Tolley, Design, fabrication and control of origami robots, *Nat Rev Mater* 3(6) (2018) 101-112.
- [17] S. Miyashita, S. Guitron, S.G. Li, D. Rus, Robotic metamorphosis by origami exoskeletons, *Sci Robot* 2(10) (2017).
- [18] C.L. Randall, E. Gultepe, D.H. Gracias, Self-folding devices and materials for biomedical applications, *Trends Biotechnol* 30(3) (2012) 138-146.
- [19] M. Jamal, S.S. Kadam, R. Xiao, F. Jivan, T.M. Onn, R. Fernandes, T.D. Nguyen, D.H. Gracias,

- Bio-Origami Hydrogel Scaffolds Composed of Photocrosslinked PEG Bilayers, *Adv Healthc Mater* 2(8) (2013) 1142-1150.
- [20] B. Sacca, R. Meyer, M. Erkelenz, K. Kiko, A. Arndt, H. Schroeder, K.S. Rabe, C.M. Niemeyer, Orthogonal Protein Decoration of DNA Origami, *Angew Chem Int Edit* 49(49) (2010) 9378-9383.
- [21] C.E. Castro, F. Kilchherr, D.N. Kim, E.L. Shiao, T. Wauer, P. Wortmann, M. Bathe, H. Dietz, A primer to scaffolded DNA origami, *Nat Methods* 8(3) (2011) 221-9.
- [22] S.M. Douglas, H. Dietz, T. Liedl, B. Hogberg, F. Graf, W.M. Shih, Self-assembly of DNA into nanoscale three-dimensional shapes, *Nature* 459(7245) (2009) 414-8.
- [23] R. Kosinski, A. Mukhortava, W. Pfeifer, A. Candelli, P. Rauch, B. Sacca, Sites of high local frustration in DNA origami, *Nat Commun* 10(1) (2019) 1061.
- [24] X. Mao, K. Li, M. Liu, X. Wang, T. Zhao, B. An, M. Cui, Y. Li, J. Pu, J. Li, L. Wang, T.K. Lu, C. Fan, C. Zhong, Directing curly polymerization with DNA origami nucleators, *Nat Commun* 10(1) (2019) 1395.
- [25] P.W. Rothemund, Folding DNA to create nanoscale shapes and patterns, *Nature* 440(7082) (2006) 297-302.
- [26] J.G. Hester, S. Kim, J. Bito, T.R. Le, J. Kimionis, D. Revier, C. Saintsing, W.J. Su, B. Tehrani, A. Traille, B.S. Cook, M.M. Tentzeris, Additively Manufactured Nanotechnology and Origami-Enabled Flexible Microwave Electronics, *P Ieee* 103(4) (2015) 583-606.
- [27] X.H. Zhou, T.Z. Li, J.H. Wang, F. Chen, D. Zhou, Q. Liu, B.J. Li, J.Y. Cheng, X.C. Zhou, B. Zheng, Mechanochemical Regulated Origami with Tough Hydrogels by Ion Transfer Printing, *Acs Applied Materials & Interfaces* 10(10) (2018) 9077-9084.
- [28] B.Y. Ahn, D. Shoji, C.J. Hansen, E. Hong, D.C. Dunand, J.A. Lewis, Printed Origami Structures, *Adv Mater* 22(20) (2010) 2251-+.
- [29] P. Colombo, G. Mera, R. Riedel, G.D. Soraru, Polymer-Derived Ceramics: 40 Years of Research and Innovation in Advanced Ceramics, *J Am Ceram Soc* 93(7) (2010) 1805-1837.
- [30] E. Ionescu, H.-J. Kleebe, R. Riedel, Silicon-containing polymer-derived ceramic nanocomposites (PDC-NCs): Preparative approaches and properties, *Chemical Society Reviews* 41(15) (2012) 5032-5052.
- [31] A. Zocca, C.M. Gomes, A. Staude, E. Bernardo, J. Günster, P. Colombo, SiOC ceramics with ordered porosity by 3D-printing of a preceramic polymer, *Journal of Materials Research* 28(17) (2013) 2243-2252.
- [32] E. Zanchetta, M. Cattaldo, G. Franchin, M. Schwentenwein, J. Homa, G. Brusatin, P. Colombo, Stereolithography of SiOC Ceramic Microcomponents, *Adv Mater* 28(2) (2016) 370-376.
- [33] P. Colombo, J. Schmidt, G. Franchin, A. Zocca, J. Günster, Additive manufacturing techniques for fabricating complex ceramic components from preceramic polymers, *Am. Ceram. Soc. Bull* 96(3) (2017) 16-23.
- [34] L. Brigo, J.E.M. Schmidt, A. Gandin, N. Michieli, P. Colombo, G. Brusatin, 3D Nanofabrication of SiOC Ceramic Structures, *Advanced Science* (2018) 1800937.
- [35] N. Travitzky, A. Bonet, B. Dermeik, T. Fey, I. Filbert-Demut, L. Schlier, T. Schlordt, P. Greil, Additive manufacturing of ceramic-based materials, *Adv Eng Mater* 16(6) (2014) 729-754.
- [36] G. Liu, Y. Zhao, G. Wu, J. Lu, Origami and 4D printing of elastomer-derived ceramic structures, *Sci Adv* 4(8) (2018).
- [37] D. Zhang, E. Peng, R. Borayek, J. Ding, Controllable Ceramic Green-Body Configuration for

- Complex Ceramic Architectures with Fine Features, *Adv Funct Mater* 29(12) (2019) 1807082.
- [38] S. Naficy, R. Jalili, S.H. Aboutalebi, R.A. Gorkin III, K. Konstantinov, P.C. Innis, G.M. Spinks, P. Poulin, G.G. Wallace, Graphene oxide dispersions: tuning rheology to enable fabrication, *Materials Horizons* 1(3) (2014) 326-331.
- [39] J.E. Smay, G.M. Gratson, R.F. Shepherd, J. Cesarano, J.A. Lewis, Directed colloidal assembly of 3D periodic structures, *Adv Mater* 14(18) (2002) 1279-1283.
- [40] J. Schmidt, P. Colombo, Digital light processing of ceramic components from polysiloxanes, *Journal of the European Ceramic Society* 38(1) (2018) 57-66.
- [41] R. Harshe, C. Balan, R. Riedel, Amorphous Si (Al) OC ceramic from polysiloxanes: bulk ceramic processing, crystallization behavior and applications, *Journal of the European Ceramic Society* 24(12) (2004) 3471-3482.
- [42] P. Taheri, A. Bokka, P. Asgari, J. Jeon, J.C. Lang, R. Campostrini, G.D. Sorarù, P. Kroll, Novel Sulfur-Containing Cross-Linking Agent for Si-Based Preceramic Polymers, *Macromolecular Chemistry and Physics* (2019) 1900380.
- [43] M. Biesuz, P. Bettotti, S. Signorini, M. Bortolotti, R. Campostrini, M. Bahri, O. Ersen, G. Speranza, A. Lale, S. Bernard, First synthesis of silicon nanocrystals in amorphous silicon nitride from a preceramic polymer, *Nanotechnology* 30(25) (2019) 255601.
- [44] C. Hwang, Q. Yang, S. Xiang, V. Domnich, A.U. Khan, K.Y. Xie, K.J. Hemker, R.A. Haber, Fabrication of dense B4C-preceramic polymer derived SiC composite, *Journal of the European Ceramic Society* 39(4) (2019) 718-725.
- [45] K.-W. Gyak, N.K. Vishwakarma, Y.-H. Hwang, J. Kim, H.-s. Yun, D.-P. Kim, 3D-printed monolithic SiCN ceramic microreactors from a photocurable preceramic resin for the high temperature ammonia cracking process, *Reaction Chemistry & Engineering* 4(8) (2019) 1393-1399.
- [46] J.M. Hundley, Z.C. Eckel, E. Schueller, K. Cante, S.M. Biesboer, B.D. Yahata, T.A. Schaedler, Geometric characterization of additively manufactured polymer derived ceramics, *Additive Manufacturing* 18 (2017) 95-102.
- [47] W. Zhao, G. Shao, M. Jiang, B. Zhao, H. Wang, D. Chen, H. Xu, X. Li, R. Zhang, L. An, Ultralight polymer-derived ceramic aerogels with wide bandwidth and effective electromagnetic absorption properties, *Journal of the European Ceramic Society* 37(13) (2017) 3973-3980.
- [48] L.M. Johnson, L. Gao, C.W. Shields IV, M. Smith, K. Efimenko, K. Cushing, J. Genzer, G.P. López, Elastomeric microparticles for acoustic mediated bioseparations, *Journal of nanobiotechnology* 11(1) (2013) 22.
- [49] B. Thong-On, B. Rutnakornpituk, U. Wichai, M. Rutnakornpituk, Magnetite nanoparticle coated with amphiphilic bilayer surfactant of polysiloxane and poly (poly (ethylene glycol) methacrylate), *Journal of Nanoparticle Research* 14(7) (2012) 953.
- [50] M. Rezakazemi, A. Vatani, T. Mohammadi, Synergistic interactions between POSS and fumed silica and their effect on the properties of crosslinked PDMS nanocomposite membranes, *RSC Advances* 5(100) (2015) 82460-82470.
- [51] N. Stafie, D. Stamatialis, M. Wessling, Effect of PDMS cross-linking degree on the permeation performance of PAN/PDMS composite nanofiltration membranes, *Separation and purification technology* 45(3) (2005) 220-231.
- [52] Y. Fu, G. Xu, Z. Chen, C. liu, D. Wang, C. Lao, Multiple metals doped polymer-derived SiOC

- ceramics for 3D printing, *Ceramics International* 44(10) (2018) 11030-11038.
- [53] M. Graczyk-Zajac, D. Vrankovic, P. Waleska, C. Hess, P.V. Sasikumar, S. Lauterbach, H.-J. Kleebe, G.D. Sorarù, The Li-storage capacity of SiOC glasses with and without mixed silicon oxycarbide bonds, *Journal of Materials Chemistry A* 6(1) (2018) 93-103.
- [54] M. Narisawa, K. Terauds, R. Raj, Y. Kawamoto, T. Matsui, A. Iwase, Oxidation process of white Si–O–C (–H) ceramics with various hydrogen contents, *Scripta Materialia* 69(8) (2013) 602-605.
- [55] L. David, R. Bhandavat, U. Barrera, G. Singh, Silicon oxycarbide glass-graphene composite paper electrode for long-cycle lithium-ion batteries, *Nat Commun* 7 (2016) 10998.
- [56] S. Gates, D. Neumayer, M. Sherwood, A. Grill, X. Wang, M. Sankarapandian, Preparation and structure of porous dielectrics by plasma enhanced chemical vapor deposition, *Journal of applied physics* 101(9) (2007) 094103.
- [57] A. Grill, D.A. Neumayer, Structure of low dielectric constant to extreme low dielectric constant SiCOH films: Fourier transform infrared spectroscopy characterization, *Journal of applied physics* 94(10) (2003) 6697-6707.
- [58] C.S. Yang, Y.H. Yu, K.-M. Lee, H.-J. Lee, C.K. Choi, Investigation of low dielectric carbon-doped silicon oxide films prepared by PECVD using methyltrimethoxysilane precursor, *Thin Solid Films* 506 (2006) 50-54.

2.2 SiOC scaffolds with tunable structure-performance relationship

2.2.1 Introduction

Additive Manufacturing (AM) enables the production of parts with complex 3D architectures not easily achievable with traditional manufacturing processes [1-5]. The demands for products with increasing higher structural complexity and resolution, have led to the development of a number of AM technologies, such as Direct Ink Writing (DIW) for colloidal inks [6,7], Fused Deposition Modelling (FDM) usually for polymer filaments [8,9], Digital Light Processing (DLP) for photo-sensitive resins (sometimes also containing ceramic particles) [10,11], Selective Laser Melting (SLM) for metals [12], and so on. In particular, DIW, also known as Robocasting, is the most common-used AM approach which was first developed in 1996 as a method for producing geometrically complex ceramic green bodies [13]. During the DIW process, inks are extruded under pressure from a nozzle moving along a continuous in-plane path to fabricate 3D structures layer by layer according to the designed STL file. This technology and the associated equipment have less requirements in comparison with competing fabrication approaches, which need for instance heating/melting (often in inert atmosphere) or ultraviolet light curing, and therefore can be employed with a wide range of different raw materials for different applications. They include, for instance, hydrogel/polyelectrolyte for photonic crystals [14,15], geopolymers for biodiesel production [16], ceramic powders and silk fibroin for tissue engineering [17,18], electrolytes for energy storage [19,20], etc.

DIW of preceramic polymers is a suitable approach for the fabrication of ceramic components with complex architectures, and therefore can be employed to explore the relationship between structure and selected properties of log-pile scaffolds, enabling the design of components with optimized performance as a function of the selected application. Several works have discussed the relationship between structure and mechanical properties of polymer components produced by FDM, in which the

influences of process parameters, such as building orientation, layer thickness and feed rate, etc., was discussed [8,21-24]. Few studies, however, have so far focused on the structure-performance relationship of ceramic components fabricated by DIW.

In our work, the effect of the architecture on the mechanical properties and gas permeability of SiOC ceramic manufactured by DIW was investigated, as a function of the filament size, the spacing between filaments and the angle of deflection between adjacent layers. For the purpose of comparison, the structures were designed with a similar value of their total porosity. SiOC was selected for this investigation because it can be obtained from easily sourced precursors (polysiloxanes), which are insensitive to air and moisture, inexpensive, and commercially available in a variety of physical and chemical structures [10,25]. In addition, the precursor used in this work possesses appropriate rheological properties with shear-thinning behavior and high storage modulus, ensuring successful printing by DIW [26]. Due to their excellent properties including high elastic modulus, chemical stability at high temperature, biocompatibility, and superior thermal and electrical conductivity in comparison to silicate ceramics, SiOC materials have been applied in many fields, such as waste water/gas filtration, noise absorption, bone tissue engineering, energy storage, etc. [27]. The results from this investigation on the structure-dependence relationship could be also applied to ceramic materials produced from other precursors or to other ceramic materials.

2.2.2 Experimental

The fabrication of 3D SiOC scaffolds using the same precursor has already been presented in a previous paper [26]. Briefly, a commercially available elastomeric silicone adhesive (SE 1700 Clear, Dow Corning Co., USA) was used as the preceramic polymer precursor. As shown in **Fig. 2.11a**, the homogenous ink was obtained by mixing the silicone with its curing agent (10:1 wt ratio) in a centrifugal mixer. Then the ink was transferred into a syringe followed by degassing. The 3D printing was performed at the room temperature using a delta printer (Delta Wasp 2040 Turbo, WASP,

Massa Lombarda, Italy). Scaffolds with a dimension of $13.6 \times 13.6 \times 4.6 \text{ mm}^3$ were fabricated by extruding the ink from 200 and 400 μm conical nozzles, layer by layer, under a pressure of 0.3-0.6 MPa and a X-Y motion speed of 5-10 mm/s. Different structures were designed (as shown in **Fig. 2.11b, c**) for investigating the influence of the scaffolds' architecture on their mechanical properties, varying parameters such as filament diameter, spacing between filaments and angle of deflection between layers. The shifted architecture corresponds to that of a 90° scaffold in which each layer is translated by a value corresponding to the filament size with respect to the previous one.

The printed scaffolds were kept in a dryer under 75°C for 30 mins to complete the cross-linking. The cross-linked scaffolds were put into a tube furnace under 99.99% N_2 for pyrolysis according to this schedule: from room temperature to 300°C (dwelling for 3h), then to 1000°C (dwelling for 2h) with a heating rate of $1^\circ\text{C}/\text{min}$.

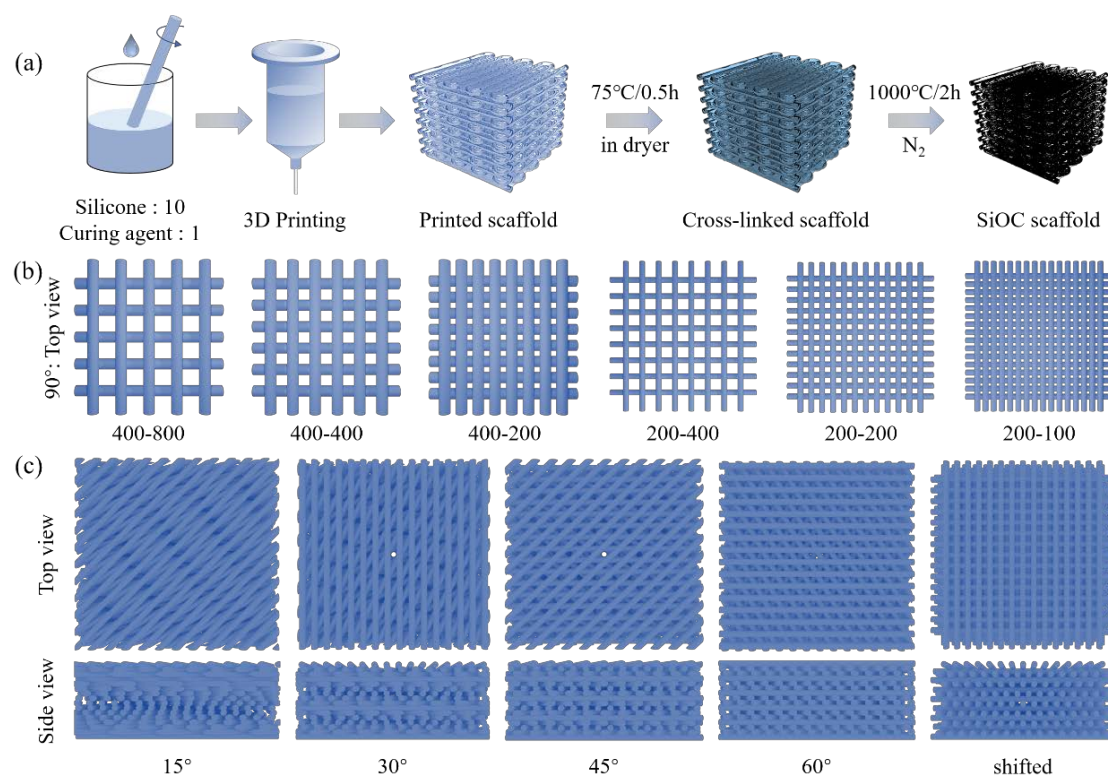


Fig. 2.11 (a) Flow diagram of the preparation of 3D SiOC scaffolds by direct ink writing; (b) Top views of regular scaffolds (90° angle of deflection) with different filament diameters (400 and 200 μm) and spacings; (c) Top and side views of

designed scaffolds with different angles of deflection between adjacent layers: 15°, 30°, 45°, 60° and shifted.

Morphology and microstructure were observed by SEM (FEI Quanta 200 ESEM, Eindhoven, The Netherlands) equipped with energy dispersive X-ray Spectroscopy. Mechanical tests were carried out using a universal testing machine (Instron 1121 UTM, Instron Danvers, MA, USA) with a displacement rate of 0.5 mm/min, on samples with a size of $10 \times 10 \times 3 \text{ mm}^3$.

The size of samples before and after sintering was measured with a digital caliper. The geometric density (ρ_g) was determined by calculating mass/volume ratios, and the apparent density (ρ_a) and true density (ρ_t) were measured on scaffolds and powder obtained from grinding the scaffolds using a helium pycnometer (Micromeritics AccuPyc 1330, Norcross, GA, USA). Open porosity (p_o) was determined by $p_o = \left(1 - \frac{\rho_g}{\rho_a}\right) * 100\%$; total porosity (p_t) was determined by $p_t = \left(1 - \frac{\rho_g}{\rho_t}\right) * 100\%$.

The gas permeability of scaffolds with different architectures was measured at room temperature on disc-shaped samples with a diameter of 14 mm and a thickness of 4 mm, using the equipment reported in previous literature [28]. The data were fitted according to Forchheimer's equation [29-31], expressed as:

$$\frac{P_i^2 - P_o^2}{2P_o L} = \frac{\mu}{k_1} v_s + \frac{\rho}{k_2} v_s^2 \quad \text{Eq. 1}$$

where P_i and P_o are the fluid pressure at the entrance and exit of the samples, v_s is the fluid velocity, L is the thickness of sample, μ the fluid viscosity, ρ the fluid density. k_1 and k_2 are the Darcian and non-Darcian permeability, respectively.

2.2.3 Results and discussion

2.2.3.1 Morphology and mechanical properties of 3D scaffolds with a 90° angle of deflection

Fig. 2.12 shows the morphology of scaffolds with a 90° angle of deflection

fabricated by varying the diameter and spacing of the filaments. Scaffolds extruded with a 400 μm nozzle were designed with spacings of 800, 400, 200 μm (images before and after pyrolysis are shown in **Fig. 2.12a-c**, respectively). The surface morphology of pyrolyzed scaffolds shows a well-defined log-pile structure with filaments possessing a regular and well controlled shape; the filament spacing appears narrower than the designed one because of the linear shrinkage occurring during pyrolysis (note: the uneven spacing between some filaments is due to an artifact deriving from hardware limitations of the specific printer used, and is particularly evident when the distance between adjacent filaments is narrower). Usually, the main problem occurring when using preceramic polymers is the formation of cracks upon heat treatment, due to the large gas release and shrinkage occurring during the polymer-to-ceramic conversion. In this case, no macroscopic cracks were observed in the pyrolyzed filaments, indicating that the shrinkage did not lead to significant stresses in the material.

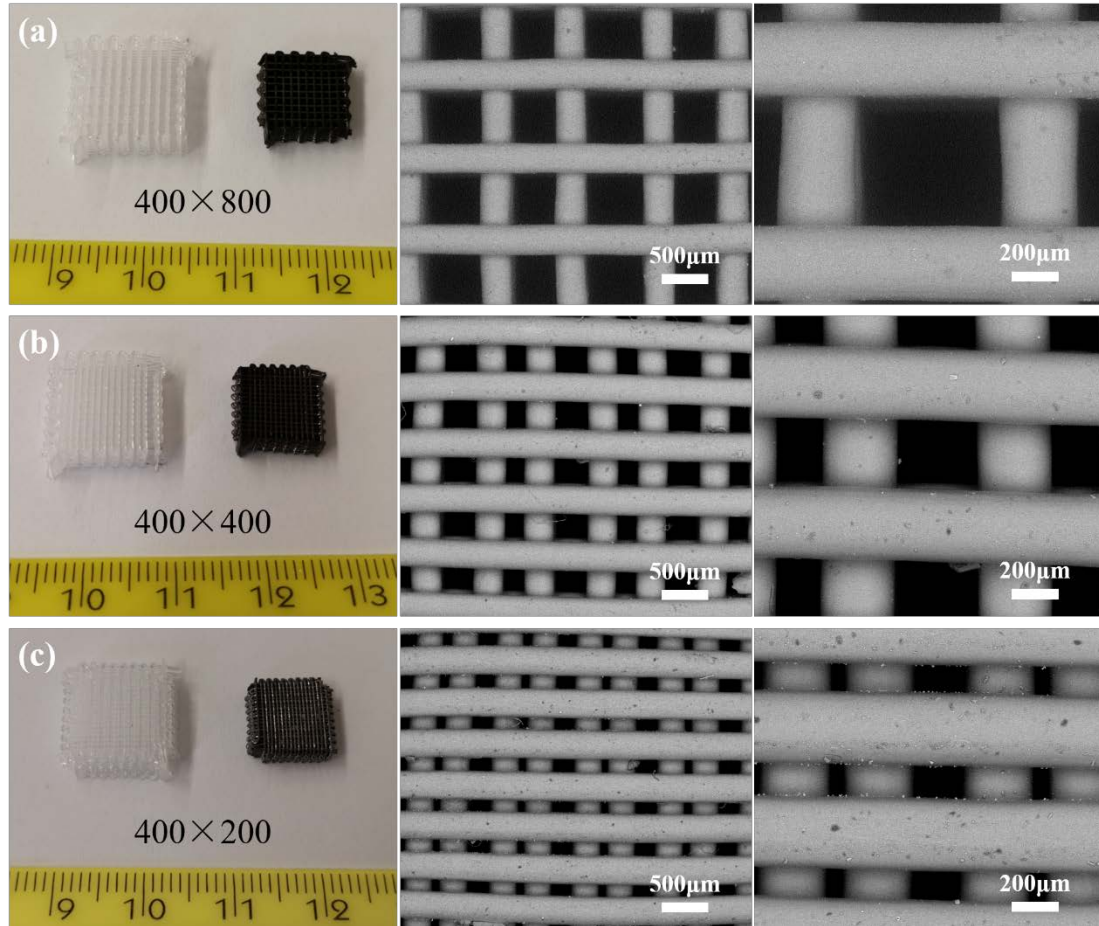


Fig. 2.12 Digital images and microstructures of scaffolds manufactured with different filament spacing: (a-c) 800 μm, 400 μm, 200 μm, respectively.

From the cross-sections in **Fig. 2.13a-c**, it is clear that nearly no deformation due to sagging can be detected both in the as printed and pyrolyzed state in the spanning portion of the filaments, which is 2 times larger than their diameter, demonstrating the good suitability of the rheological properties of the preceramic ink for the DIW process, and the homogeneous shrinkage occurring during pyrolysis. Nearly circular cross-sections (**Fig. 2.13d-f**) throughout the samples furthermore indicate a high degree of shape retention and ability to support the upper layers during printing, due to the fast recovery of the viscosity of the ink upon exiting from the nozzle [26]. A very good bonding between perpendicular filaments belonging to adjacent layers can be observed (inset in **Fig. 2.13d**), leading to the very good integrity of the whole structure,

promoting mechanical stability and performance [32,33]. High magnification (inset in **Fig. 2.13f**) shows that inside a filament no macro-pores or macro-cracks are visible, indicating that no significant defects are present after pyrolysis. Likewise, filaments without macro-cracks and macro-pores and a well-retained shape can be observed at the surface and in the cross-section of the scaffolds printed using a 200 μm nozzle (**Fig. 2.14**).

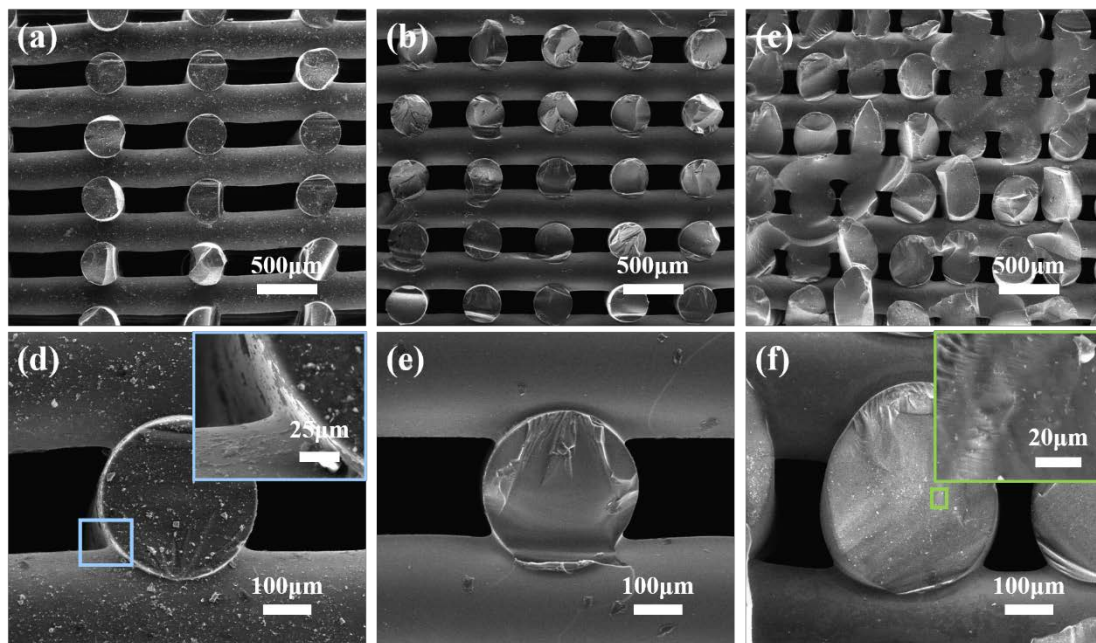


Fig. 2.13 Morphology of the cross-section of scaffolds manufactured with different filament spacing: (a), (d) 800 μm (The inset is bonding region between two perpendicular filaments from two adjacent layers); (b), (e) 400 μm ; (c), (f) 200 μm (The inset is high-magnification image of the center of a filament cross-section).

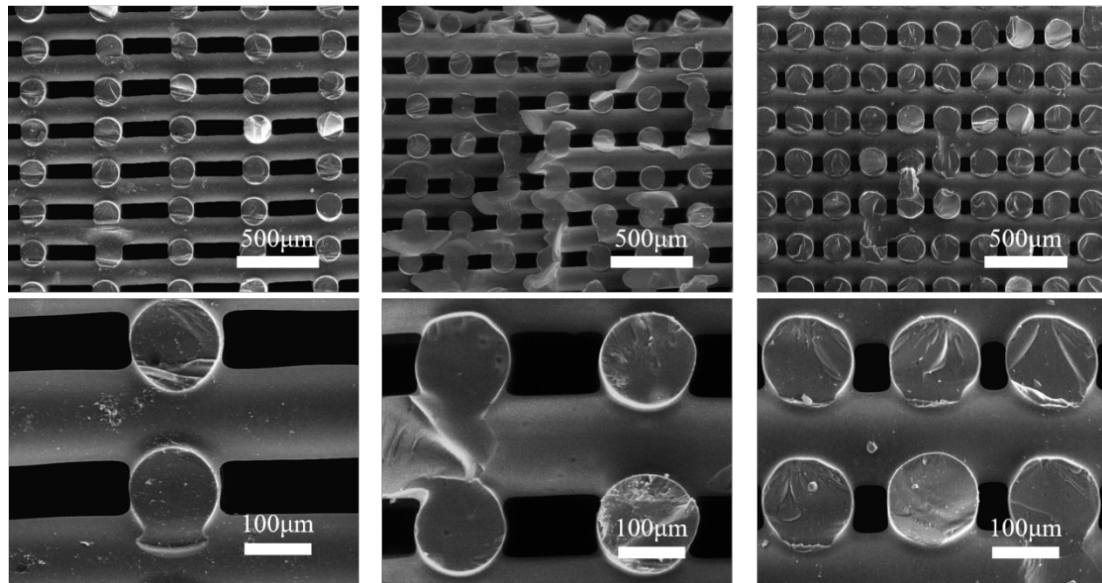


Fig. 2.14 Morphology of the cross-section of scaffolds with filaments with a diameter of 200 μm and different spacing ((a) 400 μm ; (b) 200 μm ; (c) 100 μm).

Tab. 2.3 reports the physical properties of the SiOC scaffolds. Measurements for samples before and after pyrolysis indicate that a homogenous shrinkage occurred in the x/y/z directions for both kind of scaffolds fabricated using 200 and 400 μm nozzles. The linear shrinkage of the filaments after pyrolysis was about 20%, giving a filament size after pyrolysis of ~ 163 and ~ 313 μm , respectively. Even though the volume shrinkage was as high as ~ 50 vol%, leading to a total porosity value in the range of 51-83 vol%, the scaffolds retained a very good structural integrity after pyrolysis, and were able to accommodate the large volume change without the creation of any visible defects such as macro-cracks or delamination among the filaments from different layers. Indeed, the porosity in the pyrolyzed struts was negligible, and the difference between the designed porosity and the open porosity could be simply due to the effect of the pyrolysis on the evolution of the samples' volume.

Tab. 2.3 Summary of some physical properties of the printed scaffolds after pyrolysis.

Diameter× Spacing	Shrinkage x (%)	Shrinkage y (%)	Shrinkage z (%)	Volume Shrinkage (%)	Apparent density (g·cm⁻³)	True density (g·cm⁻³)	Open porosity (vol %)	Total porosity (vol %)	Designed porosity (vol %)	$\sigma/[\sigma_{fb}]$ (MPa)
200×100	19.5 ± 0.9	19.8 ± 1.1	21.1 ± 0.6	49.0 ± 1.5	2.117 ±	2.130 ±	49.8 ± 1.1	50.1 ± 1.1	37.5	154.7 ± 0.3/[790.1]
200×200	19.1 ± 0.6	18.6 ± 0.8	20.1 ± 1.1	47.4 ± 0.9	0.005	0.003	65.4 ± 1.2	68.7 ± 1.1	52.2	64.5 ± 5.4/[574.4]
200×400	19.3 ± 0.8	18.7 ± 1.0	19.3 ± 2.6	47.1 ± 2.1			74.5 ± 0.4	74.6 ± 0.4	67.5	16.7 ± 2.6/[435.4]
400×200	22.4 ± 1.4	22.7 ± 1.2	21.9 ± 0.9	53.1 ± 1.1	2.115 ±	2.128 ±	52.5 ± 1.1	52.8 ± 1.1	37.4	56.7 ± 13.8/[309.2]
400×400	21.8 ± 1.2	21.9 ± 0.7	21.9 ± 0.6	52.3 ± 0.8	0.003	0.003	62.2 ± 0.1	62.4 ± 0.1	51.6	33.8 ± 4.1/[242.0]
400×800	22.6 ± 1.1	22.7 ± 0.6	17.2 ± 1.5	50.4 ± 1.5			74.0 ± 1.0	74.1 ± 1.0	66.1	5.6 ± 0.6/[142.0]

Representative stress-strain curves of scaffolds fabricated with different filament sizes and spacings are shown in **Fig. 2.15a**. The mechanical behavior is similar to that reported for other 3D scaffolds. Specifically, the stress-strain curves can be divided into three regions during compression (see **Fig. 2.15b**): (I) an initial linear region where filament joints bear the applied load, followed by (II) a yield plateau due to the sliding of filament layers and, finally, (III) a stiffer region where the scaffolds compact and the stress increases quickly until failure [34-36]. It should be noted that, differently from cellular structures such as foams [37-40], these log-pile scaffolds did not display any load bearing capability after reaching the maximum stress and were subjected to catastrophic failure.

Despite their substantial amount of total porosity, the SiOC scaffolds exhibited a very good compression strength, exceeding 150 MPa at 51.49 vol% porosity. This is related to the specific morphology of the 90° scaffolds with well aligned and regularly spaced load bearing elements, providing continuous vertical solid regions to support the applied stress (see also later). For both scaffolds with different filament diameters, the strength increased with the decreasing of filament spacing as well as porosity. This could be explained considering that a smaller spacing between filaments leads to a higher number of columns bearing the compressing stress within a given volume [21,41].

When comparing the results of two scaffolds with different filament size (200×200 vs 400×200, 200×400 vs 400×400), no significant relationship between strength and filament size could be observed, while the strength-porosity dependence was still evident, suggesting the dominant influence of porosity over filament size. The compression strength of highly porous materials over a large porosity range (> 0.7) can be described using a power law relationship, as proposed by Gibson and Ashby [42,43]:

$$\frac{\sigma}{\sigma_{fb}} \approx 0.3 (1 - p)^{3/2} \quad \text{Eq. 2}$$

where σ is the compression strength of the porous body, σ_{fb} is the filament bending

strength of a nonporous body of the same material, p is the total porosity of the sample. Considering the fact that the porosity of scaffolds in our work is in the range of 0.5-0.75, another equation was applied that is suitable for a porosity range of 0.2-0.7, with corrections made to above one as follows [42,43]:

$$\frac{\sigma}{\sigma_{fb}} \approx 0.23 (1 - p)^{3/2} (1 + (1 - p)^{1/2}) \quad \text{Eq. 3}$$

The filament bending strength σ_{fb} was calculated from the experimental data according to Eq. 2 and Eq. 3, and listed in **Tab. 2.3**. The calculated bending strength for 400 μm filament is in the range of 141-309 MPa, which is smaller than that of 200 μm filaments. The values are close to the results reported in previous literature concerning the bending strength of polymer-derived SiOC rods (which was of the order of $\sim 10^2$ MPa) [44-53]. **Fig. 2.15c** shows the compression stress and density of the 3D printed SiOC scaffolds produced in our work compared with that of porous SiOC samples obtained using other approaches, or ceramic/metal foams and carbon/graphene aerogels reported in the literature [10,54-71]. We can conclude that 3D printed SiOC scaffolds with this log-pile architecture (angle of deflection = 90°) possessed excellent strength and a high strength to density ratio, higher than most SiOC porous materials, including mesoporous and hierarchical SiOCs obtained by freeze casting, direct foaming and stereolithography. Furthermore, the value of strength in the range of $0.35\sim 1.01 \text{ g/cm}^3$ is comparable to that of other materials from the literature.

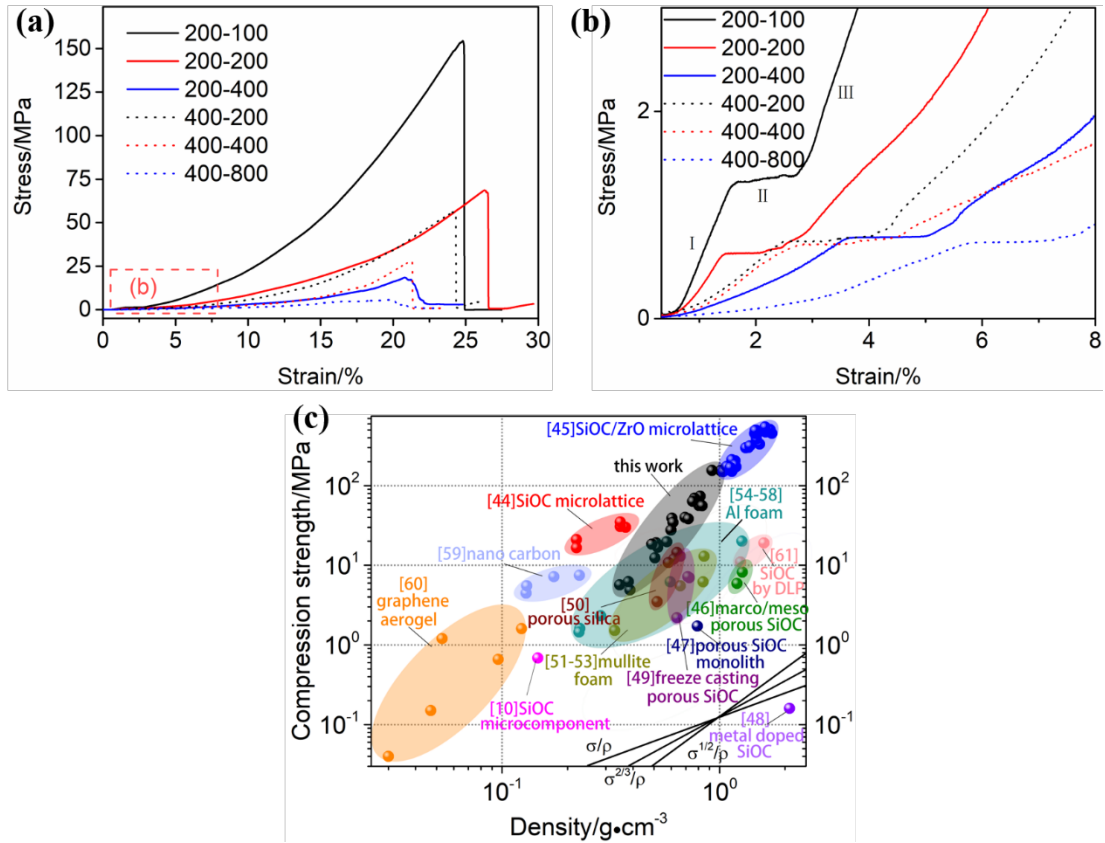


Fig. 2.15 (a) Representative stress-strain curves of scaffolds with different filament sizes and spacings; (b) enlarged part at 0-8% strain; (c) compression strength–density Ashby chart. Data in the chart were obtained either from literature (where specified) or from the CES Edupack 2019 (Granta Design) software database.

2.2.3.2 Comparison of scaffolds printed with different angles of deflection

To investigate the influence of the angle of deflection between adjacent layers on the mechanical properties, scaffolds with a filament size of 400 μm and a spacing of 400 μm (400 \times 400 μm) were printed. The measured physical properties for these scaffolds are reported in **Tab. 2.4**. The total porosity was virtually independent on the angle of deflection, in accordance with the design and considering that a fixed spacing between filament was maintained, and was around 65-67 vol%, with the only exception of the 90° sample which had a slightly smaller total porosity (~62 vol%).

Tab. 2.4 Summary of the physical properties of scaffolds with different angles of deflection between adjacent layers (filament size 400 μm , spacing 400 μm).

Deflection angle	Geometrical density ($\text{g}\cdot\text{cm}^{-3}$)	Open porosity (vol %)	Total porosity (vol %)	Compression strength (MPa)
15°	0.69 \pm 0.03	67.2 \pm 1.3	67.4 \pm 1.3	7.6 \pm 0.3
30°	0.73 \pm 0.05	65.3 \pm 2.2	65.5 \pm 2.2	11.5 \pm 0.7
45°	0.69 \pm 0.02	67.0 \pm 1.0	67.2 \pm 1.0	7.4 \pm 1.6
60°	0.74 \pm 0.04	65.1 \pm 1.8	65.3 \pm 1.8	23.5 \pm 0.6
90°	0.59 \pm 0.01	62.2 \pm 0.1	62.4 \pm 0.1	33.8 \pm 4.7
Shifted	0.72 \pm 0.06	66.1 \pm 2.8	66.3 \pm 2.8	27.4 \pm 6.0

The morphology of the samples after pyrolysis (see **Fig. 2.16**) demonstrates that the shape of the scaffolds was well retained with respect to the designed architecture (see **Fig. 2.11c**), again indicating the suitability of the ink material for printing these structures by DIW. The top view clearly visualizes the effect of implementing an angle of deflection on each subsequent layer on the architecture of the scaffold. The cross-sections of the samples from the side view show no sagging of the spanning parts, demonstrating that it was possible to retain the same high quality in the printed parts as that of the more regular scaffold (90°), and that the volumetric shrinkage occurring during pyrolysis did not lead to any macroscopic deformation.

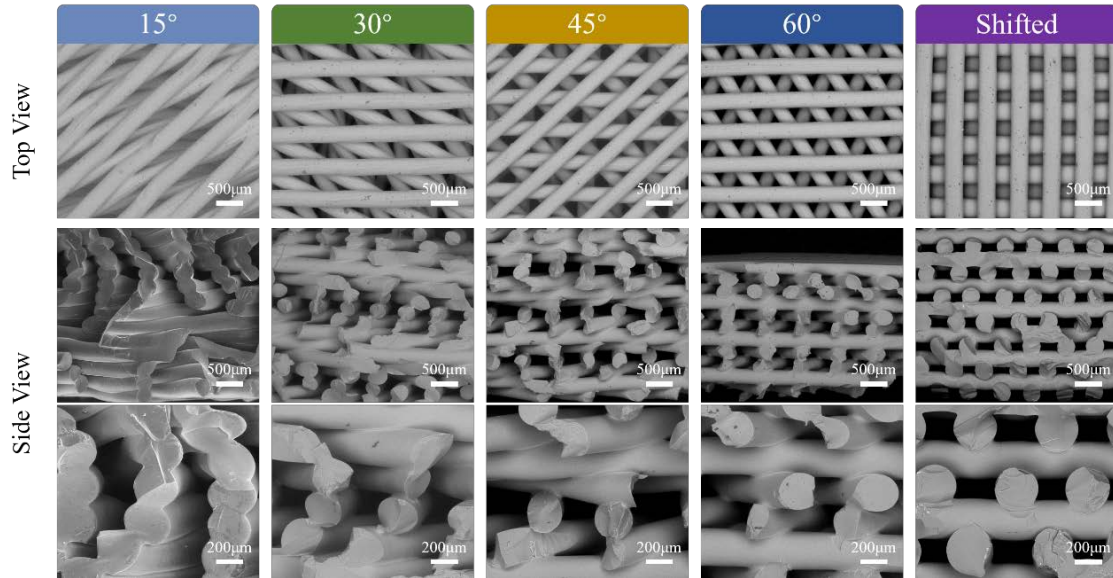


Fig. 2.16 Morphology (top view and side view) of SiOC scaffolds with different angles of deflection: 15°, 30°, 45°, 60° and shifted.

The compression strength (see **Fig. 2.17**) varies from 7.6 ± 0.3 to 33.8 ± 4.7 MPa when varying the angle of deflection from 15° to 90°, in dependence on the contact area between the filaments belonging to adjacent layers, which modified the stress profiles generated in the samples and the mechanism of failure (i.e. buckling vs bending). Strength increased with increasing angle of deflection, although the 45° sample did not follow the trend. The 90° sample had the highest strength, as expected in accordance with its architecture. In fact, according to previous literature [72,73], scaffolds with a smaller angle of deflection experience lower local stresses in the joint areas and the filaments tend to easily slide with respect to each other. Compared with the shifted structure in which the filaments never directly lay underneath one another, the regular scaffold (90°) possesses continuous solid columns in the vertical direction, forming pillars better resisting the applied compression pressure [74,75].

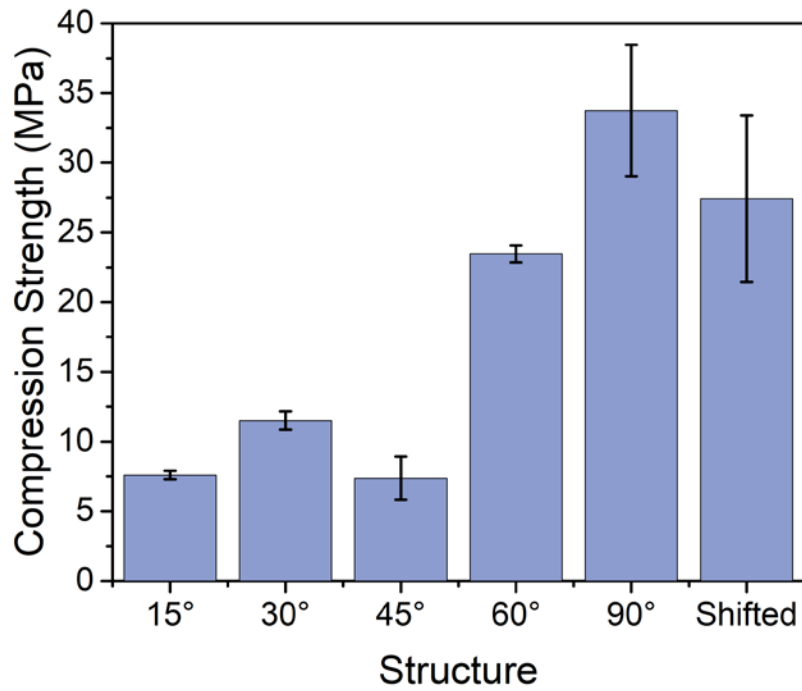


Fig. 2.17 Compression strength of scaffolds 3D printed with different angles of deflection and with a shifted architecture.

Besides affecting the size of the contact areas between filaments belonging to adjacent layers, varying the angle of deflection also modifies the pore geometry, generating more complex polygonal pores but without significantly changing the amount of total porosity of the scaffolds. Therefore, similarly to the mechanical strength, the permeability of the structures can also be tuned.

The gas permeability data and the corresponding fitting lines according to Forchheimer's equation are shown in **Fig. 2.18**. The value for k_1 and k_2 constants (see Eq. 1) are given in **Tab. 2.5**. The coefficients of determination R^2 for the fitting are over 0.99, indicating the influence of both viscous and inertial effects on the pressure drop.

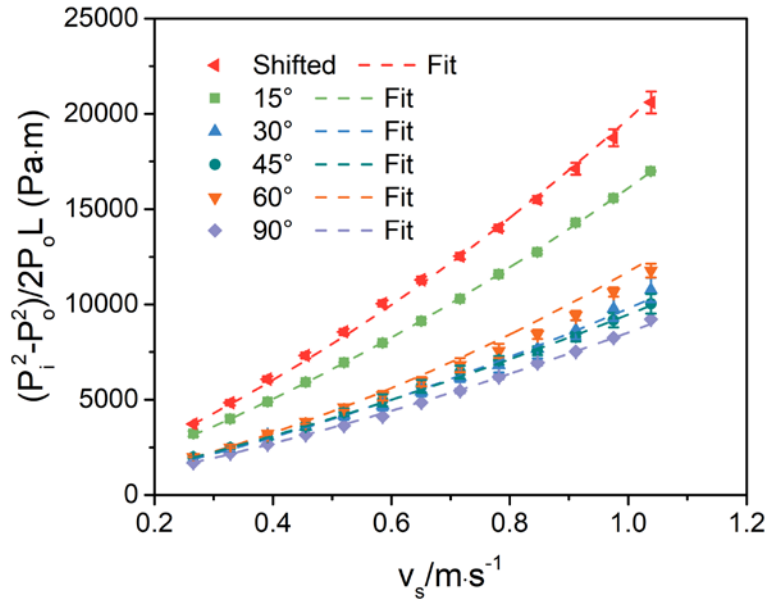


Fig. 2.18 Gas permeability of scaffolds printed with different angles of deflection and a shifted architecture; fitting lines are according to Forchheimer's equation.

Tab. 2.5 Summary of permeability coefficients according to Forchheimer's equation.

Permeability coefficients	15°	30°	45°	60°	90°	Shifted
$k_1(\text{m}^2) \times 10^{-9}$	1.78±0.03	3.26±0.09	2.66±0.10	3.05±0.12	3.42±0.04	1.41±0.01
$k_2(\text{m}) \times 10^{-4}$	2.07±0.09	2.79±0.29	4.60±0.26	2.44±0.06	3.68±0.04	1.87±0.11

We can conclude that the scaffold with a 90° angle of deflection shows the highest permeability due to its straight pore channel in the vertical direction, while the shifted scaffold has the lowest permeability because its structure contains highly tortuous internal channel offering a stronger resistance to the perpendicular gas flow, as indicated from the pressure drop curves as well as k_1 and k_2 values, which are the parameters related to the contraction or enlargement of the pore section and tortuosity along the flow path [76]. We can also observe that the samples printed with a 30, 45 and 60° deflection angle possessed a rather similar pressure drop curves, indicating that no significant trend exist between the permeability and the deflection angle in this range

of values, while scaffolds with a 15° deflection angle possessed a lower permeability, generally following the expectation that smaller deflection angles with more tortuous channels lead to low fluid permeability. The map in **Fig. 2.19**, proposed by Innocentini et al. [77-79], classifies a variety of porous media according to their permeability level (k_1 and k_2) and applications. It confirms that the high permeability of SiOC scaffolds in this work is comparable to that of highly porous open cell ceramic foams obtained by the replica technique, making them well suited for filtering and catalysis applications.

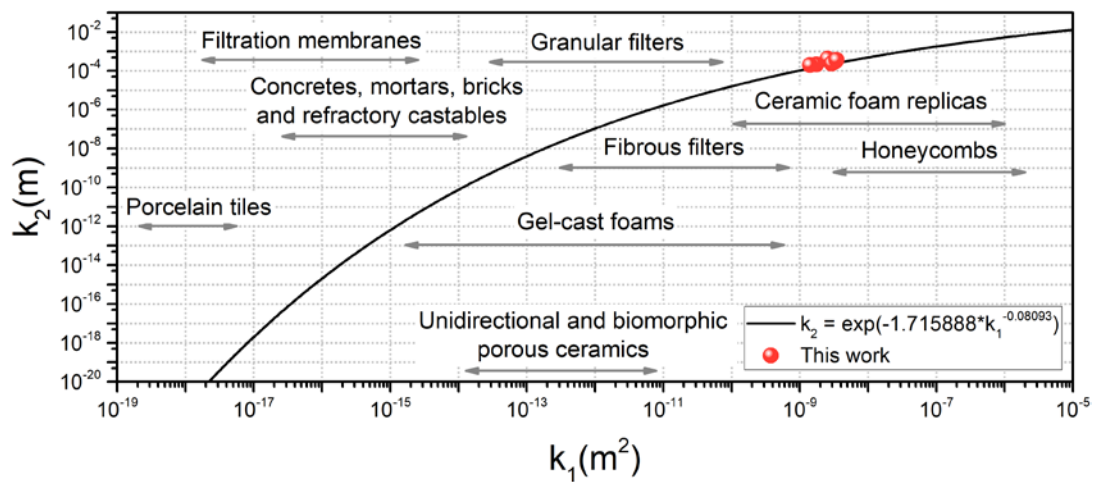


Fig. 2.19 Position of the permeability data for the SiOC scaffolds with different architectures produced in this work on a line fitting a large volume of experimental data for porous structures of different nature available in the literature (adapted from Innocentini et al. [77-79]).

We can therefore conclude that by modifying the architecture of the scaffolds it is possible to control both the mechanical strength and permeability to fluids, which are very important parameters for their application in fields such as filtration or catalysis. Of particular significance is the possibility of varying the gas permeability without affecting the total porosity of a sample, modifying the tortuosity of the flow paths and therefore the contact time between the fluid and the solid skeleton.

Moreover, since the investigated properties are structure-dependent, the findings

can be extended to other systems, such as scaffolds made from geopolymers, which show promise for the above applications, due to the intrinsic mesoporosity of their solid phase [80,81].

2.2.4 Conclusions

SiOC scaffolds were fabricated from a preceramic polymer by Direct Ink Writing, and the influence of their architecture on the compression strength and gas permeability was investigated. Decreasing the spacing between filaments led to a higher strength due to the decreasing of porosity, while the influence of filament size on mechanical properties was not significant and was outweighed by the effect of the amount of porosity. Changing the angle of deflection between adjacent layers affected both mechanical properties and gas permeability. The compression strength increased with the increasing of the angle of deflection from 15 to 90°, due to the variation of the contact area between filaments belonging to adjacent layers, while the permeability decreased though not with a constant trend, owing to a change in the pore architecture without modifying the total porosity. It is therefore possible to print scaffolds with an architecture which maximizes the desired properties for a specific application.

2.2.5 References

- [1] I. Gibson, D.W. Rosen, B. Stucker, *Additive manufacturing technologies*, Springer 2014.
- [2] S.C. Ligon, R. Liska, J.r. Stampfl, M. Gurr, R. Mülhaupt, *Polymers for 3D printing and customized additive manufacturing*, *Chemical reviews* 117(15) (2017) 10212-10290.
- [3] N. Guo, M.C. Leu, *Additive manufacturing: technology, applications and research needs*, *Frontiers of Mechanical Engineering* 8(3) (2013) 215-243.
- [4] A. Zocca, P. Colombo, C.M. Gomes, J. Günster, *Additive manufacturing of ceramics: issues, potentialities, and opportunities*, *J Am Ceram Soc* 98(7) (2015) 1983-2001.
- [5] J. Deckers, J. Vleugels, J.-P. Kruth, *Additive manufacturing of ceramics: a review*, *Journal of Ceramic Science and Technology* 5(4) (2014) 245-260.
- [6] J.A. Lewis, G.M. Gratson, *Direct writing in three dimensions*, *Materials Today* 7(7-8) (2004) 32-39.
- [7] J.A. Lewis, J.E. Smay, J. Stuecker, J. Cesarano, *Direct ink writing of three-dimensional ceramic structures*, *J Am Ceram Soc* 89(12) (2006) 3599-3609.
- [8] O.A. Mohamed, S.H. Masood, J.L. Bhowmik, *Optimization of fused deposition modeling process parameters: a review of current research and future prospects*, *Advances in Manufacturing* 3(1) (2015) 42-53.
- [9] H. Wu, W. Fahy, S. Kim, H. Kim, N. Zhao, L. Pilato, A. Kafi, S. Bateman, J. Koo, *Recent developments in polymers/polymer nanocomposites for additive manufacturing*, *Progress in Materials Science* 111 (2020) 100638.
- [10] E. Zanchetta, M. Cattaldo, G. Franchin, M. Schwentenwein, J. Homa, G. Brusatin, P. Colombo, *Stereolithography of SiOC Ceramic Microcomponents*, *Adv Mater* 28(2) (2016) 370-376.
- [11] J. Schmidt, P. Colombo, *Digital light processing of ceramic components from polysiloxanes*, *Journal of the European Ceramic Society* 38(1) (2018) 57-66.
- [12] C.Y. Yap, C.K. Chua, Z.L. Dong, Z.H. Liu, D.Q. Zhang, L.E. Loh, S.L. Sing, *Review of selective laser melting: Materials and applications*, *Applied physics reviews* 2(4) (2015) 041101.
- [13] J.N. Stuecker, J.E. Miller, R.E. Ferrizz, J.E. Mudd, J. Cesarano, *Advanced support structures for enhanced catalytic activity*, *Industrial & engineering chemistry research* 43(1) (2004) 51-55.
- [14] J. Chen, L. Xu, M. Yang, X. Chen, X. Chen, W. Hong, *Highly Stretchable Photonic Crystal Hydrogels for a Sensitive Mechanochromic Sensor and Direct Ink Writing*, *Chemistry of Materials* 31(21) (2019) 8918-8926.
- [15] G.M. Gratson, F. García-Santamaría, V. Lousse, M. Xu, S. Fan, J.A. Lewis, P.V. Braun, *Direct-write assembly of three-dimensional photonic crystals: conversion of polymer scaffolds to silicon hollow-woodpile structures*, *Adv Mater* 18(4) (2006) 461-465.
- [16] M.D. Innocentini, R.F. Botti, P.M. Bassi, C.F. Paschoalato, D.L. Flumignan, G. Franchin, P. Colombo, *Lattice-shaped geopolymer catalyst for biodiesel synthesis fabricated by additive manufacturing*, *Ceramics International* 45(1) (2019) 1443-1446.
- [17] Q. Fu, E. Saiz, A.P. Tomsia, *Direct ink writing of highly porous and strong glass scaffolds for load-bearing bone defects repair and regeneration*, *Acta biomaterialia* 7(10) (2011) 3547-3554.
- [18] S. Ghosh, S.T. Parker, X. Wang, D.L. Kaplan, J.A. Lewis, *Direct-write assembly of microperiodic*

- silk fibroin scaffolds for tissue engineering applications, *Adv Funct Mater* 18(13) (2008) 1883-1889.
- [19] T.S. Wei, B.Y. Ahn, J. Grotto, J.A. Lewis, 3D printing of customized li-ion batteries with thick electrodes, *Adv Mater* 30(16) (2018) 1703027.
- [20] Z. Lyu, G.J. Lim, R. Guo, Z. Kou, T. Wang, C. Guan, J. Ding, W. Chen, J. Wang, 3D-Printed MOF-Derived Hierarchically Porous Frameworks for Practical High-Energy Density Li–O₂ Batteries, *Adv Funct Mater* 29(1) (2019) 1806658.
- [21] M. Domingos, F. Intranuovo, T. Russo, R. De Santis, A. Gloria, L. Ambrosio, J. Ciurana, P. Bartolo, The first systematic analysis of 3D rapid prototyped poly(epsilon-caprolactone) scaffolds manufactured through BioCell printing: the effect of pore size and geometry on compressive mechanical behaviour and in vitro hMSC viability, *Biofabrication* 5(4) (2013) 045004.
- [22] H. Gonabadi, A. Yadav, S. Bull, The effect of processing parameters on the mechanical characteristics of PLA produced by a 3D FFF printer, *The International Journal of Advanced Manufacturing Technology* 111(3) (2020) 695-709.
- [23] W. Wu, P. Geng, G. Li, D. Zhao, H. Zhang, J. Zhao, Influence of layer thickness and raster angle on the mechanical properties of 3D-printed PEEK and a comparative mechanical study between PEEK and ABS, *Materials* 8(9) (2015) 5834-5846.
- [24] J.M. Chacón, M.A. Caminero, E. García-Plaza, P.J. Núñez, Additive manufacturing of PLA structures using fused deposition modelling: Effect of process parameters on mechanical properties and their optimal selection, *Materials & Design* 124 (2017) 143-157.
- [25] X. Liu, Y.L. Li, F. Hou, Fabrication of SiOC ceramic microparts and patterned structures from polysiloxanes via liquid cast and pyrolysis, *J Am Ceram Soc* 92(1) (2009) 49-53.
- [26] K. Huang, H. Elsayed, G. Franchin, P. Colombo, Complex SiOC ceramics from 2D structures by 3D printing and origami, *Additive Manufacturing* 33 (2020) 101144.
- [27] C. Stabler, E. Ionescu, M. Graczyk-Zajac, I. Gonzalo-Juan, R. Riedel, Silicon oxycarbide glasses and glass-ceramics: “All-Rounder” materials for advanced structural and functional applications, *J Am Ceram Soc* 101(11) (2018) 4817-4856.
- [28] S. Corradetti, M. Manzolaro, S.M. Carturan, M. Ballan, L. Centofante, G. Lilli, A. Monetti, L. Morselli, D. Scarpa, A. Donzella, A. Zenoni, A. Andrighetto, The SPES target production and characterization, *Nuclear Instruments and Methods in Physics Research Section B: Beam Interactions with Materials and Atoms* 488 (2021) 12-22.
- [29] M.D. Innocentini, A.R. Pardo, V.C. Pandolfelli, Modified pressure-decay technique for evaluating the permeability of highly dense refractories, *J Am Ceram Soc* 83(1) (2000) 220-22.
- [30] M.D. Innocentini, M.G. Silva, B.A. Menegazzo, V.C. Pandolfelli, Permeability of refractory castables at high temperatures, *J Am Ceram Soc* 84(3) (2001) 645-647.
- [31] M.D. Innocentini, A.R. Pardo, V.C. Pandolfelli, Influence of air compressibility on the permeability evaluation of refractory castables, *J Am Ceram Soc* 83(6) (2000) 1536-1538.
- [32] R. Landers, R. Mülhaupt, Desktop manufacturing of complex objects, prototypes and biomedical scaffolds by means of computer-assisted design combined with computer-guided 3D plotting of polymers and reactive oligomers, *Macromolecular Materials and Engineering* 282(1) (2000) 17-21.

- [33] J.M. Sobral, S.G. Caridade, R.A. Sousa, J.F. Mano, R.L. Reis, Three-dimensional plotted scaffolds with controlled pore size gradients: Effect of scaffold geometry on mechanical performance and cell seeding efficiency, *Acta Biomater* 7(3) (2011) 1009-18.
- [34] C. Zhang, L. Zhang, L. Liu, L. Lv, L. Gao, N. Liu, X. Wang, J. Ye, Mechanical behavior of a titanium alloy scaffold mimicking trabecular structure, *Journal of orthopaedic surgery and research* 15(1) (2020) 1-11.
- [35] D. Ronca, F. Langella, M. Chierchia, U. D'Amora, T. Russo, M. Domingos, A. Gloria, P. Bartolo, L. Ambrosio, Bone tissue engineering: 3D PCL-based nanocomposite scaffolds with tailored properties, *Procedia Cirp* 49 (2016) 51-54.
- [36] M.E. Hoque, W.Y. San, F. Wei, S. Li, M.-H. Huang, M. Vert, D.W. Hutmacher, Processing of polycaprolactone and polycaprolactone-based copolymers into 3D scaffolds, and their cellular responses, *Tissue Engineering Part A* 15(10) (2009) 3013-3024.
- [37] H. Peng, Z. Fan, J. Evans, Factors affecting the microstructure of a fine ceramic foam, *Ceramics international* 26(8) (2000) 887-895.
- [38] J. Qiao, Y. Wen, Preparation and characterization of magnesium aluminate ($MgAl_2O_4$) spinel ceramic foams via direct foam-gelcasting, *Ceramics International* 46(1) (2020) 678-684.
- [39] F. Li, Z. Kang, X. Huang, X.-G. Wang, G.-J. Zhang, Preparation of zirconium carbide foam by direct foaming method, *Journal of the European Ceramic Society* 34(15) (2014) 3513-3520.
- [40] M. Scheffler, P. Colombo, *Cellular ceramics: structure, manufacturing, properties and applications*, John Wiley & Sons 2006.
- [41] D. Hutmacher, M. Hoque, Y. Wong, Design, fabrication and physical characterization of scaffolds made from biodegradable synthetic polymers in combination with RP systems based on melt extrusion, *Virtual prototyping & bio manufacturing in medical applications*, Springer 2008, pp. 261-291.
- [42] L. Gibson, M. Ashby, *Cellular Solids: Structure and Properties*. Cambridge Univ Press, Cambridge, UK (1999).
- [43] I. Gibson, M.F. Ashby, The mechanics of three-dimensional cellular materials, *Proceedings of the royal society of London. A. Mathematical and physical sciences* 382(1782) (1982) 43-59.
- [44] P.V.W. Sasikumar, G. Blugan, N. Casati, E. Kakkava, G. Panusa, D. Psaltis, J. Kuebler, Polymer derived silicon oxycarbide ceramic monoliths: Microstructure development and associated materials properties, *Ceramics International* 44(17) (2018) 20961-20967.
- [45] G.M. Renlund, S. Prochazka, R.H. Doremus, Silicon oxycarbide glasses: Part II. Structure and properties, *Journal of Materials Research* 6(12) (2011) 2723-2734.
- [46] M. Esfahanian, R. Oberacker, T. Fett, M.J. Hoffmann, Development of dense filler-free polymer-derived SiOC ceramics by field-assisted sintering, *J Am Ceram Soc* 91(11) (2008) 3803-3805.
- [47] G.D. Sorarù, E. Dallapiccola, G. D'Andrea, Mechanical Characterization of Sol-Gel-Derived Silicon Oxycarbide Glasses, *J Am Ceram Soc* 79(8) (1996) 2074-2080.
- [48] J.-H. Eom, Y.-W. Kim, Effect of starting particle size and barium addition on flexural strength of polysiloxane-derived SiOC ceramics, *Journal of the Ceramic Society of Japan* 123(1435) (2015) 142-146.
- [49] M. Mazo, A. Nistal, A. Caballero, F. Rubio, J. Rubio, J. Oteo, Influence of processing conditions

- in TEOS/PDMS derived silicon oxycarbide materials. Part 1: Microstructure and properties, *Journal of the European Ceramic Society* 33(6) (2013) 1195-1205.
- [50] S. Walter, G. Soraru, H. Brequel, S. Enzo, Microstructural and mechanical characterization of sol gel-derived Si–O–C glasses, *Journal of the European Ceramic Society* 22(13) (2002) 2389-2400.
- [51] J.-H. Eom, Y.-W. Kim, Flexural strength of polysiloxane-derived strontium-doped SiOC ceramics, *Journal of the Korean Ceramic Society* 52(1) (2015) 61-65.
- [52] F. Berndt, P. Jahn, G. Motz, G. Ziegler, A. Rendtel, Monolithic SiOC ceramics with tailored porosity, *Key Engineering Materials* 206 (2002).
- [53] N.C. Fontão, M. Wilhelm, K. Rezwani, Asymmetric polysiloxane-based SiOC membranes produced via phase inversion tape casting process, *Materials & Design* 198 (2021) 109328.
- [54] Z.C. Eckel, C.Y. Zhou, J.H. Martin, A.J. Jacobsen, W.B. Carter, T.A. Schaedler, 3D PRINTING Additive manufacturing of polymer-derived ceramics, *Science* 351(6268) (2016) 58-62.
- [55] G. Liu, Y. Zhao, G. Wu, J. Lu, Origami and 4D printing of elastomer-derived ceramic structures, *Sci Adv* 4(8) (2018).
- [56] H. Zhang, C.L. Fidelis, M. Wilhelm, Z. Xie, K. Rezwani, Macro/mesoporous SiOC ceramics of anisotropic structure for cryogenic engineering, *Materials & Design* 134 (2017) 207-217.
- [57] C. Vakifahmetoglu, P. Colombo, A. Pauletti, C.F. Martin, F. Babonneau, SiOC ceramic monoliths with hierarchical porosity, *International Journal of Applied Ceramic Technology* 7(4) (2010) 528-535.
- [58] Y. Fu, G. Xu, Z. Chen, D. Wang, C. Lao, Multiple metals doped polymer-derived SiOC ceramics for 3D printing, *Ceramics International* 44(10) (2018) 11030-11038.
- [59] N. Arai, K.T. Faber, Hierarchical porous ceramics via two-stage freeze casting of preceramic polymers, *Scripta Materialia* 162 (2019) 72-76.
- [60] S. Rajpoot, R. Malik, Y.-W. Kim, Effects of polysiloxane on thermal conductivity and compressive strength of porous silica ceramics, *Ceramics International* (2019).
- [61] S. Ge, L. Lin, H. Zhang, Y. Bi, Y. Zheng, J. Li, X. Deng, S. Zhang, Synthesis of hierarchically porous mullite ceramics with improved thermal insulation via foam-gelcasting combined with pore former addition, *Advances in Applied Ceramics* 117(8) (2018) 493-499.
- [62] H. Qian, X. Cheng, H. Zhang, R. Zhang, Y. Wang, Preparation of porous mullite ceramics using fly ash cenosphere as a pore-forming agent by gelcasting process, *International Journal of Applied Ceramic Technology* 11(5) (2014) 858-863.
- [63] S. Ding, Y.P. Zeng, D. Jiang, Fabrication of mullite ceramics with ultrahigh porosity by gel freeze drying, *J Am Ceram Soc* 90(7) (2007) 2276-2279.
- [64] I. Jeon, T. Asahina, The effect of structural defects on the compressive behavior of closed-cell Al foam, *Acta materialia* 53(12) (2005) 3415-3423.
- [65] R. Kumar, H. Jain, S. Sriram, A. Chaudhary, A. Khare, V.A. Ch, D. Mondal, Lightweight open cell aluminum foam for superior mechanical and electromagnetic interference shielding properties, *Materials Chemistry and Physics* 240 (2020) 122274.
- [66] A. Moloodi, R. Raiszadeh, Fabricating Al foam from turning scraps, *Materials and Manufacturing Processes* 26(7) (2011) 890-896.
- [67] U. Ramamurty, A. Paul, Variability in mechanical properties of a metal foam, *Acta materialia* 52(4)

- (2004) 869-876.
- [68] L. Huang, H. Wang, D. Yang, F. Ye, Z. Lu, Effects of scandium additions on mechanical properties of cellular Al-based foams, *Intermetallics* 28 (2012) 71-76.
- [69] X. Zhang, A. Vyatskikh, H. Gao, J.R. Greer, X. Li, Lightweight, flaw-tolerant, and ultrastrong nanoarchitected carbon, *Proceedings of the National Academy of Sciences* 116(14) (2019) 6665-6672.
- [70] C. Zhu, T.Y.J. Han, E.B. Duoss, A.M. Golobic, J.D. Kuntz, C.M. Spadaccini, M.A. Worsley, Highly compressible 3D periodic graphene aerogel microlattices, *Nature Communications* 6 (2015) 6962.
- [71] Z. Li, Z. Chen, J. Liu, Y. Fu, C. Liu, P. Wang, M. Jiang, C. Lao, Additive manufacturing of lightweight and high-strength polymer-derived SiOC ceramics, *Virtual and Physical Prototyping* 15(2) (2020) 163-177.
- [72] D.W. Hutmacher, T. Schantz, I. Zein, K.W. Ng, S.H. Teoh, K.C. Tan, Mechanical properties and cell cultural response of polycaprolactone scaffolds designed and fabricated via fused deposition modeling, *Journal of Biomedical Materials Research: An Official Journal of The Society for Biomaterials, The Japanese Society for Biomaterials, and The Australian Society for Biomaterials and the Korean Society for Biomaterials* 55(2) (2001) 203-216.
- [73] L. Moroni, J. De Wijn, C. Van Blitterswijk, Three-dimensional fiber-deposited PEOT/PBT copolymer scaffolds for tissue engineering: Influence of porosity, molecular network mesh size, and swelling in aqueous media on dynamic mechanical properties, *Journal of Biomedical Materials Research Part A: An Official Journal of The Society for Biomaterials, The Japanese Society for Biomaterials, and The Australian Society for Biomaterials and the Korean Society for Biomaterials* 75(4) (2005) 957-965.
- [74] A. Gleadall, D. Visscher, J. Yang, D. Thomas, J. Segal, Review of additive manufactured tissue engineering scaffolds: relationship between geometry and performance, *Burns Trauma* 6 (2018) 19.
- [75] T.B. Woodfield, J. Malda, J. De Wijn, F. Peters, J. Riesle, C.A. van Blitterswijk, Design of porous scaffolds for cartilage tissue engineering using a three-dimensional fiber-deposition technique, *Biomaterials* 25(18) (2004) 4149-4161.
- [76] M.D.M. Innocentini, R.K. Faleiros, R. Pisani, I. Thijs, J. Luyten, S. Mullens, Permeability of porous gelcast scaffolds for bone tissue engineering, *Journal of Porous Materials* 17(5) (2009) 615-627.
- [77] M.D. Innocentini, P. Sepulveda, V.R. Salvini, V.C. Pandolfelli, J.R. Coury, Permeability and structure of cellular ceramics: a comparison between two preparation techniques, *J Am Ceram Soc* 81(12) (1998) 3349-3352.
- [78] M. Inocentini, A. Pardo, V. Pandolfelli, Permeability, *J Am Ceram Soc* 85(6) (2002) 1517-1521.
- [79] N.P. Stochero, E.G. de Moraes, A.C. Moreira, C.P. Fernandes, M.D.M. Innocentini, A.P. Novaes de Oliveira, Ceramic shell foams produced by direct foaming and gelcasting of proteins: Permeability and microstructural characterization by X-ray microtomography, *Journal of the European Ceramic Society* 40(12) (2020) 4224-4231.
- [80] R. Botti, M. Innocentini, T. Faleiros, M. Mello, D. Flumignan, L. Santos, G. Franchin, P. Colombo, Additively manufactured geopolymer structured heterogeneous catalysts for biodiesel production,

Applied Materials Today 23 (2021) 101022.

- [81] L.K. dos Santos, R.F. Botti, M.D. de Mello Innocentini, R.F.C. Marques, P. Colombo, A.V. de Paula, D.L. Flumignan, 3D printed geopolymer: An efficient support for immobilization of *Candida rugosa* lipase, *Chemical Engineering Journal* 414 (2021) 128843.

2.3 Cylindrical SiOC lattices by Direct Ink Writing with a robotic arm

2.3.1 Introduction

Among additive manufacturing technologies, Direct Ink Writing (DIW) is one of the most versatile techniques, since it allows printing many classes of materials such as polymers, ceramics, metals and composites. The technique consists in extruding an ink with suitable rheological properties onto a support. The rheology characteristics that an ink must possess for successful DIW printing are: shear thinning (pseudoplastic) behavior with a yield stress, fast recovery times and overall viscosity values compatible with the extrusion equipment and the need to generate structures that do not spontaneously deform under gravity. The pseudoplasticity allows for the ink to flow through the nozzle at low shear stresses, meaning low pressures ($P < 1$ MPa) and/or slow extruder rotation speeds and power (depending on the extrusion equipment used); fast recovery times allow for the printed ink to rapidly transition to a solid-like state before collapsing under its own weight (this is more critical for high density inks, such as metal-based ones) or due to the weight of successive layers.

Usually, a three-axis printer is used, with the printing head in motion whilst the flat support is fixed on the plane. Depending on the ink composition, the printed structure may require different post treatments, such as thermal curing and/or photocuring (elastomers, polymer matrix composites), de-binding and sintering (ceramics and metals). Recently, the use of self-curable polymer binders, such as modified epoxy resin, was explored in order to allow for fast recovery times and higher degree of freedom in shaping [1].

Among polymers, besides the production of biocompatible hydrogels [2], DIW was also used to print highly stretchable elastomers for wearable thermotherapy [3]. Various ceramic compositions have been printed so far, starting from highly loaded polymeric inks where the ceramic phase can be loaded as is or synthesized in-situ during pyrolysis

of silicon-based polymers [4], for applications as biomaterials (bone substitutes in non-load bearing applications), filters and catalyst supports. DIW was also tested for printing metallic powders (mainly Ti and Ti-based alloys and composites) in the shape of metallic scaffolds [5-8] or more complex structures and various compositions [9-11]. Metallic scaffolds of the above compositions were proposed as bone substitutes for load bearing applications.

Very recently, Fused Deposition Modeling printing units have been put on the market (i.e., Markforged Metal X), providing an alternative route for printing metals to the more popular Selective Laser Melting (SLM) or Electron Beam Melting (EBM) technologies.

However, some limitations are associated to the simplicity of the technology and low investment cost of the DIW printing unit, when printing ceramics and metals:

(1) The ink formulation must be strictly controlled in order to achieve the proper rheological properties. For this reason, not all materials can be printed, and a proper ink must be formulated for each material/composition.

(2) The binder burn-out may leave behind C, N, O residues that negatively affect the mechanical properties of the metallic structures.

(3) The binder burn-out is, for both metals and ceramics, a critical step that can result in cracking and uncomplete densification of the parts.

(4) Only three-axis printers have been developed so far for printing metal and ceramic-based DIW inks, thus limiting the range of possible printable geometries.

Furthermore, if metal oxides are used as precursors for metal structures [10], the final component undergoes high volumetric shrinkage (up to 80%).

DIW of elastomers using double curved inflatable surfaces [12,13] or cylindrical mandrels [14] was demonstrated for the production of biomedical devices and dielectric actuators, pneumatic artificial muscles and soft robotics.

In this work, we used elastomeric based inks [15], containing both ceramic and

metallic fillers (such as CaSiO_3 precursors and Ti6Al4V powders), and we extruded the produced inks onto a rotating and translating cylindrical support (mandrel), using a 5-axes robot. The mandrel could be easily removed, without any thermal or chemical process.

The proposed route shows how complex shapes (cylindrical reticulated structures) of different compositions (SiOC , CaSiO_3 and Ti6Al4V-based composites) can be produced by DIW, thus widening the range of printable geometries and applications. The movement of the substrate potentially allows for printing in a continuous process; moreover, various extruders could be simultaneously implemented in the same setup, in order to print multi-material components with curved surfaces.

In addition, the use of elastomeric based inks enables an easy removal of the printed structure from the support, and it allows for additional re-shaping of the printed structure before pyrolysis and/or sintering.

2.3.2 Materials and Methods

2.3.2.1 Starting materials and ink formulations

A two-component silicone elastomer (PDMS, DOWSIL™ SE 1700, Dow, USA), gas-atomized Ti-6Al-4V powders with size $\leq 10 \mu\text{m}$ (d_{50}) and purity $\sim 99.7\%$ (TLS Technik Spezialpulver, Bitterfeld, Germany), and calcium carbonate powders (CaCO_3 , $\sim 10 \mu\text{m}$, Industrie Bitossi, Vinci, Italy), as calcium oxide precursor for the generation of a CaSiO_3 bioceramic, were used as starting materials in different combinations.

Different inks were developed for printing 3D porous lattices based on SiOC , titanium alloy (TiV4Al6) and wollastonite (CaSiO_3), as follows:

(a) The silicone adhesive was used as the preceramic polymer precursor generating a SiOC amorphous ceramic after pyrolysis. The ink was prepared by mixing the silicone base (part A) with its proprietary curing agent (part B) at a 10:1 wt ratio, as suggested

by the manufacturer [15].

(b) For the material based on the titanium alloy (TiV4Al6), the titanium powder was mixed at a ratio of 80:20 wt% into the DOWSIL™ SE 1700 (two-component silicone; Part A and Part B), which was used as a main binder controlling the viscosity of the ink.

(c) Calcium carbonate powder was added as an active filler in the DOWSIL™ SE 1700 silicone, to produce wollastonite (CaSiO₃) ceramic lattices after the heat treatment [16].

All inks were mixed in a planetary mixer (ARE 250, Thinky, Japan) for 15 min (2000 rpm/min), in order to obtain homogenous pastes without aggregates ensuring a continuous extrusion during the Direct Ink Writing. The inks were then placed into syringes, followed by degassing in the planetary mixer before printing. Then, DIW of all inks was performed at room temperature through conical plastic nozzles (410 μm, Nordson, USA).

2.3.2.2 Experimental setup used for the printing process

In **Fig. 2.20**, a schematic overview of the printing setup implemented for this work is reported. An Adept Viper Articulated Robotic arm was used in order to move the mandrel both with a translational motion along the x axis and a rotational one about the same axis. The mandrel was a commercially available PVC tube with 38 mm outer diameter. The PVC tube was connected to the printing arm by means of a 3D printed customized plastic support. During the printing operations, the tube was covered by a silicone coated Teflon foil. The syringe was filled with the ink and the piston, and it was connected to the compressed air supply. The positioning of the syringe over the tube was adjusted manually.

The ink was extruded from the nozzle forming 3D patterns layer by layer with well-defined inter-layer spacing (80 % of the nozzle diameter), using a gas pressure of 0.3-

0.6 MPa. The cylindrical support was moved in the x direction with a speed of 10 mm/s and rotated with a speed of 9 rpm.

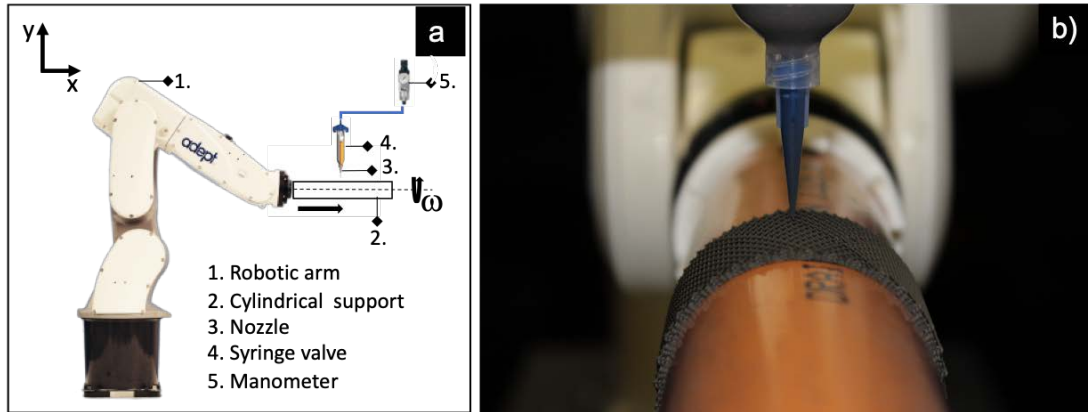


Fig. 2.20 Schematic representation of the setup used in this work. a) system setup; b) image of a sample during printing

In order to achieve the grid pattern shown in **Fig. 2.20a**, a proper robotic task was defined and written in the robotic language (Adept V+) suitable for the manipulator employed.

The grid pattern was designed with the purpose of printing empty cylinders with meshed walls with a total height of 60 mm, an internal diameter of 38 mm and a thickness corresponding to 6 layers; each layer was composed of parallel struts with $d \sim 410 \mu\text{m}$ crossing the previous one at 45° . Each ink filament of the grid was obtained by imposing a rotation of 45° to the mandrel for each translational movement of 60 mm. Then, a rotation of 5° without translation was used to separate the next filament from the already printed one. At this point, the two movements were repeated until the robot generated a full cylindric structure by performing a 360° rotation. Then, the robot lowered the mandrel with a movement of 0.32 mm ($\sim 0.8d$) in the negative y axis direction. The next layer was obtained by repeating the same translation movement, imposing a rotation to the mandrel in the opposite direction with respect to the previous one.

It is important to observe that the accuracy of the robot within the work-area used in this experiment (~1 mm) does not allow to achieve the proposed task with the needed precision. For this reason, a proper calibration step was introduced. Moreover, the trajectory planner was set to move the robot with a constant speed and with proper connection arcs between the paths. This approach enabled the syringe to deposit the ink filament on the PVC tube with the required precision.

2.3.2.3 Heating and characterization of the printed parts

After the printing process, the lattices were left on the PVC tube and kept at 75°C for 60 min to solidify through cross-linking of the DOWSIL™ SE 1700 silicone. To produce SiOC lattices, the samples were pyrolyzed at 1000°C for 2h with a heating rate of 1°C/min and an intermediate dwelling step at 300°C, with a hold time of 3h. The heat-treatment was carried out in a tube furnace under inert atmosphere (99.99 % N₂), and the preceramic cylinders were placed vertically in the ceramic tube without any additional support. The titanium-based lattices were sintered under high vacuum (10⁻⁵ mbar), using a heating rate of 0.5 up to 500°C with 3h holding time, and then heating to 1450°C, for 2h, under Ar with a heating rate of 2°C/min. The Ti6Al4V elastomeric lattice was kept on a graphite rod in order to enable shape retention when positioning it horizontally during pyrolysis. This configuration was necessary due to the small size of the tube diameter and crucible, that didn't allow for vertical positioning. The wollastonite lattices were ceramized both in static air and N₂ flow using a heating rate of 0.5°C up to 1000°C and a dwelling time of 2h at the maximum temperature. Again, the preceramic cylinders were placed vertically in the ceramic tube without any support. The printed parts before and after pyrolysis were visually analysed by field emission gun-scanning electron microscopy (FEG-SEM; Quanta 250 Fei, Eindhoven, The Netherlands) using 20 kV voltage, 5 µm spot size and 10 mm working distance. Ceramic and metallic raw powders, as well as fabricated specimens after the thermal

treatments, were analysed by X-ray diffractometry (XRD, Bruker D8 Advance, Milano, Italy) using Cu-K α radiation at 40 mV and 40 mA, with a resolution of 0.05° for 2 s. The shrinkage before and after the thermal treatments was measured by Image Analysis software (Image J) on 2D scanned surfaces. At least 5 measurements both for cell size (area) and strut size (diameter) for each composition were performed. The weight loss of the printed parts during the heat treatments was also measured.

Results and Discussion

In **Fig. 2.21**, the three lattices (SiOC, Ti6Al4V-based composite and CaSiO₃, respectively) are shown after printing and crosslinking (**Fig. 2.21a-c**) and after pyrolysis (**Fig. 2.21d-f**). After printing and crosslinking very well-defined structures were obtained, showing defect-free geometries. During pyrolysis, some distortions occurred, in particular for the SiOC (**Fig. 2.21d**) and the Ti6Al4V composite (**Fig. 2.21e**) samples. In the case of the SiOC sample, the distortion from the original shape may be derived from the positioning of the sample inside the oven, being the printed lattice highly stretchable even after crosslinking, due to the absence of fillers. In the case of the Ti6Al4V composite sample, the use of the graphite rod during pyrolysis induced stresses in the lattice structure, inhibiting its shrinkage and leading the structure to partial failure. The presence of the reactive CaCO₃ fillers in the ink reduced the criticalities upon pyrolysis for the CaSiO₃ sample (at least at the macroscopic level), which are mainly due to the volume variation occurring during heating.

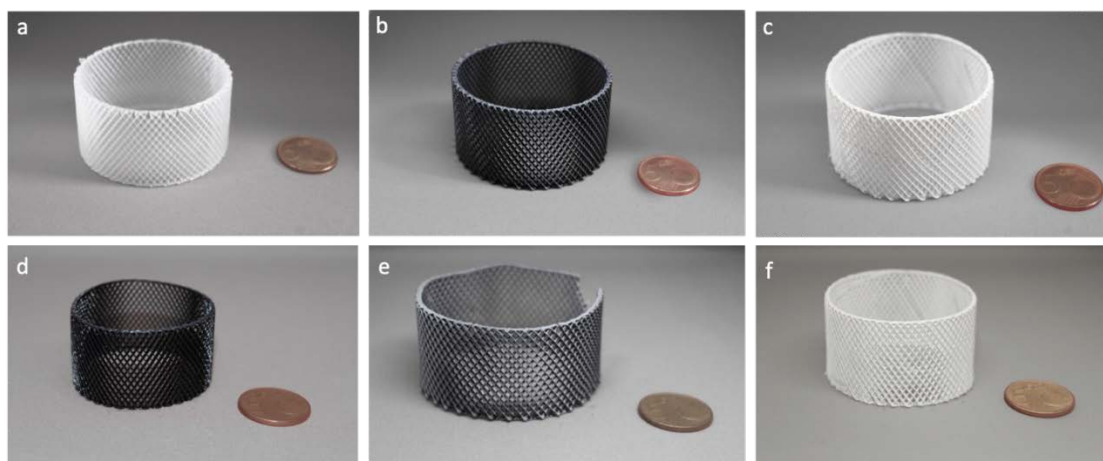


Fig. 2.21 As printed and cross-linked lattice structures (a) PDMS, b) PDMS plus Ti6Al4V, c) PDMS plus CaCO₃; the same structures after pyrolysis (d) SiOC, e) Ti6Al4V composite, f) CaSiO₃, sintered in air).

Fig. 2.22 shows SEM images of the PDMS sample after printing and crosslinking (**Fig. 2.22a, c**) and pyrolysis (**Fig. 2.22b, d**). The as printed structure showed an optimal shape retention that was confirmed at the microscopic level after pyrolysis, when a crack-free structure and smooth surface were obtained. A good adhesion between different filaments can be observed, both before and after pyrolysis.

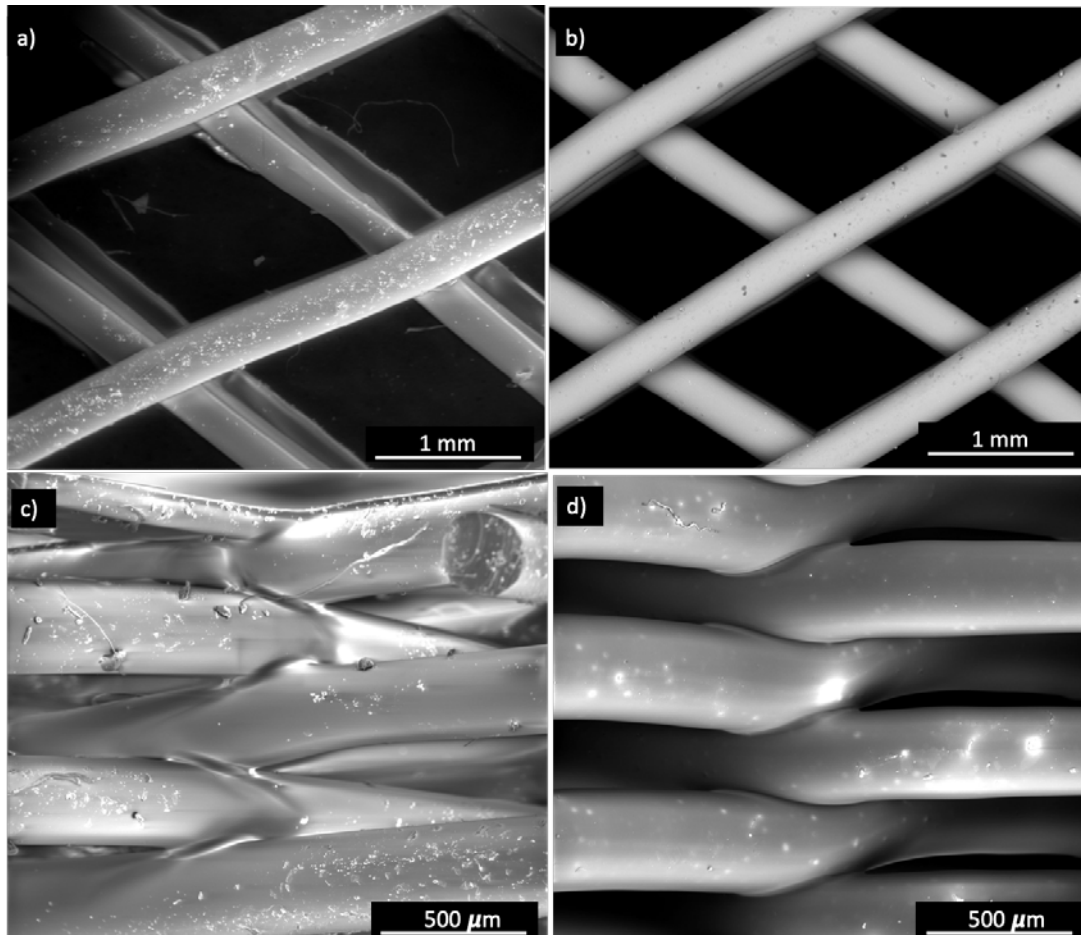


Fig. 2.22 SEM images of the printed PDMS lattices after crosslinking (a,c) and pyrolysis (b,d).

In **Fig. 2.23**, the PDMS-Ti6Al4V sample after printing and crosslinking is shown (a,c). In this case, the struts show a slight collapse on the adjacent layer (**Fig. 2.23c**), probably due to the high density of the metallic powders in the ink. However, after pyrolysis these defects appear to have been compensated by the thermally induced stresses and associated volume shrinkage (**Fig. 2.23b, d**). In the final structure, the presence of the Ti6Al4V sintered powders is clearly visible, generating a rough surface. No cracks were visible in the Ti6Al4V composite samples.

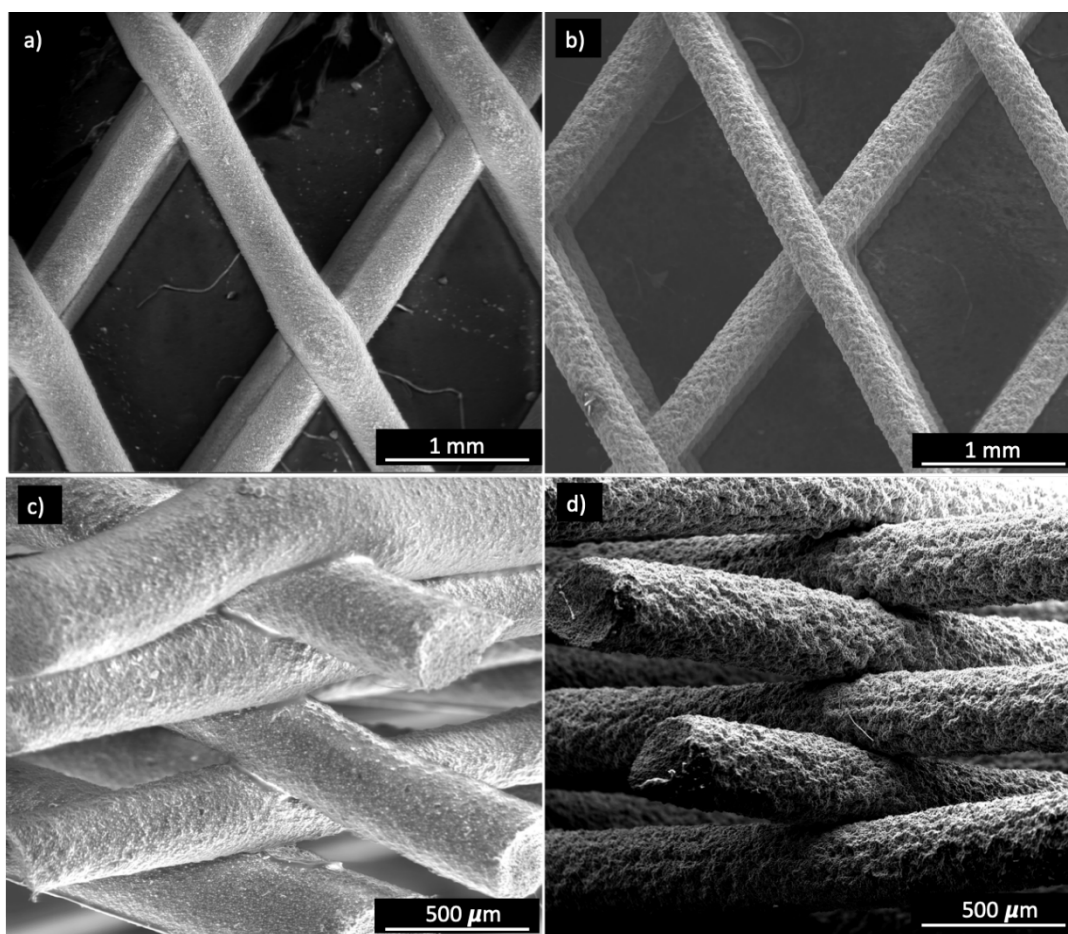


Fig. 2.23 SEM images of PDMS plus Ti6Al4V lattices after crosslinking (a,c) and of the Ti6Al4V composite lattices after pyrolysis (b,d).

The PDMS-CaSiO₃ lattice is shown after printing and crosslinking (**Fig. 2.24a, d**) and after heating in air (**Fig. 2.24b, e**) and nitrogen (**Fig. 2.24c, f**). After firing, some cracks were visible on the struts' surface of the CaSiO₃ lattice heated in air, whilst a completely crack-free structure was obtained upon pyrolysis under nitrogen flow. This can be attributed to a reduced shrinkage when pyrolyzing under nitrogen, as reported in Table 1 (8.7% vs 15.7% in air). Firing PDMS in air causes the oxidation of all carbon atoms present in the polymeric chain through an exothermic reaction that can lead to the formation of local cracks, generating highly reactive SiO₂ that can then form CaSiO₃ together with the CaO deriving from the thermal decomposition of the CaCO₃ powders.[16] When using nitrogen as the pyrolysis atmosphere, carbon atoms are

retained in the structure either bonded to Si or as a separate phase, generating a SiOC material with reduced local thermal stresses [16,17].

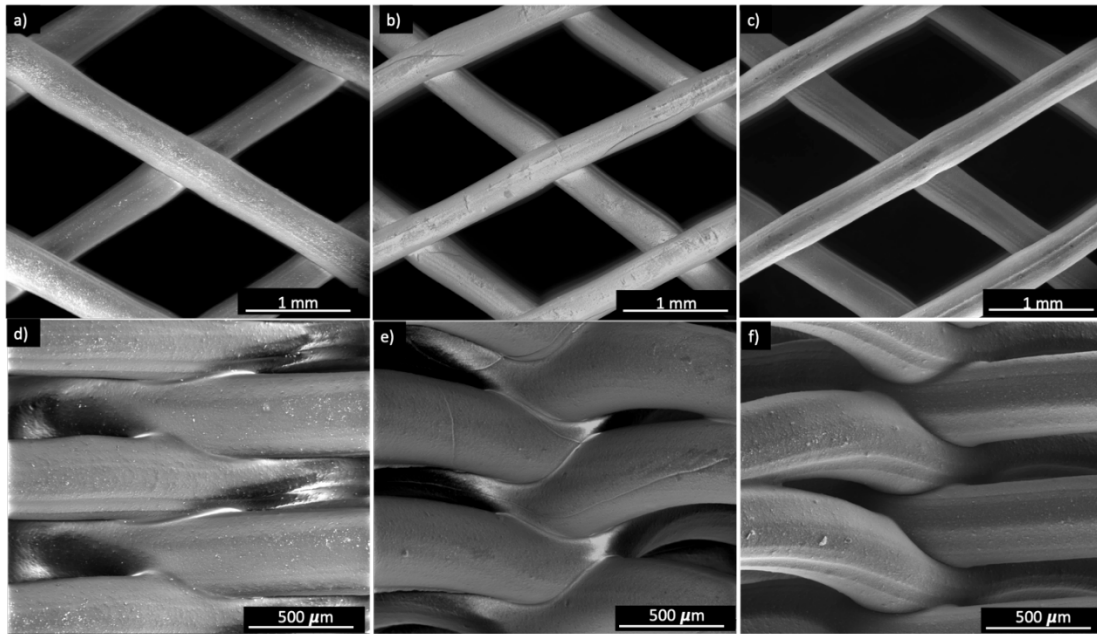


Fig. 2.24 SEM images of PDMS plus CaCO_3 lattices after crosslinking (a,c) and of CaSiO_3 lattices after firing in air (b, d) or pyrolysis in N_2 (e, f).

This is confirmed by the data reported in Table 1. The struts' diameter shrinkage, as well as the cells' area shrinkage, show different trends: the pure PDMS ink showed a high shrinkage both for struts and cells' area (30.5% and 37.1 %, respectively), as expected. The inks containing filler powders showed a limited struts' and cells' area shrinkage (ranging from 8.7% to 15.7% and from -3.6% to 22.7%, respectively). In the case of the PDMS plus CaCO_3 ink, a higher strut shrinkage was measured for samples heat treated in air, as discussed above. In the case of the PDMS plus Ti6Al4V ink, the high struts' shrinkage and the negative shrinkage (expansion) can be attributed to the stress induced by the use of the graphite rod upon pyrolysis. The measured weight loss (**Tab. 2.6**) for pure PDMS samples upon pyrolysis is compatible with the organic moieties' elimination and the full conversion of PDMS to a SiOC ceramic. For PDMS plus Ti6Al4V the reduced weight loss during thermal treatment is due to the reaction of

Si and C atoms with Ti and V as discussed in the following. The higher weight loss for PDMS plus CaCO₃ is compatible with CaCO₃ thermal decomposition (with CO₂ emission) that starts occurring at T > 550°C and depends on heating rate and CO₂ concentration in the atmosphere [18].

Tab. 2.6 Measured linear shrinkage and weight loss of the printed lattice structures after pyrolysis in N₂ or vacuum-Ar, or firing in air.

Sample	$\Delta d\%$ (strut diameter)	$\Delta A\%$ (cell area)	$\Delta wt\%$
PDMS (N ₂)	30.5 ± 0.1	37.1 ± 1.0	27.5
PDMS+Ti6Al4V (vacuum-Ar)	19.7 ± 2.0	-3.6 ± 0.1	9.5
PDMS+CaCO ₃ (Air)	15.7 ± 0.4	21.9 ± 0.1	39.0
PDMS+CaCO ₃ (N ₂)	8.7 ± 0.5	22.7 ± 0.1	36.0

SEM investigations on the cross-section of the struts of the lattice structures, not reported here for the sake of brevity, showed that dense microstructures were achieved in all cases, indicating that the mixing and degassing procedure for the production of the inks did not introduce unwanted porosity.

The crystalline phase assemblage of the printed lattice structures after the heat treatment was investigated (**Fig. 2.25**). The XRD pattern for the pyrolyzed SiOC is shown in **Fig. 2.25a**, where the broad peak is typical of an amorphous material that doesn't contain any crystalline phases. The XRD pattern of the Ti6Al4V-based composite shows, besides the main peaks of titanium metal (PDF#89-3725), the formation of titanium silicide (PDF#78-1429) along with traces of vanadium carbide (PDF#65-3772), see **Fig. 2.25b**. The reactivity of Ti6Al4V towards Si and C atoms present in the silicone binder was already observed in our previous work [19]. The presence of calcium silicate crystals is shown in Figure 6c and 6d, testifying the reaction

between the silicone binder and the calcium carbonate particles in the ink. The only crystal phase that formed after the treatment in air was Wollastonite-2M (PDF#27-0088), along with Pseudowollastonite (PDF#89-6463) for the samples heat treated in nitrogen, as already reported in [4].

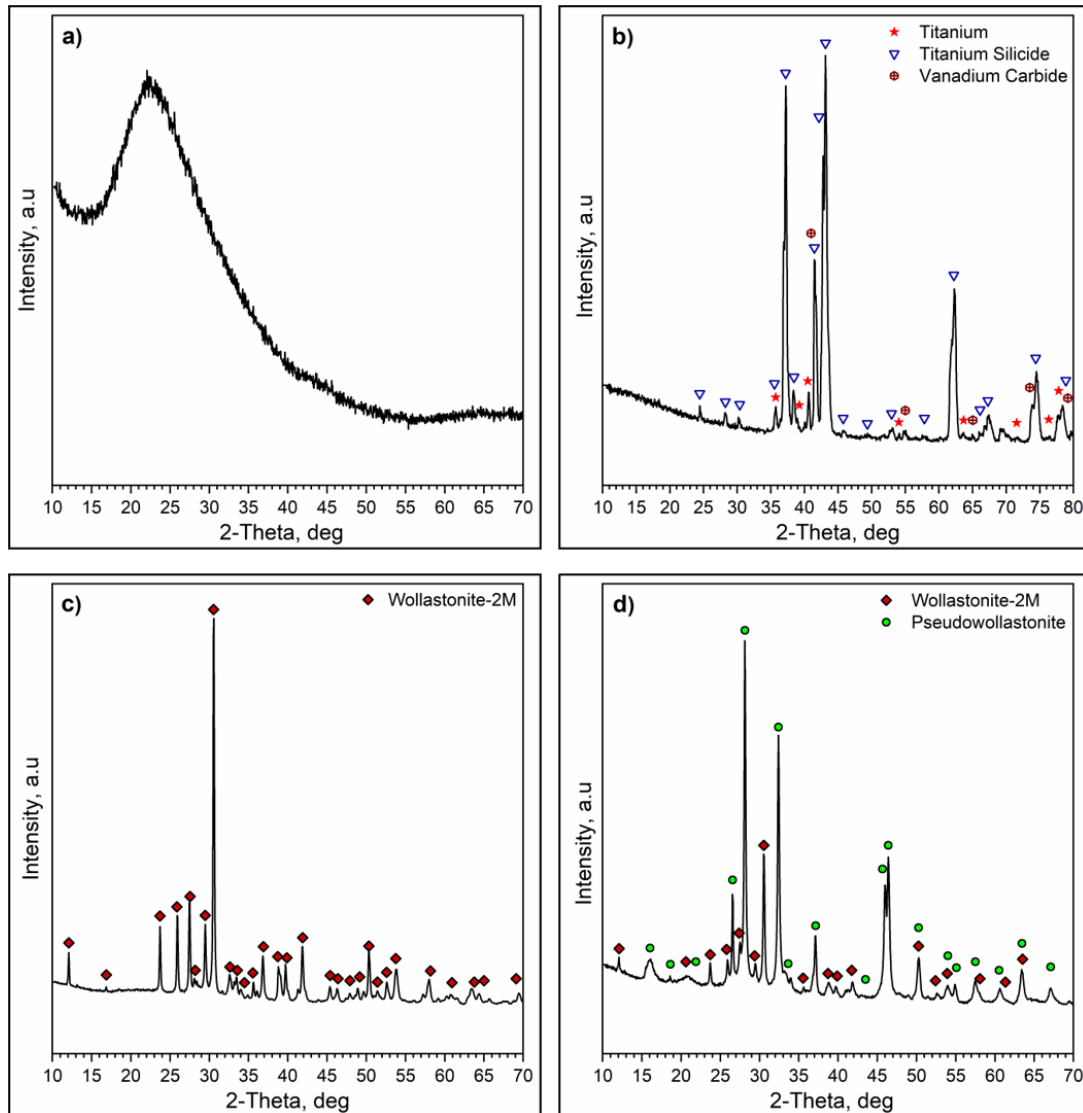


Fig. 2.25 XRD patterns of the cellular lattices after the heat treatments: a) PDMS after pyrolysis at 1000°C; b) PDMS plus Ti6Al4V after pyrolysis at 1400°C; PDMS plus CaCO₃ after heating at 1000°C c) in air, d) in nitrogen.

2.3.3 Conclusions

In this work, we produced cylindrical lattice structures made of SiOC glass, Ti6Al4V-based composite and CaSiO₃ bioceramic, by means of Direct Ink Writing combined with a rotating cylindrical mandrel operated by a robotic arm. The use of elastomer-based inks allowed printing a highly stretchable structure that could be easily removed from the mandrel without the need of any mechanical or chemical procedures. The printed structures showed sufficient shape retention after curing. Upon heating, the PDMS converted to an amorphous SiOC ceramic, while the PDMS plus Ti6Al4V and PDMS plus CaCO₃ inks were converted to a Ti6Al4V-based composite and a CaSiO₃ bioceramic, respectively. For the three compositions tested so far, a satisfactory shape retention after heating was demonstrated, thus showing the high potential of this technology to produce curved lattice components made of glass, ceramic or metal. For metal-based inks, the use of silicon free elastomers is necessary in order to avoid the formation of brittle compounds. The structures here proposed represent a proof of concept of the feasibility of the method and open the way for the production of further curved lattice structures, which are of crucial interest for applications such as highly personalized medicine devices (bone grafts, stents, ...) and multi-material components.

2.3.4 References

- [1] D. Zhang, W. Jonhson, T.S. Herng, Y.Q. Ang, L. Yang, S.C. Tan, E. Peng, H. He, J. Ding, A 3D-printing method of fabrication for metals, ceramics, and multi-materials using a universal self-curable technique for robocasting, *Materials Horizons* 7(4) (2020) 1083-1090.
- [2] Y. Cheng, K.H. Chan, X.-Q. Wang, T. Ding, T. Li, X. Lu, G.W. Ho, Direct-ink-write 3D printing of hydrogels into biomimetic soft robots, *ACS nano* 13(11) (2019) 13176-13184.
- [3] Y. Wang, Z. Yu, G. Mao, Y. Liu, G. Liu, J. Shang, S. Qu, Q. Chen, R.W. Li, Printable Liquid-Metal@ PDMS Stretchable Heater with High Stretchability and Dynamic Stability for Wearable Thermo-therapy, *Advanced Materials Technologies* 4(2) (2019) 1800435.
- [4] A. Zocca, G. Franchin, H. Elsayed, E. Gioffredi, E. Bernardo, P. Colombo, Direct ink writing of a preceramic polymer and fillers to produce hardystonite ($\text{Ca}_2\text{ZnSi}_2\text{O}_7$) bioceramic scaffolds, *J Am Ceram Soc* 99(6) (2016) 1960-1967.
- [5] H. Elsayed, N. Novak, M. Vesenjok, F. Zanini, S. Carmignato, L. Biasetto, The effect of strut size on microstructure and compressive strength of porous Ti6Al4V lattices printed via Direct Ink Writing, *Materials Science and Engineering: A* 787 (2020) 139484.
- [6] B. Song, C. Kenel, D.C. Dunand, 3D ink-extrusion printing and sintering of Ti, Ti-TiB and Ti-TiC microlattices, *Additive Manufacturing* 35 (2020) 101412.
- [7] M. Coffigniez, L. Gremillard, S. Balvay, J. Lachambre, J. Adrien, X. Boulnat, Direct-ink writing of strong and biocompatible titanium scaffolds with bimodal interconnected porosity, *Additive Manufacturing* 39 (2021) 101859.
- [8] H. Elsayed, P. Rebesan, G. Giacomello, M. Pasetto, C. Gardin, L. Ferroni, B. Zavan, L. Biasetto, Direct ink writing of porous titanium (Ti6Al4V) lattice structures, *Materials Science and Engineering: C* 103 (2019) 109794.
- [9] S.L. Taylor, A.E. Jakus, R.N. Shah, D.C. Dunand, Iron and Nickel Cellular Structures by Sintering of 3D-Printed Oxide or Metallic Particle Inks, *Adv Eng Mater* 19(11) (2017) 1600365.
- [10] B.Y. Ahn, D. Shoji, C.J. Hansen, E. Hong, D.C. Dunand, J.A. Lewis, Printed origami structures, *Adv Mater* 22(20) (2010) 2251-2254.
- [11] E. Hong, B.Y. Ahn, D. Shoji, J.A. Lewis, D.C. Dunand, Microstructure and mechanical properties of reticulated titanium scrolls, *Adv Eng Mater* 13(12) (2011) 1122-1127.
- [12] F.B. Coulter, B.S. Coulter, E. Papastavrou, A. Ianakiev, Production techniques for 3D printed inflatable elastomer structures: part II—four-axis direct ink writing on irregular double-curved and inflatable surfaces, *3D Printing and Additive Manufacturing* 5(1) (2018) 17-28.
- [13] M. Schaffner, J.A. Faber, L. Pianegonda, P.A. Rühls, F. Coulter, A.R. Studart, 3D printing of robotic soft actuators with programmable bioinspired architectures, *Nature communications* 9(1) (2018) 1-9.
- [14] K. Reeser, A.L. Doiron, Three-dimensional printing on a rotating cylindrical mandrel: a review of additive-lathe 3D printing technology, *3D Printing and Additive Manufacturing* 6(6) (2019) 293-307.
- [15] K. Huang, H. Elsayed, G. Franchin, P. Colombo, Complex SiOC ceramics from 2D structures by 3D printing and origami, *Additive Manufacturing* 33 (2020) 101144.

- [16] H. Elsayed, P. Colombo, Crack-free silicate bioceramics from preceramic polymers, *Advances in Applied Ceramics* 115(4) (2016) 193-199.
- [17] P. Colombo, G. Mera, R. Riedel, G.D. Soraru, Polymer-derived ceramics: 40 years of research and innovation in advanced ceramics, *J Am Ceram Soc* 93(7) (2010) 1805-1837.
- [18] K. Caldwell, P. Gallagher, D. Johnson Jr, Effect of thermal transport mechanisms on the thermal decomposition of CaCO₃, *Thermochimica Acta* 18(1) (1977) 15-19.
- [19] A. Fabrizi, F. Bonollo, P. Colombo, L. Biasetto, In Situ Reinforcement of Ti6Al4V Matrix Composites by Polymer-Derived-Ceramics Phases, *Adv Eng Mater* 17(6) (2015) 866-875.

3 Hierarchically porous polymer-derived SiOC scaffolds from a silicone resin and fillers

3.2 Introduction

Highly porous and lightweight ceramic components are of interest in a number of applications such as filtration [1-3], biomedicine [4,5], catalysis [6-8], energy storage [9,10] and chemical sensing [11,12] due to their tunable thermal, electrical and mechanical properties provided by the presence of pores. Considering that nowadays it is often expected that a device possesses some degree of multifunctionality, in order to satisfy ever increasing demands from complex applications, it has been demonstrated that hierarchical porous structures with pore size over multiple length scales greatly outperform components with non-hierarchical porosity [13]. Generally, interconnected macropores confer high convective heat, improved mixing as well as high mass transfer rate, while the microporous framework provides the desired functionality. For example, in scaffolds for biomedical applications the macropores enable the penetration and growth of cells and blood vessels, while micropores are beneficial for cell attachment and in situ drug delivery [14-16]. In catalytic applications, the macropores deliver low pressure drop and fluid turbulence, while the micropores provide selective gas adsorption and filtration [17,18].

Several studies have proposed numerous synthesis methods for the fabrication of ceramic components with interconnected macropores, including direct foaming, replica technique, emulsion templating, phase separation and additive manufacturing [19-25]. Among those methods, direct foaming and emulsion templating are widely used for their facility in creating a large range of pore sizes, and several cellular ceramic systems (TiO_2 , SiO_2 , SiOC, Al_2O_3 , Si_3N_4 , SiC, ZrO_2 , ...) with pores from ~ 5 to ~ 500 μm have been fabricated [26-29]. However, closed pores tend to be generated due to the thermodynamically unstable nature of liquid foams and emulsions, leading to

challenges in accurately controlling the pore size distribution. This limits their application in some fields (e.g. catalysis, where the broad pore size distribution of the fabricated cellular ceramics leads to a non-uniform behavior in operation) [30].

Recently, the rising of additive manufacturing technologies has enabled the fabrication of highly porous ceramics with a non-stochastic architecture, and more specifically some research has demonstrated the possibility of obtaining ceramics with hierarchical porosity in multiple shapes and length scales. Studart et al. [25,31] fabricated porous ceramic structures with tunable micropore structure by combining direct ink writing (DIW) and a modified emulsion/foam templating. Lewis et al. [32] obtained architected cellular ceramics with tailored stiffness using a foamed ink stabilized by colloidal particles for direct foam writing. Yang et al. [33] exploited the characteristics of boehmite gel foams to manufacture complex-shape hierarchically porous structures using DIW, by controlling the pH. Porous Al₂O₃ and TiO₂ ceramic with multi-scaled porosity were also fabricated from oil/bubble-in-water emulsions [34,35]. All these works demonstrated that it is possible to obtain components with cellular struts, but the range of pore sizes achievable and the precise combination of different pore sizes within a single strut remains a challenge, due to the intrinsic randomness of the cellular network generated by these approaches.

In our work, an alternative and tailorable fabrication method is proposed for the production of ceramic components with hierarchical and tunable porosity by Direct Ink Writing of an ink comprised of a preceramic polymer and Polymethyl methacrylate (PMMA) sacrificial microbeads. The use of preceramic polymer precursors enables the fabrication at relatively low temperature (e.g., 1000 to 1200°C) of ceramics with compositions not obtainable from non-molecular processing routes, and the presence of carbon nano-sized clusters affords functional properties, such as electrical conductivity, piezoresistivity, luminescence) to the material [36]. Furthermore, ceramics derived from silicone precursors have been proposed as electrodes for

electrochemical storage devices [37] or as bioceramic scaffolds for biomedical applications [38-40], and these applications would benefit from the presence of additional porosity within the struts of the scaffolds, providing increase geometric surface area to the components.

In our work, precise and tunable control over the pore sizes and hierarchical structures is provided by the size of the sacrificial templates, and the mixing of particles with different dimensions provides a further degree of liberty in the design of the overall pore architecture.

The combination of additive manufacturing and sacrificial PMMA beads enabled the fabrication of highly porous and strong SiOC ceramic components with pore sizes ranging from hundreds of nanometers to millimeters.

3.3 Experimental

3.3.1 Ink preparation for DIW

A commercial polymethylsiloxane, SILRES[®] MK (Wacker-Chemie GmbH, München, Germany) was used as the preceramic precursor for SiOC. Polymethyl methacrylate (PMMA), with a range of diameters (A 910W, A 210, A 500, Cray Valley Waterborne Polymers Department, Atofina Italia, Milan, Italy; MP-1000, MX-500, Esprix Technologies, Sarasota, FL), were used as sacrificial templates for the generation of pores. As shown in **Fig. 3.1**, the ink was prepared by dissolving MK into isopropanol (weight ratio = 5.37:1) followed by homogeneously mixing for 15 mins at 2000 rpm in planetary mixer (ARE 250, Thinky, Japan) at room temperature. Then, PMMA microbeads were added to the prepared solution followed by mixing for 5 mins at 2000 rpm. Finally, a cross-linking agent (GF91, Wacker-Chemie GmbH, München, Germany) was added to the above solution at 2 wt% with respect to MK, mixing for 2 mins at 2000 rpm. For investigating the influence of the content and size of the PMMA particles, inks were prepared with microbeads of 0.46, 5, 10, 25 and 50 μm nominal size, and in

an amount of 50, 60, 70, 80 vol%. Moreover, inks containing PMMA particles with different sizes were also produced, for fabricating hierarchically porous structures with a wider range of pore sizes.

3.3.2 Fabrication of porous scaffolds by DIW

A delta printer (2040 Turbo, Wasproject, Italy) was used to fabricate scaffolds according to a CAD file. Scaffolds were designed with dimension of $13.6 \times 13.6 \times 4.62$ mm³, and a designed macro-porosity of 40 vol%. Inks were extruded in ambient conditions on a plastic sheet, to provide appropriate adhesion, from a 0.4 mm nozzle (Nordson Italia, Milano, Italy) to form 0-90° scaffolds with inter-spacing of 0.33 mm between adjacent layers (z axis) and an in plane spacing (x-y axis) between filaments of 0.4 mm. The moving speed of nozzle along x-y plane was 5-10 mm/s and an air pressure of 0.3-0.6 MPa was used. Uncontrolled evaporation of isopropanol from the ink occurred during printing, and it assisted the quick recovery of high viscosity of the ink after exiting from the nozzle, contributing to the possibility of fabricating structures with undeformed suspended struts. After printing, the scaffolds were placed into a tube furnace for crosslinking and pyrolysis under inert atmosphere (99.99% N₂). The heating went from room temperature to 300°C at a rate of 1°C/min with 3h dwelling time for PMMA removal, followed by heating to 1000°C at the same rate with 2h dwelling time. Cooling was carried out in the furnace without controlling the rate.

3.3.3 Characterization

A rotational rheometer (Discovery HR-1 hybrid rheometer, TA Instruments, UK) equipped with a 50 mm diameter plate-plate geometry was used, with a set temperature of 20°C and a gap of 0.5 mm. The shear rate interval was 0.01 ~ 200 s⁻¹, and the frequency was 1 Hz. The shear strain interval for amplitude sweep was 0.001 ~ 200%. Thermogravimetric analysis (TGA/DSC 3+, Mettler Toledo, Switzerland) was carried

out heating rate of 10°C/min up to 1000°C in N₂.

The morphology and microstructure of the samples were observed by scanning electron microscopy (SEM, Quanta 200 ESEM, FEI, The Netherlands). The distribution of pore sizes was assessed by image analysis from SEM micrographs (measuring at least 100 pore sizes per sample) using ImageJ 1.52a, and the data were converted to three-dimensional values using the stereological equation $D_{\text{sphere}} = D_{\text{circle}} / 0.785$, in which D_{circle} is the diameter of the pore derived from the two dimensional SEM images and D_{sphere} is the effective diameter of pore in the three dimensional volume [41-43]. The size of samples before and after sintering were measured by a digital caliper. The geometric density (D_g) was determined by calculating mass/volume ratios. The apparent density (D_a) and true density (D_t) were measured on scaffolds and powder obtained from grinding the scaffolds using helium pycnometry (Micromeritics AccuPyc 1330, Norcross, GA, USA). The open porosity P_o was calculated from: $P_o = (1 - D_g / D_a) \times 100 \%$, the total porosity from: $P_t = (1 - D_g / D_t) \times 100 \%$, and the closed porosity from: $P_c = P_t - P_o$.

Compression tests were performed using a universal testing machine (Instron 1121 UTM, Instron Danvers, MA, USA) with a cross head displacement rate of 0.5 mm/min, applying the load perpendicularly to the printing direction of the scaffolds. The samples size for test was $10 \times 10 \times 3 \text{ mm}^3$. The data reported are the average for at least five measurements per type of sample.

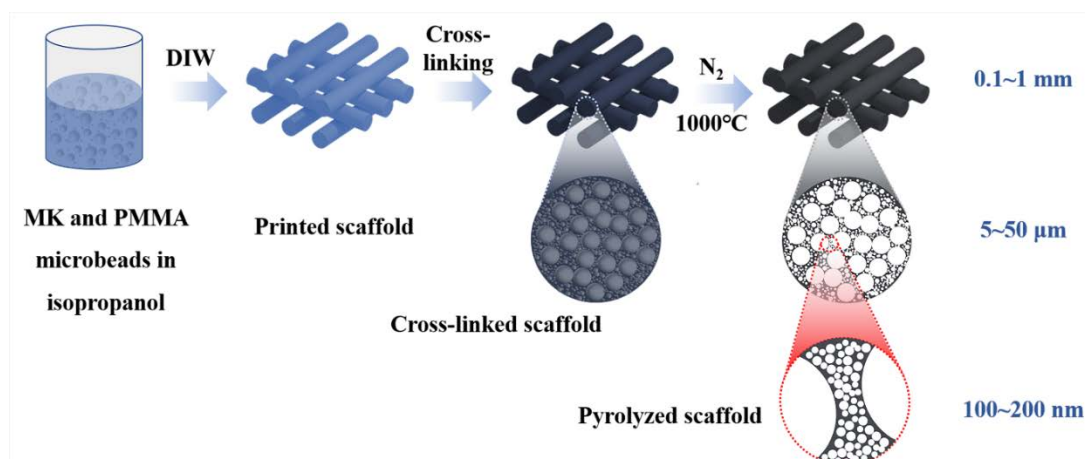


Fig. 3.1 Fabrication procedure of hierarchically porous SiOC scaffolds.

3.4 Result and discussion

3.4.1 Rheological properties of the inks

The main rheological properties of an ink, including viscosity and modulus, always play an important role in DIW processing. Shear-thinning behavior and high modulus are required for achieving a smooth extrusion under pressure and enable precise shape retention after printing. The rheology test results are reported in **Fig. 3.2**. As shown in **Fig. 3.2a** for inks containing 25 μm PMMA particles, all inks possessed a shear thinning behavior, with viscosity values decreasing from 10^3 to 20 Pa·s with shear rate increasing from 0.05 to 100 s^{-1} , with a more pronounced slope for the sample containing 80 vol% of particles. The particle content affected also the viscosity, with increasing values observed for increasing solid particles content, as expected. **Fig. 3.2b** shows the storage (G') and loss modulus (G'') of those inks. All the inks had sufficiently high G' plateau values, thereby enabling adequate shape retention after extrusion, and increasing the solid particle content led to a higher storage modulus, because a higher particle amount can contribute to the formation of a stronger particle-assembled network. Only the ink containing 80 vol% of particles possessed a high G' value of 5.6

$\times 10^3$ Pa, and displayed a reversal of the values between G' and G'' before and after a yield point (occurring at a yield stress = 24.45 Pa), demonstrating that during printing the ink behaved as a liquid while it had a solid-like behavior after extrusion from the nozzle [44,45]. When the particle content was 70 vol% or lower, however, the G'' modulus was higher than G' over the entire testing range of shear stresses, indicating that the inks behaved as a viscoelastic liquid. We can therefore attribute the good shape retention of the scaffolds produced using these inks to the rapid evaporation of isopropanol after printing, which compensates for their liquid-like behavior at low concentrations of the preceramic polymer precursor. Inks containing 80 vol% of PMMA particles with different sizes were also characterized (**Fig. 3.2c,d**). The rheological curves indicate that the viscosity of inks with particles of different size were in the range of 10^4 to 10^6 Pa·s and no significant effect of particle size on the shear-thinning behavior was observed, apart from when the smallest particles were used, while all the curves related to G' and G'' modulus show the presence of yield stress values of $10\sim 10^3$ Pa and suitably high G' modulus from 10^4 to 2×10^6 Pa, guaranteeing their printability.

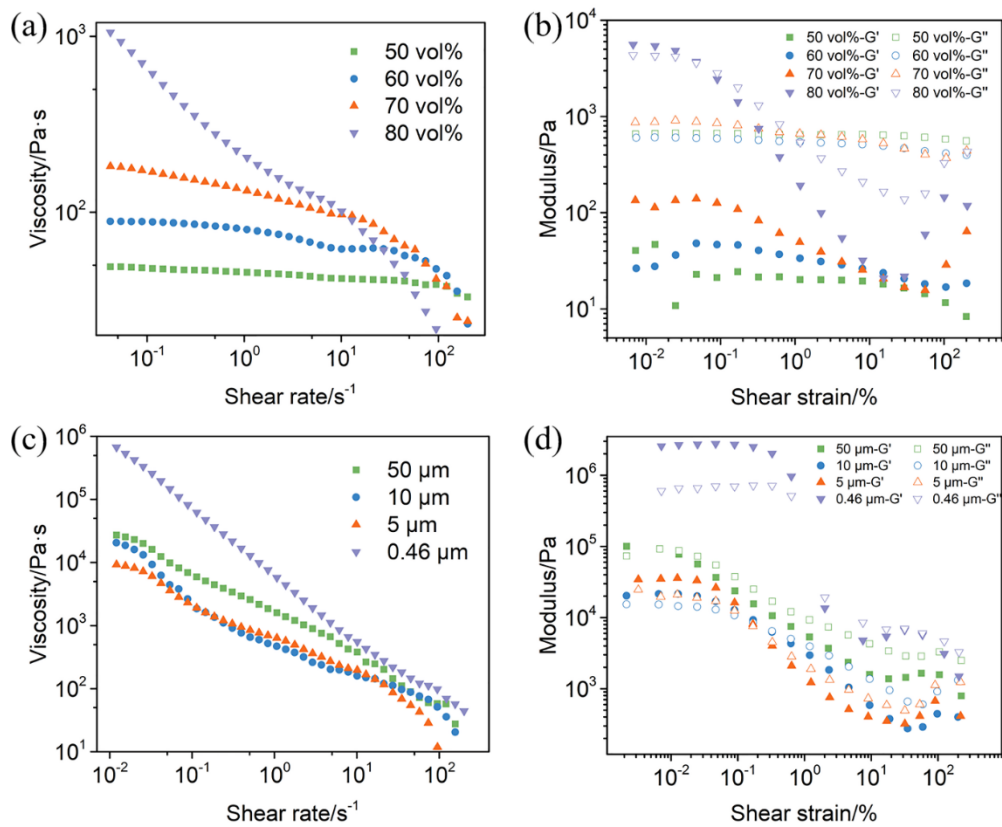


Fig. 3.2 (a) Viscosity as a function of shear rate, and (b) storage (G') and loss (G'') modulus vs shear stress of inks with different content of 25 μm PMMA particles (50, 60, 70, 80 vol%). (c) Viscosity and (d) modulus of inks with 80 vol% of PMMA particles of different size (0.46, 5, 10, 50 μm).

3.4.2 Pyrolysis and microstructure of printed scaffolds

To evaluate the appropriate heating program to employ for the pyrolysis of the printed scaffolds, TGA was conducted on as-printed scaffolds as well as on pure MK and 25 μm PMMA microbeads. **Fig. 3.3** indicates that the ceramic yield of MK is 80.32 wt% at 1000°C, which is sufficiently high to lead to a limited shrinkage and prevent crack formation during pyrolysis. The decomposition of PMMA starts at 220°C and ends at nearly 400°C, with no residual char even when pyrolyzing in inert atmosphere. Obviously, the weight loss of the scaffolds increases with increasing their PMMA particles content.

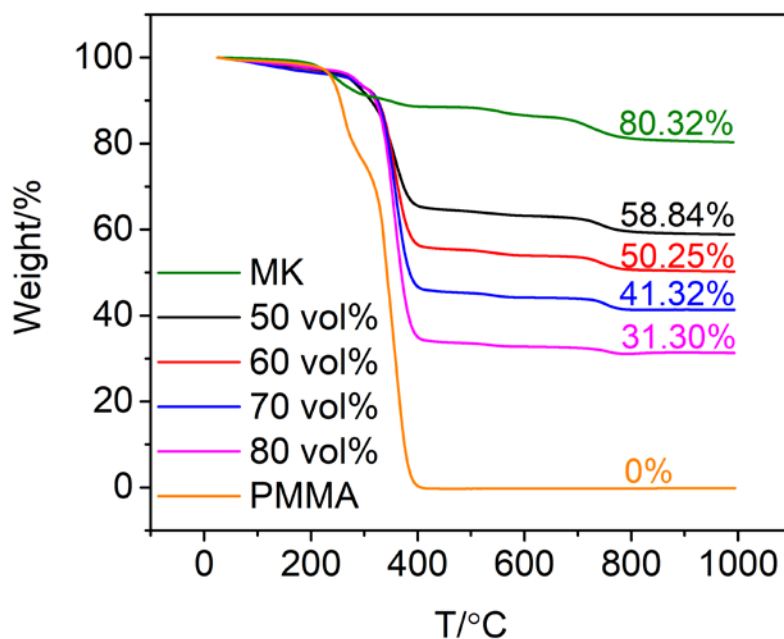


Fig. 3.3 TGA curves of as-printed scaffolds fabricated using inks with different amounts of 25 μm PMMA particles, as well as of pure 25 μm PMMA microbeads and MK silicone resin.

Digital images (**Fig. 3.4**) show the macro morphology of scaffolds with different volume fraction and size of PMMA particles, before and after ceramization. The scaffolds fully retained the shape after both printing and the heat treatment. **Fig. 3.5** shows the microstructure of the surface of the pyrolyzed scaffolds produced using inks containing different amounts of 25 μm PMMA particles. We can observe that, for this size of the sacrificial template particles, a scaffold containing 50 vol% of microbeads (**Fig. 3.5a, b**) possesses only a few open pores at the surface. With the increasing of solid content, more and more pores are present at the surface, with size in the range of 1~20 μm (**Fig. 3.5c-h**). Shrinkage deriving from the decomposition of PMMA and the polymer-to-ceramic conversion of the silicone preceramic polymer left no visible defects (such as cracks or residual porosity within the SiOC solid skeleton) or distortion of the printed filaments.

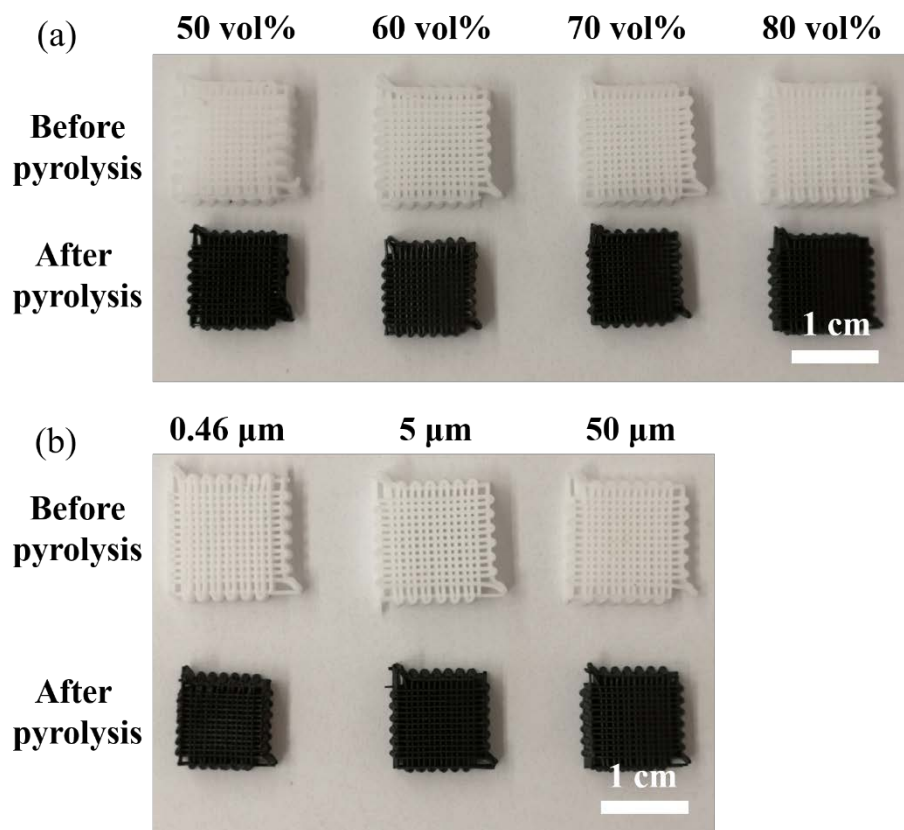


Fig. 3.4 Digital images of scaffolds before and after pyrolysis. Scaffolds fabricated using inks containing: (a) different volume fractions of 25 μm PMMA particles; (b) PMMA particles of different size (70 vol% for 0.46 μm; 80 vol% for 5 and 10 μm).

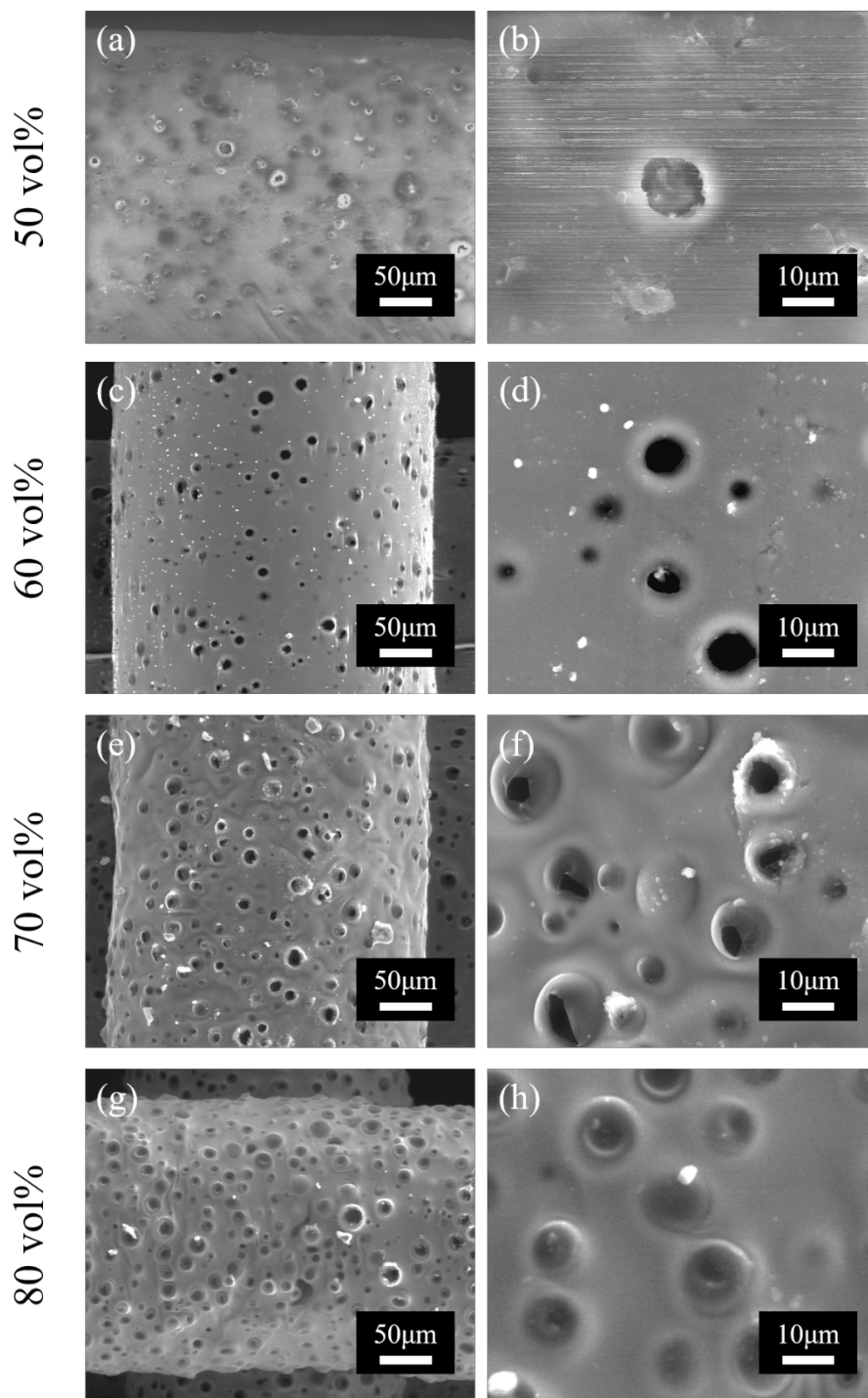


Fig. 3.5 Surface of pyrolyzed scaffolds fabricated using inks with different amounts of 25 μm PMMA particles. (a-d) 50, 60, 70, 80 vol%, (e-h) corresponding magnified images, respectively.

Cross-sections of pyrolyzed scaffolds (**Fig. 3.6**) fabricated from inks containing

different amounts of 25 μm PMMA particles further confirm that all the wood-pile structures were well retained after pyrolysis, without deformation or sagging observed in the spanning region of the filaments. Notably, most pores inside the 50 vol% filament were closed (isolated) without interconnection with neighboring ones (**Fig. 3.6a**), evidently because the percolation threshold for particles of this size was not achieved. In fact, cell windows (interconnecting pores) are generated in the areas where direct contact between PMMA particles occurs [46]. By contrast, well defined cellular structure with a random distribution of interconnecting pores was achieved by increasing the content of microbeads from 60 to 80 vol% (**Fig. 3.6b-d**). The cell window size ranged from ~ 1.5 to ~ 8 μm in all samples (**see Fig. 3.7**), and the amount of pore interconnections, as observed from the SEM images, appeared to increase with increasing microbeads content. The shape of the pores reflected the shape of the sacrificial templating particles, and the nearly spherical and symmetric shape of most pores showcases the precise morphology control that can be obtained with this approach and demonstrates that a homogeneous shrinkage in all directions occurred during pyrolysis and PMMA decomposition.

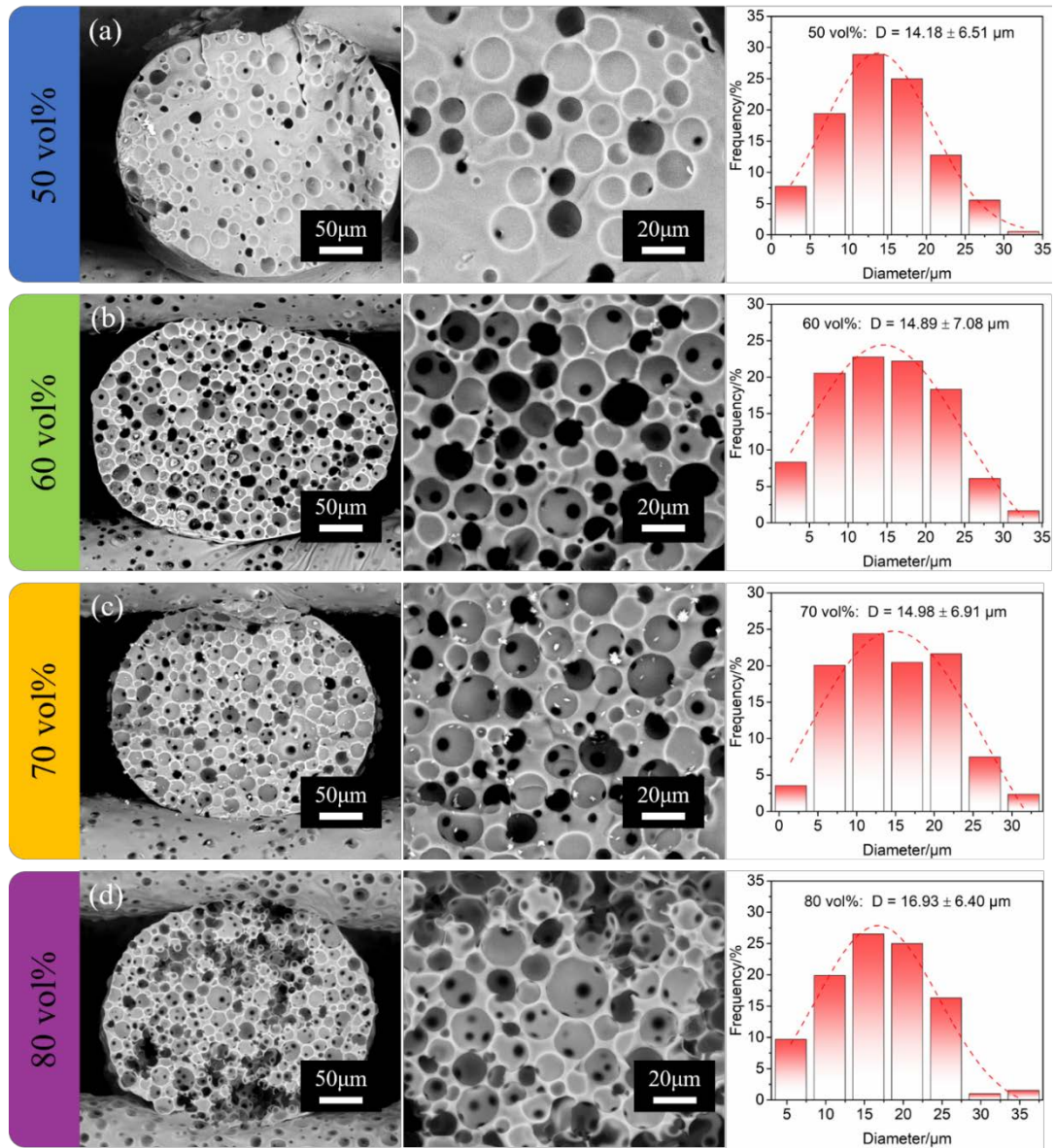


Fig. 3.6 Cross-section and pore size distribution of scaffolds fabricated using inks with different content of 25 µm PMMA particles: (a-d) 50, 60, 70, 80 vol%, respectively.

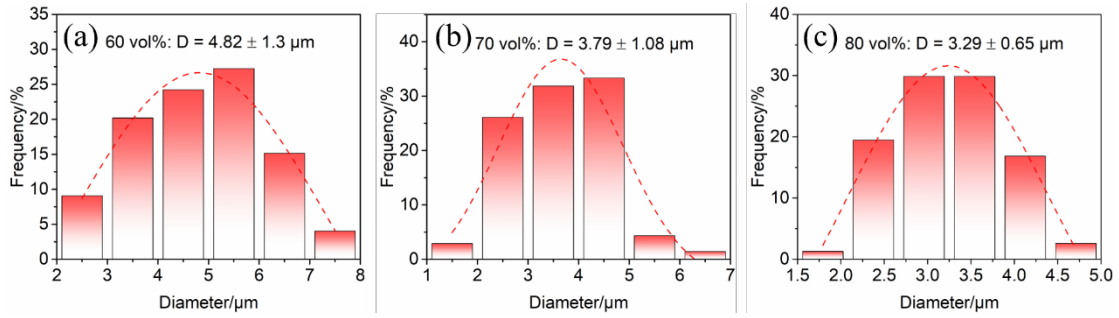


Fig. 3.7 Cell window analysis of scaffolds fabricated using inks containing 60, 70 and 80 vol% of 25 μm PMMA particles, according to the SEM images.

Cutaway views of filaments in **Fig. 3.8** confirm that a very well defined interconnected porous structure was also present along the entire axial direction of the filaments. The pores were homogeneously distributed within the SiOC structure, indicating that the mixing between the dissolved silicone resin and the microbeads was carried out efficiently and appropriately, and that no solid-liquid phase separation occurred during printing.

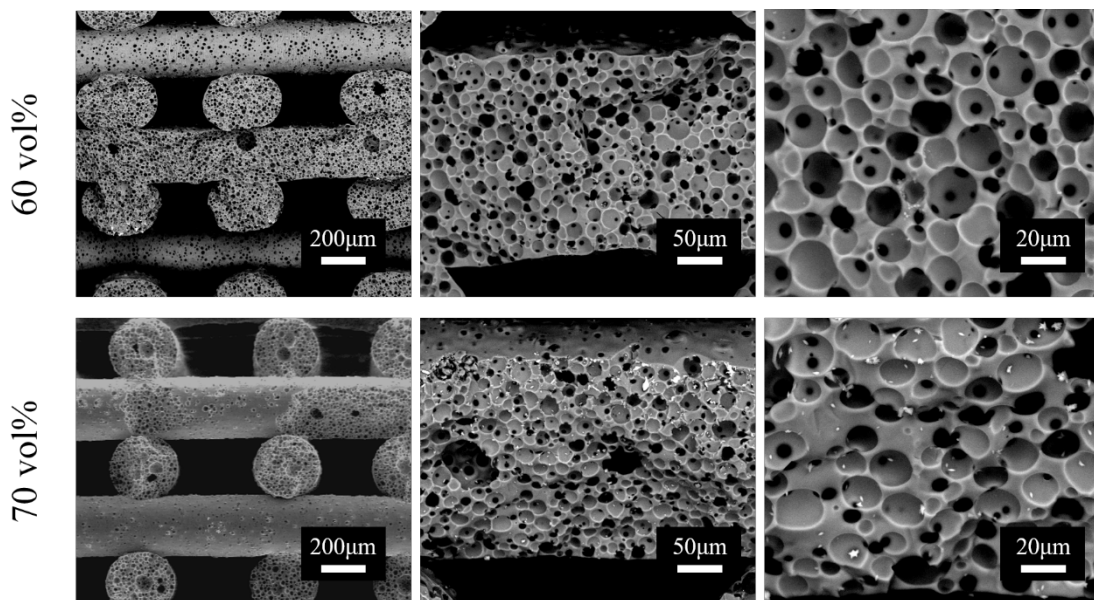


Fig. 3.8 Cutaway view of filaments of scaffolds fabricated using inks containing 60 and 70 vol% of 25 μm PMMA particles.

The characterization of the pore size distribution, carried out by image analysis, shows that the pore size inside the filaments was in the range of 1~35 μm , with an average at about 15 μm . The smaller average pore size with respect to the original PMMA particles size (see Fig. 3.9) derives, of course, from the shrinkage occurring during pyrolysis of the preceramic polymer after the removal of PMMA.

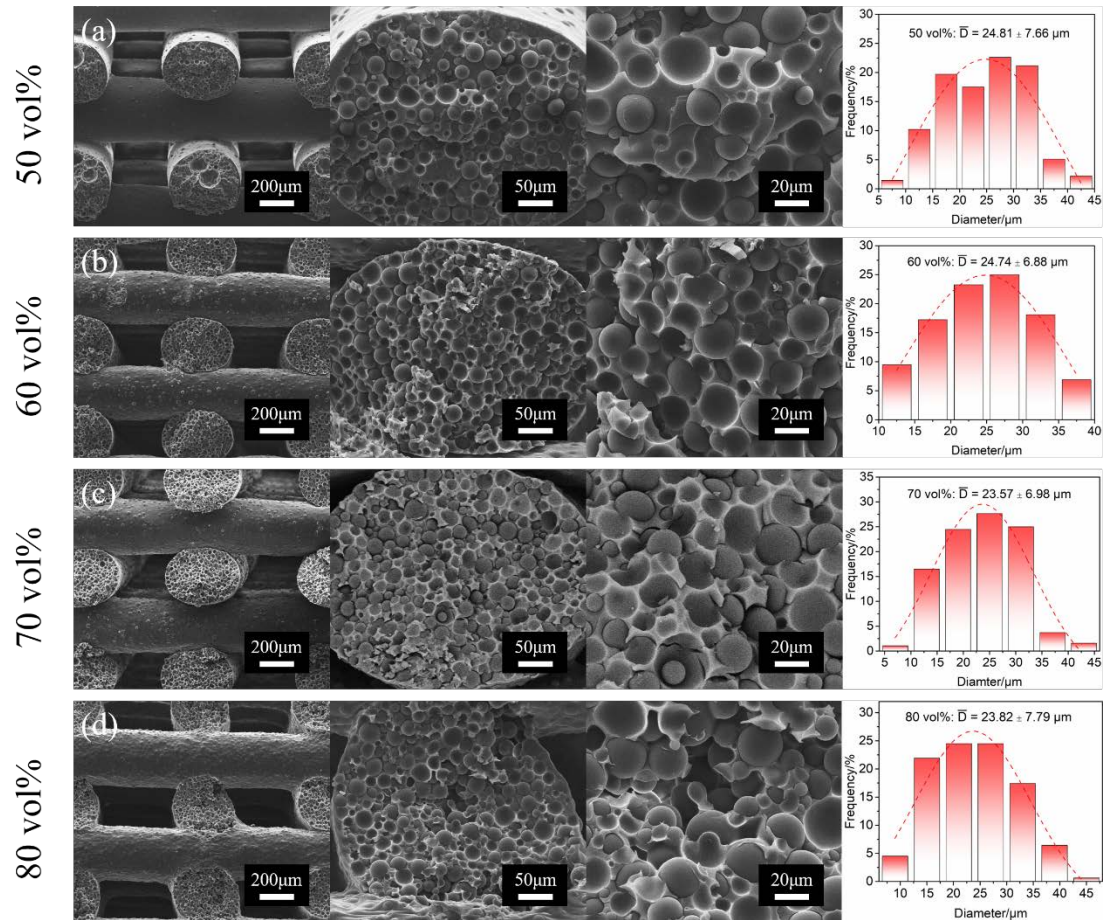


Fig. 3.9 Cross-section microstructures and pore size distributions of filaments from scaffolds fabricated using inks containing different amounts of 25 μm PMMA particles before pyrolysis: (a-d) 50 ($24.81 \pm 7.66 \mu\text{m}$), 60 ($24.74 \pm 6.88 \mu\text{m}$), 70 ($23.57 \pm 6.98 \mu\text{m}$), 80 vol% ($23.82 \pm 7.79 \mu\text{m}$) (left image: cross-section of the scaffolds).

It is evident that, in terms of pore architecture, the 3D printed scaffolds had pores

with two length scales, namely mm-scale macropores between filaments as per the CAD design, and μm -scale pores deriving from the decomposition of the sacrificial PMMA particles. Moreover, interconnecting pores were generated when a sufficient amount of microbeads was present in the ink. Both mm-scale pores and μm -scale pores are highly tailorable, making this approach very suitable for precisely controlling the cellular architecture and therefore the performance of the ceramic components.

To further demonstrate the tunability of the pore morphology, samples containing 80 vol% of PMMA particles with different size were also printed. **Fig. 3.10** shows the microstructure and distribution of pore size of these scaffolds, after pyrolysis. Considering the scaffold manufactured using an ink containing 5 μm PMMA particles (**Fig. 3.10b**), we can clearly observe a very homogeneous porous microstructure, with several cell windows interconnecting adjacent cells. Their presence in the cell walls and particularly at the surface of the filaments (see **Fig. 3.11**) certainly would increase the overall permeability of the structure. With increasing PMMA particle size, the pore size obviously increased (**Fig. 3.10c,d**), while the number of cell windows tended to decrease, due to stereological factors. Image analysis showed that the average pore sizes were 0.29 ± 0.04 (0.46 μm), 4.26 ± 1.43 (5 μm), 7.27 ± 2.48 (10 μm), 38.12 ± 11.63 μm (50 μm), respectively, with the wider distribution for the 50 μm sample due to the lower degree of uniformity in size of the starting sacrificial microbeads. The filament diameter after pyrolysis was similar for most inks, independently on the PMMA particle size (see **Fig. 3.12**); some differences might be due to a possible different expansion coefficient for the different particles, linked for instance to the molecular weight of the PMMA and its cross-linking degree.

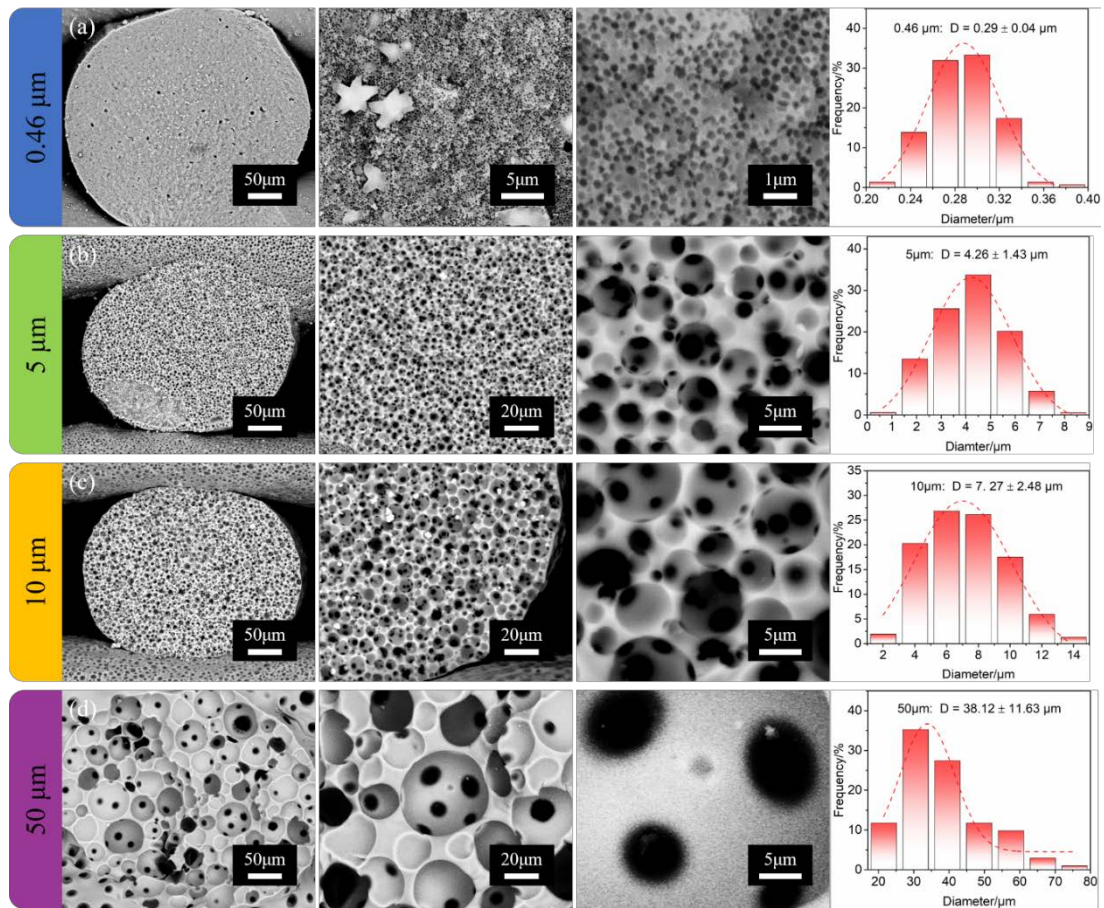


Fig. 3.10 Microstructure and pore size distribution of scaffolds fabricated using inks with PMMA particles of different size: (a) 0.46 (70 vol%); (b-c) 5, 10, 50 μm (80 vol%), respectively.

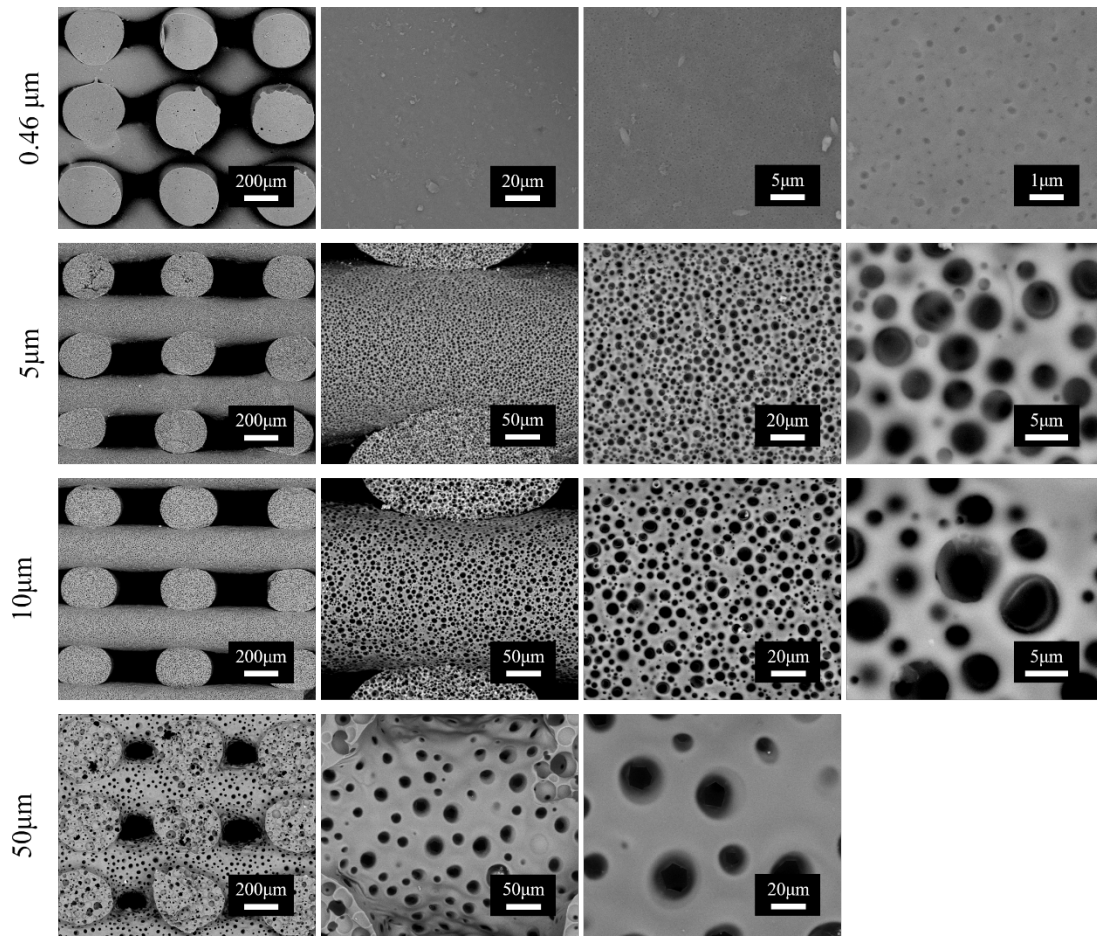


Fig. 3.11 Surface of filaments from scaffolds fabricated using inks containing 80 vol% of particles of different size: 5, 10, 50 μm (left image: cross-section of the scaffolds).

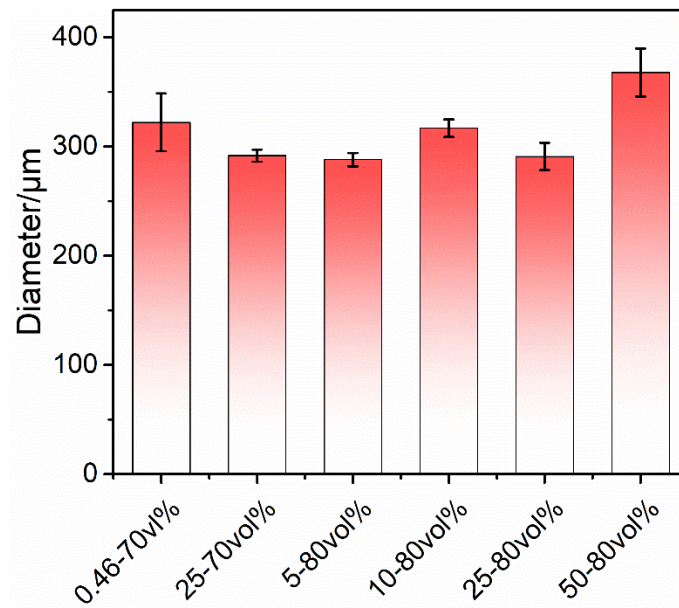


Fig. 3.12 Average diameter of filaments (after pyrolysis) from scaffolds fabricated using inks containing different amounts of PMMA microbeads of different size.

To diversify even further the hierarchical porous structures that can be obtained with this approach, we also manufactured samples with inks simultaneously containing PMMA particles of different size. Images of scaffolds produced using an ink containing particles of two different sizes (50/5 μm, 25/0.46 μm; 40 vol% small particles, 40 vol% large particles; total particles = 80 vol%) show that the smaller particles located themselves within the struts and walls of cells generated by the larger particles (see **Fig. 3.13**), increasing the interconnectivity among them, as qualitatively observe from the SEM images (presence of cell windows between adjacent pores).

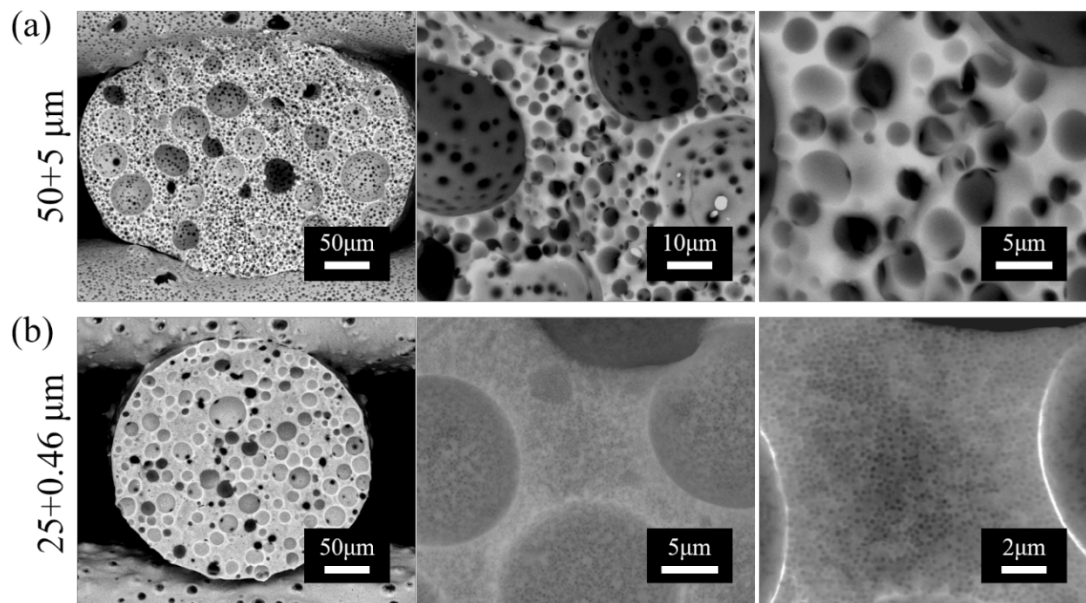


Fig. 3.13 Microstructure of scaffolds fabricated using inks containing multi-scale PMMA particles (40 vol% small particles, 40 vol% large particles; total particles = 80 vol%).

In **Fig. 3.14** we report additional images showing the microstructure of a scaffold manufactured using an ink containing particles of 4 different sizes (25/10/5/0.46 μm; 20 vol% each; total particles = 80 vol%), which contains three length scales of pore sizes.

With the inks developed in this work, the designed macropores between filaments can be fabricated in the range of 0.1 to 1 mm, without sagging of the suspended struts. Then, filaments with a cellular structure with variable pore size can be obtained by the introduction of sacrificial PMMA microbeads in the inks. Moreover, the addition of microbeads of different diameter within the same ink introduces further (mainly interconnected) pores in the cell walls and struts.

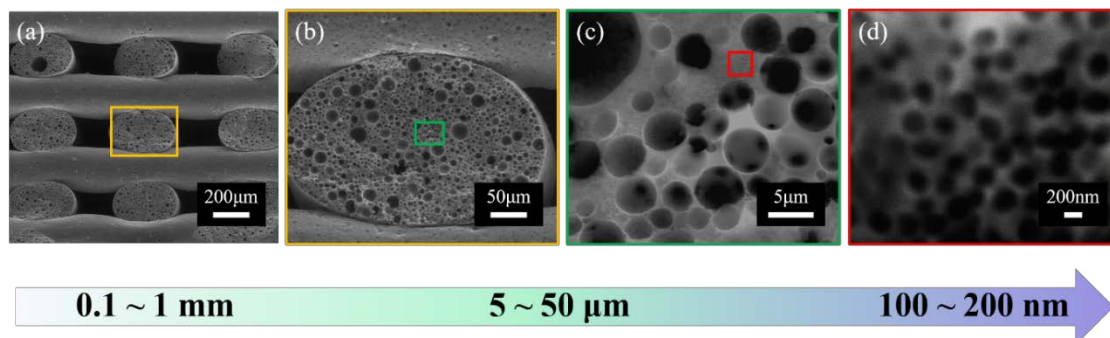


Fig. 3.14 Microstructure of a scaffold fabricated using inks containing multi-scale PMMA particles (25/10/5/0.46 μm ; total particles = 80 vol%).

3.4.3 Mechanical properties of printed scaffolds

The mechanical properties of porous ceramics also play an important role in several application fields, especially when structural support is also one of the requirements. **Tab. 3.1** reports the physical properties of scaffolds with different porosity values, manufactured using inks containing PMMA particles of different size after pyrolysis. All the samples displayed a similar isotropic linear shrinkage of $\sim 20\%$ along the x-y-z axis directions, indicating that pyrolysis enabled the fabrication of ceramic scaffold without deformation. No significant effect on the shrinkage of the scaffolds was observed with varying content of PMMA particles in the ink, since the solid part of the skeleton was always comprised of the same silicone resin. The higher shrinkage for the sample produced using an ink containing 0.46 μm microbeads might be attributed to some pore closure due to viscous flow during pyrolysis (see also the lower total porosity value for this sample). No formation of (macro-)defects, such as cracks or undesired voids, was observed even for the highest volume shrinkage values.

The total porosity of the scaffolds increased from 70.2 to 87.8 vol% with increasing content of sacrificial PMMA microbeads from 50 to 80 vol%, as expected, demonstrating the effectiveness of the proposed approach to generate pores in a wide range of both sizes and volume. The measured closed porosity was large at low volumes

of PMMA particles (up to 24 vol% for the sample fabricated using only 50 vol% of 25 μm microbeads), decreasing with increasing their amount (down to 2 vol% for the sample fabricated using 80 vol% of 25 μm microbeads), in agreement with the SEM observations. We should point out that, when investigating the effect of particle size, the solid content of the ink with 0.46 μm particles was only 70 vol%, since the ink with 80 vol% microbeads was too viscous to print.

Tab. 3.1 Physical properties of scaffolds fabricated using inks with different PMMA particles content and size after pyrolysis

Particle size (μm)	Volume fraction (vol%)	Volume shrinkage (%)	x (%)	y (%)	z (%)	Apparent density (g/cm^3)	Open porosity (vol%)	Total porosity (vol%)
25	50	52.3 \pm 1.1	21.9 \pm 0.5	21.5 \pm 0.7	22.2 \pm 1.6	1.27 \pm 0.06	46.2 \pm 2.2	70.2 \pm 1.0
25	60	50.1 \pm 1.4	20.9 \pm 0.6	20.7 \pm 0.7	20.3 \pm 2.0	1.78 \pm 0.24	66.8 \pm 4.9	75.8 \pm 0.8
25	70	50.3 \pm 1.4	21.1 \pm 0.3	20.7 \pm 0.4	20.4 \pm 2.0	1.88 \pm 0.08	77.1 \pm 3.2	80.7 \pm 2.0
25	80	48.8 \pm 0.6	20.2 \pm 0.2	20.0 \pm 0.7	19.8 \pm 0.9	1.92 \pm 0.01	85.8 \pm 0.3	87.8 \pm 0.3
0.46	70	56.9 \pm 0.7	25.4 \pm 1.2	25.0 \pm 0.7	23.0 \pm 1.2	1.83 \pm 0.07	69.5 \pm 3.1	74.9 \pm 3.2
5	80	46.7 \pm 1.9	19.7 \pm 0.5	19.6 \pm 0.6	17.4 \pm 2.6	1.97 \pm 0.05	84.7 \pm 0.5	86.5 \pm 0.9
10	80	45.4 \pm 1.2	19.2 \pm 0.7	18.6 \pm 0.9	17.0 \pm 1.7	2.0 \pm 0.04	85.8 \pm 0.8	87.0 \pm 0.7

Mechanical tests (**Fig. 3.15a**) showed that increasing content of PMMA particles reduced significantly the compression strength, from 7.5 ± 1.9 to 0.9 ± 0.1 MPa, due to the higher porosity and in accordance with the general equation proposed by Ashby [47]. In addition to the total amount of porosity, the mechanical properties of porous ceramics are also related to the pore size, with samples possessing micro-cellular struts performing better than those with macro-cellular struts, in **Fig. 3.15b**. The data shown in Table 1 in fact confirm that, at the same volume of porosity, samples produced with inks containing smaller particles had higher strength, in agreement with the literature [46,48]. In particular, scaffolds manufactured using an ink containing 70 vol% of $0.46 \mu\text{m}$ PMMA particles had a very remarkable strength of 8.2 ± 3.1 MPa, an almost double value with respect to scaffolds manufactured with $25 \mu\text{m}$ microbeads. In **Fig. 3.16** we report a summary of the data concerning some porous ceramic structures fabricated either by additive manufacturing or by other techniques (e.g., direct foaming or the replica method) [25,49-64]. The comparison indicates that the compressive strength of our samples is among the highest reported so far both for 3D printed and non 3D printed (e.g., foams) highly porous components with the same amount of total porosity.

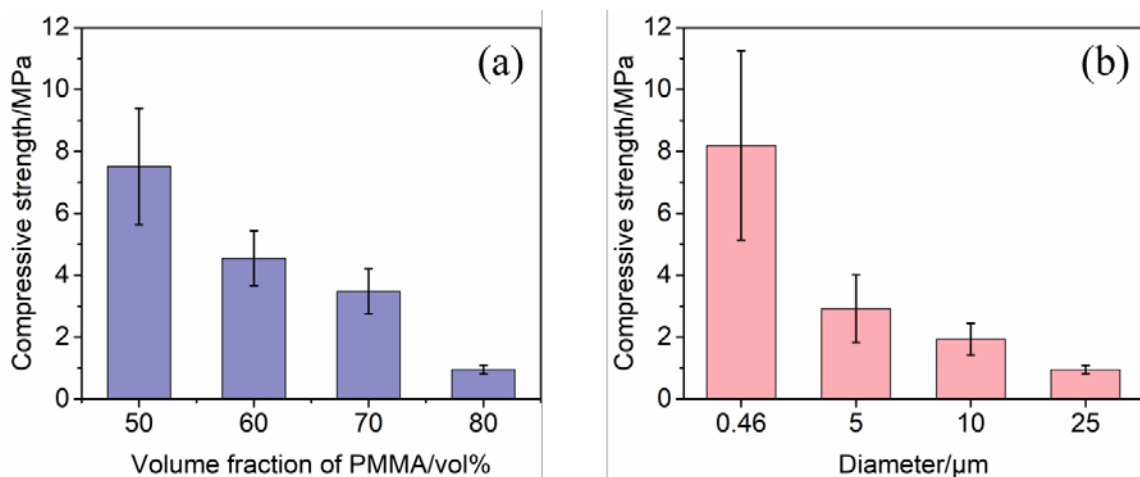


Fig. 3.15 Compression strength of scaffolds fabricated using inks (a) with different contents of $25 \mu\text{m}$ PMMA particles, and (b) with different particle size (total particles: 80 vol% for 5, 10, 25 μm ; 70 vol% for 0.46 μm).

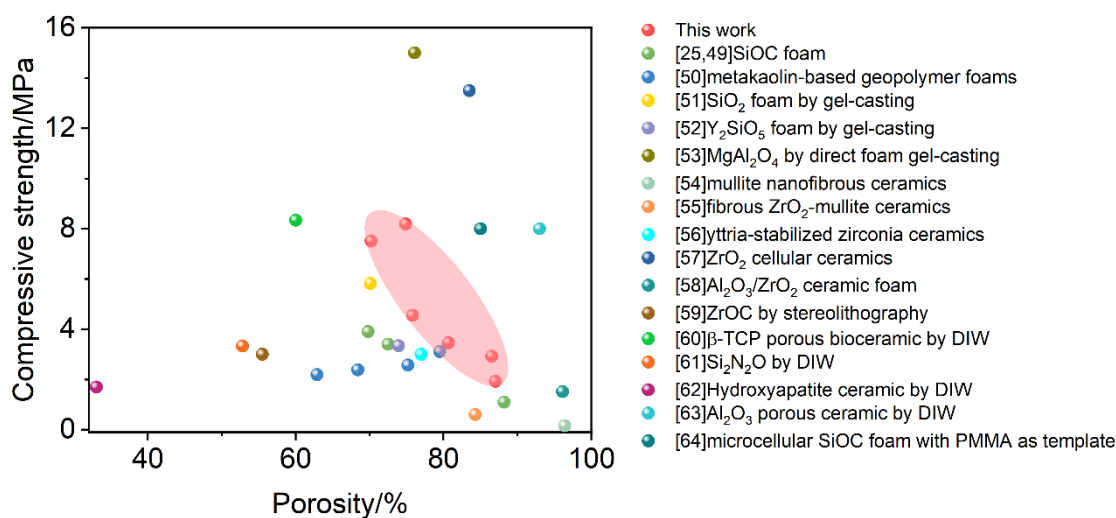


Fig. 3.16 Comparison between the compressive strength of samples produced in this work and results reported in the literature for 3D printed and non 3D printed porous ceramics.

It is interesting to observe that, evidently, it was the porosity (average pore size and total volume) in the filaments the controlling parameter for the mechanical strength of the scaffolds, considering that the macro-porosity amount and the filament size was the same, by design, for each of them (40 vol% and 400 μm , respectively). We can posit that brittle porous ceramic structures are subjected to a size effect because of greater probability of finding critical surface defects (flaws), and previous studies indicated a higher probability of finding critical defects in thicker struts of porous ceramics with bigger pores [48,65]. In this work, the strut size inside the filaments decreased with decreasing pore size at the same microbeads volume, due to their decreasing diameter, leading to an enhancement of the strength because of decreasing strut surface area [66]. Therefore, the scaffolds with filaments with smaller pores tend to outperform those with filaments containing larger pores. It should be noted that it was difficult, using a 0.4 mm nozzle and an ink containing 80 vol% of 50 μm microbeads, to fabricate scaffolds possessing enough layers for carrying out the mechanical test. Therefore, only SEM

images of these samples were reported in this paper.

Gibson and Ashby [47,67] have described the general relationships for the compressive strength of a cellular material as:

$$\frac{\sigma}{\sigma_s} = C \left(\frac{\rho}{\rho_s} \right)^n$$

where σ and σ_s are the compressive strength of the porous and solid material, and ρ/ρ_s is the relative density defined as the density of the component (ρ) divided by the density of the solid material constituting the struts (ρ_s). Here, the ρ_s of solid SiOC was taken as 2.23 g/cm³, as measured by pycnometry on a finely ground specimen. C is a dimensionless constant related to the geometric configuration of the porous material and the exponent n is 3/2 or 2 depending on if the pore morphology is open or closed, respectively. A linear-regression fit according to the above relationship (see **Fig. 3.17**) demonstrates an exponent of 2.36 for the compressive strength (correlation coefficients of $R^2 = 0.98$). The less rigorous fitting may come from the different pore morphology when comparing our samples with Ashby's model [68]. The morphology of foams in Ashby's model consists of non-spherical either totally open pores or closed pores of the same size, while the printed scaffolds in this work contain both the macro pores between the printed filaments as well as the open and closed pores inside the filaments (closed porosity in the filaments was present especially in scaffolds fabricated using inks with lower PMMA content, see **Fig. 3.5** and **Fig. 3.6**). What's more, the strength of scaffolds that were obtained using the same amount of PMMA particles with different size deviated from the fitting line, further suggesting the influence of the pore size inside the filaments on the mechanical properties.

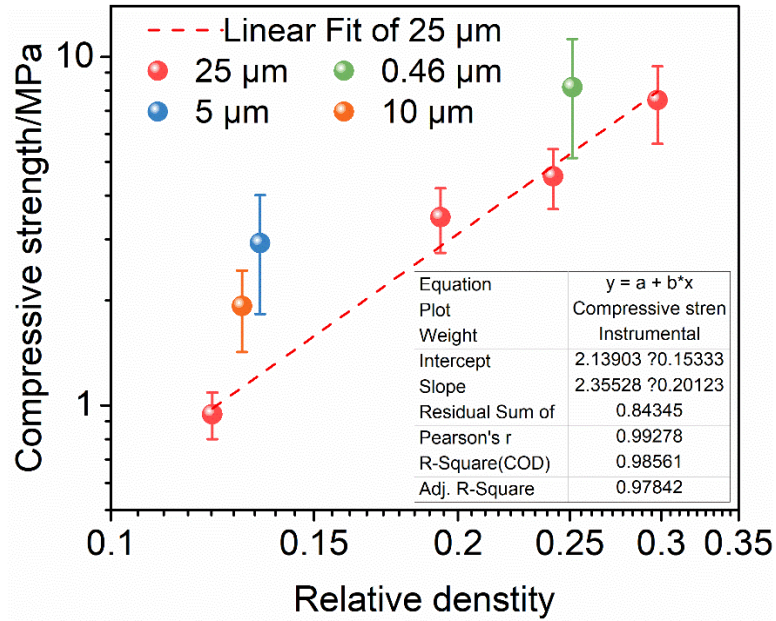


Fig. 3.17 Compressive strength of scaffolds fabricated using inks containing PMMA particles of different size as the function of relative density (the linear fitting is for data for samples fabricated using 25 μm particles).

3.5 Conclusions

The fabrication of SiOC ceramics with hierarchical porosity was investigated with the aim of achieving tunable and controllable multi-scale pore structures using additive manufacturing and sacrificial templates. Scaffolds based on filaments containing spherical and interconnected pores were fabricated without defects, such as cracks or deformations after printing and pyrolysis. The amount and size of PMMA particles contained in the inks affected the main characteristics of the scaffolds (i.e. density, porosity), and the mechanical strength. A high content of PMMA microbeads helped to improve the interconnectivity between adjacent pores inside the filaments. High compressive strength of 8.2 ± 3.1 MPa was obtained when using 0.46 μm microbeads. Combination of microbeads with various particle sizes contributed to the generation of hierarchical pores at different length scales, from ~ 100 nm to mm. The possibility of

manufacturing scaffolds possessing filaments with interconnected porosity and greatly increased geometric surface as well as enhanced compressive strength will prove beneficial for applications such as catalyst support, biomedical components, energy devices, etc.

3.6 References

- [1] D. Das, K. Nijhuma, A.M. Gabriel, G.P.F. Daniel, D.d.M.I. Murilo, Recycling of coal fly ash for fabrication of elongated mullite rod bonded porous SiC ceramic membrane and its application in filtration, *Journal of the European Ceramic Society* 40(5) (2020) 2163-2172.
- [2] L. Yu, M. Kanezashi, H. Nagasawa, T. Tsuru, Phase inversion/sintering-induced porous ceramic microsheet membranes for high-quality separation of oily wastewater, *Journal of Membrane Science* 595 (2020) 117477.
- [3] J. Liu, B. Ren, Y. Wang, Y. Lu, L. Wang, Y. Chen, J. Yang, Y. Huang, Hierarchical porous ceramics with 3D reticular architecture and efficient flow-through filtration towards high-temperature particulate matter capture, *Chemical Engineering Journal* 362 (2019) 504-512.
- [4] E. Papynov, O. Shichalin, Y.E. Skurikhina, V. Turkutuyukov, M. Medkov, D. Grishchenko, A. Portnyagin, E. Merkulov, V. Apanasevich, B. Geltser, ZrO₂-phosphates porous ceramic obtained via SPS-RS “in situ” technique: Bacteria test assessment, *Ceramics International* 45(11) (2019) 13838-13846.
- [5] T. Crouzier, F. Sailhan, P. Becquart, R. Guillot, D. Logeart-Avramoglou, C. Picart, The performance of BMP-2 loaded TCP/HAP porous ceramics with a polyelectrolyte multilayer film coating, *Biomaterials* 32(30) (2011) 7543-7554.
- [6] A. Zampieri, P. Colombo, G.T. Mabande, T. Selvam, W. Schwieger, F. Scheffler, Zeolite coatings on microcellular ceramic foams: a novel route to microreactor and microseparator devices, *Adv Mater* 16(9-10) (2004) 819-823.
- [7] T. Konegger, L.F. Williams, R.K. Bordia, Planar, polysilazane-derived porous ceramic supports for membrane and catalysis applications, *J Am Ceram Soc* 98(10) (2015) 3047-3053.
- [8] H.Q. Trinh, Y.S. Mok, Plasma-catalytic oxidation of acetone in annular porous monolithic ceramic-supported catalysts, *Chemical Engineering Journal* 251 (2014) 199-206.
- [9] M. Zhou, T. Lin, F. Huang, Y. Zhong, Z. Wang, Y. Tang, H. Bi, D. Wan, J. Lin, Highly conductive porous graphene/ceramic composites for heat transfer and thermal energy storage, *Adv Funct Mater* 23(18) (2013) 2263-2269.
- [10] Y. Zhang, Y. Bao, D. Zhang, C.R. Bowen, Porous PZT ceramics with aligned pore channels for energy harvesting applications, *J Am Ceram Soc* 98(10) (2015) 2980-2983.
- [11] S. Basu, M. Saha, S. Chatterjee, K.K. Mistry, S. Bandyopadhyay, K. Sengupta, Porous ceramic sensor for measurement of gas moisture in the ppm range, *Materials Letters* 49(1) (2001) 29-33.
- [12] D.S. Karousos, A.I. Labropoulos, A. Sapalidis, N.K. Kanellopoulos, B. Iliev, T.J. Schubert, G.E. Romanos, Nanoporous ceramic supported ionic liquid membranes for CO₂ and SO₂ removal from flue gas, *Chemical Engineering Journal* 313 (2017) 777-790.
- [13] F. Akhtar, L. Andersson, S. Ogunwumi, N. Hedin, L. Bergström, Structuring adsorbents and catalysts by processing of porous powders, *Journal of the European Ceramic Society* 34(7) (2014) 1643-1666.
- [14] M. Xu, H. Li, D. Zhai, J. Chang, S. Chen, C. Wu, Hierarchically porous nagelschmidite bioceramic-silk scaffolds for bone tissue engineering, *J Mater Chem B* 3(18) (2015) 3799-3809.
- [15] D. Khang, J. Choi, Y.M. Im, Y.J. Kim, J.H. Jang, S.S. Kang, T.H. Nam, J. Song, J.W. Park, Role of

- subnano-, nano- and submicron-surface features on osteoblast differentiation of bone marrow mesenchymal stem cells, *Biomaterials* 33(26) (2012) 5997-6007.
- [16] Z. Yi, K. Wang, J. Tian, Y. Shu, J. Yang, W. Xiao, B. Li, X. Liao, Hierarchical porous hydroxyapatite fibers with a hollow structure as drug delivery carriers, *Ceramics International* 42(16) (2016) 19079-19085.
- [17] M.V. Twigg, J.T. Richardson, Fundamentals and applications of structured ceramic foam catalysts, *Industrial & engineering chemistry research* 46(12) (2007) 4166-4177.
- [18] P. Colombo, C. Vakifahmetoglu, S. Costacurta, Fabrication of ceramic components with hierarchical porosity, *Journal of Materials Science* 45(20) (2010) 5425-5455.
- [19] X. Deng, J. Wang, J. Liu, H. Zhang, F. Li, H. Duan, L. Lu, Z. Huang, W. Zhao, S. Zhang, Preparation and characterization of porous mullite ceramics via foam-gelcasting, *Ceramics International* 41(7) (2015) 9009-9017.
- [20] X. Wang, J.-M. Ruan, Q.-Y. Chen, Effects of surfactants on the microstructure of porous ceramic scaffolds fabricated by foaming for bone tissue engineering, *Materials Research Bulletin* 44(6) (2009) 1275-1279.
- [21] A. Imhof, D. Pine, Ordered macroporous materials by emulsion templating, *Nature* 389(6654) (1997) 948-951.
- [22] K. Nakanishi, N. Tanaka, Sol-gel with phase separation. Hierarchically porous materials optimized for high-performance liquid chromatography separations, *Accounts of Chemical Research* 40(9) (2007) 863-873.
- [23] R. Mouazer, S. Mullens, I. Thijs, J. Luyten, A. Buekenhoudt, Silicon carbide foams by polyurethane replica technique, *Adv Eng Mater* 7(12) (2005) 1124-1128.
- [24] S. Moon, J.Q. Kim, B.Q. Kim, J. Chae, S.Q. Choi, Processable Composites with Extreme Material Capacities: Towards Designer High Internal Phase Emulsions and Foams, *Chemistry of Materials* (2020).
- [25] C. Minas, D. Carnelli, E. Tervoort, A.R. Studart, 3D Printing of Emulsions and Foams into Hierarchical Porous Ceramics, *Adv Mater* 28(45) (2016) 9993-9999.
- [26] C. Vakifahmetoglu, P. Colombo, A. Pauletti, C.F. Martin, F. Babonneau, SiOC ceramic monoliths with hierarchical porosity, *International Journal of Applied Ceramic Technology* 7(4) (2010) 528-535.
- [27] H. Maekawa, J. Esquena, S. Bishop, C. Solans, B.F. Chmelka, Meso/macroporous inorganic oxide monoliths from polymer foams, *Adv Mater* 15(7-8) (2003) 591-596.
- [28] F. Carn, A. Colin, M.F. Achard, H. Deleuze, Z. Saadi, R. Backov, Rational design of macrocellular silica scaffolds obtained by a tunable sol-gel foaming process, *Adv Mater* 16(2) (2004) 140-144.
- [29] T. Sen, G. Tiddy, J. Casci, M. Anderson, Macro-cellular silica foams: synthesis during the natural creaming process of an oil-in-water emulsion, *Chemical communications* (17) (2003) 2182-2183.
- [30] I. Gräf, A.-K. Rühl, B. Kraushaar-Czarnetzki, Experimental study of heat transport in catalytic sponge packings by monitoring spatial temperature profiles in a cooled-wall reactor, *Chemical Engineering Journal* 244 (2014) 234-242.
- [31] L. Alison, S. Menasce, F. Bouville, E. Tervoort, I. Mattich, A. Ofner, A.R. Studart, 3D printing of sacrificial templates into hierarchical porous materials, *Sci Rep* 9(1) (2019) 409.

- [32] J.T. Muth, P.G. Dixon, L. Woish, L.J. Gibson, J.A. Lewis, Architected cellular ceramics with tailored stiffness via direct foam writing, *Proceedings of the National Academy of Sciences* 114(8) (2017) 1832-1837.
- [33] X. Zhang, W. Huo, J. Liu, Y. Zhang, S. Zhang, J. Yang, 3D printing boehmite gel foams into lightweight porous ceramics with hierarchical pore structure, *Journal of the European Ceramic Society* 40(3) (2020) 930-934.
- [34] S.S.L. Chan, M.L. Sesso, G.V. Franks, Direct ink writing of hierarchical porous alumina-stabilized emulsions: Rheology and printability, *J Am Ceram Soc* (2020).
- [35] M.A. Torres Arango, D. Kwakye-Ackah, S. Agarwal, R.K. Gupta, K.A. Sierros, Environmentally friendly engineering and Three-Dimensional printing of TiO₂ hierarchical mesoporous cellular architectures, *Acs Sustainable Chemistry & Engineering* 5(11) (2017) 10421-10429.
- [36] P. Colombo, G. Mera, R. Riedel, G.D. Soraru, Polymer-derived ceramics: 40 years of research and innovation in advanced ceramics, *J Am Ceram Soc* 93(7) (2010) 1805-1837.
- [37] S.B. Mujib, R. Cuccato, S. Mukherjee, G. Franchin, P. Colombo, G. Singh, Electrospun SiOC ceramic fiber mats as freestanding electrodes for electrochemical energy storage applications, *Ceramics International* 46(3) (2020) 3565-3573.
- [38] A. Zocca, G. Franchin, H. Elsayed, E. Gioffredi, E. Bernardo, P. Colombo, A. Bandyopadhyay, Direct Ink Writing of a Preceramic Polymer and Fillers to Produce Hardystonite (Ca₂ZnSi₂O₇) Bioceramic Scaffolds, *J Am Ceram Soc* 99(6) (2016) 1960-1967.
- [39] S.S. Ramirez Caballero, H. Elsayed, S. Tadier, A. Montembault, E. Maire, L. David, T. Delair, P. Colombo, L. Grémillard, Fabrication and characterization of hardystonite-chitosan biocomposite scaffolds, *Ceramics International* 45(7) (2019) 8804-8814.
- [40] H. Elsayed, P. Colombo, E. Bernardo, Direct ink writing of wollastonite-diopside glass-ceramic scaffolds from a silicone resin and engineered fillers, *Journal of the European Ceramic Society* 37(13) (2017) 4187-4195.
- [41] M.S. Cilla, M.R. Morelli, P. Colombo, Open cell geopolymer foams by a novel saponification/peroxide/gelcasting combined route, *Journal of the European Ceramic Society* 34(12) (2014) 3133-3137.
- [42] D. ASTM, 3576, Standard test method for cell size of rigid cellular plastics, *Annual book of ASTM standards* 8.
- [43] C. Vakifahmetoglu, E. Pippel, J. Woltersdorf, P. Colombo, Growth of One-Dimensional Nanostructures in Porous Polymer-Derived Ceramics by Catalyst-Assisted Pyrolysis. Part I: Iron Catalyst, *J Am Ceram Soc* 93(4) (2010) 959-968.
- [44] J.E. Smay, J. Cesarano, J.A. Lewis, Colloidal inks for directed assembly of 3-D periodic structures, *Langmuir* 18(14) (2002) 5429-5437.
- [45] J.E. Smay, G.M. Gratson, R.F. Shepherd, J. Cesarano, J.A. Lewis, Directed colloidal assembly of 3D periodic structures, *Adv Mater* 14(18) (2002) 1279-1283.
- [46] P. Colombo, Macro- and micro-cellular porous ceramics from preceramic polymers, *Composites Science and Technology* 63(16) (2003) 2353-2359.
- [47] M.F. Ashby, R.M. Medalist, The mechanical properties of cellular solids, *Metallurgical Transactions A* 14(9) (1983) 1755-1769.

- [48] P. Colombo, E. Bernardo, L. Biasetto, Novel microcellular ceramics from a silicone resin, *J Am Ceram Soc* 87(1) (2004) 152-154.
- [49] S.S.R. Caballero, H. Elsayed, S. Tadier, A. Montembault, E. Maire, L. David, T. Delair, P. Colombo, L. Gremillard, Fabrication and characterization of hardystonite-chitosan biocomposite scaffolds, *Ceramics International* 45(7) (2019) 8804-8814.
- [50] U.K. Roopavath, S. Malferrari, A. Van Haver, F. Verstreken, S.N. Rath, D.M. Kalaskar, Optimization of extrusion based ceramic 3D printing process for complex bony designs, *Materials & Design* 162 (2019) 263-270.
- [51] Y. Ma, H. Dai, X. Huang, Y. Long, 3D printing of bioglass-reinforced β -TCP porous bioceramic scaffolds, *Journal of Materials Science* 54(14) (2019) 10437-10446.
- [52] Y. Fu, Z. Chen, G. Xu, Y. Wei, C. Lao, Preparation and stereolithography 3D printing of ultralight and ultrastrong ZrOC porous ceramics, *Journal of Alloys and Compounds* 789 (2019) 867-873.
- [53] H. Tian, Q.-s. Ma, Y. Pan, W.-d. Liu, Structure and mechanical properties of porous silicon oxycarbide ceramics derived from silicone resin with different filler content, *Ceramics International* 39(1) (2013) 71-74.
- [54] H. Tian, Q.-s. Ma, Effects of exterior gas pressure on the structure and properties of highly porous SiOC ceramics derived from silicone resin, *Materials Letters* 66(1) (2012) 13-15.
- [55] W. Huo, X. Zhang, Y. Chen, Z. Hu, D. Wang, J. Yang, Ultralight and high-strength bulk alumina/zirconia composite ceramic foams through direct foaming method, *Ceramics International* 45(1) (2019) 1464-1467.
- [56] J. Liu, H. Yang, B. Ren, Y. Rong, X. Xi, Y. Lu, Y. Zhao, J. Yang, Highly porous ZrO₂ cellular ceramics with 3D network architecture, *Ceramics International* 46(6) (2020) 7149-7154.
- [57] L. Hu, C.-A. Wang, Effect of sintering temperature on compressive strength of porous yttria-stabilized zirconia ceramics, *Ceramics International* 36(5) (2010) 1697-1701.
- [58] X. Hou, Z. Liu, Z. Liu, L. Yuan, J. Yu, Porous fibrous ZrO₂-mullite ceramics prepared via tert-butyl alcohol-based gel-casting, *Ceramics International* 44(12) (2018) 13580-13587.
- [59] Y. Zhang, Y. Wu, X. Yang, D. Li, X. Zhang, X. Dong, X. Yao, J. Liu, A. Guo, High-strength thermal insulating mullite nanofibrous porous ceramics, *Journal of the European Ceramic Society* 40(5) (2020) 2090-2096.
- [60] J. Qiao, Y. Wen, Mechanical and dielectric properties of porous magnesium aluminate (MgAl₂O₄) spinel ceramics fabricated by direct foaming-gelcasting, *Ceramics International* 46(2) (2020) 1442-1447.
- [61] Z. Hou, J. Liu, H. Du, H. Xu, A. Guo, M. Wang, Preparation of porous Y₂SiO₅ ceramics with relatively high compressive strength and ultra-low thermal conductivity by a TBA-based gel-casting method, *Ceramics International* 39(2) (2013) 969-976.
- [62] H. Xu, J. Liu, A. Guo, H. Du, Z. Hou, Porous silica ceramics with relatively high strength and novel bi-modal pore structure prepared by a TBA-based gel-casting method, *Ceramics International* 38(2) (2012) 1725-1729.
- [63] H. Jin, Z. Yang, D. Cai, D. Jia, Y. Zhou, 3D printing of porous Si₂N₂O ceramics based on strengthened green bodies fabricated via strong colloidal gel, *Materials & Design* 185 (2020) 108220.

- [64] C. Bai, G. Franchin, H. Elsayed, A. Conte, P. Colombo, High strength metakaolin-based geopolymer foams with variable macroporous structure, *Journal of the European Ceramic Society* 36(16) (2016) 4243-4249.
- [65] C. Vakifahmetoglu, T. Semerci, G.D. Soraru, Closed porosity ceramics and glasses, *J Am Ceram Soc* 103(5) (2020) 2941-2969.
- [66] R. Brezny, D.J. Green, The effect of cell size on the mechanical behavior of cellular materials, *Acta metallurgica et materialia* 38(12) (1990) 2517-2526.
- [67] L.J. Gibson, M.F. Ashby, *Cellular solids: structure and properties*, Cambridge university press 1999.
- [68] P. Colombo, J.R. Hellmann, D.L. Shelleman, Mechanical properties of silicon oxycarbide ceramic foams, *J Am Ceram Soc* 84(10) (2001) 2245-2251.

4 Embedded Direct Ink Writing of Freeform Ceramic Components

4.2 Introduction

Additive Manufacturing (AM) has drawn much attention for the design and development of advanced ceramic components for high-performance applications including biomedicine, tissue engineering, wearable electronics, energy storage etc. [1-4], due to its advantages such as fast speed, increasingly large printing envelope, near-net-shape, low cost and so on [5-8]. During recent years, several AM techniques have been developed, including selective laser sintering (SLS), binder jetting (BJ), vat photopolymerization (digital light processing - DLP, stereolithography appearance - SLA), extrusion-based printing (direct ink writing - DIW, fused deposition modeling - FDM) [9,10]. Among them, DIW has been an established fabrication method for ceramic components due to the combination of high resolution and the ability to form complex ceramics directly from colloidal building blocks [11,12]. Specifically, DIW processing involves extruding an ink from nozzles and assembling into 3D structures layer by layer followed by solidification resulting from gelation, evaporation of a solvent or cross-linking [13-15], without requiring a strict control on the chemical structure of the precursors and irradiation conditions, as in the case of photolithography, or the need to provide high laser absorption, as for SLS, or the ability to provide fast binding, as for binder jetting [16]. However, these days much more sophisticated and complex architectures are desired for the increasing requirements of advanced applications, such as geometries possessing large overhangs and filigree structures, which are difficult to fabricate without supports, since a very strict control on the rheology of the ink is necessary [17].

Embedded DIW (EDIW) is an emerging AM technique derived from DIW, constituting an alternative for printing suspended and complex architectures without individual supports which require post printing removal, involving the extrusion of inks

into a soft supporting medium while the nozzle moves along the designed printing paths[18,19]. Generally, the two sources of instability related to the retention or loss of shape of printed structures are the surface tension and gravity, leading to undesirable sagging and buckling of suspended features [20]. These instabilities could be eliminated by printing the structures inside a supporting medium possessing optimized rheological properties. To enable the processing, the supporting medium should exhibit an appropriately low yield stress τ_y , to allow for the easy movement of the printing nozzle, and a sufficiently high storage modulus G' for preventing the printed filament from sagging [18,21,22]. However, the printed filament features could be lost due to the stress generated by the nozzle movement, if the yield stress is too low. In addition, shear thinning behavior and rapid recovery of elasticity are required for eliminating the crevices created behind the moving nozzle. Furthermore, it's also important to take account of the chemical stability of interface between the ink and the supporting medium. Previous literature has reported several investigations concerning printing inks inside a soft supporting medium. Lewis et al. [22,23] fabricated microvascular networks and a stretchable strain sensor using multicomponent material systems containing a gel as supporting medium and a second fluid filler to fill the generated crevices. Tsao et al. [24] developed a self-healing emulsion glass as the supporting medium for DIW with the assistance of UV or thermal curing. Angelini et al. [20] created finely detailed multidimensional structures (e.g., vascular networks) composed of living cells using a gel containing microscale particles. Although all those investigations show the potential possibility to fabricate fine detailed structures inside soft supporting medium, strict requirements like UV light or the presence of secondary fillers complicate the processing and introduce uncontrollable factors. Meanwhile, only a recent investigation of EDIW of ceramic components can be found in the literature, in which the authors also used a preceramic polymer as the material constituting the ink but an additional thermal cross-linking step was required [16].

In our work, we propose an alternative method for the fabrication of complex and suspended ceramic structures using a supporting medium based on a gel comprised of vegetable oil and fumed silica. The prepared self-healing supporting medium and the preceramic polymer ink used as the ceramic source facilitate the easy fabrication of ceramic components without requiring UV (or thermal) solidification, or a second fluid filler. The rheological properties of the supporting medium were controlled and optimized by varying the content of fumed silica, aiming at retaining the structure features during printing and following pyrolysis. Moreover, the influence of printing speed and air pressure on the filament characteristics was investigated. To illustrate the ease and flexibility of this method, several complex structures with detailed features were fabricated, such as coils and a hollow cylinder. Besides using the preceramic as raw materials, we also demonstrated that ceramic and metal powder-based inks can be used with this supporting medium, therefore showcasing the great versatility of this approach for printing a variety of different materials.

4.3 Experimental

4.3.1 Materials

The supporting medium was composed of sunflower oil (Panorama, Pam, Italy) and hydrophobic fumed silica (Aerosil[®] 106, Evonik Industries AG, Germany) as thickening agent for adjusting the rheology of the supporting medium. A commercial polymethylsiloxane, SILRES[®] MK (Wacker-Chemie GmbH, München, Germany) was used as the starting material to obtain a SiOC ceramic. Geniosil GF91 (Wacker-Chemie GmbH, München, Germany) was used as the cross-linking agent for the preceramic polymer. Ti₂AlC (particle size ~ 12 μm, Beijing Tian Ma Zhi Hui Technology Co., Ltd., China), Al₂O₃ (particle size < 5 μm, Sigma -Aldrich, Merck KGaA, Darmstadt, Germany) and Ti (particle size <10 μm, TLS Technik GmbH & Co. Spezialpulver KG,

Germany) were selected for demonstrating the universality of this supporting medium. Polyvinyl butyral (PVB, 80%, 9.000–10.000 g/mol, Sigma-Aldrich, St. Louis, MO, USA) and Polyethylene glycol (PEG, 950–1.050 g/mol, Sigma-Aldrich, St. Louis, MO, USA) were used as binder agents for all powder-based inks.

4.3.2 Preparation of the supporting medium

The supporting medium was obtained by adding fumed silica into sunflower oil in different amounts (10, 13, 16, 19 wt%) followed by mixing for 10 minutes at 2000 rpm using a planetary mixer (ARE 250, Thinky, Japan) at room temperature.

4.3.3 Preparation of the inks

The preceramic ink was prepared by dissolving MK into isopropanol at a designed weight ratio in the range of 75 ~ 90 wt% followed by mixing for 15 mins at 2000 rpm using a planetary mixer (ARE-250, Thinky, Japan). Then, 2 wt% of Geniosil GF91, with respect to the weight of MK, was added into the solution mixing for 2 min at 2000 rpm. 0.1 wt % red dye (Squires Kitchen, England) was added for providing visibility to the printed structures. An ink containing Ti_2AlC was produced based on previous literature [25]. In brief, PVB and PEG were added into deionized water (water ratio PVB: PEG: deionized water = 3:2:4) followed by magnetic stirring at 60°C for 60 mins. Then, 81 wt% Ti_2AlC was added into the prepared binder solution followed by mixing for 15 minutes at 2000 rpm in a planetary mixer. Preparation of inks with Al_2O_3 and Ti powders shared the same procedure, except for the powder content which was 77 and 90 wt%, respectively. After transferring the ink into a syringe, the syringe was put in the mixer and defoamed by mixing at 600 rpm for 5 mins.

2.3. Printing inks into the supporting medium

A delta printer (2040 Turbo, Wasproject, Italy) was used to fabricate parts according to a CAD file. The printed coils were designed with a diameter of 8 mm and

different pitches (2, 2.5, 3, 4 mm). The ink was extruded into the supporting medium using a 400 μm nozzle (Nordson Italia, Milano, Italy), the nozzle movement speed was varied in the 0.5-20 mm/s range, and an air pressure of 0.05-0.6 MPa was applied. After cross-linking or solidification, the printed structures were extracted from the supporting medium and rinsed under running tap water.

4.3.4 Heating treatments

For printed coils produced from MK, pyrolysis was carried out in a tube furnace under nitrogen (99.99%) atmosphere at 1000°C for 2h, with a heating rate of 1°C/min. Cooling was carried out in the furnace, without controlling the rate. For Ti_2AlC and Ti spirals, sintering was carried out in flowing argon atmosphere for 4 h at 1400°C (with a heating rate of 2°C /min up to 600°C and of 3°C /min up to at 1400°C). For Al_2O_3 , sintering was carried out in muffle furnace in air, with heating rate of 4 h at 1400°C (with a heating rate of 2°C /min up to 600°C and of 3°C /min up to at 1400°C).

4.3.5 Characterization

A rotational rheometer (Discovery HR-1 hybrid rheometer, TA Instruments, UK) equipped with a 50 mm diameter plate-plate geometry, with a gap of 0.5 mm, was used. The shear rate interval was 0.01 ~ 200 s^{-1} , and the frequency was 1 Hz. The shear strain interval for the amplitude sweep test was 0.001 ~ 200%. The morphology of the printed structures, including the filament diameter, was characterized by optical stereomicroscopy (Stemi 2000-C, Carl Zeiss, Oberkochen, Germany) and scanning electron microscopy (FEI Quanta 200 ESEM, Eindhoven, The Netherlands).

4.4 Result and discussion

4.4.1 Rheological properties

The supporting medium was fabricated using fumed silica as the thickening agent,

due to its ability to form network structures based on intertwined chain-like assemblies of colloidal particles and oil when the percolation threshold is reached, generating a gel[26]. Conversion between breaking and rebuilding of the network structure occurs under the dynamic shear stress caused by the moving nozzle, allowing for the embedding and shape retention of the extruded ink filaments (see **Fig. 4.1a**). Using this developed supporting medium, we employed a preceramic polymer ink to build a suspended coil with a height of 2 cm in only a few seconds, a printing speed which is much faster than that of photolithography or binder jetting technologies (**Fig. 4.1b, c**).

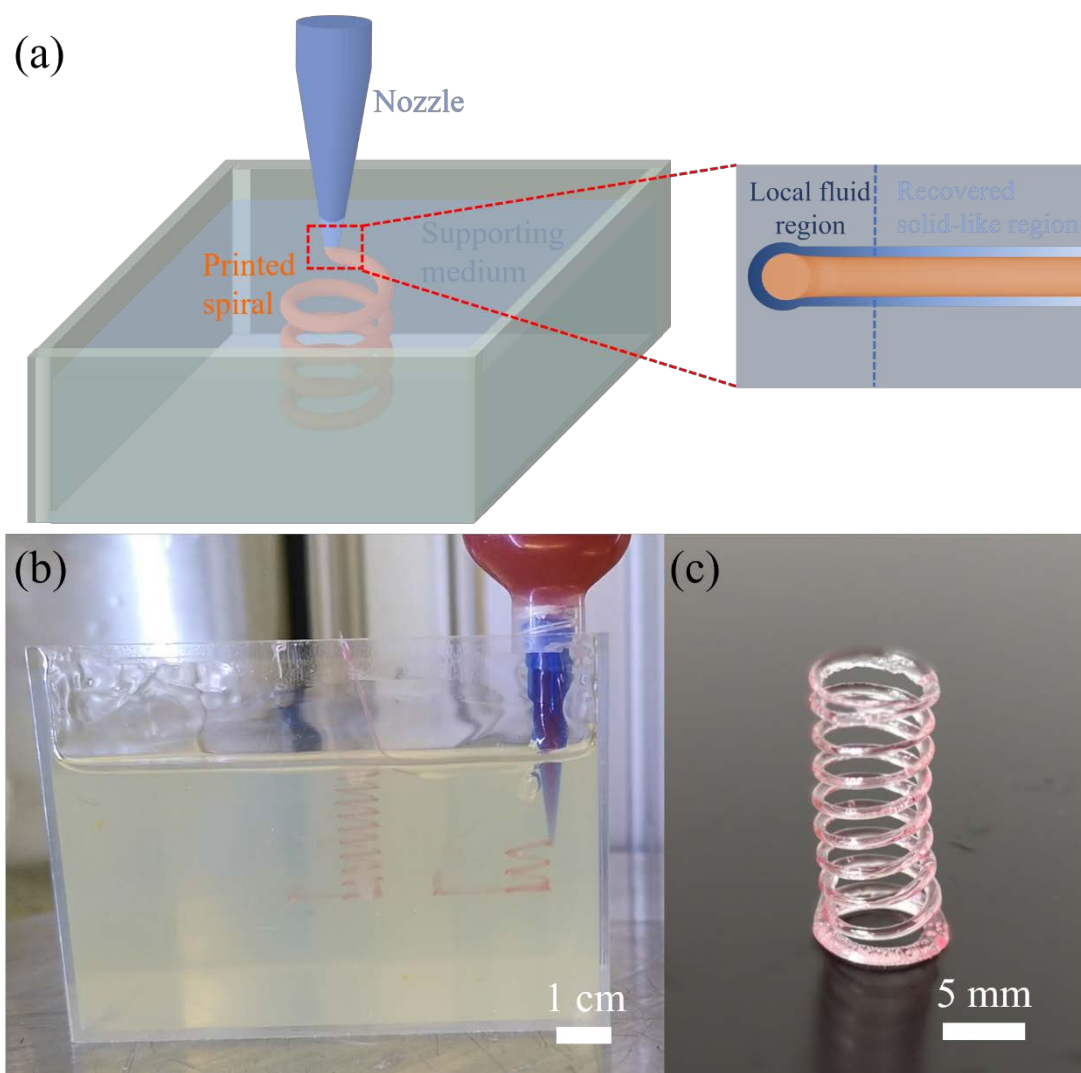


Fig. 4.1 (a) Schematic of embedded direct ink writing, (b) printing a coil into the supporting medium, (c) coil printed using a preceramic ink.

Rheological tests were carried on the supporting medium containing different contents of fumed silica (10, 13, 16, 19 wt%). **Fig. 4.2a** shows that all the supporting medium compositions displayed a shear thinning behavior, with viscosity decreasing at least two orders of magnitude when the shear rate increased from 0.01 to 102 s⁻¹ (~ 400 to 1 Pa·s, when considering the medium with 19 wt% of fumed silica). More viscous supporting media result from the higher content of fumed silica, as expected, due to the more interaction between the colloidal particles within the oil. Storage/loss modulus (G' / G'') curves as a function of the shear strain (**Fig. 4.2b**) displayed a linear viscoelastic region at lower shear strain, where G' was independent on the shear strain and higher than G'' , indicating that the system had a solid-like behavior [13,27]. Furthermore, the simple standard tube inversion test showed that no apparent flow occurred after inversely standing the vials for 1h, confirming the solid-like behavior of the supporting medium in the absence of shear stresses higher than the force of gravity itself (see **Fig. 4.3**)[24,28]. After the crossing point where G' is equal to G'' (where the shear stress is called yield stress τ_y), G' became lower than G'' and decreased rapidly because of the breaking of the gel network, indicating a that the system had liquid-like behavior. The transformation from solid to liquid confirmed that the supporting medium had the desired properties for performing EDIW. Furthermore, G' increased from 385.1 to 2131.4 Pa with the increasing content of fumed silica, providing a sufficiently high modulus to support the printed structures inside the medium. An appropriately low τ_y value, in the range of 8.1 ~ 33.7 Pa, assured the possibility of freely moving the printing nozzle and prevented the breaking up of the printed filament (details about G' and τ_y are summarized in **Tab. 4.1**). According to previous literature [29], a crevice forms only when the yield stress is larger than the hydrostatic pressure at a given depth h , described by $\tau_y \geq \rho gh$, where ρ is density of the supporting medium and g is the acceleration of gravity. Considering the rheological properties of the four supporting media developed

in this work, the minimum depth for achieving the formation of a crevice was 0.86, 1.36, 2.09 and 3.44 mm (ρ was 0.966, 0.983, 0.996, 1.001 g/cm³), respectively, which is quite easy to achieve.

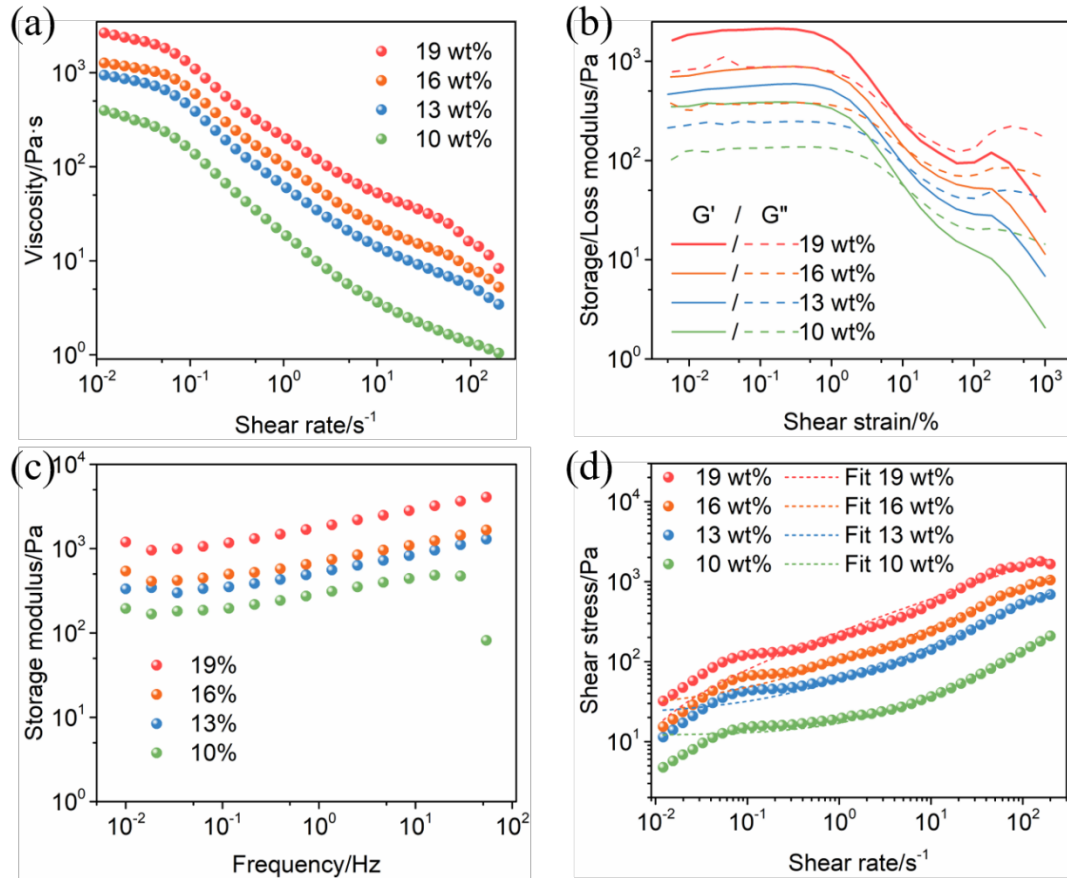
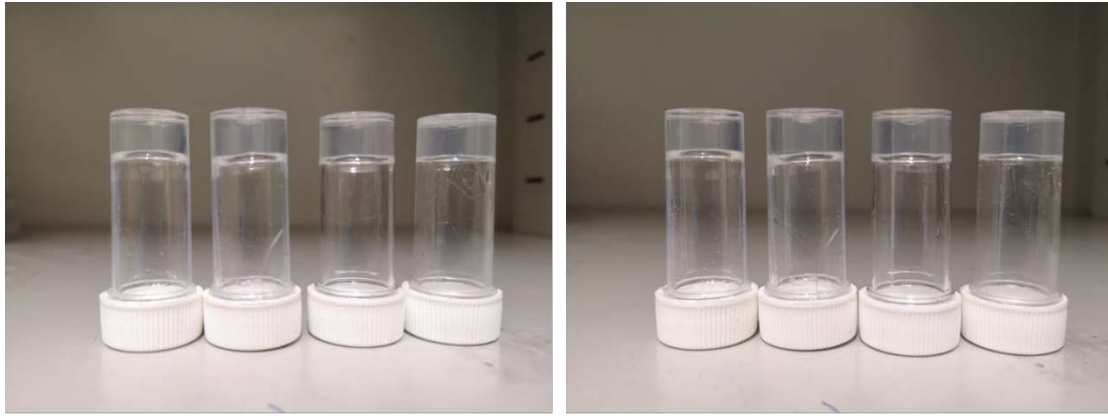


Fig. 4.2 Rheological tests for the supporting media with different contents of fumed silica: (a) viscosity vs shear rate, (b) storage/loss modulus (G' / G'') vs shear strain, (c) storage modulus vs frequency at 0.5% shear strain, (d) shear stress vs shear rate (dashed lines are the fitting curves from the Herschel–Bulkley model).



T = 0

T = 1h

Fig. 4.3 Tube inversion test.

Tab. 4.1 Experimental and fitting rheological parameters for the four different supporting media

Content (wt%)	Experimental			Fitting	
	G' (Pa)	τ_y (Pa)	τ'_y (Pa)	K	n
10	385.1	8.1	11.9	5.2	0.69
13	590.9	13.1	21.4	37.6	0.55
16	879.8	20.4	24.0	76.1	0.50
19	2131.4	33.7	30.7	265.5	0.38

Fig. 4.2c shows that in the frequency sweep test at 0.5% shear strain, G' displayed few changes when the frequency increased from 0.01 to 100 Hz, indicating that the supporting medium would remain stable during the printing procedure. For investigating the recovery time related to the supporting medium, a three intervals thixotropic test was performed (see **Fig. 4.4**). During the test, 0.1% ($\tau < \tau_y$) and 100% ($\tau > \tau_y$) shear strain was applied for 1 minute in the 1st and 2nd interval, then a 0.1% shear strain was applied for 3 minutes in the 3rd interval. The results show that G' increased immediately at the beginning of the 3rd interval, and became 5 ~ 10 times higher than G'' within 20 seconds, indicating the quick modulus recovery required for

holding in place the printed structures, enabling the retention of their shape.

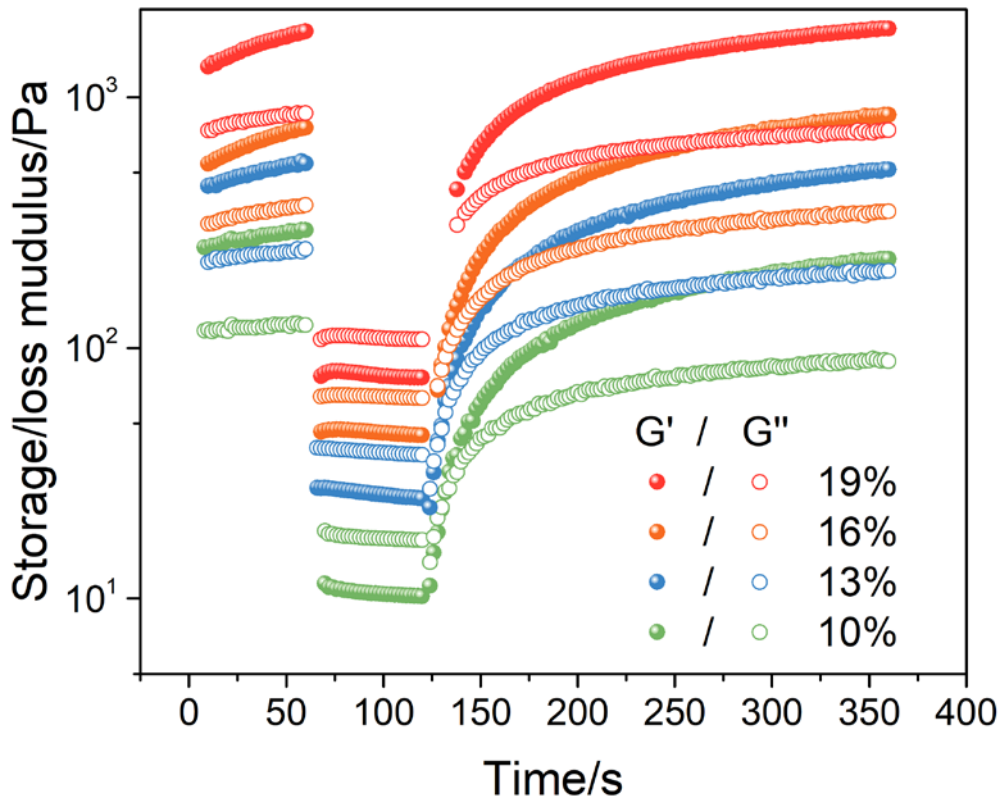


Fig. 4.4 Three intervals thixotropic test for supporting media with different contents of fumed silica. At a frequency of 1 Hz. 0.1% shear strain ($\tau < \tau_y$) was applied for 1 minute in the first phase and 100% shear strain ($\tau > \tau_y$) for 1 minute in the second phase. Then 0.1% shear strain was applied for 3 minutes in the third phase.

To describe the shear thinning behavior of the ink flowing from the printing nozzle under pressure, the Herschel–Bulkley model was adopted [27]:

$$\tau = \tau_y + K\dot{\gamma}^n$$

where τ is the shear stress, τ_y is yield stress, $\dot{\gamma}$ is shear rate, K is a viscosity parameter and n ($n < 1$) is the shear thinning exponent. The shear stress-shear rate curves and the corresponding fitting curves according to the above equation are reported in **Fig. 4.2d**. All the fitting parameters from fitting are listed in **Tab. 4.1.**, and the R^2 correlation coefficient was 0.998, 0.995, 0.994 and 0.974 for the supporting media

containing either 10, 13, 16 or 19 wt% of fumed silica, respectively. We can observe that the experimental results were fitted quite well by the chosen theoretical model, with τ'_y values from the fitting quite close to the experimental ones τ_y except for the deviation at low $\dot{\gamma}$ values in the $10^{-2} \sim 10^{-1} \text{ s}^{-1}$ range, where near Newtonian behavior dominates [30]. The value for n was smaller than 1 for all the supporting media, confirming that they possessed a shear thinning behavior. Increasing K values with increasing content of fumed silica indicates an increase of the viscosity of the supporting media, in agreement with the results shown in **Fig. 4.2a**. Concerning the flow of a fluid caused by the traveling of a nozzle within it, the Oldroyd number (Od) and Reynolds number (Re) were calculated (see) (see **Tab. 4.2**) according to previous literature[18,31,32], in order to further assess the effect of the fluid on the retention of the main features of the printed structures. Od is defined as the ratio of the yield stress to viscous stresses, providing the dimension of the yield region around the nozzle and Re is the ratio of inertial to viscous forces. The Od number increased with the decreasing of content of fumed silica, leading to a smaller yield region around the nozzle (which is limited to 3~4 times the nozzle diameter under a similar Od number) and increasing the geometrical precision of the printed features.[18] The Re number likewise decreased with increasing the content of fumed silica, but it was quite small for all the media indicating stable flow conditions with few disturbances affecting the printed structures.

Tab. 4.2 Summary of Od and Re numbers for the four supporting media.

SiO ₂ content/ wt %	10	13	16	19
Od	1.48	0.40	0.23	0.09
Re	6.72×10^{-2}	1.05×10^{-2}	5.37×10^{-3}	1.6×10^{-3}

4.4.2 Ink printability and control of the filament diameter in different supporting media

When investigating the printability of an ink, we need to consider two key factors concerning the embedded DIW process, that is: a) facile extrusion of the paste from the nozzle and b) stable retention of the printed material within the supporting medium. Therefore, we report the results concerning the relationship between the amount of MK in the preceramic ink and the content of fumed silica in the supporting medium (see **Fig. 4.5**). When the amount of fumed silica was too low (< 8 wt%), the medium was not able to provide enough support to the extruded material, leading to the sinking and loss of shape of the printed structure (**Fig. 4.6a**). When the fumed silica content was too high (≥ 21 wt%), the nozzle had difficulties in moving inside the supporting medium. When using a 400 μm nozzle and a maximum air pressure of 0.6 MPa, an amount of MK in the ink higher than 90 wt% resulted in clogging. Inks with a MK content lower than 75 wt% were too liquid to be printed into a continuous filament. Furthermore, unstable printing tended to occur when there was a large difference between the amount of MK in the ink and the amount of fumed silica in the supporting medium (region 1 and 3 in **Fig. 4.5**, see later). In region 1, where ink with higher MK content and supporting medium with low fumed silica amount were used, the printed filament would be dragged by the moving nozzle, due to the relatively low yield stress of the supporting medium, leading to a much smaller coil (**Fig. 4.6b**) than the one fabricated using a combination of MK and fumed silica content within the region 2, corresponding to the conditions of good printability (**Fig. 4.6c**). In region 3, the printed filament assumed a distorted, ribbon-like shape (**Fig. 4.6d**) instead of maintaining the desired cylindrical cross-section, due to the relatively high storage modulus of the supporting medium containing a large amount of fumed silica, generating additional stresses within the printed material.

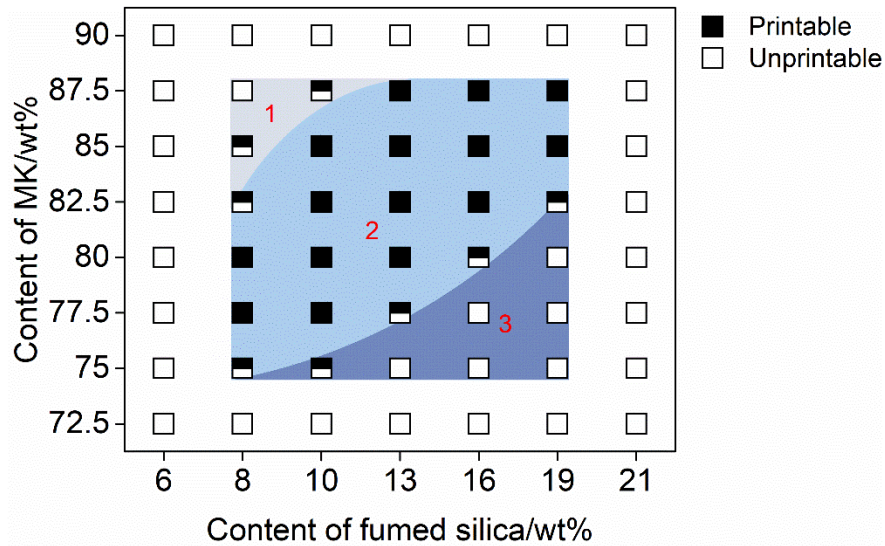


Fig. 4.5 Printability as the function of the content of MK in the of the preceramic ink and of fumed silica in the supporting medium.

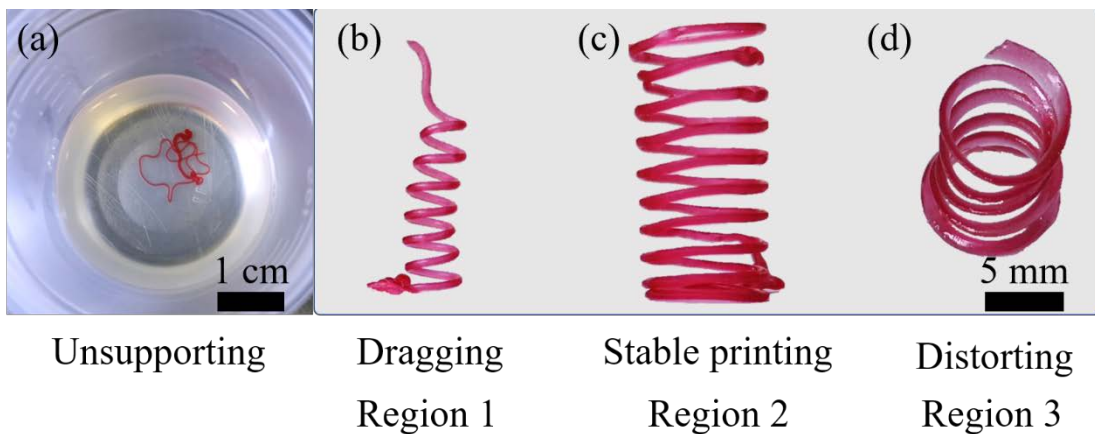


Fig. 4.6 Example of printability/not printability for different ink/supporting medium combinations: (a) unsupporting medium, (b) filament dragging, (c) stable printing, (d) distorted filament shape.

When performing EDIW, the diameter of the printed filament could be affected by the pressure and the nozzle movement speed, as well as the rheological characteristics of the supporting medium and of the ink. Therefore, for a given preceramic ink with a MK content of 85 wt%, we performed tests varying the dynamic pressure and the nozzle

movement speed when carrying out printing into supporting media with four different amounts of fumed silica. Considering the shape distortion when printing in a supporting medium with higher content of fumed silica, the diameter values here reported are representative only of the lateral dimension of the filament. In **Fig. 4.7** the data are reported according to 2D contour plots, in which color represents the filament diameter. The selected an ink with the MK content specified above because it was printable in all the tested supporting media. Considering the results for the samples manufactured in the supporting medium containing 10 wt% of fumed silica (**Fig. 4.7a**), the filaments tend to be larger than the nozzle diameter when printed at high pressure and lower speed, and a similar situation occurs also when processing in the other supporting media (**Fig. 4.7b-d**). We can observe that the filament diameter is less dependent on the nozzle movement speed at lower pressure in the 10 wt% silica supporting medium. However, that dependence becomes much more significant when increasing the content of fumed silica from 13 to 19 wt%, which can be attributed to the larger drag produced by the more viscous surrounding media. In the region of higher pressure (> 0.25 MPa) and speed (> 12 mm/s), the filament diameter shows few changes with respect to the nozzle diameter when printing in all supporting media. To conclude, the content of fumed silica shows a significant effect on the filament diameter: at higher contents it leads to the shifting of the suitable printing region, where the filament diameter is equal to the target diameter $400\ \mu\text{m}$ (light blue region), towards higher gas pressure and lower printing speed. Therefore, controlling the filament diameter when printing in different supporting media is possible by optimizing the gas pressure and the nozzle movement speed.

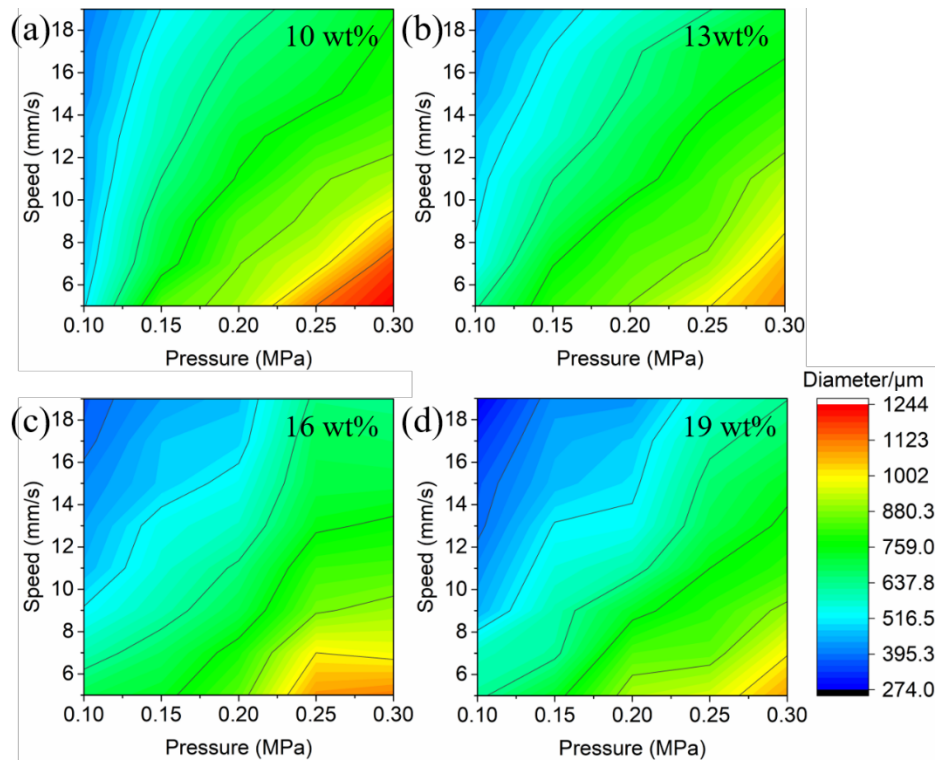


Fig. 4.7 Influence of pressure and nozzle movement speed on the diameter of filaments (before pyrolysis) printed in supporting media with different content of fumed silica: (a-d) 10, 13, 16, 19 wt%, respectively. A 400 μm nozzle was used in the test.

In addition, we can observe that the aspect ratio of the cross-section of a filament was stable and close to 1 (i.e., circular cross-section) when printing was carried out in the 10 wt% supporting medium, while it tended to increase with increasing fumed silica content (**Fig. 4.8**), indicating that the filament would become distorted if printed in a much more viscous supporting medium, since the medium applies a higher resistance to the filament during printing. Therefore, according to our findings, it is better to select a supporting medium containing relatively less fumed silica in order to maintain the target cylindrical shape of the printed filament.

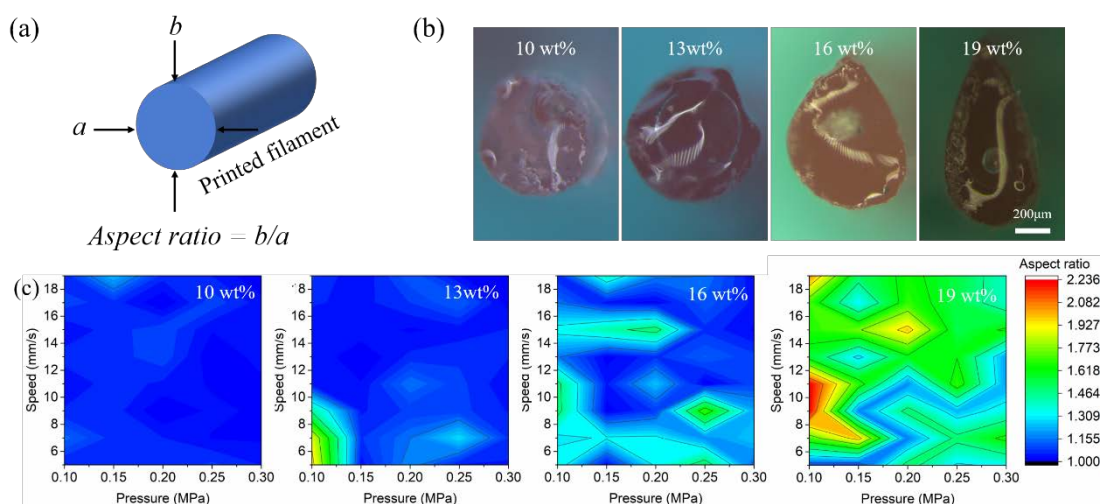


Fig. 4.8 (a) filament aspect ratio definition; (b) representative images of filament cross-section in four supporting media (pressure: 0.15 MPa, moving speed: 7 mm/s; (c) 2D contour plots of aspect ratio of filament cross-section under different pressure and moving speed.

4.4.3 Embedded DIW

When using the supporting medium with 10 wt% of fumed silica, suspended coils were fabricated in an efficient and facile way, as shown in **Fig. 4.9**. Several coils were printed within the same supporting medium (**Fig. 4.9a, b**), stably standing separate without sinking or sagging. **Fig. 4.9c** shows that an Archimedes screw with the base of coil (with diameter of 4 mm and length of 2 cm) printed in vertical direction could maintain the shape very well after extraction from the supporting medium. Coils with different pitches (2, 2.5, 3, 4 mm) (**Fig. 4.9d**) were fabricated, to further explore the stability of printed structures inside the supporting medium. Measurement of the coil pitches after printing (**Fig. 4.10**) indicates a high degree of retention (95~99%) with respect to the designed ones, confirming the high stability and accuracy achievable with this DIW method. The coils displayed a linear shrinkage of ~25% in the vertical direction, after pyrolysis, preserving the original shape without observing the presence

of any cracks. However, **Fig. 4.9e** shows some distortions due to inhomogeneous shrinkage deriving from the irregular suspended shape; the use of supports during pyrolysis might enable improving the shape retention during heating. **Fig. 6** shows the microstructure of the surface and cross-section of a pyrolyzed coil. We can point out that, differently from the layered surface structures typically observed in parts printed by DLP/SLS (stair stepping effect), the surface of samples fabricated by embedded DIW is smoother, potentially leading to higher strength for the components due to a reduction of the surface flaws (**Fig. 4.11a**) [33]. A dense, pore and crack-free filament cross-section can be seen in **Fig. 4.11b**, demonstrating that no macro-defects were introduced into the filament during the printing procedure.

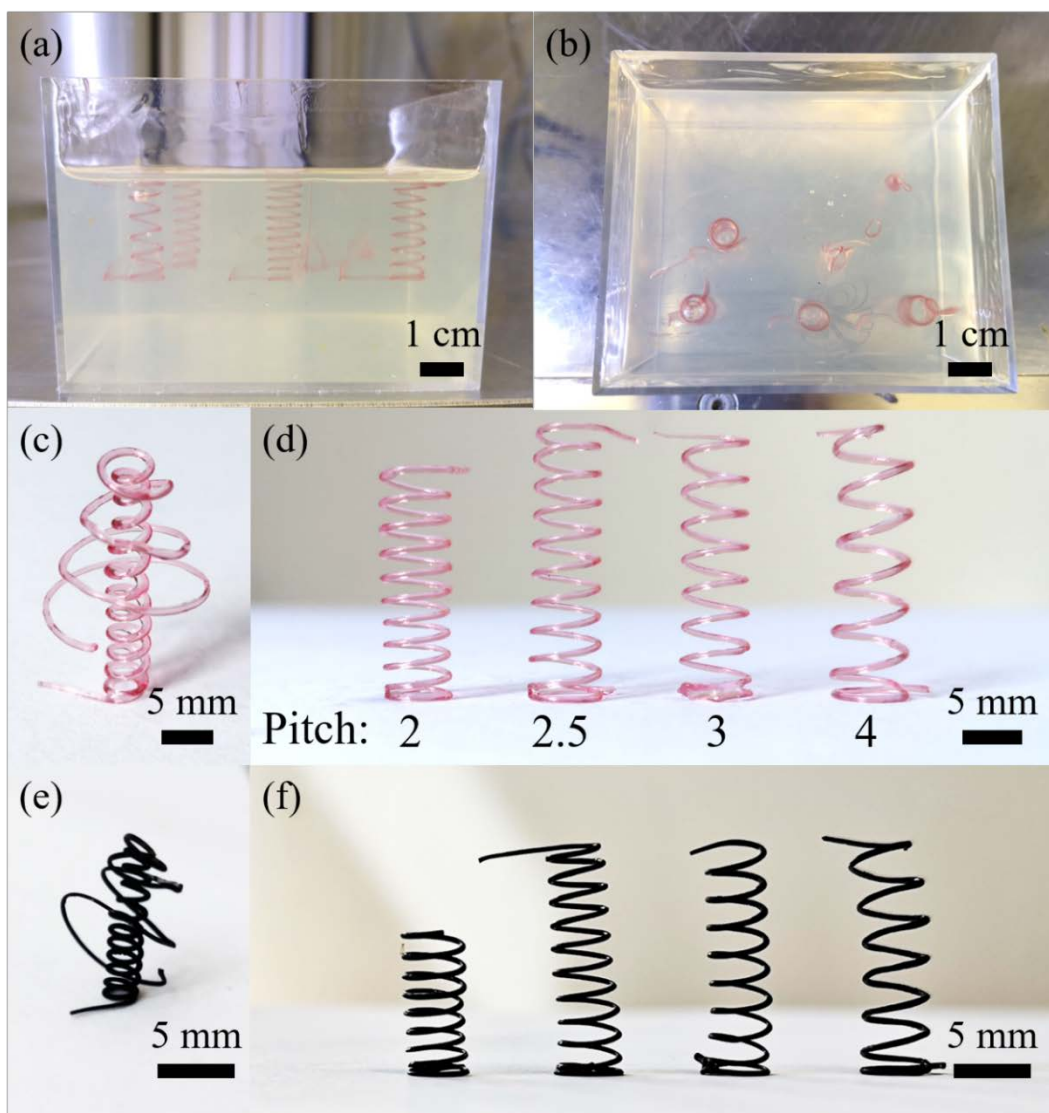


Fig. 4.9 Digital images of supporting medium (10 wt% fumed silica) with printed coils: (a) front view, (b) top view; (c) printed Archimedes screw and (d) coils with different pitches (2, 2.5, 3, 4 mm, respectively); (e, f) pyrolyzed samples.

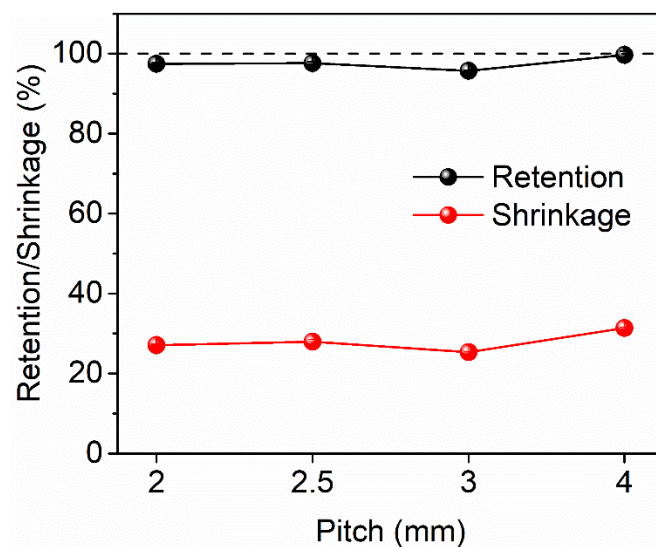


Fig. 4.10 Retention (before pyrolysis) and shrinkage (after pyrolysis) of coil pitches.

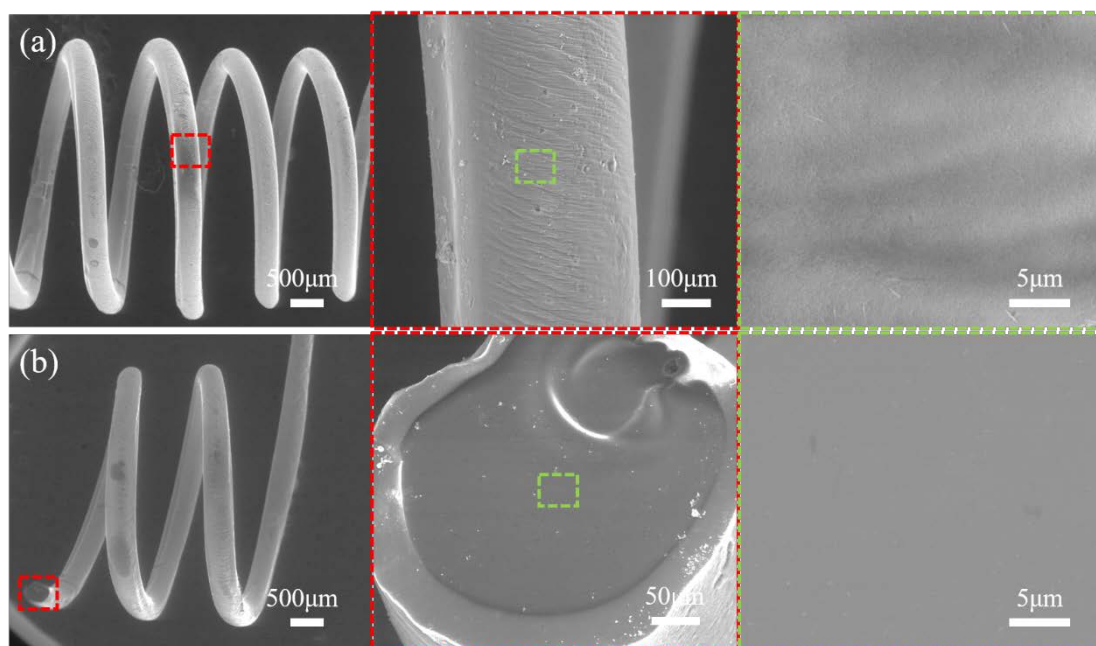


Fig. 4.11 Microstructure of the surface (a) and cross-section (b) of a coil (after pyrolysis).

To further characterize the ability of the supporting medium to sustain filaments printed in very different directions, a sagging test was carried out by printing 2 cm long individual filaments at different angles inside the medium containing 10 wt% of fumed silica (**Fig. 4.12**). We can observe that no sagging can be detected and all the filaments

remained suspended at the correct designed angles, even with the large length-to-diameter ratio of 50, demonstrating the possibility of fabricating structures with very long spanning features (note: the lines that can be seen in **Fig. 4.12** protruding from the end of the printed filaments - where the blue arrows end – are due to fact that the adopted printing system does not allow for an immediate stop of flow, and therefore some material was further extruded from the nozzle after ending the individual filament print job).

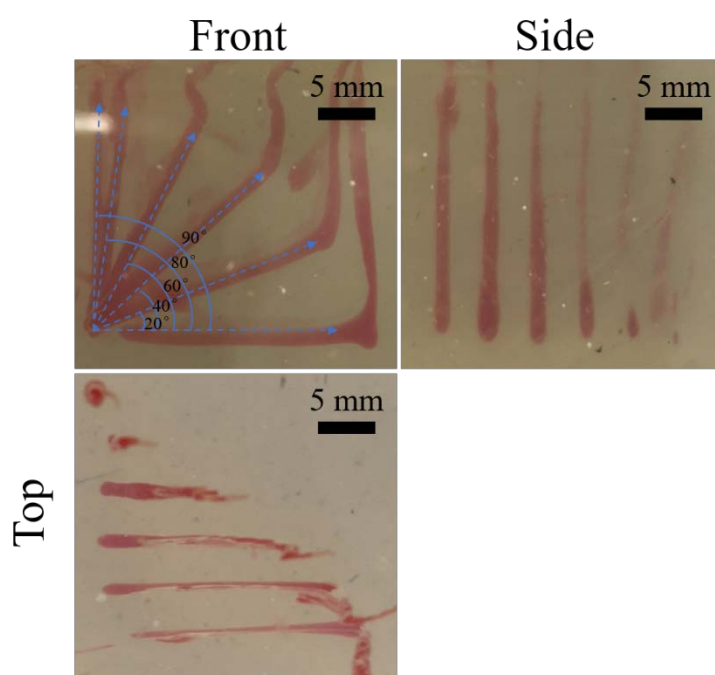


Fig. 4.12 Sagging test for filaments (with a length of 2 cm) printed at different angles: 0, 20, 40, 60, 80, 90°. Images from different views.

To further demonstrate the flexibility of this method, other complex structures were fabricated, possessing such suspended structures that would be very difficult to print using the normal DIW approach, without a very strict and complex control of the ink rheology (in particular, the recovery time of the initial high viscosity after extrusion from the nozzle should be extremely small). 3D letters reading “UNIPD” were printed by designing a continuous path along different direction (**Fig. 4.13a**), proving the

possibility of omnidirectional freeform printing using this approach. A little distortion in the fabricated structures occurred due to the dragging of the ink during traveling of the nozzle from one position to the next. This is caused by the use of a manually operated on-off gas pressurized system, and can be improved by using a precision automatic valve. A hollow cylinder composed of circles and wave-like curves was printed as well (**Fig. 4.13b**), showing no deformation and a very good degree of shape retention in comparison to the design after both printing and pyrolysis.

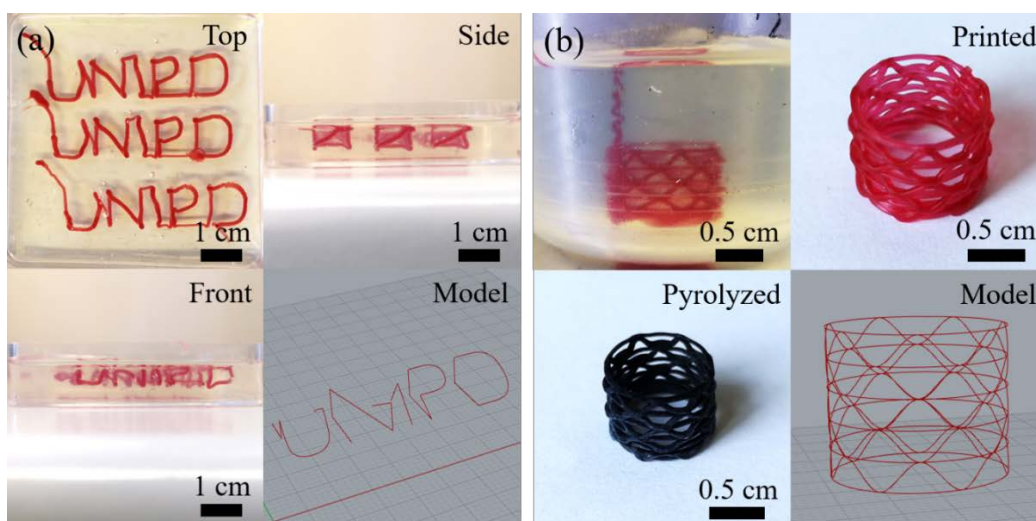


Fig. 4.13 3D model and printed parts: (a) “UNIPD” letters; (b) hollow cylinder with structured walls ($\Phi 12 \times 10$ mm) before and after pyrolysis.

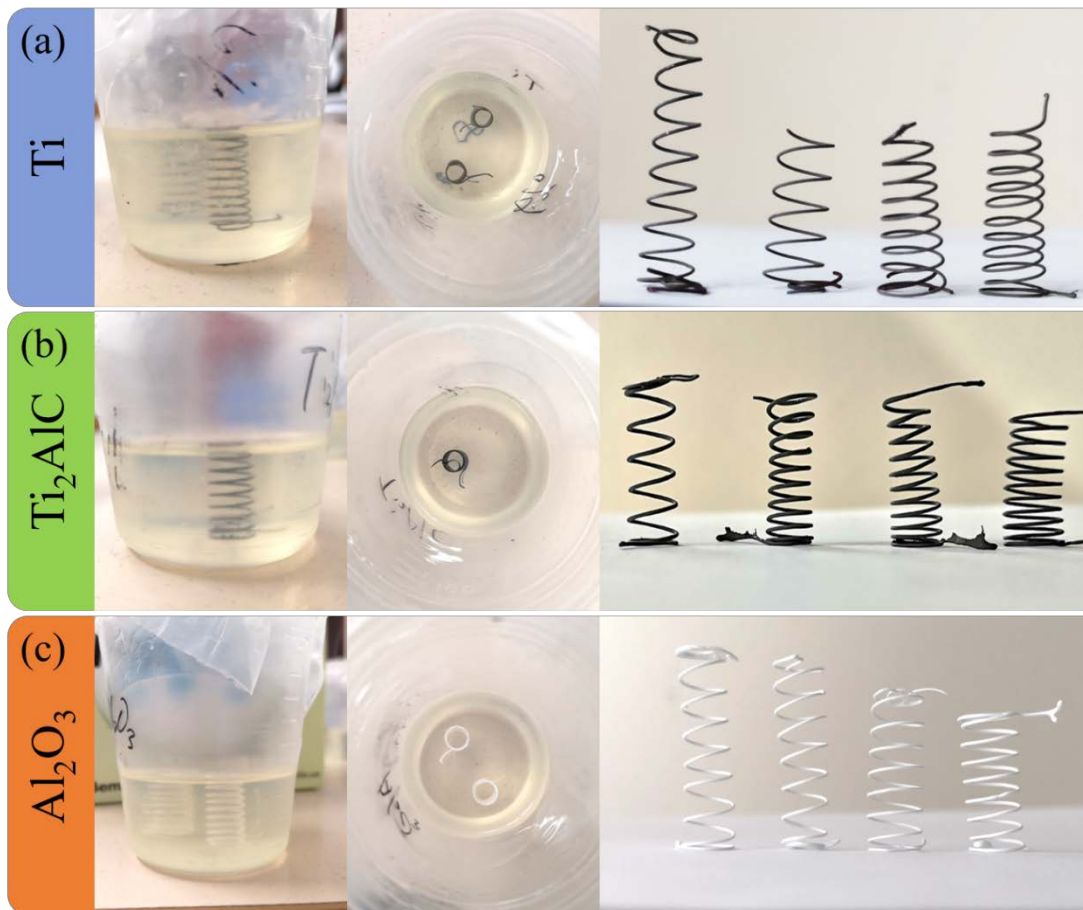


Fig. 4.14 Printing with inks composed of metal or ceramic powders (before sintering):
 (a) Ti, (b) Ti_2AlC , (c) Al_2O_3 .

Besides basing most of our experiments on the printing of a preceramic ink, we wanted to demonstrate that the EDIW approach could be successfully applied to the fabrication of complex structures made of other materials. Therefore, we printed inks based on three different powders, namely Ti, Ti_2AlC and Al_2O_3 , using a supporting medium containing 10 wt% of fumed silica. Similarly to when printing the pure preceramic ink, coils with different pitches were able to stand freely in the supporting medium, showing no sagging nor deformation after extraction (see **Fig. 4.14a-c**; sample). The possibility of free-forming different materials, such as preceramic polymers, metal and ceramic powders, into components with complex and suspended architectures greatly extends the applicability of DIW for the fabrication of structures

with advanced geometrical features, previously precluded to this printing technology, suitable for a wide range of specialty applications.

4.5 Conclusions

In summary, the fabrication of preceramic polymers into components with complex and suspended structures was achieved by embedded DIW using a supporting medium composed of vegetable oil and fumed silica. Printability was investigated as a function of the content of the preceramic polymer in the ink and of the fumed silica in the supporting medium, and the rheological tests enabled to assess the range of yield stress and modulus values for system that were suitable for printing the chosen ink. The investigation of the printing parameters indicated that gas pressure and nozzle movement speed have a great impact on the diameter of the printed filaments, which is much more significant when increasing the content of fumed silica in the supporting medium. Complex freeform structures, such as coils, 3D letters and hollow cylinders with structured walls, not printable using only DIW, were fabricated without sagging or other deformations, possessing high quality surfaces and dense, defect-free cross-sections, after pyrolysis. Last but not least, successful printing of inks based on metal and ceramic powders into suspended structures was achieved, demonstrating that embedded DIW is a highly versatile method that can be used with materials possessing different characteristics, such as density. This work may offer a promising opportunity for fabricating sophisticated structures in fields such as tissue engineering, biomedicine, electronic device and so on, significantly extending the range of applicability of the DIW additive manufacturing approach to the fabrication of components with complex architectures.

4.6 References

- [1] I. Nabipour, The future of 3D printing technology in biomedicine, (2015).
- [2] S. Bose, S. Vahabzadeh, A. Bandyopadhyay, Bone tissue engineering using 3D printing, *Materials today* 16(12) (2013) 496-504.
- [3] S. Coppola, G. Nasti, M. Todino, F. Olivieri, V. Vespini, P. Ferraro, Direct writing of microfluidic footpaths by pyro-EHD printing, *ACS Applied Materials & Interfaces* 9(19) (2017) 16488-16494.
- [4] F. Zhang, M. Wei, V.V. Viswanathan, B. Swart, Y. Shao, G. Wu, C. Zhou, 3D printing technologies for electrochemical energy storage, *Nano Energy* 40 (2017) 418-431.
- [5] N. Travitzky, A. Bonet, B. Dermeik, T. Fey, I. Filbert-Demut, L. Schlier, T. Schlordt, P. Greil, Additive manufacturing of ceramic-based materials, *Adv Eng Mater* 16(6) (2014) 729-754.
- [6] Z.C. Eckel, C.Y. Zhou, J.H. Martin, A.J. Jacobsen, W.B. Carter, T.A. Schaedler, 3D PRINTING Additive manufacturing of polymer-derived ceramics, *Science* 351(6268) (2016) 58-62.
- [7] P. Colombo, J. Schmidt, G. Franchin, A. Zocca, J. Günster, Additive manufacturing techniques for fabricating complex ceramic components from preceramic polymers, *Am. Ceram. Soc. Bull* 96(3) (2017) 16-23.
- [8] N. Guo, M.C. Leu, Additive manufacturing: technology, applications and research needs, *Frontiers of Mechanical Engineering* 8(3) (2013) 215-243.
- [9] A. Zocca, P. Colombo, C.M. Gomes, J. Günster, Additive manufacturing of ceramics: issues, potentialities, and opportunities, *J Am Ceram Soc* 98(7) (2015) 1983-2001.
- [10] J. Deckers, J. Vleugels, J.-P. Kruth, Additive manufacturing of ceramics: a review, *Journal of Ceramic Science and Technology* 5(4) (2014) 245-260.
- [11] J.A. Lewis, J.E. Smay, J. Stuecker, J. Cesarano, Direct ink writing of three-dimensional ceramic structures, *J Am Ceram Soc* 89(12) (2006) 3599-3609.
- [12] H. Elsayed, P. Colombo, E. Bernardo, Direct ink writing of wollastonite-diopside glass-ceramic scaffolds from a silicone resin and engineered fillers, *Journal of the European Ceramic Society* 37(13) (2017) 4187-4195.
- [13] J.E. Smay, G.M. Gratson, R.F. Shepherd, J. Cesarano, J.A. Lewis, Directed colloidal assembly of 3D periodic structures, *Adv Mater* 14(18) (2002) 1279-1283.
- [14] R.L. Walton, M.A. Fanton, R.J. Meyer Jr, G.L. Messing, Dispersion and rheology for direct writing lead-based piezoelectric ceramic pastes with anisotropic template particles, *J Am Ceram Soc* 103(11) (2020) 6157-6168.
- [15] A.L. Troksa, H.V. Eshelman, S. Chandrasekaran, N. Rodriguez, S. Ruelas, E.B. Duoss, J.P. Kelly, M.R. Cerón, P.G. Campbell, 3D-printed nanoporous ceramics: Tunable feedstock for direct ink write and projection microstereolithography, *Materials & Design* 198 (2021) 109337.
- [16] M. Mahmoudi, C. Wang, S. Moreno, S.R. Burlison, D. Alatalo, F. Hassanipour, S.E. Smith, M. Naraghi, M. Minary-Jolandan, Three-Dimensional Printing of Ceramics through "Carving" a Gel and "Filling in" the Precursor Polymer, *ACS Appl Mater Interfaces* (2020).
- [17] G. Li, S. Tang, L. Yang, L. Qian, F. Liu, Z. Fan, K. Zuo, Q. Wei, W. Jiang, Fabrication of soluble salt-based support for suspended ceramic structure by layered extrusion forming method, *Materials & Design* 183 (2019) 108173.

- [18] A.K. Grosskopf, R.L. Truby, H. Kim, A. Perazzo, J.A. Lewis, H.A. Stone, Viscoplastic Matrix Materials for Embedded 3D Printing, *ACS Applied Materials & Interfaces* 10(27) (2018) 23353-23361.
- [19] T.J. Hinton, A. Hudson, K. Pusch, A. Lee, A.W. Feinberg, 3D Printing PDMS Elastomer in a Hydrophilic Support Bath via Freeform Reversible Embedding, *ACS Biomater Sci Eng* 2(10) (2016) 1781-1786.
- [20] T. Bhattacharjee, S.M. Zehnder, K.G. Rowe, S. Jain, R.M. Nixon, W.G. Sawyer, T.E. Angelini, Writing in the granular gel medium, *Sci Adv* 1(8) (2015) e1500655.
- [21] R.L. Truby, J.A. Lewis, Printing soft matter in three dimensions, *Nature* 540(7633) (2016) 371-378.
- [22] J.T. Muth, D.M. Vogt, R.L. Truby, Y. Menguc, D.B. Kolesky, R.J. Wood, J.A. Lewis, Embedded 3D printing of strain sensors within highly stretchable elastomers, *Adv Mater* 26(36) (2014) 6307-12.
- [23] W. Wu, A. DeConinck, J.A. Lewis, Omnidirectional printing of 3D microvascular networks, *Adv Healthc Mater* 23(24) (2011) H178-H183.
- [24] S.W. Hu, P.J. Sung, T.P. Nguyen, Y.J. Sheng, H.K. Tsao, UV-Resistant Self-Healing Emulsion Glass as a New Liquid-like Solid Material for 3D Printing, *ACS Appl Mater Interfaces* (2020).
- [25] H. Elsayed, A. Chmielarz, M. Potoczek, T. Fey, P. Colombo, Direct ink writing of three dimensional Ti₂AlC porous structures, *Additive Manufacturing* 28 (2019) 365-372.
- [26] F. Ehrburger, V. Guérin, J. Lahaye, Phenomenological study of gelification of liquids by pyrogenic silicas, *Colloids and surfaces* 9(4) (1984) 371-383.
- [27] J.E. Smay, J. Cesarano, J.A. Lewis, Colloidal inks for directed assembly of 3-D periodic structures, *Langmuir* 18(14) (2002) 5429-5437.
- [28] M. George, R.G. Weiss, Low molecular-mass organic gelators, *Molecular Gels*, Springer 2006, pp. 449-551.
- [29] C.S. O'Bryan, T. Bhattacharjee, S.R. Niemi, S. Balachandar, N. Baldwin, S.T. Ellison, C.R. Taylor, W.G. Sawyer, T.E. Angelini, Three-dimensional printing with sacrificial materials for soft matter manufacturing, *MRS bulletin* 42(8) (2017) 571-577.
- [30] D.V. Boger, Demonstration of upper and lower Newtonian fluid behaviour in a pseudoplastic fluid, *Nature* 265(5590) (1977) 126-128.
- [31] D.L. Tokpavi, A. Magnin, P. Jay, Very slow flow of Bingham viscoplastic fluid around a circular cylinder, *Journal of Non-Newtonian Fluid Mechanics* 154(1) (2008) 65-76.
- [32] B. Deglo De Besses, A. Magnin, P. Jay, Viscoplastic flow around a cylinder in an infinite medium, *Journal of Non-Newtonian Fluid Mechanics* 115(1) (2003) 27-49.
- [33] C. Paredes, F.J. Martínez-Vázquez, H. Elsayed, P. Colombo, A. Pajares, P. Miranda, Evaluation of direct light processing for the fabrication of bioactive ceramic scaffolds: Effect of pore/strut size on manufacturability and mechanical performance, *Journal of the European Ceramic Society* 41(1) 892-900.

5 Concluding remarks and future perspectives

This work was performed focusing on three aspects of the fabrication of PDC-based components with DIW: (I) inks based on different preceramic polymers, (II) DIW assisted by other techniques, (III) investigation of structure-dependent relationships.

For the first aspect, in this work we used two different preceramic polymers: MK and PDMS, both of which show high ceramic yield (MK: 80.32 wt%, PDMS: 72.5 wt%). The difference between them is that the crosslinked green body of MK is rigid while that of PDMS is flexible. Therefore, MK were applied in embedded DIW for suspended structure while the flexibility of PDMS enabled the secondary shaping processes after printing toward further sophisticated ceramic architectures.

For the second aspect, to address the limitation of DIW towards the fabrication of complex ceramic structures (including macro and micro structures), other techniques (origami, robotic arm, supporting bath and sacrificial template) were used for fabricating SiOC structures, such as sharply curved and twisted ones, cylindrical lattices, suspended and highly spanning structures, hierarchically porous architectures.

For the third aspect, after the study on how to enable printing of a wide range of shapes, we investigated the dependence of selected properties on the printed structure, including mechanical properties and air permeability and demonstrating the possibility of performance enhancement by optimization of the architecture of the component without reducing its porosity.

An interesting future possibility is studying multi-materials component system by Embedded Ink Writing. With the evolution of technology, it's often desirable to develop multi-functional components and devices comprised of multi-materials to meet the increasing requirements. Additive manufacturing of multi-materials would be a great candidate to integrate various properties (such as mechanical, electrical and chemical properties, etc.) into individual components, with a wide range of applications. As mentioned in the section "Embedded Direct Ink Writing of Freeform Ceramic

Components”, we successfully printed suspended structures not only from a preceramic polymer but also using inks based on metal and ceramic powders. As long as coupled with multi-nozzle system, it would be feasible to achieve sophisticated multi-materials component (e.g. composites of ceramic and metal) in a fast and cost-efficient way. It’s a promising strategy for the fabrication of multi-material systems, though there are some issues that will need to be addressed, such as the interfacial bonding and post heating treatment.

Another interesting study could be DIW of a sacrificial material (e.g., water or oil) into a solution of preceramic polymer to achieve the design of an internal structure within a ceramic component, with potential application in porous ceramic and microfluidics. Being opposite to the embedded DIW approach mentioned in the part “Summary of results”, where printing is performed by extruding a preceramic polymer into a soft supporting medium, printing inside a preceramic polymer solution would allow for the drawing of internal continuous pore structures, especially for ordered hierarchical porous ceramic parts (although we fabricated hierarchical porous structures with assistance of sacrificial template PMMA, the arrangement of pores is still stochastic). In addition, PDCs have a high potential in microfluids, due to their superior chemical and thermal stability, and the flexibility and free-form design of an internal channel structure provided by “carving inside preceramic polymer” would be worth exploring. By modification of the sacrificial template or of the preceramic polymer solution and additives, it should be possible to retain the hollow structures inside a solution of preceramic polymer after printing and solidification.

Curriculum Vitae

Education:

10/2018-present

Ph.D. - Department of Industrial Engineering, University of Padova, Italy

09/2016-/07/2018

M.S. - Shanghai Institute of Ceramic, Chinese Academy of Science (SICCAS), China

09/2015-/07/2016

M.S. - University of Science and Technology of China, China

09/2011-07/2015

B.S. - Changchun University of Science and Technology, China

List of publications related to this thesis

- [1] **K. Huang**, H. Elsayed, G. Franchin, P. Colombo, Additive manufacturing of SiOC scaffolds with tunable structure-performance relationship, *Journal of the European Ceramic Society* (in press)
- [2] **K. Huang**, H. Elsayed, G. Franchin, P. Colombo, Embedded direct ink writing of freeform ceramic components, *Applied Materials Today* 23 (2021) 101005.
- [3] **K. Huang**, H. Elsayed, G. Franchin, P. Colombo, 3D printing of Polymer-Derived SiOC with Hierarchical and Tunable Porosity, *Additive Manufacturing* 36 (2020) 101549.
- [4] **K. Huang**, H. Elsayed, G. Franchin, P. Colombo, Complex SiOC ceramics from 2D structures by 3D printing and origami, *Additive Manufacturing* 33 (2020) 101144.
- [5] Y. Feng, X. Guo, **K. Huang**, H. Elsayed, G. Franchin, H. Gong, P. Colombo, Enhanced electromagnetic microwave absorption of SiOC ceramics targeting the integration of structure and function, *Journal of the European Ceramic Society* 41 (2021) 6393-6405.
- [6] L. Biasetto, G. Franchin, H. Elsayed, G. Boschetti, **K. Huang**, P. Colombo, Direct Ink Writing of cylindrical lattice structures: A proof of concept, *Open Ceramics* 7 (2021) 100139.
- [7] G. Franchin, H. Elsayed, R. Botti, **K. Huang**, J. Schmidt, G. Giometti, A. Zanini, A. De Marzi, M. D'Agostini, P. Scanferla, Y. Feng, P. Colombo, "Additive manufacturing of ceramics from liquid feedstocks," submitted to *CJME:AMF*

List of conference presentations related to this thesis

1. **Kai Huang**, Giorgia Franchin, Hamada Elsayed, Paolo Colombo, Polymer-derived SiOC ceramics with complex architectures by direct ink writing and origami, yCAM 2019, Mons, Belgium (Poster)
2. **Kai Huang**, Hamada Elsayed, Giorgia Franchin, Paolo Colombo, Shakir Mujib, Santanu Mukherjee, Gurpreet Singh, Polymer-derived SiOC ceramics for energy storage applications, XVI EcerS Conference, Torino, Italy, 2019 (Oral presentation)
3. **Kai Huang**, Giorgia Franchin, Hamada Elsayed, Paolo Colombo, Direct Ink Writing of Polymer-Derived SiOC with Tunable and Hierarchical Porosity, 45th ICCAC-Virtual Only, 2021 (Oral presentation)
4. **Kai Huang**, Giorgia Franchin, Hamada Elsayed, Paolo Colombo, Embedded Direct Ink Writing of Freeform Ceramic Components, MS&T 21, October, 2021(Oral presentation)